Theoretical and experimental studies of wave impact underneath decks of offshore platforms

A thesis submitted in partial fulfillment of the
requirements for the degree of
doktor ingeniør
by

Rolf Jarle Baarholm

Trondheim, 2001

Department of Marine Hydrodynamics
Faculty of Marine Technology
Norwegian University of Science and Technology

Abstract

The main objective of this thesis has been to study the phenomenon of water impact underneath the decks of offshore platforms due to propagating waves. The emphasis has been on the impact loads. Two theoretical methods based on two-dimensional potential theory have been developed, a Wagner based method (WBM) and a nonlinear boundary element method (BEM). A procedure to account for three-dimensional effects is suggested. The deck is assumed to be rigid. Initial studies of the importance of hydroelasticity for wave loads on an existing deck structure have been performed. For a given design wave, the local structural responses were found to behave quasi-static. Global structural response has not been studied.

In the Wagner based method gravity is neglected and a linear spatial distribution of the relative impact velocity along the deck is assumed. The resulting boundary value problem is solved analytically for each time step. A numerical scheme for stepping the wetted deck area in time is presented.

The nonlinear boundary element method includes gravity, and the exact impact velocity is considered. The incident wave velocity potential is given a priori, and a boundary value problem for the perturbation velocity potential associated with the impact is defined. The boundary value problem is solved for each time step by applying Green's second identity. The exact boundary conditions are imposed on the exact boundaries. A Kutta condition is introduced as the fluid flow reaches the downstream end of the deck. At present, the BEM is only applicable for fixed platform decks.

To validate the theories, experiments have been carried out in a wave flume. The experiments were performed in two-dimensional flow condition with a fixed horizontal deck at different vertical levels above the mean free surface. The vertical force on the deck and the wetting of the deck were the primary parameters measured. Only regular propagating waves were applied.

When a wave hits the deck, the structure experiences a positive slamming dominated force (upward directed) during the initial water entry phase, followed by a negative force during the water exit phase. The force in the latter phase is dominated by a negative added mass force due to negative vertical fluid particle accelerations in the wave crest. The positive force peak is highly dependent on the impact condition and is especially sensitive to the initial deck clearance.

The magnitude of the negative force peak is less dependent on the impact condition. This peak occurs when the wetting of the deck is at its maximum and its magnitude may be larger than the positive force peak. Thus, the water exit phase is important for global effects. The initial impact yields the highest average pressures and is critical for local structural response in the deck.

Comparisons between experiments and theory have been performed for a number of impact conditions. Second order Stokes' theory is used to describe the incident waves. The Wagner based method describes the water entry phase well. Both the magnitude and the duration of the positive force peak are well predicted. The computations for the water exit phase are less satisfactory. The WBM overestimates the magnitude of the negative force peak and it underestimates the duration of the water exit phase.

In the nonlinear boundary element method, the impact induced vertical force on the deck is calculated by imposing conservation of fluid momentum and by using direct pressure integration. These two approaches yield similar force histories except during the final stage of water exit, where they tend to diverge. This is caused by inaccuracies in the numerical solution and in the formulation of the boundary value problem. The force at this stage is small. The BEM yields results that compare well with experiments for both the water entry and the water exit phase. Especially for the water exit phase the BEM is superior to the Wagner based method.

Acknowledgements

This work has been carried out under the supervision of Professor Odd M. Faltinsen at the Department of Marine Hydrodynamics, Norwegian University of Science and Technology. His contributions and continuous guidance are highly acknowledged.

The work was made possible by the financial support by Norsk Hydro. Dr. Kjell Herfjord at Norsk Hydro has supervised the study. His guidance and encouragement are appreciated.

My fellow students and the staff at the Department of Marine Hydrodynamics and the Department of Marine Structures deserve gratitude for encouragement and for making the process enjoyable both socially and scientifically. Special thanks go to Olav Rognebakke for numerous fruitful discussions, extensive assistance on computer related topics and for proofreading. Marilena Greco, Svein Ersdal and Gro S. Baarholm are also acknowledged for proofreading. I am also grateful to Ketil Foldal for feeding me and for letting me sleep on his sofa during my stays in Bergen.

My love and my gratitude go to my wife, Gro. Her patience and continuous support has been crucial.

Contents

Nomenclature

General Rules

- Symbols are generally defined where they appear in the text for the first time.
- Matrices and vectors are represented by bold face characters.
- Overdots signify differentiation with respect to time.
- log(x) returns the natural logarithm of x.
- sgn(x) returns the sign of x.

Subscripts

a	Amplitude value of an oscillating function
i	Fluid particle number, element number, DOF
max	Maximum value
min	Minimum value
D	Quantity due to disturbance
I	Quantity due to incident waves
FK	Froude-Kriloff load

Superscripts

exp	Experimental value
in	Inner expansion
j	Time increment number
out	Outer expansion
(∞)	High frequency limit

Roman symbols

$\mathbf{A}$	Added mass matrix
A_{ij}	Added mass matrix element no. ij
A_1	Dipole strength
A_2	Multipole strength
a	Radius of circular cylinder
$a(t)$	Earth-fixed coordinate of downstream body/ fluid intersection
B_{ij}	Damping matrix element no. ij
$\boldsymbol{B}$	Damping matrix
B	Breadth of deck, breadth of cylinder
b	Breadth of flange
$b(t)$	Earth-fixed coordinate of upstream body/ fluid intersection
$\boldsymbol{C}$	Restoring matrix
$c(t)$	Half-length of wetted area
C_D	Drag coefficient
D	Draft
E	Young's modulus
$\boldsymbol{F}_{\mathrm{exc}}$	Excitation vector
F_i	Exciting force in DOF i
g	Gravitational acceleration
H	Wave height
H_d	Design wave height
H_{100}	Wave height with 10^{-2} annual exceedance probability
H_{10000}	Wave height with 10^{-4} annual exceedance probability
$H_n(x)$	Hilbert transforms
H_S	Significant wave height
$H_{\eta\zeta}(\cdot)$	Transfer function
I	Area moment of inertia of cross section of beam
i	Complex unit,$i = \sqrt{-1}$
I_{down}	Downstream body/ free surface intersection
I_{up}	Upstream body/ free surface intersection
$J(\kappa)$	Correction factor for 3D-effects in WBM
$J_2(\kappa)$	Correction factor for 3D-effects in BEM
k	Wave number
k_θ	Spring stiffness
KC	Keulegan-Carpenter number
L	Length of platform deck
L	Length of beam
l_i	Length of i-th element in BEM
M_B	Mass per unit area of beam
$\boldsymbol{M}$	Mass matrix

N	Number of fluid particles
N	Number of elements
N_B	Number of elements on the body surface
N_F	Number of elements on the free surface
$\boldsymbol{n}$	Unit normal vector
$p - p_0$	Overpressure
p_0	Atmospheric pressure
r	Radial distance
S_B	Instantaneous wetted body surface
$\bar{S}_B$	Mean wetted body surface
S_F	Free surface
S_∞	Far field control surface
s	Curvilinear coordinate
t	Time
t_0	Time instant of first impact
Δt	Time step
$\overline{\Delta t}$	Time step normalized by the wave period
T	Wave period
T_d	Design wave period
T_{w1}	Wet eigenperiod of beam
u	Horizontal velocity
$\boldsymbol{U}$	Body velocity vector
U_n	Normal velocity of body
$U_{I_{down}}$	Velocity of I_{down}
$\boldsymbol{V}$	Fluid velocity vector
V_R	Relative impact velocity
V_0	Mean impact velocity
V_1	Slope of impact velocity distribution
W	Complex potential
w	vertical fluid velocity
(x, z)	Coordinate system used in boundary value problems
(x_0, z_0)	Earth fixed coordinate system
$(\tilde{x}, \tilde{z})$	Body fixed coordinate system
$(\hat{x}, \hat{z})$	Complex coordinate system
$\tilde{x}_A$	Downstream coordinate of wetted area
$\tilde{x}_b$	Far field coordinate
$\tilde{x}_F$	Upstream coordinate of wetted area
$\tilde{x}_L$	Far field upstream coordinate
$\tilde{x}_R$	Far field downstream coordinate
$\hat{y}$	Complex coordinate

Z	Complex coordinate

Greek symbols

α_{free}	Parameter in BEM
β	Dead rise angle
$\gamma(x)$	Vortex distribution
γ	Euler's constant 0.57721 56649...
δ_1	First order phase for forced oscillations
δ_a	Downstream jet thickness
δ_b	Upstream jet thickness
ζ	Wave elevation
ζ_I	Incident wave elevation
ζ_D	Wave elevation due to impact
$\ddot{\boldsymbol{\eta}}$, $\dot{\boldsymbol{\eta}}$ and $\boldsymbol{\eta}$	Acceleration, the velocity and displacement matrices
$\ddot{\eta}_i$, $\dot{\eta}_i$ and η_i	Acceleration, the velocity and displacement in degree of freedom i
η_{ag0}	deck clearance in still water
$\eta_{ag}(x,t)$	Instantaneous air gap
$\eta_z(x,t)$	Instantaneous deck clearance
θ	Polar coordinate
θ_i	Phase for i-th DOF
κ	Aspect ratio of wetted portion of the deck
λ	Wavelength
(ξ,η)	Source point
π	The constant 3.1415926...
σ	Standard deviation
τ	Complex coordinate
Φ	Total fluid velocity potential
Φ	Inner velocity potential
ϕ	Diffraction velocity potential
ϕ_I	Velocity potential of incident waves
ϕ_{loc}	Local velocity potential
ψ_{loc}	Local stream function
ω	Wave frequency
ω	Oscillation frequency
∇	Submerged volume

Abbreviations

2D	Two-dimensional
3D	Three-dimensional
BEM	Boundary element method
BVP	Boundary value problem
DOF	Degree of freedom
WBM	Wagner based method

Mathematical operators and other symbols

∇	Gradient (Hamilton) operator
∇^2	Laplace operator
$\sum$	Summation
$\lvert\ \rvert$	Absolute value (modulus)

CHAPTER 1

Introduction

1.1 Background and motivation

Water impact loads on offshore structures have been of concern for designers during the past 25 years. In the early years, the main interest was focused on impact forces on horizontal structural members located in the splash zone, see *e.g.* Dalton and Nash (1976), Kaplan and Silbert (1976), Faltinsen et al. (1977) and Sarpkaya (1978). Water impact on decks of platforms was of less concern.

It is common practice to design the lower deck of offshore platforms to be above the maximum predicted wave level. When the first generation of bottom-mounted platforms were designed, the knowledge was limited regarding wave heights and variability of environmental conditions with time. Even if the bottom-mounted platform is designed with a safe deck clearance, this will in many cases be reduced in time. This reduction can be caused by either settlement of the platform due to its own weight or by foundation subsidence and reservoir compaction. Therefore, the deck may be imposed to wave induced loads which were not accounted for in the original design. Due to these uncertainties in the safety level, it is important to accurately predict the hydrodynamic loads and the structural response due to wave impact underneath decks of existing fixed platforms. The significant level of subsidence at the Ekofisk field launched the need to re-examine all the platforms in the area with respect to wave impact, see *e.g.* Broughton and Horn (1987).

Health & Safety Executive (HSE (1998)) gives a review of requirements for air gap provision for fixed platform according to past, present and future guidelines. Different regional approaches from the UK (Health & Safety Executive), USA (American Petroleum Institute) and Norway (Norwegian Petroleum Directorate) are presented and compared with a draft ISO standard which is seeking to evolve a state-of-the-art position. The UK and US practices dictate a finite margin between the extreme wave crest and the deck at maximum tide, *e.g.* $\geq$ 1.5m air gap above 100

Figure 1.1: *Model test of semi-submersible in extreme waves.*

years design wave crest is recommended by API. The air gap accounts for settlement, subsidence, and uncertainties in environmental data. By contrast, Norwegian standards set no absolute value, but requires a sufficient air gap for the probability of structural damage to be less than 10^{-4} per year when all uncertainties are accounted for. The draft ISO standard is evolving towards the same approach.

When the oil and gas production moves to deeper waters, bottom-mounted platforms become less applicable. In deep water, floaters such as semi-submersibles are often used. Also for floaters it has been customary to neglect any probability of waves reaching the deck, relying on that the air gap provides a sufficient margin of safety. Even though water impact events have not been accounted for in the design, existing floaters have experienced damages from waves impacting on the lower deck structure. The deck height of floaters is limited by weight and stability considerations, and this makes the air gap a substantial cost driver for the platform. In the design of new floaters, one might allow some extreme waves to hit the deck structure. Reduction of deck clearance of existing floaters may occur when they are in damaged condition or due to failure in ballast systems. The deck clearance of existing floaters may also be decreased if higher production is desired. Accordingly, increased storage capacity and deck weight must be compensated by reduced deck clearance. This implies higher risk of wave impacts. A wave impact event is depicted in Figure 1.1. The snapshot is taken during a model test of a semi-submersible in extreme waves. A good structural design of the deck in this case requires accurate assessment of both wave kinematics and hydrodynamic load response due to wave impact. The latter will be the main topic of this work.

In addition to massive wave impact events similar to the one depicted in Figure 1.1, run-up of water along platform legs can also cause water impacts underneath platform decks. Impacts caused by run-up are localized in space and crucial for local structural responses, but they are unimportant for global effects. Run-up is not considered in this work.

1.2 Previous work

The general problem of hydrodynamic impact has been studied extensively motivated by *e.g.* its importance for horizontal members in the splash zone of offshore platforms, bottom and bow-flare slamming on ships, green water impact on deck structures of ships and wetdeck slamming on catamarans. Faltinsen (2000b) gives an overview of the many water impact problems in ship and ocean engineering. Water impact is also crucial for numerous problems within coastal engineering. First ground-breaking studies on water impact of solid bodies were performed by von Kármán (1929) and Wagner (1932). Von Karman analyzed the impact loads on sea plane floats during landing by imposing conservation of fluid momentum. Wagner modified von Karman's method to account for "pile-up" of water caused by the presence of the body. Further, Wagner studied the details of the flow at the spray roots, where the maximum pressure occurs for small local dead-rise angles. Both von Karman and Wagner assume two-dimensional flow and implicitly small local dead-rise angles. By local dead-rise angle it is meant the angle between the body surface tangent and the horizontal plane. These impact formulae inspired much research in the field of ship slamming. Zhao and Faltinsen (1992) studies the influence on the vertical acceleration of a catamaran due wave slamming on the wetdeck. Comprehensive reviews of works related to ship slamming are given in *e.g.* Kvålsvold (1994) and in Haugen (1999). Rognebakke and Faltinsen (2000) study the damping of sloshing motion due to fluid/ tank roof impact. Bow-stem slamming and green-water impact on deck structures are of concern for floating production, storage and offloading units (FPSO). Green-water problems are often associated with the "dam-breaking" problem. This is studied by *e.g.* Buchner (1995) and Greco et al. (2000). Korobkin and Pukhnachov (1988) give a good review of the numerical and analytical methods which have been used to study the initial stage of water impact with solid bodies. They focus on the effect of compressibility and find that in the initial stage of impact the flow will be supersonic.

The work performed on wave impact under platform decks is more limited, but it has been considered by many researchers. An early work on this topic was performed by ElGhamry (1963). He presented a theoretical and experimental investigation of the vertical forces on a horizontal dock due to periodic waves. His conclusion was that for non-breaking waves, two kinds of vertical forces act on the dock, namely an upward directed force caused by vertical fluid velocities and a downward force which originates from the negative pressures associated with the advancing of the trough under the dock.

Furudoi and Murota (1966) conducted an experimental investigation of the vertical force acting on an overhang at a wall due to impacting standing waves. They developed formulae for loads on protrusions in terms of water depth and standing wave properties. The same problem was later studied by Ramkema (1978), who included air cushion compression in the theoretical model.

An extensive study on wave induced uplift pressures on platforms was performed by French (1969). He carried out experiments on a fixed horizontal deck exposed to solitary waves. The positive pressures due to impact were found to be related to the wave celerity, and a simple theoretical formula was developed. Negative pressures were observed when the wave became detached from the platform. Following on from French's and from other experiments, Lai and Lee (1989) developed a Galerkin finite element method for this problem. Their numerical results compare well with the experiments.

Denson and Priest (1971) performed experiments to study the pressure distribution on the underside of an elevated horizontal deck in shallow water, due to impact of a solitary wave. The destructive effects of shallow water wave action on platforms during hurricanes were of concern. The experimental results were generalized by means of dimensionless parameters based on the wave height, the water depth, the initial deck clearance and the deck's length and width. Denson and Priest (1972) presented a study of the total vertical force on the deck for the same problem. They concluded that the maximum uplift force depends on the degree to which the structure interferes with the wave motion, and that it decreases with increasing water depth. No theoretical approach to the problem was attempted.

Cooker and Peregrine (1995) present a pressure-impulse theory for impact of an incompressible fluid on a solid surface or on a second fluid. Wood (1997) uses the pressure impulse theory to study wave impact on structures, and Wood and Peregrine (1998) extended this to study wave impact on a structure with trapped air.

Shih and Anastasiou (1989) and Shih and Anastasiou (1992) presented a laboratory study of wave induced up-lift pressures acting on a horizontal platform. Water was allowed to flow over the deck, and the wave crests used in the experiments greatly exceeded the deck clearance. They divide the pressure history into three phases. At the time instant when the wave hits the deck an impact pressure of high magnitude and short duration is exerted. To detect this pressure in the experiments, a very high sampling frequency must be applied. This initial phase is first followed by a slowly varying positive and then by a slowly varying negative pressure. Since the high pressure is very localized in space and time, the magnitude is generally not important for the structural response. The important quantity is the integrated force impulse acting on the structure causing local hydroelastic vibration. This is noted in Faltinsen (1997). Kvålvold et al. (1995) presented measured peak pressures on a plate from drop tests on waves. The results for a given wave and a given drop speed showed a tremendous scatter while the resulting maximum strains were not sensitive. Kvålvold et al. (1995) concluded therefore that focus on the peak pressure itself may be misleading from a design point of view.

The subsidence of Ekofisk, launched several studies on the wave loading and on the structural response due to deck impact. Broughton and Horn (1987) performed a re-analysis of the Ekofisk platform 2/4C. They obtained theoretical results for the maximum vertical force on the deck during water entry by considering a slamming force from a von Karman type of approach. No estimate of the water exit force was found. A more extensive theoretical analysis procedure for the assessment of the impact loading is given by Kaplan (1992). His model considers also the water exit force, *i.e.* the force when the wetted area diminishes. Also Kaplan uses a von Karman approach, but he includes both the slamming force and the added mass force due to the wetting of the deck. In addition, he includes a drag force by using a drag coefficient for viscous flow passed a flat plate. However, the physical basis for using a drag formulation can be questioned since viscous flow separation does not occur in the present problem. The fluid velocities and accelerations within the crest region, are represented in a similar manner as in linear theory, but nonlinear Wheeler stretching relations are used. In Kaplan et al. (1995) theoretical results for both solid and porous decks are compared to experiments by Murray et al. (1995). Kaplan's method describes the maximum impact force well, while the scatter between theory and experiments is somewhat larger for the negative water entry force. The duration of the water entry/ water exit process is not discussed. According to HSE (1998), Kaplan's approach is state-of-the-art in predicting impact loads on platform decks.

1.3 Outline of the thesis

The thesis is roughly divided into three main parts, which are presented according to the temporal evolution of this work.

The first part describes a Wagner based method for solving water impact underneath an impermeable deck of a fixed or a floating platform, due to incident propagating waves. This part is covered in Chapter 2 and Chapter 3. In the former the theoretical background for the method is presented. A hydrodynamic boundary value problem is defined and an analytical solution is derived. Expressions for the impact loading in both two-dimensional and three-dimensional flow conditions are given. In the latter the numerical scheme for solving wave-in-deck events by the Wagner based method is outlined. Assumptions and limitations are discussed and a parametric study is carried out.

The second part of the thesis concerns the experimental work performed. This is presented in Chapter 4, where the experimental program is described and the findings are discussed. Comparisons between results from laboratory tests and theoretical results obtained by using the Wagner based method are presented and discussed.

Chapter 5 and Chapter 6 cover the third of the main parts, dealing with boundary element methods. Chapter 5 starts out by discussing the motivations for developing a boundary element method (BEM) to study the wave-in-deck problem. Further, the mathematical formulation for two-dimensional boundary element methods is outlined. A linear BEM and a fully nonlinear BEM for forced oscillations of cylinders have been developed and validated. In Chapter 6 the developed nonlinear BEM is extended to solve the deck impact problem. The method is described and discussed. Numerical results are compared with the experiments.

Finally, in Chapter 7 the main conclusions are listed and some suggestions for further research are given.

1.4 Contributions of the thesis

From the author's point of view, three main contributions can be addressed to work, each of them associated with the corresponding main part outlined in Section 1.3.

The first contribution is the development of the Wagner based method. This is a simple method for analyzing water impact on platform decks, and it is solved by establishing a boundary value problem similar to the one presented in Zhao and Faltinsen (1992) for slamming on the wetdeck of catamarans. The main enhancement when comparing with the analysis procedure described by Kaplan (1992), is that the present method accounts for the free surface deformations caused by the impact and ensures a better description of the wave kinematics. The Wagner based method is applicable for floaters. But Kaplan (1987) has also applied his von Karman based method to moving bodies. He considers flat bottom slamming on advanced marine vehicles. Two-dimensional theory is applied for the Wagner based method , but an estimate of three-dimensional effects is given. Knowing its limitations, designers may use this method to obtain good estimates for impact loads and rigid body responses.

The experiments represent a valuable contribution. The impact conditions tested in the laboratory are documented, and time series of both the loading on the deck and the wetting of the deck are given for all cases. This may be a valuable source of reference for researchers who want to validate theories for such impact events. Efforts have been made to properly describe the physics of the problem, and the use of pictures and sketches in the description has been emphasized.

The final contribution of this thesis comes from the nonlinear boundary element method for deck impact. This method yields results that compare well with experiments for both the water entry phase and the water exit phase. Especially for water exit, this method is superior to the Wagner based method and Kaplan's approach. Its weaknesses are also discussed.

This work has partially been discussed in Baarholm and Faltinsen(2000, 2001) and in Baarholm et al. (2001).

CHAPTER 2

The hydrodynamic formulation for the Wagner based method

2.1 Introduction

The impact theories by von Kármán (1929) and Wagner (1932) facilitates the derivation of simple analytical solutions for the initial impact of circular cylinders and wedges on a calm free surface, see *e.g.* Faltinsen (1990). The simple expressions provide satisfactory results for wedges with small dead-rise angles. The discrepancies between the analytical results and those of more refined methods, such as a fully nonlinear boundary element method, increases for increasing dead-rise angle. Zhao et al. (1996) developed a generalized Wagner's method for slamming of two-dimensional bodies. This method differs from the analytical one, since it uses the exact body boundary condition. By using Green's second identity to solve the velocity potential on the body, Zhao et al. (1996) obtained good results for slamming of wedges with finite dead-rise angles.

Motivated by these results, it was decided to develop a method analogous to the generalized Wagner's method for solving wave impact underneath deck's of offshore platforms. The problem to be solved is the impact process of a wave that reaches the deck at the front end of a platform and propagates downstream along the length of the deck. The main target of this work is to determine the time evolution of the hydrodynamic forces and moments acting on the deck. For a floater, the rigid body response due to the water impact must also be found simultaneously, since this affects the hydrodynamic impact loading on the deck.

In this chapter, the theoretical bases for the method will be described. In the following, this method is denoted as the Wagner based method.

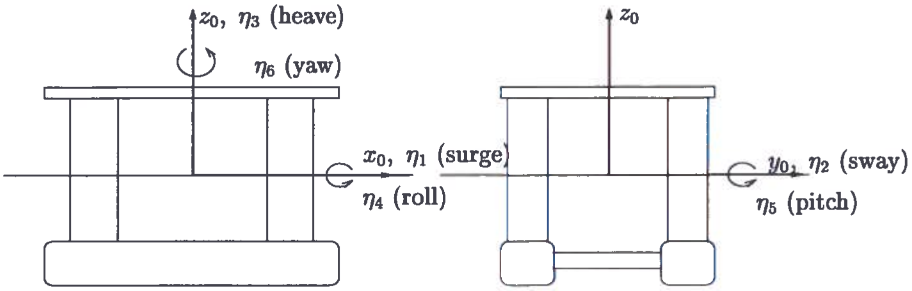

Figure 2.1: *Definition of rigid body motion modes.*

2.2 Definition of motions and coordinate systems

Propagating incident waves are assumed. The rigid body motion is described by six degrees of freedom with respect to a global coordinate system, (x_0, y_0, z_0). The (x_0, y_0, z_0)-coordinate system is earth fixed and attached to the mean body position, *i.e.* no drift forces are assumed and thus the body has zero mean velocity. The coordinate system is right-handed, with positive z_0-axis vertically upwards through the body's center of gravity. The x_0y_0-plane is located on the undisturbed free surface. Let the oscillatory translatory displacements parallel to the x_0-, y_0-, and z_0-axis be referred to as surge, sway, and heave respectively, and denoted as η_1, η_2, and η_3. The angular oscillatory displacements of the rotational motions about the same axes are denoted as η_4, η_5, and η_6, *i.e.* roll, pitch and yaw respectively. See the illustration in Figure 2.1.

A two-dimensional problem is assumed. Accordingly, the y_0-axis can be omitted. This is the situation shown in Figure 2.2, where the waves propagate along the positive x_0-axis. Small body motions are assumed so that $\sin\eta_5 \approx \eta_5$ and that $\cos\eta_5 \approx 1$. Three coordinate systems are shown in the figure. The $(\tilde{x}, \tilde{z})$-coordinate system is right-handed and body fixed. Its axes and origin are located so that the coordinate system coincides with the global earth-fixed coordinate system when the body is in its mean position. The relationship between the body fixed and the earth fixed coordinate systems may be written as

$$x_0 = \tilde{x} + \eta_1 \quad \text{and} \quad z_0 = \tilde{z} + \eta_3 - \tilde{x}\eta_5 \tag{2.1}$$

The third coordinate system has its origin in the center of the instantaneous wetted part of the deck. The front end, or upstream end, of the wetted length is defined as $\tilde{x}_F$, while the aft end, or downstream end, of the wetted length is denoted as $\tilde{x}_A$, when measured in the body-fixed $\tilde{x}\tilde{z}$-reference frame. Similarly to the notation used in Faltinsen (1990) for impact problems, half of the wetted deck length is denoted as c, so that the total length of the wetted part of the deck is equal to $2c$. This gives the following relations between the xz- and the $\tilde{x}\tilde{z}$-coordinate systems.

$$x = \tilde{x} - \tilde{x}_F - c \quad \text{and} \quad z = \tilde{z} - \eta_{ag0} \; , \tag{2.2}$$

where η_{ag0} is the deck clearance in still water. The different coordinate systems are shown in Figure 2.2.

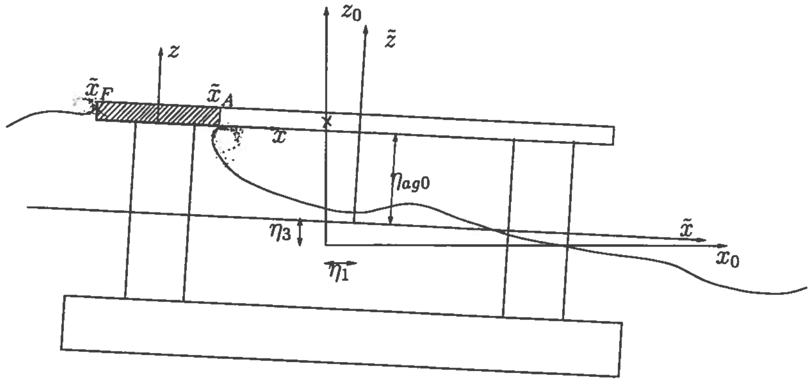

Figure 2.2: *The coordinate systems used in the calculations. The shaded area defines the wetted length of the deck.*

For the case with a bottom mounted platform the two first coordinate systems will be equal, and the x_0z_0-coordinate system will be obsolete.

2.3 The hydrodynamic boundary value problem

Two-dimensional, irrotational flow and an incompressible fluid are assumed. Accordingly, potential flow theory is applied and viscous effects are neglected. The approximation of two-dimensional flow requires head or beam sea and that the incident waves are long relative to the diameter of the platform legs, see Section 3.2.2. A velocity potential $\Phi = \phi + \phi_I$ is introduced to describe the flow around the platform. ϕ and ϕ_I are the velocity potential associated to the disturbances due to the impact and the velocity potential of the undisturbed incident waves, respectively. A hydrodynamic boundary value problem for the perturbation velocity potential ϕ can be set up for each time instant and for a given wetted body area.

The fluid flow is governed by the two-dimensional Laplace equation,

$$\nabla^2\phi = \frac{\partial^2\phi}{\partial x^2} + \frac{\partial^2\phi}{\partial z^2} = 0 \ , \tag{2.3}$$

which must be satisfied in the entire fluid domain. To solve Equation (2.3), boundary conditions on both the free surface and the wetted body surface are also required.

2.3.1 The free surface conditions

The dynamic free surface condition is obtained from Bernoulli's equation by imposing atmospheric pressure on the free surface. It is assumed that the impact occurs over a small time instant, meaning that the gravitational acceleration g is negligible relative to the impact induced fluid accelerations, and that the rate of change of ϕ with time is generally larger than the rate of change of ϕ with respect to the spatial coordinates. This gives $\frac{\partial\phi}{\partial t} = 0$ on the free surface. Since the initial value of ϕ is zero, this gives $\phi = 0$ on the free surface. When solving the boundary value problem this condition is applied on the horizontal line $z = 0$, *i.e.* the dynamic free surface condition becomes

$$\phi = 0 \qquad \text{on} \quad z = 0 \tag{2.4}$$

This condition implies that no waves will be generated. This dynamic free surface condition if often used in impact studies, starting with von Kármán (1929). Wagner (1932) used this condition in the outer domain (*i.e.* outside the spray root).

In addition, the kinematic free surface condition states that a fluid particle on the free surface remains on the free surface. Also the kinematic condition is satisfied on $z = 0$.

2.3.2 The body boundary condition

The body boundary condition is defined as

$$\frac{\partial \Phi}{\partial n} = \mathbf{U} \cdot \mathbf{n} \qquad \text{on the wetted body surface} \tag{2.5}$$

where $\frac{\partial}{\partial n}$ denotes differentiation along the normal direction to the body surface, $\mathbf{U}$ is the velocity of the body, and $\mathbf{n} = (n_1, n_3)$ is the unit normal vector of the body surface. $\mathbf{n}$ is positive into the fluid domain. In principle, $\mathbf{U}$ gets contributions from both rigid body motions and from flexible modes. For a fixed, rigid body the right hand side of Equation (2.5) becomes zero.

Solving for $\frac{\partial \phi}{\partial n}$, Equation (2.5) becomes

$$\frac{\partial \phi}{\partial n} = \mathbf{U} \cdot \mathbf{n} - \frac{\partial \phi_I}{\partial n} \qquad \text{on the body surface} \tag{2.6}$$

For impact with small local dead-rise angle, *i.e.* small angle between the body surface and the free surface at their intersections, Equation (2.6) may be approximated as, Faltinsen (1990);

$$\frac{\partial \phi}{\partial z} = -V_R(x, t) \qquad \text{on} \quad z = 0 \quad \text{and} \quad |x| < c(t) \tag{2.7}$$

where V_R is the relative impact velocity. $2c(t)$ is an approximation of the wetted length of the deck. The boundary value problem for ϕ is illustrated in Figure 2.3. The shaded rectangle symbolizes the instantaneous wetted area, and the xz-coordinate system has its origin at the center of this area. The relative impact velocity, $V_R(x, t)$, is a function of both space and time. In the section below, the solution of this boundary value problem will be discussed.

2.4 Derivation of the velocity potential

The classical impact problem, with $\phi = 0$ on $z = 0$ and spatially constant V_R, yields analytical expressions for the velocity potential on the body and for the fluid velocity at the free surface. Kvålsvold (1994) and Haugen (1999) study the impact on the wet deck of catamarans. They

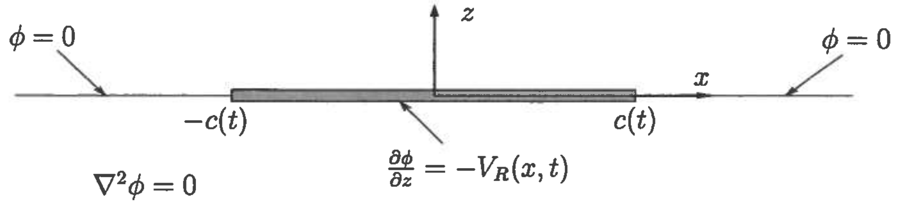

Figure 2.3: *The linearized hydrodynamic boundary value problem.*

apply the high frequency free surface condition (*i.e.* $\phi = 0$) but assume that the structural responses of the deck are important for the hydrodynamic loading and must be accounted for. They write the normal velocity of the body in terms of a Fourier cosine series when they solve the boundary value problem. In this work it is assumed that the flexible modes in the deck may be neglected and that spatial variation of V_R can be approximated by a linear function. A similar assumption is made by Zhao and Faltinsen (1992). This will be discussed in Section 3.2.4. The body boundary condition can now be written as

$$\frac{\partial\phi}{\partial z} = -V_0 - V_1 x \qquad \text{on } z = 0 \text{ and } |x| < c(t) \tag{2.8}$$

In order to approach this problem mathematically, a dimensionless boundary value problem is introduced. This is shown in Figure 2.4. The boundary value problem is on the same form as the lifting problem, discussed in Newman (1977). Newman solved this problem by using a distribution of potential vortices along the wetted length, and here an identical approach will be pursued.

The general solution for the vortex distribution γ is on the form

$$\gamma(x) = \frac{2}{\pi}\frac{1}{(1-x^2)^{\frac{1}{2}}}\left\{ ⨍_{-1}^{1} \frac{V(\xi)(1-\xi^2)^{\frac{1}{2}}}{\xi - x}\, d\xi + C \right\} \tag{2.9}$$

where $⨍$ denotes the principle value integral and C is a constant that is determined by an additional condition analogous to the Kutta condition for the lifting problem. $V(\xi)$ is the relative impact velocity on the wetted part of the body surface.

Assumed $V(\xi) = -V_0 - V_1\xi$ and introducing this expression in Equation (2.9), the vortex distribution can be written in terms of the so-called Hilbert transforms $H_n(x)$, defined as

$$H_n(x) = ⨍_{-1}^{1} \frac{\xi^n\, d\xi}{(\xi - x)(1-\xi^2)^{\frac{1}{2}}} \ ,$$

since

$$⨍_{-1}^{1} \frac{(1-\xi^2)^{\frac{1}{2}}\, d\xi}{\xi - x} = ⨍_{-1}^{1} \frac{(1-\xi^2)\, d\xi}{(\xi - x)(1-\xi^2)^{\frac{1}{2}}} \tag{2.10}$$

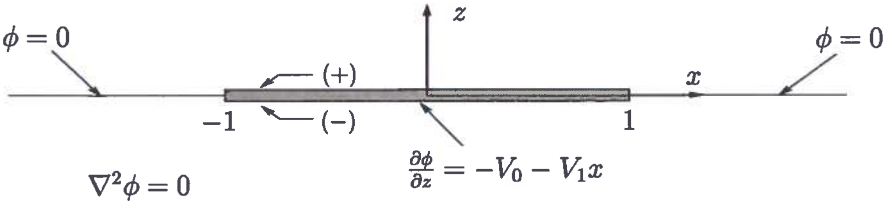

Figure 2.4: *The dimensionless boundary value problem. The length parameters are made dimensionless by dividing by instantaneous chord length, c. The (+) indicates the upper side of the cut, $z = 0^+$, and the (−) indicates the lower side, $z = 0^-$, see Equations (2.12) and (2.13).*

The solution of $H_n(x)$ is given in Newman (1977). In particular, $H_0(x) = 0$ and the solution for $n \geq 1$ is given by

$$H_n(x) = I_{n-1} + xH_{n-1}(x)$$

where

$$I_n(x) = \int_{-1}^{1} \frac{x^n dx}{(1-x^2)^{\frac{1}{2}}} = \begin{cases} \pi \frac{1 \cdot 3 \cdot 5 \cdot \ldots \cdot (n-1)}{2 \cdot 4 \cdot 6 \cdot \ldots \cdot (n)}, & n \text{ even} \\ 0, & \text{otherwise.} \end{cases}$$

In this specific case, n up to 3 is involved. By using the solution for H_n, the constant and the linear terms of the velocity distribution give

$$\int_{-1}^{1} \frac{-V_0(1-\xi^2)\,d\xi}{(\xi - x)(1-\xi^2)^{\frac{1}{2}}} = +V_0\pi x \quad \text{and} \quad \int_{-1}^{1} \frac{-V_1\xi(1-\xi^2)\,d\xi}{(\xi - x)(1-\xi^2)^{\frac{1}{2}}} = -V_1\left(\frac{\pi}{2} - \pi x^2\right),$$

for the integral in (2.9). Thus, the expression for the vortex distribution can be written as

$$\gamma(x) = \frac{2}{\pi}\frac{C}{(1-x^2)^{\frac{1}{2}}} + \frac{2V_0 x}{(1-x^2)^{\frac{1}{2}}} - \frac{V_1}{(1-x^2)^{\frac{1}{2}}} + \frac{2V_1 x^2}{(1-x^2)^{\frac{1}{2}}} \tag{2.11}$$

From the lifting problem discussed by Newman (1977), it is known that the velocity components induced on the body, by the vortex distribution $\gamma(x)$, are given by

$$u_\pm = \frac{\partial\phi_\pm}{\partial x} = \mp\frac{1}{2}\gamma(x) \tag{2.12}$$

and

$$w_\pm = -\frac{\partial\phi_\pm}{\partial z} = -\frac{1}{2\pi}\int_{-1}^{1} \frac{\gamma(\xi)}{\xi - x}\,d\xi\ , \tag{2.13}$$

where u and w are the horizontal and vertical velocity, respectively. The signs in the subscript indicates whether it is refers to the velocity on top (+) of the cut or on the underside (−) of the cut (see Figure 2.4). In the present case only the velocities on the underside of the cut are of physical interest. By inserting Equation (2.9) into Equation (2.12), it becomes possible to find an expression for the velocity potential on the underside of the cut in the form of

$$\begin{aligned}\phi(x, z=0^-) &= \int_{-1}^{x} \frac{1}{2}\gamma(\xi)\, d\xi \\ &= \frac{C}{\pi}\left(\sin^{-1} x + \frac{\pi}{2}\right) - V_0\sqrt{1-x^2} - \frac{1}{2}V_1 x\sqrt{1-x^2}\end{aligned} \tag{2.14}$$

Assuming that the velocity potential associated with V_0 is symmetric about $x = 0$ and the velocity potential associated with V_1 is anti-symmetric about $x = 0$, implies $C = 0$. In the so-called lifting problem C is determined by the Kutta condition at the trailing edge. Since an ambient horizontal velocity also is present in the present problem, one may have imposed a Kutta condition. Later in Chapter 6 when the boundary element method is used, the Kutta condition is imposed in the solution. In dimensional terms, the velocity potential now becomes

$$\phi(x) = -V_0\sqrt{c^2-x^2} - \frac{1}{2}V_1 x\sqrt{c^2-x^2} \quad \text{on } z=0,\ |x| \le c \tag{2.15}$$

The chord length $c(t)$ is still unknown. To determine the wetted length of the deck, $2c(t)$, the vertical fluid velocity on the free surface has to be found. This requires the complex velocity potential, W, to be known in the whole fluid domain. This is found by setting up an expression that is consistent with Equation (2.15) and that satisfies the boundary conditions. The complex potential is expressed as

$$W = -V_0\sqrt{c^2-Z^2} - \frac{1}{2}V_1 Z\sqrt{c^2-Z^2} + iV_0 Z + i\frac{1}{2}V_1 Z^2\ , \tag{2.16}$$

where the complex variable $Z = x + iz$ and i is the complex unit. $Z + c$ and $Z - c$ are defined as in Figure 2.5 where $-\pi < \theta_i < \pi$. Since $W = \phi + i\psi$, one can note that expression (2.16) is consistent with (2.15) for $z = 0$ and $|x| \le c(t)$, and that $\phi = 0$ on $z = 0$ outside the body. The complex potential must also satisfy the body boundary condition. The complex velocity can be written as

$$\begin{aligned}\frac{dW}{dZ} &= u(x,z) - iw(x,z) \\ &= \frac{V_0 Z}{\sqrt{c^2-Z^2}} - \frac{1}{2}V_1\sqrt{c^2-Z^2} + \frac{1}{2}\frac{V_1 Z^2}{\sqrt{c^2-Z^2}} + iV_0 + iV_1 Z\end{aligned} \tag{2.17}$$

On the wetted body surface, *i.e.* at $|x| \le c(t)$ and $z = 0$, this yields the following real horizontal and vertical velocities:

$$\begin{aligned}u &= \frac{V_0 x}{\sqrt{c^2-x^2}} - \frac{1}{2}V_1\sqrt{c^2-x^2} + \frac{1}{2}\frac{V_1 x^2}{\sqrt{c^2-x^2}} \\ &= \frac{V_0 x}{\sqrt{c^2-x^2}} - \frac{1}{2}\frac{V_1 c^2}{\sqrt{c^2-x^2}} + \frac{V_1 x^2}{\sqrt{c^2-x^2}}\end{aligned} \tag{2.18}$$

and

$$w = -V_0 - V_1 x \tag{2.19}$$

The vertical velocities in Equation (2.8) and in Equation (2.19) are equal, *i.e.* the suggested complex potential satisfies the boundary condition on the body. Similarly, Equation (2.18) and Equation (2.11) can be compared. One stress that $u = \frac{1}{2}\gamma$ on body, that Equation (2.11) was developed for a dimensionless chord length and that the constant C is set equal to zero. From this it can be concluded that, consistently with the boundary value problem defined in Figure 2.4, the complex potential in Equation (2.16) yields the correct velocities on the wetted part of the deck.

Note that this solution gives zero fluid velocities at infinite distance from the body. Far away from the body $\sqrt{c^2 - Z^2} = iZ\left(1 - \frac{1}{2}(\frac{c}{Z})^2 - O(\frac{c}{Z})^4\right)$ and $\frac{1}{\sqrt{c^2-Z^2}} = -\frac{i}{Z}\left(1 + \frac{1}{2}(\frac{c}{Z})^2 + O(\frac{c}{Z})^4\right)$, and the complex velocity can be written as

$$\begin{aligned}\frac{dW}{dZ} &\approx -iV_0\left(1 + \frac{1}{2}\left(\frac{c}{Z}\right)^2\right) - \frac{i}{2}V_1 Z\left(1 - \frac{1}{2}\left(\frac{c}{Z}\right)^2\right) \\ &\quad - \frac{i}{2}V_1 Z\left(1 + \frac{1}{2}\left(\frac{c}{Z}\right)^2\right) + iV_0 + iV_1 Z \\ &= -\frac{i}{2}\frac{V_0 c^2}{Z^2}\end{aligned} \tag{2.20}$$

This means that the velocities due to the impact tend to zero as Z^{-2} away from the body.

The suggested complex potential given in Equation (2.16) satisfies the boundary value problem sketched in Figure 2.3 with $V_R(x,t) = V_0 + V_1 x$. The vertical velocity on the free surface, *i.e* at $|x| \geq c(t)$ and $z = 0$, can now be derived from the complex velocity. For simplicity, the square root expression is rewritten by introducing polar coordinates as

$$\sqrt{c^2 - Z^2} = \sqrt{r_1\, r_2}\; e^{i\frac{1}{2}(\theta_1+\theta_2)+i\frac{\pi}{2}} \tag{2.21}$$

where the definition of the symbols in (2.21) are given in Figure 2.5. The square root expression for the two different cases, $x < -c(t)$ and $x > c(t)$, must be examined. This is done by setting, respectively, $\theta_1 = \theta_2 = 0$ and $\theta_1 = \theta_2 = -\pi$ in Equation (2.21). For the first case the square root expression is equal to $i\sqrt{x^2 - c^2}$, while for the latter case it is equal to $-i\sqrt{x^2 - c^2}$. This means that the vertical velocity on the free surface can be written as:

$$\frac{\partial\phi}{\partial z} = \frac{V_0|x|}{\sqrt{x^2 - c^2}} + \frac{1}{2}\operatorname{sgn}(x)V_1\left(\sqrt{x^2 - c^2} + \frac{x^2}{\sqrt{x^2 - c^2}}\right) - V_0 - V_1 x \tag{2.22}$$

for $|x| > c(t)$.

Except from the signs, which are opposite due to a different body boundary condition, Equation (2.22) and Equation (2.15) are the same as the expressions given in Zhao and Faltinsen (1992). Note that the vertical velocity is singular at the body/ free surface intersections.

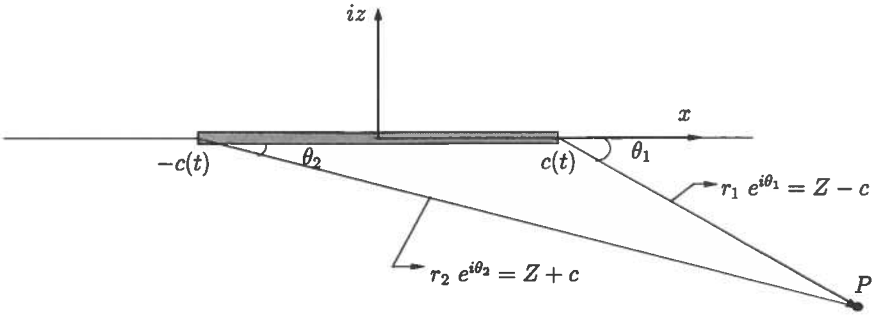

Figure 2.5: *The distance from the ends of the cut to an arbitrary point P in the fluid.*

2.5 Impact pressure and normal force on the deck

Once the perturbation velocity potential on the body is known, an expression for the impact pressure on the deck may be derived. The hydrodynamic pressure on the deck follows from Bernoulli's equation. Assuming large fluid accelerations implies that the impact event has short duration and that the rate of change of ϕ with respect to time, is generally larger than the rate of change with respect to the spatial coordinates. This means that the velocity squared term $-\frac{1}{2}\rho|\nabla\phi|^2$ can be neglected relative to $-\rho\frac{\partial\phi}{\partial t}$. This is consistent with neglecting the velocity squared term in the free surface condition in the outer fluid domain. In the inner domain discussed below, however, the velocity squared term is important. A first approximation for the dynamic fluid pressure on the body due to ϕ is given by

$$p - p_0 = -\rho\frac{\partial\phi}{\partial t} \tag{2.23}$$

The $-\rho\frac{\partial\phi}{\partial t}$ term is determined for the velocity potential as given in Equation (2.15). In this context and in the rest of this section the pressure due to ϕ_I is disregarded. Its contributions to the total pressure is discussed in Section 3.4. In the following discussion, the upstream and downstream body/ free surface intersection will be denoted as $a(t)$ and $b(t)$, respectively, in earth fixed coordinates, so that $x(t) = x_0 - (a(t) - c(t))$ or $x(t) = x_0 - (b(t) + c(t))$. Figure 2.6 illustrates the relationship between the coordinates. By exerting this relationship, the following expression for the impact pressure on the wetted body surface is obtained as

$$\begin{aligned} p_{\text{outer}} - p_0 = {} & \rho(V_0 + \frac{1}{2}V_1 x)\frac{\left[c\frac{dc}{dt} + x\left(-\frac{dc}{dt} + \frac{da}{dt}\right)\right]}{\sqrt{c^2 - x^2}} \\ & + \rho\left[\frac{\partial V_0}{\partial t} + \frac{1}{2}\frac{\partial V_1}{\partial t}x + \frac{1}{2}V_1\left(\frac{dc}{dt} - \frac{da}{dt}\right)\right]\sqrt{c^2 - x^2} \end{aligned} \tag{2.24}$$

Since the pressure obtained from Equation (2.24) is singular at the body/ free surface intersections, the hydrodynamic pressure must be studied in more detail. The singular pressure is a consequence of incorrect free surface conditions in the immediate vicinity of $|x| = c(t)$, thus the solution is not valid in this region.

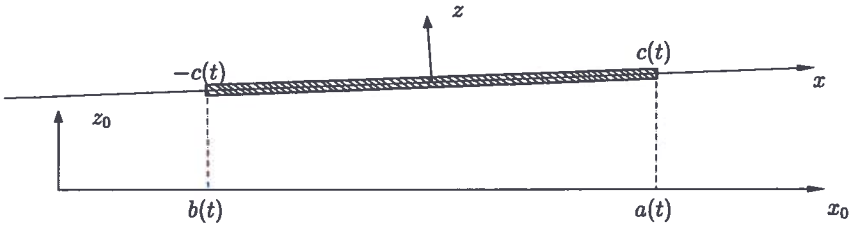

Figure 2.6: *The relationship between the local and the earth fixed coordinate system.*

The free surface condition $\phi = 0$ was obtained by neglecting gravity and the velocity squared terms in the exact free surface conditions, but the solution of the boundary value problem leads to singular vertical velocities at the intersection points. To obtain the correct pressure in the vicinity of the body/ free surface intersections, an inner solution to account for the jets that will develop at the intersections must be derived. Wagner (1932) uses a local jet solution to find the pressure distribution close to the jet root, *i.e.* near $|x| = c(t)$. At small dead-rise angles it is possible to use Wagner's analysis in combination with matched asymptotic expansion to solve the boundary value problem. Armand and Cointe (1986) did that when studying water impact of a circular cylinder. Zhao and Faltinsen (1993) use Wagner's solution for an inner region together with a matched asymptotic expansion, to find a composite solution for the velocity potential and the pressure valid everywhere along the body. The same procedure will be followed here to determine a composite solution for the pressure in the region $0 \leq x \leq c(t)$.

2.5.1 Inner expansions of outer solutions

The inner expansions of the *outer* velocity potential ϕ and the *outer* pressure on the body near the downstream intersection $\tilde{x} = a(t)$ is obtained by letting $x \to c(t)$ on the body. This implies that $c^2 - x^2 \approx 2c(c - x)$, which gives the inner expansions of the *outer* velocity potential and the *outer* pressure as

$$\begin{aligned} \phi^{\text{in}} &= -(V_0 + \frac{1}{2}V_1 c)\sqrt{2c(c-x)} \\ &= -(V_0 + \frac{1}{2}V_1 c)\sqrt{2c(a-x_0)} \end{aligned} \tag{2.25}$$

and

$$\begin{aligned} (p_{\text{outer}} - p_0)^{\text{in}} &= \rho(V_0 + \frac{1}{2}V_1 c)\frac{c\frac{da}{dt}}{\sqrt{2c(c-x)}} \\ &= \rho(V_0 + \frac{1}{2}V_1 c)\frac{c\frac{da}{dt}}{\sqrt{2c(a-x_0)}} \end{aligned} \tag{2.26}$$

respectively. Similarly, inner expansions near the upstream body/ free surface intersection $\tilde{x} = b(t)$ are determined by letting $x \to -c(t)$ on the body.

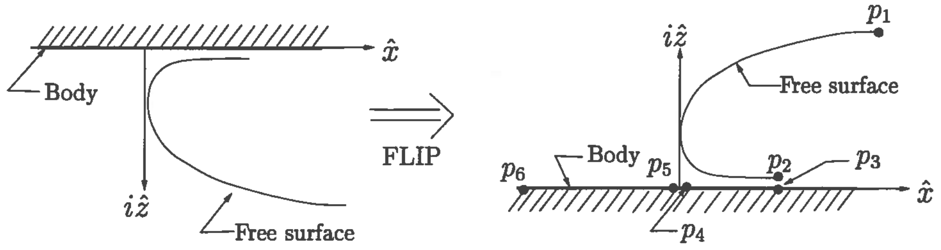

Figure 2.7: *The steady system that follows the spray root*

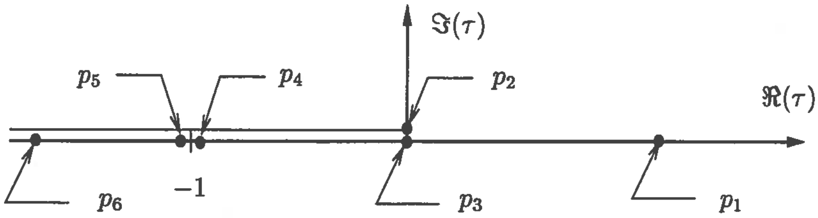

Figure 2.8: *The boundary value problem mapped onto the complex τ-plane. The points p_i corresponds to the transformed values of the corresponding points indicated in Figure 2.7.*

2.5.2 Inner solution of the impact pressure

The intersection point between the body and free surface in the outer flow solution moves tangentially to the body with a velocity $\dot{a}(t)$ relative to the earth fixed coordinate system. A new local reference frame, the $\hat{y}$-plane, that moves with this velocity is introduced in the inner flow. The complex coordinate is given by $\hat{y} = \hat{x} + i\hat{z}$. In this reference system the problem is steady. Next, an auxiliary complex τ-plane is introduced. The relationship between the $\hat{y}$-plane and the τ-plane is given by the conformal mapping, Wagner (1932);

$$\hat{x} + i\hat{z} = \frac{\delta_a}{\pi}\left[\log\left(-\frac{1}{\tau}\right) + 4i\sqrt{\tau} + \tau + 5\right] \tag{2.27}$$

where the quantity δ_a is defined as the thickness of the spray at $x_0 = a$. The jet is mapped onto $\tau = 0$, the free surface is transformed onto the positive real axis, and the body onto the negative real axis, see Figure 2.7 and Figure 2.8.

On the body, $\tau = -|\tau|$. This means that

$$x_0 - a = x - c = \hat{x} = \frac{\delta_a}{\pi}\left[\log|\tau| - 4i\sqrt{|\tau|} - |\tau| + 5\right] \tag{2.28}$$

The inner flow potential is according to Wagner

$$\Phi = -U\frac{\delta_a}{\pi}\left(1 + \log|\tau| - |\tau|\right) \tag{2.29}$$

2.5.3 Matching of inner and outer solutions

The outer expansion for the inner potential is found by letting $|\tau| \to \infty$. This gives the following expressions

$$\hat{x} = -\frac{\delta_a}{\pi}|\tau| \tag{2.30}$$

and

$$\Phi \approx U\frac{\delta_a}{\pi}|\tau| = -U\hat{x} \tag{2.31}$$

for the leading order terms of the real coordinate $\hat{x}$ and of the inner potential Φ

One must recall that the origin of the $\hat{y}$-plane moves with the body/ free surface intersection found in the outer flow solution. In order to compare the two solutions, they must be described in the same reference frame. The inner solution is therefore rewritten as

$$\phi_{\ \mathbf{inner}} = \Phi + U\hat{x} \tag{2.32}$$

where U is the propagation velocity of the spray root relative to the earth-fixed coordinate system, *i.e.* $U = \frac{da}{dt}$ for the downstream jet. From Equation (2.31) and Equation (2.32) it follows that in order for $\phi_{\mathbf{inner}}$ to be different form zero, one more term must be kept in the expansion of $\hat{x}$:

$$\hat{x} = \frac{\delta_a}{\pi}\left[-4\sqrt{|\tau|} - |\tau|\right] \tag{2.33}$$

The expression for the inner potential can then be found as

$$\phi_{\mathbf{inner}} = -4\frac{\mathrm{da}}{\mathrm{dt}}\frac{\delta_a}{\pi}\sqrt{\frac{|\hat{x}|\pi}{\delta_a}} \tag{2.34}$$

From this one the outer expansion follows as

$$\begin{aligned}(\phi_{\mathbf{inner}})^{\mathrm{out}} &= -4\frac{da}{dt}\sqrt{\frac{\delta_a}{\pi}}\sqrt{|x_0 - a|} \\ &= -4\frac{da}{dt}\sqrt{\frac{\delta_a}{\pi}}\sqrt{|x - c|}\end{aligned} \tag{2.35}$$

The matching of Equation (2.25) and Equation (2.35) leads to the expression

$$\delta_a = \frac{\pi}{8}\frac{(V_0 + \frac{1}{2}V_1 c)^2 c}{\left(\frac{da}{dt}\right)^2} \tag{2.36}$$

for the jet thickness.

The pressure due to the inner flow solution in the vicinity of $x = c(t)$ is derived by Wagner (1932) as

$$p_{\text{inner}} - p_0 = 2\rho \left(\frac{da}{dt}\right)^2 \sqrt{|\tau|} \left(1 + \sqrt{|\tau|}\right)^{-2}, \tag{2.37}$$

where τ is related to x by Equation (2.28). Wagner found this expression by using Bernoulli's equation on the flow that is steady in the inner frame of reference. By letting $\hat{x} \to \infty$ in the inner solution, an outer expansion is obtained. This implies that $|\tau| \to \infty$, yielding

$$\begin{aligned}
(p_{\text{inner}} - p_0)^{\text{out}} &= 2\rho \left(\frac{da}{dt}\right)^2 \frac{1}{\sqrt{|\tau|}} = 2\rho \left(\frac{da}{dt}\right)^2 \frac{1}{\sqrt{\hat{x}}} \sqrt{\frac{\delta_a}{\pi}} \\
&= \rho \left(\frac{da}{dt}\right) \frac{\left(V_0 + \frac{1}{2} V_1 c\right) c}{\sqrt{2c}} \Big/ \sqrt{\hat{x}} \\
&= \rho \left(V_0 + \frac{1}{2} V_1 c\right) \frac{c\left(\frac{da}{dt}\right)}{\sqrt{2c\,(c - x)}} \\
&= \rho \left(V_0 + \frac{1}{2} V_1 c\right) \frac{c\left(\frac{da}{dt}\right)}{\sqrt{2c\,(a - x_0)}}
\end{aligned} \tag{2.38}$$

This is the same expression as the inner expansion of the outer solution for the pressure, given in Equation (2.26).

2.5.4 Composite solution for pressure

The pressure distribution in the region $0 \leq x \leq c(t)$ is found by adding the inner and the outer solution and subtracting terms that are in common.

$$\begin{aligned}
p - p_0 &= (p_{\text{outer}} - p_0) + (p_{\text{inner}} - p_0) - (p_{\text{common}} - p_0) \\
&= \rho(V_0 + \frac{1}{2} V_1 x) \frac{\left[c\frac{dc}{dt} + x\left(-\frac{dc}{dt} + \frac{da}{dt}\right)\right]}{\sqrt{c^2 - x^2}} \\
&\quad + \rho \left[\frac{\partial V_0}{\partial t} + \frac{1}{2}\frac{\partial V_1}{\partial t} x + \frac{1}{2} V_1 \left(\frac{dc}{dt} - \frac{da}{dt}\right)\right] \sqrt{c^2 - x^2} \\
&\quad + 2\rho \left(\frac{da}{dt}\right)^2 \sqrt{|\tau|} \left(1 + \sqrt{|\tau|}\right)^{-2} - \rho \left(V_0 + \frac{1}{2} V_1 c\right) \frac{c\left(\frac{da}{dt}\right)}{\sqrt{2c\,(c - x)}}
\end{aligned} \tag{2.39}$$

where $|\tau|$ is evaluated from Equation (2.27).

The composite solution for the pressure in the region $-c(t) \leq x \leq 0$ is written as

$$\begin{aligned}
p - p_0 &= \rho(V_0 + \frac{1}{2} V_1 x) \frac{\left[c\frac{dc}{dt} + x\left(\frac{dc}{dt} + \frac{db}{dt}\right)\right]}{\sqrt{c^2 - x^2}} \\
&\quad + \rho \left[\frac{\partial V_0}{\partial t} + \frac{1}{2}\frac{\partial V_1}{\partial t} x - \frac{1}{2} V_1 \left(\frac{dc}{dt} + \frac{db}{dt}\right)\right] \sqrt{c^2 - x^2} \\
&\quad + 2\rho \left(\frac{db}{dt}\right)^2 \sqrt{|\tau|} \left(1 + \sqrt{|\tau|}\right)^{-2} - \rho \left(V_0 - \frac{1}{2} V_1 c\right) \frac{c\left(\frac{db}{dt}\right)}{\sqrt{2c\,(c + x)}}
\end{aligned} \tag{2.40}$$

where $|\tau|$ is related to x by

$$x_0 - b = x + c = \hat{x} = \frac{\delta_b}{\pi}\left[\log|\tau| - 4i\sqrt{|\tau|} - |\tau| + 5\right] \tag{2.41}$$

In the jet regions, $|x| > c(t)$, the pressure is given by the inner solution.

If $a(t)$ or $b(t)$ are stationary the inner pressure and the common pressure term vanish, but the pressure in the vicinity of the intersection remains finite. As an example, if $b(t) = -\frac{L}{2}$ for a fixed deck then $\frac{db}{dt}$ becomes zero. This enforces the two last terms in Equation (2.40) to be zero also. By letting $x \to -c(t)$ Equation (2.40) can be approximated by

$$\begin{aligned}(p - p_0)(x \to -c) \approx\ & \rho(V_0 - \frac{1}{2}V_1 c)\frac{c\frac{db}{dt}}{2c}\sqrt{c+x} \\ & + \rho\left[\frac{\partial V_0}{\partial t} - \frac{1}{2}\frac{\partial V_1}{\partial t}c - \frac{1}{2}V_1\frac{dc}{dt}\right]\sqrt{2c(c+x)}\end{aligned} \tag{2.42}$$

which approaches zero. Similarly, when $\frac{da}{dt} = 0$ it can be shown that the total pressure approaches zero as $x \to c(t)$.

If both intersection points, $a(t)$ and $b(t)$, are constants, which is the case when the deck of a fixed platform is fully wetted, the expression for the pressure reduces to

$$p - p_0 = \rho\left(\frac{\partial V_0}{\partial t} + \frac{1}{2}\frac{\partial V_1}{\partial t}x\right)\sqrt{c^2 - x^2} \quad \text{on} \quad |x| \le c \tag{2.43}$$

and is finite everywhere on the body.

2.5.5 Integrated pressure *versus* momentum analysis

The total normal force on the deck can be found by integrating the fluid pressure over the wetted surface,

$$F_3 = B\int_{-c}^{c}(p - p_0)\,dx\,,$$

B being the breadth of the deck. The force F_3 referred to in this context is the force normal to the deck, *i.e.* in z-direction. If the deck has a finite pitch angle, the normal force can be decomposed into a horizontal and a vertical component.

The impact force can be found by imposing the conservation of fluid momentum. The related derivation is given *e.g.* in Faltinsen (1990) and in the present case it can be written as

$$F_3 = \frac{d}{dt}\left(A_{33}^{(\infty)}V_R\right) \tag{2.44}$$

The derivation of (2.44) is based on the outer flow with the free surface condition $\phi = 0$. It can be shown that the inner pressure is very localized in space. This means that it dies out quickly away from $x = c(t)$, and its contribution to the integrated force is insignificant. Though the outer pressure is singular at $|x| = c(t)$ the integrated force is finite. It is straightforward to show that integration of the outer pressure and Equation 2.44 with $V_R = V_0$ give the same value of the force normal to the deck,

$$\begin{aligned}
F_3 &= B\int_{-c}^{c} (p_{\text{outer}} - p_0)\,dx \\
&= B\int_{-c}^{c} \rho(V_0 + \frac{1}{2}V_1 x)\frac{\left[c\frac{dc}{dt} + x\left(-\frac{dc}{dt} + \frac{da}{dt}\right)\right]}{\sqrt{c^2 - x^2}}\,dx \\
&+ B\int_{-c}^{c} \rho\left[\frac{\partial V_0}{\partial t} + \frac{1}{2}\frac{\partial V_1}{\partial t}x + \frac{1}{2}V_1\left(\frac{dc}{dt} - \frac{da}{dt}\right)\right]\sqrt{c^2 - x^2}\,dx \\
&= \pi\rho\frac{dc}{dt}BcV_0 + \rho\frac{\pi}{2}Bc^2\frac{\partial V_0}{\partial t} \\
&= \frac{d}{dt}\left(\frac{1}{2}\rho\pi Bc^2 V_0\right) \\
&= \frac{d}{dt}\left(A_{33}^{(\infty)}V_0\right)
\end{aligned} \tag{2.45}$$

where B is the breadth of the deck. One should note that $\dot{b} + \dot{c} = \dot{a} - \dot{c}$. In addition, the fact that one can set $V_R = V_0$ in the momentum equation to get the integrated force from the outer pressure distribution, does not imply the $V_1 x$ term in the body boundary condition to be insignificant. Conversely, V_1 is very important when determining $c(t)$ and consequently $A_{33}^{(\infty)}$. Since $V_1 x$ is anti-symmetric the pressure due to this velocity will cancel out, and intuitively, V_0 being the mean impact velocity, the result above is correct.

2.6 Added mass for a thin plate

To evaluate the force on the deck through Equation (2.44) $A_{33}^{(\infty)}$ must be found. This quantity represents the added mass of a plate with zero thickness placed on the free surface and forced to oscillate with frequency $\omega \to \infty$. The added mass of a thin plate on the free surface is equal to the half added mass of a thin plate in unbounded fluid (see page 296-298 in Newman (1977)). The two-dimensional added mass of a thin plate in unbounded fluid is given by

$$A_{33} = \rho\pi c^2\,, \tag{2.46}$$

where c is the half-breadth of the plate. This is the same as the two-dimensional added mass of a circular cylinder with a radius c. Finally, the two-dimensional high frequency limit added mass in heave of the wetted deck length is

$$A_{33}^{(\infty)} = \frac{1}{2}\rho\pi c^2\,, \tag{2.47}$$

which proves that the conclusion expressed by Equation (2.45) is correct.

2.6.1 Two-dimensional *versus* three-dimensional added mass coefficient

Three-dimensional effects will reduce the added mass. When referring to a three-dimensional plate with length equal to $2c$ and breadth equal to B, these effects will depend on the plate's aspect ratio $\kappa = \frac{2c}{B}$, *i.e.* the three-dimensional added mass can be written as

$$A_{33}^{(3D)} = \frac{1}{2}\rho\pi c^2 B J(\kappa) \tag{2.48}$$

where $J(\kappa)$ is a correction factor accounting for three-dimensional effects.

Meyerhoff (1970) has done calculations of the added masses of thin rectangular plates in infinite fluid. Meyerhoff uses a distribution of dipoles over the length (x-direction) and breadth (y-direction) of the plate to solve the resulting boundary value problem. The dipole density in x- and y-direction is expressed as a double series of Chebyshev polynomials of the second kind with unknown coefficients. The coefficients are found by imposing the body boundary condition at an equal or larger number of collocation points. Calculations are performed for a number of different aspect ratios κ, and the results are compared to empirical formulae and experimental values. These comparisons show that a simple formula developed by Blagovenshchensky (1962) yields results that are in good agreement with the theoretical results by Meyerhoff (1970). Blagovenshchensky (1962) writes the three-dimensional coefficient $J(\kappa)$ as

$$J(\kappa) = \frac{1}{\sqrt{1+\kappa^2}}\left\{1 - \frac{0.425\kappa}{(1+\kappa^2)}\right\} \tag{2.49}$$

This equation is empirical and based on measurements performed by Pabst (1930) for a plate in infinite fluid.

From Figure 2.9 it can be seen that the three-dimensional effects are significant for the added mass. For a quadratic plate, the $J(\kappa)$-coefficient will be just $\approx 55\%$ of the corresponding coefficient for an infinitely long plate. This suggests that the added mass coefficient of the wetted part of the deck varies significantly as a wave hits the front end of deck and propagates downstream. It is important in practice to account for this when using Equation (2.44) to calculate the load response due to the water impact. Figure 2.10 illustrates how $J(\kappa)$ may vary for a deck with $L/B = 2$. The wetted area is shaded. Note that the time intervals between each sketch in the figure are not identical. The $J(\kappa)$-coefficient is equal to unity at the initial impact but decreases as the wetted area increases. $J(\kappa)$ reaches a minimum when the wetted area is at its largest value. When the deck is fully wetted $\kappa = 2$ and $J(\kappa) = 0.371$. This means that the added mass is only 37.1% of the value obtained by using the two-dimensional added mass coefficient. As the water detaches from the deck, *i.e.* when κ decreases, $J(\kappa)$ starts to increase towards 1.0 again. Taking this into account the impact force on the deck associated with the perturbation potential

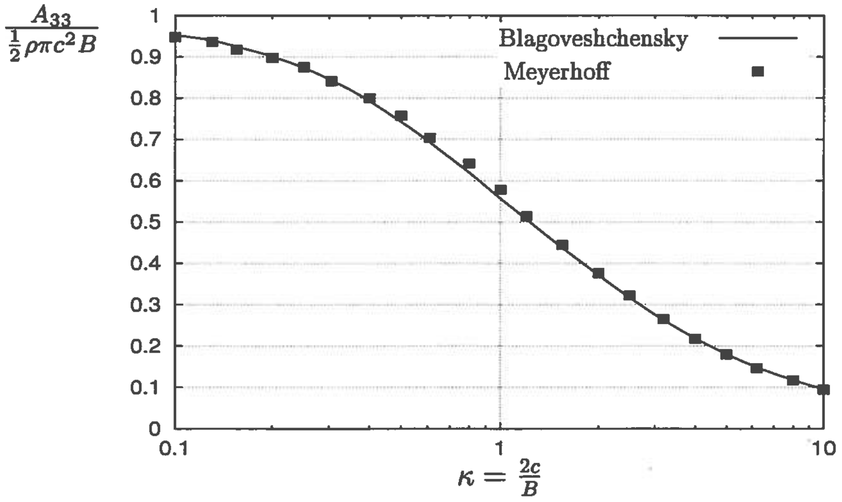

Figure 2.9: *The three dimensional added mass coefficient for a thin rectangular plate. Comparisons of numerical results by Meyerhoff (1970) to the empirical formula by Blagovenshchensky (1962) given in Equation (2.49). Note that the horizontal axis is logarithmic.*

ϕ, may be written as

$$\begin{aligned} F_3 &= \frac{d}{dt}\left(A_{33}^{(3D)} V_0\right) \\ &= J(\kappa)\frac{dA_{33}^{(2D)}B}{dt}V_0 + \frac{dJ(\kappa)}{dt}A_{33}^{(2D)}BV_0 + J(\kappa)A_{33}^{(2D)}B\dot{V}_0 \\ &= \left(J(\kappa)\rho\pi cB\dot{c} + \dot{J}(\kappa)\frac{1}{2}\rho\pi c^2 B\right)V_0 + J(\kappa)\frac{1}{2}\rho\pi c^2 B\dot{V}_0 \end{aligned} \tag{2.50}$$

Here $A_{33}^{(2D)}$ and $A_{33}^{(3D)}$ denote the high frequency limit of the two-dimensional and three-dimensional added mass, respectively. $J(\kappa)$ is given in Equation(2.49) and $\dot{J}(\kappa)$ can be written as

$$\dot{J}(\kappa) = \frac{2}{B}\dot{c}\left\{1.275\kappa^2\left(1+\kappa^2\right)^{-\frac{5}{2}} - (\kappa + 0.425)\left(1+\kappa^2\right)^{-\frac{3}{2}}\right\} \tag{2.51}$$

Accounting for three-dimensional effects in this manner implies that the wetting is calculated by two-dimensional theory. This is an approximation.

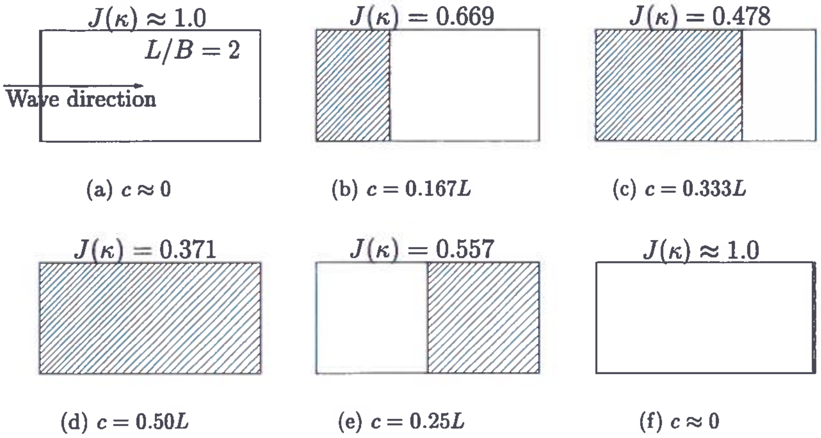

(a) $c \approx 0$ (b) $c = 0.167L$ (c) $c = 0.333L$

(d) $c = 0.50L$ (e) $c = 0.25L$ (f) $c \approx 0$

Figure 2.10: *The variation of the correction factor $J(\kappa)$ for the added mass due to three-dimensional effects, as a wave propagates along a deck. The L/B-ratio for the deck is equal to 2. The wetted part of the deck is shaded.*

CHAPTER 3

Water impact solved by the Wagner based method

3.1 Introduction

In the previous chapter the theoretical background for the Wagner based method has been presented. In this chapter a numerical scheme for solving water impact underneath a platform deck is derived and the related assumptions will be discussed. A crucial task in the numerical solution is a correct evaluation of the body/free surface intersections and of the free surface at each time instant. In the case of a floating platform, it is also important to predict well the water impact induced rigid body motions, and the related velocities and accelerations. These aspects will be thoroughly discussed in the following.

3.2 Assumptions and basic concepts

In addition to the assumptions leading to the two-dimensional boundary value problem in Figure 2.4, a set of secondary assumptions for the fluid flow and for the structure are introduced as follows

- Hydroelasticity is not important for the loading.
- Long wave approximation, *i.e.* the wavelength is large compared to the body dimensions. This means that one assume that body generated gravity waves can be neglected.
- Wave direction yields head sea or beam sea only, *i.e.* no oblique headings.
- Incident waves are modeled by second order regular wave theory.
- Impact velocity varies both in time and space.

The validity of these assumptions will be discussed in the following.

3.2.1 Importance of hydroelasticity

Hydroelasticity means that the hydrodynamic load acting on a structure is a function of the structural elastic response, which again is a function of the hydrodynamic load. The latter is always true, while the former occurs when the elasic response significantly influences the behavior of the fluid pressure. In this case a coupled fluid-structure analysis becomes necessary. Faltinsen (2000a) gives a review of hydroelastic slamming problems within ship and ocean engineering. In the present study, the structure is assumed to be infinitely stiff when the hydrodynamic pressure is calculated. This allows the hydrodynamic and structural analyses to be performed separately. This is supported by calculations performed on an existing platform using the hydroelastic theory by Faltinsen (1997). The calculations are presented in Appendix A, and the results suggest that local structural response during the water entry phase can be described by quasi-static theory. The water entry phase yields the largest averaged pressures on the wetted part of the deck.

When hydroelasticity has to be accounted for, the analysis becomes much more complicated since a coupled fluid-structural analysis is required. This can be done, either by including a simplified structural model in the theory as done *e.g.* by Haugen (1999) and by Kvålsvold (1994) for the hydroelastic analysis of wetdeck slamming on a catamaran, or by coupling the hydrodynamic analysis with a more general structural analysis. Kvålsvold (1994) uses a one-beam representation of the wetdeck while Haugen (1999) uses a three-beam model to analyze the stiffened plates in the wetdeck. The beam deflection is expressed by linear combination of eigenmodes obtained from free vibration analyses in air. This simple description of the structural behavior is not satisfactory since the lower deck of a platform is more complex than the wetdeck structure of catamarans. For isolated stiffened plates, the beam model could be applied locally, but it gives a too crude approximation for the whole deck.

Coupling of the hydrodynamic analysis with a more general dynamic structural model is at this stage difficult because it requires extensive work on structural modeling and on the prediction of the structural response. This was not considered to be within the scope of this work. Based on the discussion given in Appendix A, it was decided to neglect hydroelastic effects when performing the hydrodynamic analysis. In any case, it is important to establish a robust way of calculating the hydrodynamic pressure before introducing the mechanical response to the problem.

3.2.2 Two-dimensional flow condition

As pointed out in Chapter 2, the high frequency limit of the two-dimensional added mass coefficient of a thin plate is an important parameter when calculating the force or the pressure distribution due to water impact. Here the thin plate refers to the wetted area of the deck. A finite width of the deck violates the assumption of two-dimensional flow. However, for rectangular shaped wetted areas, the two-dimensional flow assumption can be applied, and a reduction factor given by Blagovenshchensky (1962) to account for three-dimensionality can be introduced. For an arbitrarily shaped plate the added mass coefficient has to be found numerically instead. Meyerhoff (1970) presents a numerical method for calculating the added mass for rectangular thin plates by representing the body as a distribution of normal dipoles. As shown in Figure 2.9, Meyerhoff's results compare well with results obtained by using the empirical formula (2.49) from Blagovenshchensky (1962) to account for three-dimensional effects. The panel program WAMIT (see WAMIT (2000)) has the option of having panels located on the free surface. An example of the use of this option is given in Newman et al. (1996). This option in combination with the infinite frequency option also available in the program, makes it possible to solve the high frequency added mass of arbitrarily shaped thin plates on the free surface.

The present work focuses on head and beam sea conditions. This is due to two main reasons. First, when oblique headings are considered, a numerical method for calculating added mass for the wetted area becomes necessary. If WAMIT is not to be used, this would require an extensive and time consuming code development and would make the problem of interest more complicated than necessary according to the scope of this work. Secondly, it is believed that head and beam sea give the largest impact forces on the platform and will therefore be the most severe conditions for both global structural response and for rigid body response of floaters.

Also if vertical platform members are present, the two-dimensional flow assumption will be violated since these will disturbe the flow locally. One must require that the wavelength of the incident wave to be much larger than the diameter of the platform legs ($\lambda > 5D$). In this case, waves generated by the vertical platform members are negligible relative to the incident wave. The long wave approximation is not restrictive for the present problem because wave impact events are mostly associated with long incoming waves. Diffraction due to the columns will of course give local run-up along the columns, but this is not taken into account in this work.

3.2.3 Wave conditions

Wind generated sea waves are a nonlinear random process. The nonlinearity is more prominent in severe sea states where many observations show a large excess of high crests to shallow troughs. Longuet-Higgins (1963) represents the nonlinear wave elevation ζ_I to third order as combinations of independent, regular components. In many applications in ship and ocean engineering one can disregard higher order contributions and ζ_I can be written as a linear combination of regular components. The wave kinematics can then be solved in the frequency domain, where the wave elevation is described through the wave spectrum. In general the wave spectrum is a function of both wave frequency and heading, but for long-crested sea states the spectrum is a function of the wave frequency only, given as $S_\zeta(\omega)$.

For problem such as wave impact on platform decks where the wave kinematics in the wave crest and the wave elevation are crucial, a first order representation of the irregular sea may not be sufficient. Stansberg(1993, 1994) presents a procedure for estimating second-order random wave elevation and kinematics. He describes the second-order random wave in the frequency domain by using quadratic transfer functions. Stokka (1994) has extended this method to account for third-order effects. He reports that the extreme crest heights are increased with up to 12% due to second order components, while the contribution to the extreme crest height from third order are found to be only 1% in a sea state characterized by the significant wave height H_s = 15.5m and spectral peak period T_p = 17.8s. Both the second-order and the third-order components increase the steepness of extreme waves.

In a preliminary design a regular wave may be used as an approximation of an extreme sea state. This regular wave is often denoted as the design wave. NORSOK STANDARD (1999) gives suggestions for suitable design waves. For fixed platforms the maximum wave action effects occur for the highest wave. Effects with annual exceedance probability of 10^{-2} can be determined by using the wave height H_{100} which has 10^{-2} annual exceedance probability. According to NORSOK STANDARD, H_{100} should be equal to 1.9 times the significant wave height of the corresponding sea state, and the wave period T used together with H_{100} should be varied in the range $\sqrt{6.5T_p} \leq T \leq \sqrt{11T_p}$. The wave height has dimension m and the wave period has dimension s. Further, in absence of more detailed documentation, the wave height, H_{10000}, with annual exceedance probability of 10^{-4} can be taken as $1.25H_{100}$, while the period should be increased by 5% compared to the 100 yrs value.

For floaters a specific wave period, T_d, instead of the highest wave, *e.g.* H_{100}, may be the most critical from wave effects point of view. To this purpose NORSOK STANDARD suggests that the corresponding design wave height should be taken as

$$H_d = \begin{cases} 0.22T_d^2, & \text{for } T_d \leq 6\,\text{s} \\ \frac{T_d^2}{4.5+0.02(T_d^2-36)}, & \text{for } T_d > 6\,\text{s} \end{cases} \tag{3.1}$$

for deep water waves. However, if an annual exceedance probability of 10^{-2} is desired, H_d does not have to be taken larger than $1.9H_S$, where H_S is the significant wave height that for the given wave period, corresponds to a "100 years" sea state.

In this work regular waves are used as an approximations for extreme waves. The use of regular waves, simplifies the analysis and limits the computational time.

Linear wave theory is based on the assumption that the wave steepness is small, *i.e.* $k\zeta_a$ is small. Here k is the wave number given by the dispersion relation and ζ_a is the first order wave amplitude. The derivation of the velocity potential for linear waves can be found in several books on water waves, *e.g.* in Mei (1989). Linear theory has proved to be successful in numerous respects, even in cases where its fundamental requirement, small $k\zeta_a$, has been violated. However, for waves of finite amplitude, linear theory may yield poor results for the maximum wave elevation and the description of the kinematics in the wave crest region. These are crucial parameters when solving the water impact under a platform deck problem. From this perspective it is believed that linear wave theory is insufficient, and that nonlinear waves must be utilized for obtaining accurate results for the impact loading and rigid body and structural responses.

The difference between linear theory and fully nonlinear theory is that in the former the linearized free surface boundary conditions are satisfied along a known and fixed surface. In the latter the exact boundary conditions are satisfied on the exact free surface, which is a time dependent unknown of the problem. No exact theory is able to give the solution in closed form, but several theories exist which determine the solution by using series expansion. Examples are the cnoidal waves for shallow water and the solitary waves for very shallow water depths.

For finite and infinite water depths Stokes (1847) improved the wave solution by using a second order theory instead of the linear theory. He did this by applying a perturbation technique in terms of $k\zeta_a$ as small parameter, and by keeping all terms up to second order. He applied a Taylor expansion of the free surface conditions around the mean free surface. This implies that all the terms involved have to be evaluated along this known and constant plane. In principle, Stokes theory may be extended to any order, but as the order increases the solution becomes more arduous and difficult to evaluate. The fifth order theory by Skjelbreia and Henderson (1961) is much used for engineering purposes. Schwartz (1974) presented a method for computer extension of Stokes' expansion for gravity waves to "infinite" order. Alternative methods are presented by Rienecker and Fenton (1981) and by Bryant (1983). Schwartz and Fenton (1982) give a comprehensive review of computational methods for strongly nonlinear waves.

The Stokes wave profile is symmetric about a vertical axis through the wave crest, and the wave crests are higher than the first order amplitude. Similarly, the negative extreme is smaller than the first order amplitude. The wave nonlinearity yields a free surface profile that is more peaked at the wave crest and flatter at the wave troughs than the sinusoidal profile of the linear wave. For Stokes waves of third or higher order the dispersion relation, and thus the propagation velocity of the wave, become dependent on the amplitude of the wave. The major contributions of higher order effects, both for the wave elevation and for the wave kinematics, originates from the second order terms. In this work it is assumed that second order theory is sufficient to get reliable results for the impact loading. For finite water depths and $z_0 \leq 0$ the velocity potential ϕ_I and the wave elevation ζ_I for second order Stokes waves can be written as

$$\begin{aligned} \phi_I &= \phi_I^{(1)} + \phi_I^{(2)} \\ &= \frac{\zeta_a g}{\omega}\frac{\cosh(k(h+z_0))}{\cosh(kh)}\sin(kx_0-\omega t) + \frac{3}{8}\zeta_a^2 g \frac{\cosh(2k(h+z_0))}{\sinh^4(kh)}\sin(2(kx_0-\omega t)) \end{aligned} \tag{3.2}$$

and

$$\begin{aligned} \zeta_I &= \zeta_I^{(1)} + \zeta_I^{(2)} \\ &= \zeta_a\cos(kx_0-\omega t) + \frac{\zeta_a^2 k}{4}\frac{\cosh(kh)}{\sinh^3(kh)}(2+\cosh(2kh))\cos(2(kx_0-\omega t)) \end{aligned} \tag{3.3}$$

where

ω	wave frequency
h	water depth
$\phi_I^{(1)}$, $\phi_I^{(2)}$	first and second order velocity potential, respectively
$\zeta_I^{(1)}$, $\zeta_I^{(2)}$	first and second order wave elevation, respectively

and wave number k is given from the dispersion relation

$$\omega^2 = gk\tanh(kh) \tag{3.4}$$

This is the same dispersion relation as for linear theory, but for higher order perturbations also the dispersion relation contains higher order terms. The first order terms in Equation (3.2) and

Equation (3.3) oscillate with frequency ω, while the second order terms oscillate with frequency 2ω. In order to use Equation (3.2) in the "wave zone" for $0 < z_0 \leq \zeta_i$, a Taylor expansion about $z_0 = 0$ consistent with the theoretical derivation of the potential is applied. The horizontal and vertical fluid velocities can be obtained by differentiating ϕ_I with respect to x_0 and z_0, respectively.

The expressions for infinite water depth represent the limit of Equation (3.2) and Equation (3.3) as $h \to \infty$. In this case the second order velocity potential $\phi_I^{(2)}$ vanishes and the velocity potential and the wave elevation reduce to

$$\phi_I = \frac{\zeta_a g}{\omega} e^{kz_0} \sin(kx_0 - \omega t) \tag{3.5}$$

and

$$\zeta_I = \zeta_a \cos(kx_0 - \omega t) + \frac{1}{2}\zeta_a^2 k \cos(2(kx_0 - \omega t)), \tag{3.6}$$

respectively. Finally, the dispersion relation becomes $\omega^2 = kg$.

The coordinate system used in the derivation of these expressions has its origin at the mean free surface and with the z_0-axis pointing upwards.

The accuracy of Stokes' second order theory depends on the wave steepness. In Figure 3.1 second order wave profiles are compared to "infinite" order wave profiles for four different wave steepnesses. The "infinite" order wave profile for $H/\lambda = 0.10$ is given by Schwartz (1974), while the theory presented by Bryant (1983) is used to determine the "exact" wave profile for the other H/λ-values. Bryant (1983) presents a method where the Stokes wave in deep water is represented by truncated Fourier series for ϕ_I and ζ_I. The number of harmonics used is determined by trial and error so that the set of Fourier coefficients includes all the amplitudes greater than some prescribed value. Here the error tolerance in the wave elevation was set to be $1.0 \cdot 10^{-11}$. With this error the numbers of harmonics needed for $H/\lambda = 0.073$, 0.049, and 0.031 were 22, 16 and 13, respectively. The computations are performed by Greco (2001).

The wave profiles computed by second order theory and "infinite" order theory compare very well for $H/\lambda = 0.031$ and $H/\lambda = 0.031$. For $H/\lambda = 0.073$ the deviation are larger, but still the relative error for the maximum wave elevation is less than 0.8%. When the wave steepness is increased to 0.1 the relative difference between the two different wave profiles becomes more significant. The exact wave profile is more peaked at the crest and flatter at the troughs than the second order profile. This indicates that second order wave theory is not sufficient to describe the wave properly for steep waves. However, in the following Stokes' second order theory is used to describe the incident wave elevation and kinematics.

3.2.4 Distribution of impact velocity

In Section 2.4 the boundary value problem in Figure 2.3 was solved analytically given a linearly distributed impact velocity, $V_R = V_0 + V_1 x$. In the following this functional variation in the

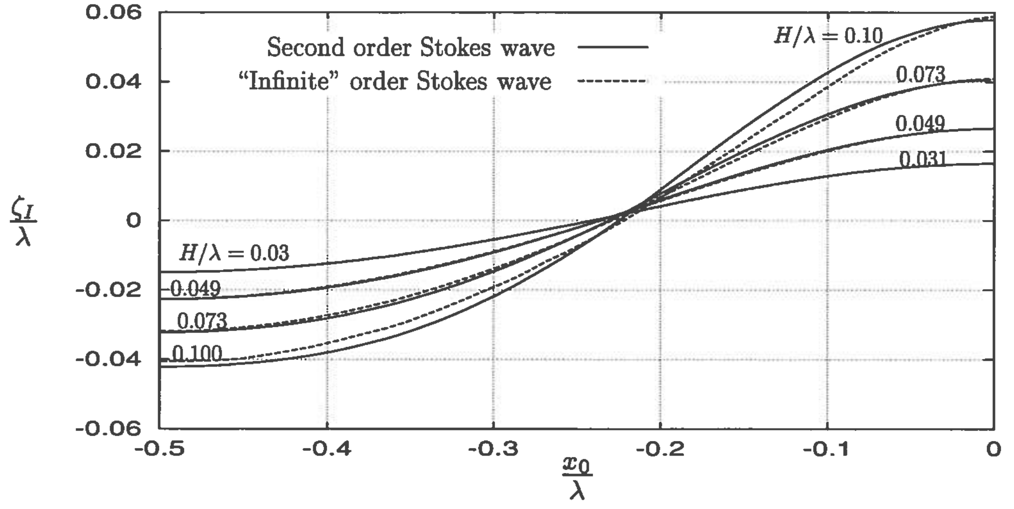

Figure 3.1: *Second order and "infinite" order wave profiles for deep water Stokes waves.*

impact velocity is assumed. This assumption leads to a fast solution of the BVP at each time instant. In the case of a general velocity distribution a Fourier series expansion can be used to represent it and the related BVP can be solved numerically in the same manner as described in Kvålsvold (1994). When the exact body boundary condition is enforced, the solution can be represented as a sum of boundary integrals through Greens' second identity, but it has to be solved numerically. This would in general lead to more time consuming calculations. Boundary value problems solved by using Greens second identity will be discussed comprehensively in Chapter 5 and Chapter 6.

It is believed that a linear distribution of the impact velocity is a reasonable assumption as long as structural response is neglected. The contribution to the impact velocity from the rigid body motion can be described at all times by a linear function. Now, the leading order term of the vertical fluid velocity on the wetted part of the deck is proportional to $\cos(kx_0 - \omega t)$, where x_0 is measured in the earth fixed coordinate system. This means that the wetted part of the body is relative short compared to the wave length the velocity distribution may be fairly well described by a linear function. The discrepancy between the exact velocity distribution and the linear approximation increases when $c(t)/\lambda$ increases, where $\lambda = 2\pi/k$ is the wave length. As will be shown later, this assumption is only important during the water entry phase, *i.e.* when the wetted area is increasing.

Figure 3.2 shows a sketch of how the impact velocity may vary across the wetted body surface. Two alternative linear approximations are suggested. Alternative 1 uses the impact velocities at the body/ free surface intersections to make a linear approximation, and the approximated

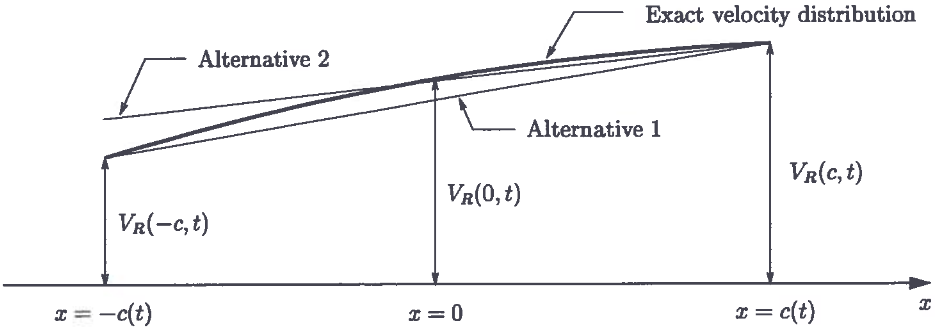

Figure 3.2: *Alternative approaches for approximating the exact impact velocity distribution by a linear distribution.*

velocity distribution may be expressed as

$$V_R(x,t) = \frac{V_R(c,t) + V_R(-c,t)}{2} + \frac{V_R(c,t) - V_R(-c,t)}{2c(t)} x(t)\,, \tag{3.7}$$

where

$V_R(-c,t)$	relative impact velocity at upstream intersection point
$V_R(c,t)$	relative impact velocity at downstream intersection point

From Figure 3.2 one can see that this approach leads to an underestimation of the impact velocity for the entire region between the intersection points.

The second alternative uses the values for the relative impact velocity at $x(t) = 0$ and at the downstream intersection point, $x(t) = c(t)$, to build up a linear distribution. This yields the following expression for the impact velocity

$$\begin{aligned} V_R(x,t) &= V_R(0,t) + \frac{V_R(c,t) - V_R(0,t)}{c(t)} x(t) \\ &= V_0(t) + V_1(t)x(t) \end{aligned} \tag{3.8}$$

where $V_R(0,t)$ is the relative impact velocity at the center of the wetted part of the body. This expression underestimates the velocity somewhat for $x(t) > 0$ while it overestimates the velocity for $x(t) < 0$. Even though this alternative also underestimates the relative impact velocity for $x(t) > 0$, it gives a better approximation than Equation (3.7) in this region. As mentioned in Section 2.5.5, the linear part of the impact velocity distribution does not contribute to the impact force directly but is crucial when determining $c(t)$. It is believed that the contribution of the impact velocity near the upstream intersection point influences the wetting of the deck the most. This suggests that approximated impact velocity in this region has to be as close as possible the real one. Alternative 2 is therefore chosen. Other alternatives than the two discussed above may in principle be used, but this has not been studied in this thesis.

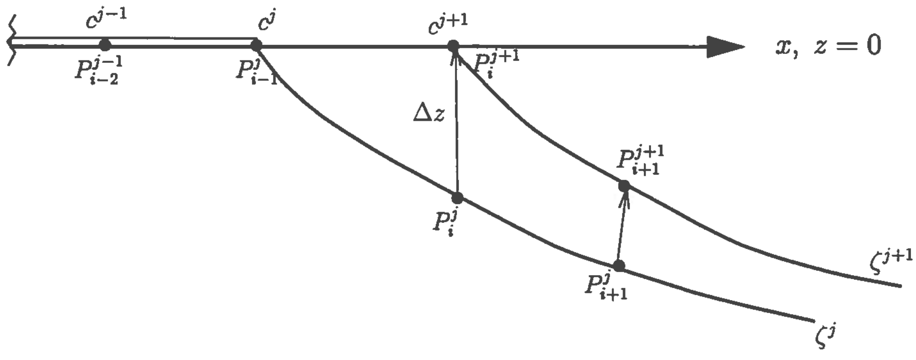

Figure 3.3: *Stepping of the free surface. The figure shows a zoom up of the body and the free surface near the downstream intersection point* c^j *and* c^{j+1} *are the chord lengths at* t^j *and* t^{j+1}*, respectively.*

3.3 The wetted length

A major task in the Wagner based methods is to determine the wetted length. The wetted length is described by $c(t)$, which is an important parameter in the boundary value problem. Wagner (1932) found the wetted length from the geometrical intersection between the body and the free surface when the pile up of water due to the impact is included. To determine the downstream body/ free surface intersection during the water entry phase a procedure similar to the generalized Wagner method described in Zhao et al. (1996), is implemented. Zhao et al. (1996) studies water entry of two-dimensional sections into an initially undisturbed free surface.

When the time instant of impact is found, the initially undisturbed free surface downstream of the impact point is discretized. The surface is divided in a finite number of fluid particles. According to the kinematic free surface condition, a fluid particle on the free surface will always stay on the free surface. The free surface evolution is thus obtained by time integration of the velocities of the free surface particles.

Let superscript j denote a time instant and subscript i denote a fluid particle, so that P^j_i is the position of particle i at $t = t^j$. Figure 3.3 illustrates the free surface ζ^j and ζ^{j+1} at time instants t^j and t^{j+1}. The free surface conditions are satisfied on the horizontal line $z = 0$. A linearly varying impact velocity is constructed and the corresponding boundary value problem is solved analytically. It is also assumed that the vertical velocity due to ϕ is the same on ζ^j as it is on $z = 0$.

Instead of using predefined time steps, the intersection points are decided a priori and the corresponding time increments are evaluated numerically. With reference to Figure 3.3, at time instant t^j particle P^j_i is the free surface particle closest to the body/ free surface intersection point. It is imposed that this particle will reach the body at time instant t^{j+1}. The required time increment then has to be $\Delta t^j = t^{j+1} - t^j$. It is also assumed that close to the body the

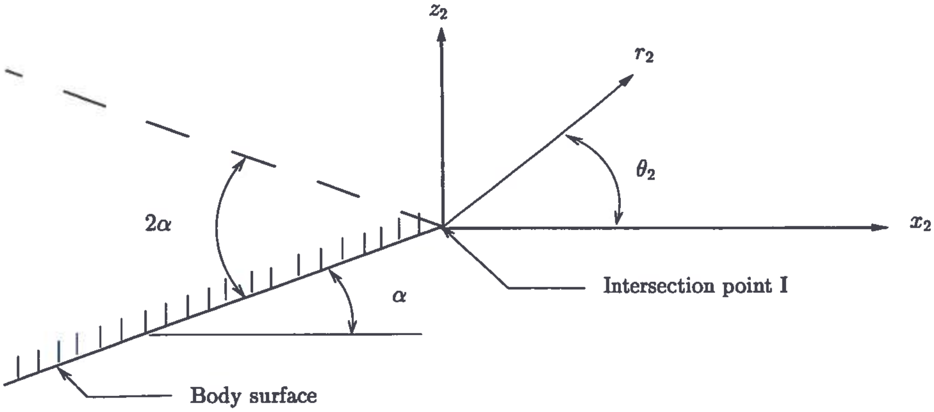

Figure 3.4: *Local polar coordinate system* (r_2, θ_2).

velocity due to the impact will dominate, and thus the horizontal velocity may be neglected for the particle closest to the body. Hence, Δt^j is found as the time the particle P_i needs to cover the vertical distance Δz (see Figure 3.3). To determine this time increment accurately a local solution of the flow close to the intersection point is needed. For the other free surface particles both vertical and horizontal velocities are accounted for.

3.3.1 Local solution near downstream intersection point

As mentioned above, the time increment Δt^j must be found by a local analysis for the flow in the vicinity of the downstream body/ free surface intersection. This can be explained by considering Equation (2.22). At the intersection points, $x(t) = \pm c(t)$ the vertical velocity is singular. This means that the vertical velocity of P_i becomes singular at the time instant t^{j+1}, and a local solution for the flow near the intersection point is therefore considered.

Assume a complex potential similar to the one found in art. 63 by Lamb (1932):

$$W(Z) = iAZ^n \tag{3.9}$$

where the complex variable $Z = x_2 + iz_2$ and A is a real value. The coordinate system for the local analysis is shown in Figure 3.4. The origin is located at the intersection point I, while α is the angle between the body and the free surface at I. The x_2-axis is horizontal with the positive axis pointing in downstream direction. The body surface is shaded while the double body mirrored about $z_2 = 0$ is indicated with dashed lines. When polar coordinates, $(r_2,\ \theta_2)$, are introduced the velocity potential and the stream function may be written as

$$\phi_{loc} = -Ar_2^n \sin(n\theta_2) \tag{3.10}$$

and

$$\psi_{loc} = Ar_2^n \cos(n\theta_2) \quad , \tag{3.11}$$

respectively, where $W = \phi_{loc} + i\psi_{loc}$. By properly choosing the value of n the irrotational solution when the boundary is characterized of two rigid walls is obtained. The equation for streamlines in the case of the corner flow is

$$r_2^n \cos(n\theta_2) = \text{constant}$$

implying that the lines $\theta_2 = \pm\frac{1}{2}\frac{\pi}{n}$ are parts of the same streamline. A solution for flow around the corner with angle 2α, is chosen by letting $n = \frac{\pi}{2(\pi-\alpha)}$. This yields

$$\phi_{loc} = -Ar_2^{\frac{1}{2}\frac{\pi}{\pi-\alpha}} \sin\left(\frac{1}{2}\frac{\pi}{(\pi-\alpha)}\theta_2\right) \tag{3.12}$$

and

$$\psi_{loc} = Ar_2^{\frac{1}{2}\frac{\pi}{\pi-\alpha}} \cos\left(\frac{1}{2}\frac{\pi}{(\pi-\alpha)}\theta_2\right) \tag{3.13}$$

The local solution must match with the boundary value problem outlined in Section 2.4, thus $\alpha = 0$. This gives $\phi_{loc} = 0$ for $\theta_2 = 0$, while along the body, *i.e.* for $\theta_2 = -\pi$, the potential becomes

$$\phi_{loc} = Ar_2^{\frac{1}{2}} \tag{3.14}$$

Further, the velocities in r_2- and θ_2-direction are given as

$$u_r = -A\frac{1}{2}r_2^{-\frac{1}{2}} \sin\left(\frac{1}{2}\theta_2\right) \tag{3.15}$$

and

$$u_\theta = -A\frac{1}{2}r_2^{-\frac{1}{2}} \cos\left(\frac{1}{2}\theta_2\right) \quad , \tag{3.16}$$

respectively, and the velocities on the free surface are found by setting $\theta_2 = 0$. Along the x_2-axis there is zero flow, and the velocity parallel to the z_2-axis can be written as

$$w_{loc} = A\frac{1}{2}r_2^{-\frac{1}{2}} \tag{3.17}$$

Δt^j is determined by using the procedure outlined in Zhao et al. (1996). Assuming that the intersection point at time instant t_{j+1} has coordinates (x_i^{j+1}, z_i^{j+1}), one can then write

$$\Delta z = \int_{t^j}^{t^{j+1}} w_{loc}\left(c(t), x_i^{j+1}\right) dt\,, \tag{3.18}$$

where Δz is the vertical distance the surface particle P_i^j has to travel before it reaches the body. $c(t)$ is the instantaneous chord length and $r_2 = (x_i^{j+1} - c(t))$. The vertical velocity w_{loc} depends on $c(t)$ and Equation (3.18) can be rewritten as

$$\Delta z = \int_{x_{i-1}^j}^{x_i^{j+1}} w_{loc}\left(c(t), x_i^{j+1}\right) \frac{dt}{dc} dc \tag{3.19}$$

The unknown coefficient A in (3.17) is found by matching the local velocity potential on the body with the global velocity potential given in Equation (2.15), and an average value A_m is used from t_j to t^{j+1}. This gives

$$\Delta z = \left(\frac{dt}{dc}\right)_m A_m \frac{1}{2} \int_{x_{i-1}^{j}}^{x_i^{j+1}} \left(x_i^{j+1} - c(t)\right)^{-\frac{1}{2}} dc = \left(\frac{dt}{dc}\right)_m A_m \left(x_i^{j+1} - x_{i-1}^{j}\right)^{\frac{1}{2}} \tag{3.20}$$

and

$$\left(\frac{dt}{dc}\right)_m = \frac{\Delta z}{A_m \left(x_i^{j+1} - x_{i-1}^{j}\right)^{\frac{1}{2}}} \tag{3.21}$$

The time increment can thus be determined as

$$\Delta t^j = \left(\frac{dt}{dc}\right)_m \left(x_i^{j+1} - x_{i-1}^{j}\right) \tag{3.22}$$

3.3.2 Stepping of the free surface

Once the time increment is found, the free surface particles are moved with their local velocities, and the new free surface position ζ^{j+1} is found. The horizontal and vertical velocities due to the incident wave are evaluated by Taylor expansion about the mean free surface correct to second order. The disturbance potential ϕ yields zero horizontal velocity, while the vertical velocity is given in Equation (2.22).

For infinite water depth, the fluid velocities on the free surface at time instant t, are given as

$$\begin{aligned} u(x_0, z_0 = \zeta, t) &= \left.\frac{\partial \phi_I}{\partial x_0}\right|_{z_0=\zeta} \approx \left.\frac{\partial \phi_I}{\partial x_0}\right|_{z_0=0} + \zeta_I^{(1)} \left.\frac{\partial^2 \phi_I}{\partial z_0 \partial x_0}\right|_{z_0=0} \\ &= \zeta_a \omega \cos\left(k x_0 - \omega t\right) + \zeta_a^2 \omega k \cos^2\left(k x_0 - \omega t\right) \end{aligned} \tag{3.23}$$

and

$$\begin{aligned} w(x, x_0, z_0 = \zeta, t) &\approx \frac{\partial \phi}{\partial z} + \left.\frac{\partial \phi_I}{\partial z_0}\right|_{z_0=0} + \zeta_I^{(1)} \left.\frac{\partial^2 \phi_I}{\partial z_0^2}\right|_{z_0=0} \\ &= \frac{V_0 |x|}{\sqrt{x^2 - c^2}} + \frac{1}{2} \operatorname{sgn}(x) V_1 \left(\sqrt{x^2 - c^2} + \frac{x^2}{\sqrt{x^2 - c^2}}\right) - V_1 x \\ &\quad + \zeta_a \omega \sin\left(k x_0 - \omega t\right) + \frac{1}{2} \zeta_a^2 \omega k \sin\left(2\left(k x_0 - \omega t\right)\right) \end{aligned} \tag{3.24}$$

Here u and w are the horizontal and vertical velocity, respectively. In Equation (3.24) the slamming induced vertical velocity is written for simplicity as a function of x. The x_0-coordinate is measured in the global earth fixed coordinate system which is convenient to use when solving the surface evolution. By combining Equation (2.1) and Equation (2.2) the relationship between the x- and x_0-coordinates and it can be obtained as

$$x = x_0 - \eta_1 - \tilde{x}_F - c \tag{3.25}$$

The velocity of a fluid particle varies with space and time. By assuming the functional variation in the velocity during the time step Δt^j, x_0- and z_0-coordinates of a particle P_i at time t^{j+1} are obtained as

$$x_{0,i}^{j+1} = x_{0,i}^{j} + \int_{t^j}^{t^{j+1}} u(x_{0,i}, z_{0,i}, \tau)\, \mathrm{d}\tau \tag{3.26}$$

and

$$z_{0,i}^{j+1} = z_{0,i}^{j} + \int_{t^j}^{t^{j+1}} w(x_{0,i}, z_{0,i}, \tau)\, \mathrm{d}\tau \tag{3.27}$$

According to the assumed time dependence for the fluid velocity, different integration schemes may be developed. The Runge-Kutta methods are a family of explicit one-step methods. They are named after Carl Runge and Wilhem Kutta and are designed to behave as the Taylor series method but without requiring analytical differentiation of the original differential equation. Due to the singular nature of the intersection point, one should only apply such method based on Taylor series expansion away from the intersection point. Approximate expressions for Equation (3.26) and Equation (3.27) can be established on the form

$$x_{0,i}^{j+1} = x_{0,i}^{j} + \Delta t^j f(x_{0,i}^{j}, z_{0,i}^{j}, t^j, \Delta t^j) \tag{3.28}$$

and

$$z_{0,i}^{j+1} = z_{0,i}^{j} + \Delta t^j g(x_{0,i}^{j}, z_{0,i}^{j}, t^j, \Delta t^j) \tag{3.29}$$

which advance the solution of $x_{0,i}$ and $z_{0,i}$, respectively, from t^j to $t^{j+1} = t^j + \Delta t^j$. $f(\cdot)$ and $g(\cdot)$ represent averaged values of the horizontal and the vertical velocity of P_i during the time increment Δt^j. Many different ways exist to evaluate the right-hand sides, $f(\cdot)$ and $g(\cdot)$, that all agree to first order, but which have different coefficients for the higher order terms. Adding up the right combination of the higher order terms, the error terms can be eliminated order by order, see *e.g.* Press et al. (1989). That is the basic idea of the Runge-Kutta methods, and the procedure for determining the higher order coefficients is described in many text books on numerical mathematics, see *e.g.* Cheney and Kincaid (1985). Abramowitz and Stegun (1964) give various specific formulae for the right hand side. In this work the classical fourth order Runge-Kutta scheme is used to step the free surface in time. The method is of fourth order since the error is $O(\Delta t^j)^5$. The coordinates of P_i at time instant t^{j+1} are written as

$$x_{0,i}^{j+1} = x_{0,i}^{j} + \frac{\Delta t^j}{6}\left(a_{i,1} + 2a_{i,2} + 2a_{i,3} + a_{i,4}\right) \tag{3.30}$$

and

$$z_{0,i}^{j+1} = z_{0,i}^{j} + \frac{\Delta t^j}{6}\left(b_{i,1} + 2b_{i,2} + 2b_{i,3} + b_{i,4}\right) \tag{3.31}$$

where $a_{i,k}$ and $b_{i,k}$ are approximations of the horizontal and vertical velocity of P_i at the beginning, at the middle and at the end of the time increment, and they can be written as

$$\begin{aligned}
a_{i,1} &= u(x^j_{0,i}, z^j_{0,i}, t^j)\\
b_{i,1} &= w(x^j_{0,i}, z^j_{0,i}, t^j)\\
a_{i,2} &= u(x^j_{0,i} + \frac{\Delta t^j}{2} a_{i,1}, z^j_{0,i} + \frac{\Delta t^j}{2} b_{i,1}, t^j + \frac{\Delta t^j}{2})\\
b_{i,2} &= w(x^j_{0,i} + \frac{\Delta t^j}{2} a_{i,1}, z^j_{0,i} + \frac{\Delta t^j}{2} b_{i,1}, t^j + \frac{\Delta t^j}{2})\\
a_{i,3} &= u(x^j_{0,i} + \frac{\Delta t^j}{2} a_{i,2}, z^j_{0,i} + \frac{\Delta t^j}{2} b_{i,2}, t^j + \frac{\Delta t^j}{2})\\
b_{i,3} &= w(x^j_{0,i} + \frac{\Delta t^j}{2} a_{i,2}, z^j_{0,i} + \frac{\Delta t^j}{2} b_{i,2}, t^j + \frac{\Delta t^j}{2})\\
a_{i,4} &= u(x^j_{0,i} + \Delta t^j a_{i,3}, z^j_{0,i} + \Delta t^j b_{i,3}, t^j + \Delta t^j)\\
b_{i,4} &= w(x^j_{0,i} + \Delta t^j a_{i,3}, z^j_{0,i} + \Delta t^j b_{i,3}, t^j + \Delta t^j)
\end{aligned}$$

This integration scheme requires the boundary value problem to be solved four times for each time step.

3.3.3 Wetted length during water exit

When the intersection point has reached the aft end of the deck it is assumed that this is wetted throughout the rest of the impact process.

Due to the vertical side on the front end of the platform deck, it is not possible to trace the free surface upstream of the wetted body in the same manner as described above. Therefore, the upstream part of the free surface is assumed to be undisturbed and the fore body/ free surface intersection is found by using a von Karman approach. von Kármán (1929) determined the wetted part of the body as the length between the geometrical intersections of the body with the undisturbed free surface. This means that the $\tilde{x}$-coordinate of the upstream intersection point, $\tilde{x}_F$, is found from

$$\eta_{ag0} + \eta_3 - \tilde{x}_F \eta_5 - \zeta_I(x_0 = \tilde{x}_F + \eta_1, t) = 0 \qquad (3.32)$$

which may be easily solved by applying *e.g.* a Newton-Raphson scheme. If the incident wave elevation is larger than the instantaneous deck clearance at $\tilde{x} = -\frac{L}{2}$, the fore intersection point is at the upstream end of the deck, *i.e.* $\tilde{x}_F = -\frac{L}{2}$. For a fixed deck the $\tilde{x}_F$ moves downstream with a velocity equal to the phase velocity of the incident wave when $\tilde{x}_F > -\frac{L}{2}$.

3.4 The impact loading on the deck

The load on the deck can be decomposed into surge and heave forces and pitch moment. The pressure and the normal force on the deck due to the disturbance potential ϕ were discussed in

Section 2.5. Though the outer pressure is singular at the intersection points these singularities are integratable and the resulting force is finite. The contribution from the inner solution to the force is negligible. Also the pitch moment evaluated by the outer pressure is finite.

The fluid pressure on the front end of the platform deck will also contribute to the loads on the deck if it is wetted. This can not be computed by the present method, but the Froude-Kriloff force can be taken into account. In the following expressions, this pressure is included in the surge force and the pitch moment, but its contribution to the heave force is disregarded.

3.4.1 Pressure and force expressions

The total velocity potential is assumed to be a linear superposition of the velocity potentials due to the disturbance and the incident waves. The quadratic term in Bernoulli's equation is neglected, which means that the total load can be found by adding the contributions from ϕ and ϕ_I.

The dynamic pressure field due to ϕ_I is found from Bernoulli's equation and it is combined with the hydrostatic pressure term $-\rho g z$. The combined pressure is denoted as the incident wave pressure and the corresponding integrated force is called the incident wave force. For a second order Stokes wave and infinite water depth, the incident wave pressure on the deck may be approximated as

$$\begin{aligned}(p-p_0)_I &\approx -\rho\frac{\partial\phi_I}{\partial t}\Big|_{z_0=0} - \rho\eta_z\frac{\partial^2\phi_I}{\partial z_0\partial t}\Big|_{z_0=0} - \rho g\eta_{z_0} \\ &= \rho\zeta_a(g+\eta_z\omega^2)\cos(kx_0-\omega t) - \rho g\eta_z\end{aligned} \tag{3.33}$$

where $\eta_z(x_0,t) = \eta_{ag0} + \eta_3 - (x_0-\eta_1)\eta_5$ is the instantaneous deck height, *i.e.* the instantaneous vertical distance from the mean free surface to the deck in the earth-fixed frame of reference. It is assumed that $\eta_z(x_0,t)$ is of the same order of magnitude as ζ_a. Note that consistent with the derivation of second order theory, the term $-\frac{1}{2}\rho|\nabla\phi_I|^2_{z_0=0}$ should also have been included in the Froude-Kriloff pressure. However, the neglected second order pressure term from the perturbation velocity potential $-\frac{1}{2}\rho|\nabla\phi|^2$ and the coupling term $-\rho\nabla\phi\cdot\nabla\phi_I$ will partly cancel the contribution from this term. Also, since the quadratic pressure term due to ϕ is neglected when deriving the dynamic free surface condition, it is reasonable to disregard $-\frac{1}{2}\rho|\nabla\phi_I|^2_{z_0=0}$ and quadratic coupling terms when computing the incident wave pressure.

Similarly, if $\zeta_I(x_0=-\frac{L}{2}+\eta_1,t) > \eta_z(x_0=-\frac{L}{2}+\eta_1,t)$ the incident wave pressure on the front end of the deck may be written as

$$\begin{aligned}(p-p_0)_I(x_0=-\frac{L}{2}+\eta_1,t) &= \rho\zeta_a\left(g+(z+\eta_z)\omega^2\right)\cos\left(k(-\frac{L}{2}+\eta_1)-\omega t\right) \\ &\quad -\rho g\left(z+\eta_z\right)\ ,\end{aligned} \tag{3.34}$$

and otherwise the pressure on the front end is equal to zero.

The total surge and heave forces due to the water impact on the platform deck may now be written as

$$\begin{aligned} F_1 &= -\frac{d}{dt}\left(A_{33}^{(\infty)} V_0\right) n_1 - \int_{S_B} (p-p_0)_I n_1 dS \\ &= -\rho\pi c B n_1 \left(J(\kappa)\dot{c} + \frac{1}{2}\dot{J}(\kappa) c\right) V_0 - \frac{1}{2}\rho\pi c^2 B J(\kappa)\dot{V}_0 n_1 - \int_{S_B} (p-p_0)_I n_1 dS \end{aligned} \tag{3.35}$$

and

$$F_3 = -\rho\pi c B n_3 \left(J(\kappa)\dot{c} + \frac{1}{2}\dot{J}(\kappa) c\right) V_0 - \frac{1}{2}\rho\pi c^2 B J(\kappa)\dot{V}_0 n_3 - B \int_{b(t)}^{a(t)} (p-p_0)_I n_3 dx_0 \tag{3.36}$$

where F_1 is the surge and F_3 is the heave force, respectively. S_B is the instantaneous wetted area with the wetted part of the front end included. When computing the added mass force, the average relative acceleration between the fluid and the body along the wetted length is used. The contribution to the surge and heave force from the incident wave pressure can be solved analytically. The full expressions are given in Appendix B.

To find the pitch moment, F_5, the pressure distribution from both the disturbance and the incident wave have to be considered. The moment arm is measured in the body fixed coordinate system $\tilde{x}\tilde{z}$. The relationship between x and $\tilde{x}$ is $\tilde{x} = x + \tilde{x}_F + c$. The outer pressure distribution due the disturbance velocity potential is given in Equation (2.24) and is here denoted as $(p-p_0)_D$. In Appendix B it is shown that the pitch moment due to the outer pressure is finite and the inner solution is therefore omitted. The total fluid pressure $(p-p_0)_{tot}$ then becomes

$$\begin{aligned} (p-p_0)_{tot} &= (p-p_0)_D + (p-p_0)_I \\ &= \rho(V_0 + V_1 x)\frac{\left[c\frac{dc}{dt} + x\left(-\frac{dc}{dt} + \frac{da}{dt}\right)\right]}{\sqrt{c^2-x^2}} \\ &+ \rho\left[\frac{\partial V_0}{\partial t} + \frac{1}{2}\frac{\partial V_1}{\partial t}x + \frac{1}{2}V_1\left(\frac{dc}{dt} - \frac{da}{dt}\right)\right]\sqrt{c^2-x^2} \\ &+ \rho\zeta_a(g + \eta_z(x,t)\omega^2)\cos\left(k(x + \tilde{x}_F + c + \eta_1) - \omega t\right) - \rho g \eta_z(x,t) \end{aligned} \tag{3.37}$$

The pitch moment may thus be written as

$$F_5 = -B\int_{-c}^{c} (x + \tilde{x}_F + c)\,(p-p_0)_{tot}\; dx + B\int_{\eta_{z0}}^{\zeta_I} (z - z_G)(p - p_I)\; dz\Big|_{\tilde{x}=-\frac{L}{2}} \tag{3.38}$$

where z_G is the z-coordinate of the center of gravity. The latter integral is set equal to zero when $\zeta_I(\tilde{x} = -\frac{L}{2}, t) < \eta_z(\tilde{x} = -\frac{L}{2}, t)$.

The full expression for the pitch moment is given in Appendix B.

3.4.2 The impact force during water exit

The impact formula (2.44) follows from pressure integration under the assumption that g is negligible and that $\frac{1}{2}|\nabla\phi|^2$ is small relative to $\frac{\partial\phi}{\partial t}$. These are the same assumptions that lead to the dynamic free surface condition $\phi = 0$. While these are reasonable assumption initially, the importance of neglected terms will grow with time. $\phi = 0$ may therefore be a poor approximation for the exact free surface condition during water exit and thus the impact formula will no longer be valid. In the same manner as in Kaplan (1992), the slamming term proportional to $\dot{c}$ is only evaluated when $\dot{c} > 0$. When $\dot{c} = 0$ the slamming term is zero, while this particular term is set equal to zero when $\dot{c} < 0$. Such treatment is commonly used in ship slamming analyses. This can be seen *e.g.* in Kaplan and Malakhoff (1978), Yamamoto et al. (1980) and Kaplan (1987).

The added mass and the incident wave force are retained also during water exit. The total pressure used in the force calculations during water exit is thus found by setting V_0 equal to zero in Equation (3.37). For the surge and the heave force the slamming term as well as V_0 are set equal to zero during water exit. Both V_0 and V_1 are set equal to zero when computing the pitch moment during water exit.

3.5 Water impact on a bottom mounted platform

In this section the theory given in Chapter 2 and in the preceding sections of this chapter is used to solve water impact underneath a fixed platform deck. This may be considered to be a special case of wave impact on a floater, but it is simpler since rigid body responses do not have to be solved. A generalization of the solution procedure to solve impact on a floating platform is straightforward, and a procedure is outlined in Appendix C. In the following a fixed horizontal deck is assumed.

The earth-fixed and body-fixed coordinate systems coincide. In regular waves, impact will occur if the maximum wave elevation is greater than the initial deck clearance. For deep water, impact will occur if $\zeta_a + \frac{1}{2}\zeta_a^2 k > \eta_{ag0}$. Time of first impact, t_0, is found from

$$\eta_{ag0} - \zeta_a \cos\left(k\frac{L}{2} + \omega t_0\right) - \frac{1}{2}\zeta_a^2 k \cos\left(2(k\frac{L}{2} + \omega t_0)\right) = 0 \tag{3.39}$$

by using the Newton-Raphson method.

The free surface downstream of $x_0 = -\frac{L}{2}$ is discretized by free surface particles, and integrated in time by a fourth order Runge-Kutta scheme as outlined in Section 3.3.2. The time increments Δt^j and the downstream intersection point during water entry are determined by the procedure described in Section 3.3.1. Since the body is fixed, the impact induced loads on the deck are the parameters to be calculated. The expressions for the incident wave loads are simplified since the motion of the platform is zero.

Since the velocity of the deck is zero, only the wave kinematics contribute to the relative impact velocity. With reference to Equation (3.8), V_0 and V_1 may now be written as

$$\begin{aligned} V_0(t) &= \frac{\partial \phi_I(\tilde{x}_F + c, t)}{\partial z_0}|_{z_0=\eta_{ag0}} \approx \frac{\partial \phi_I(\tilde{x}_F + c, t)}{\partial z_0}|_{z_0=0} + \eta_{ag0}\frac{\partial \phi_I(\tilde{x}_F + c, t)}{\partial^2 z_0^2}|_{z_0=0} \\ &= \zeta_a \omega \left(1 + \eta_{ag0} k\right) \sin\left(k(\tilde{x}_F + c) - \omega t\right) \end{aligned} \tag{3.40}$$

and

$$\begin{aligned} V_1(t) &= \frac{1}{c(t)} \left[\frac{\partial \phi_I(\tilde{x}_F + 2c, t)}{\partial z_0}|_{z_0=\eta_{ag0}} - \frac{\partial \phi_I(\tilde{x}_F + c, t)}{\partial z_0}|_{z_0=\eta_{ag0}} \right] \\ &\approx \frac{1}{c(t)} \left(\zeta_a \omega \left(1 + \eta_{ag} k\right)\right) \left(\sin\left(k(\tilde{x}_F + 2c) - \omega t\right) - \sin\left(k(\tilde{x}_F + c) - \omega t\right)\right) , \end{aligned} \tag{3.41}$$

respectively. The upstream intersection point, $\tilde{x}_F$, is found from Equation (3.32) with the platform motion set equal to zero. Similarly, the average impact acceleration $\dot{V}_0$ is only dependent on the kinematics associated to the undisturbed wave.

The fact that the platform does not move, provides many simplifications in the numerical solution of the water impact problem. The equation of motion for the platform does not to be solved, and the expressions for both the loading and the impact velocity become less complicated. Further, the wave induced platform motion, and the added mass and damping matrices of the submerged platform volume have not to be evaluated. The latter represents probably the greatest simplification. If the motion transfer functions and the added mass and damping matrices are not given, these have to be estimated first.

In the rest of this thesis, only fixed platform decks and the vertical force are considered.

3.6 Convergence tests for the Wagner based method

It is important to check the convergence of a numerical method. Parameters that may affect the solution for a problem in the time domain are the spatial discretization of the problem and the time step used in the time integration. In the Wagner based method, the time step is a part of the solution, and Δt^j and the spatial discretization of the free surface are closely connected. The convergence with respect to the discretization of the free surface must therefore be checked.

The convergence tests below and the parametric studies described in Section 3.7 are performed for a fixed deck with dimensions equal to the model used in the experiments described in next chapter. The length of the deck is 0.63m and the breadth is 0.56m. The wave conditions chosen are also taken from the same experiments. Model scale is used in the parametric study because this may be helpful when discussing the experiments presented in Chapter 4. However, the following discussion is also valid for full scale results. Length parameters are linearly scaled, while time is Froude scaled, which means that the ratio between the force in model scale and in full scale is equal to the scale factor cubed.

A portion of the free surface with a horizontal extension equal to $2L$ is discretized. The first

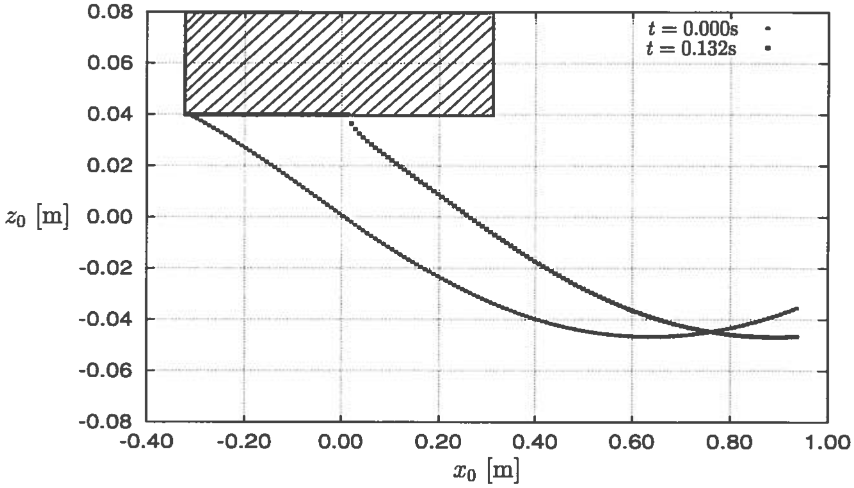

Figure 3.5: *Discretization of the free surface. 150 surface points are used. The wave condition is $T = 1.25s$ and $\zeta_a = 0.05m$. The position of the body is indicated by the shaded area.*

element in the initial grid is located at the point where the impact first occurs, *i.e.* at the front edge of the deck. The free surface points are equally spaced in x_0-direction downstream of the point of initial impact. Since the water exit is approximated by a von Karman type approach, the upstream part of the free surface does not have to be discretized. Figure 3.5 shows the initial discretization of the free surface and the discretization at a time instant when almost half of deck is wetted. In this case the surface is described by 150 fluid particles. For the latter time instant, the fluid particles upstream of the aft body/ free surface intersection point are located on the body surface.

The results for the impact force should converge as the number of free surface particles used in the calculations is increased. A more refined discretization reduces the time increments, and this should make the time integration converge. This has been studied for a number of combinations of wave condition and η_{ag0} and the results for all cases converge nicely. The number of fluid particles needed in order to obtain converged results varies from case to case. For the majority of the cases tested the results converge rapidly, and 100-150 particles are sufficient for the relative errors for the maximum and mimimum force, $F_{\max}$ and $F_{\min}$, to be less than 1%. Figure 3.6 shows an example of a case that converges easily and a case that needs a large number of particles to converge. N is the number of fluid particles used in the calculations. The case in Figure 3.6(a) corresponds to $\eta_{ag0} = 0.04$m, $T = 1.25$s and $\zeta_a = 0.06$m. This yields a relative violent impact and the deck gets fully wetted for a part of the duration of the water impact event. A plot of the corresponding converged wetted length is given in Figure 3.10(b). The results for the total impact force converge rapidly. Good results are obtained with $N = 100$. Once the downstream edge of the deck is wetted, the number of particles is irrelevant for the force calculations. Figure 3.6 shows a plot for the calculated values of the largest positive force,

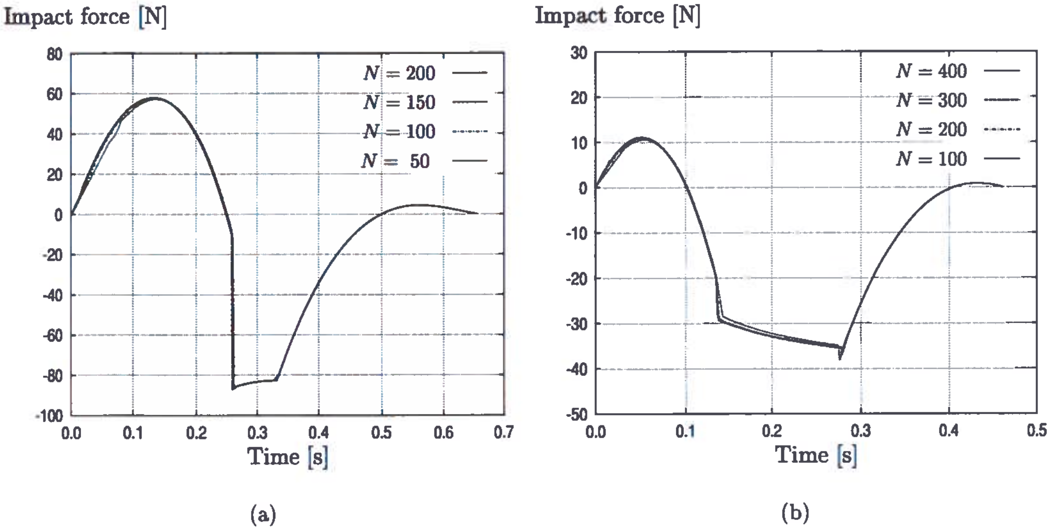

(a) (b)

Figure 3.6: *The convergence of the impact force results with respect to the number of free surface particles, N, used in the calculations. The case depicted in the left figure has $\eta_{ag0} = 0.04m$, $T = 1.25s$ and $\zeta_a = 0.06m$. The case to the right has $\eta_{ag0} = 0.06m$, $T = 1.25s$ and $\zeta_a = 0.06m$.*

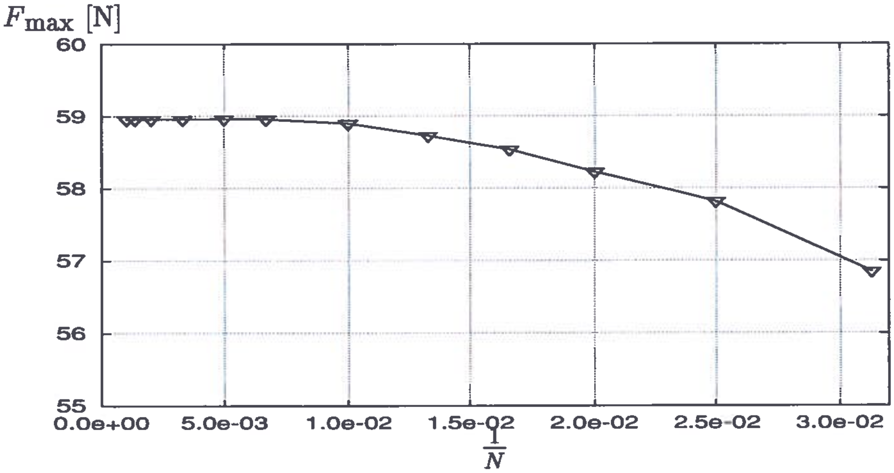

Figure 3.7: *Convergence of F_{max} for $\eta_{ag0} = 0.04m$, $T = 1.25s$ and $\zeta_a = 0.06m$.*

$F_{\max}$, for the same impact condition. $F_{\max}$ approaches 58.96N as N is increased. The error made for $F_{\max}$ with $N = 100$ is less than 0.1% when comparing to the converged result. Figure 3.6(b) gives the total impact force results for a "gentle" impact event, where $\eta_{ag0} = 0.06$m, $T = 1.25$s and $\zeta_a = 0.06$m. The positive impact force during the initial stage of the impact seems to be well described when using $N = 200$. However, the negative force peak does not converge so quickly. In the negative force region before F_{min} is reached, the wetted length is still increases slightly, while the water exit has started at the downstream edge of the deck. The slamming force is still not set equal to zero, but the total force is dominated by the negative added mass force. As a consequence, a small change in the velocity of the upstream intersection point influences both the slamming and the added mass forces. When N is sufficiently large the total impact force and the wetted length results converge. $N = 300$ yields good results.

For most of the cases the results converge fast but for some cases a finer discretization is needed to obtain convergence. Particularly for the region where the force is negative. The computation time increases approximately as N^2, which means that by increasing N by a factor 2, the computation time increases approximately by a factor 4. Unless N becomes very large, the computation time is small and convergence tests are not expensive to perform. The CPU-time for the case plotted in Figure 3.6(a) with $N = 200$ is approximately 5 seconds on a 450MHz Pentium II computer.

3.7 Parametric study for the Wagner based method

A parametric study to determine the importance of the primary parameters governing the vertical impact loading on the deck is performed by using the Wagner based method. This may be helpful when trying to understand the physics of the problem. The main parameters governing the impact force can be listed to be the wave amplitude, the wave period and the deck clearance in still water. The latter is here denoted as deck height. Additional effects may be cushioning due to entrapped air, compressibility of the fluid and three-dimensional effects in the waves. These are assumed to be of minor importance.

The force on the deck may be divided into three components as shown in Equation (3.36). These are the slam force, the added mass force and the incident wave force, respectively.

The water entry/ water exit process due to a regular propagating wave hitting the deck, yields a force history where the structure experiences a positive slamming dominated up-lift force during the initial water entry phase. This is followed by a negative force dominated by the negative added mass force. For many impact conditions the incident wave force becomes larger than the magnitude of the added mass force during the final part of water exit, and the total force becomes thus positive. Figure 3.8 presents the total force on the deck, as well as the contribution from each of the terms mentioned above for two different cases. Both cases have a first order wave amplitude $\zeta_a = 0.06\text{m}$ and deck heigth $\eta_{ag0} = 0.04\text{m}$, but different wave periods, $T = 1.11\text{s}$ and $T = 1.43\text{s}$, respectively. Similarly, Figure 3.9 gives the total force and the different components for two wave amplitudes when the wave period and the deck height are kept fixed and equal to $T = 1.25\text{s}$ and $\eta_{ag0} = 0.04\text{m}$, respectively.

The positive water entry force is dominated by the slamming force caused by the rapid increase of added mass. F_{max} also gets a significant contribution from the incident wave force, while the added mass force yields a negative contribution of the same order of magnitude. The

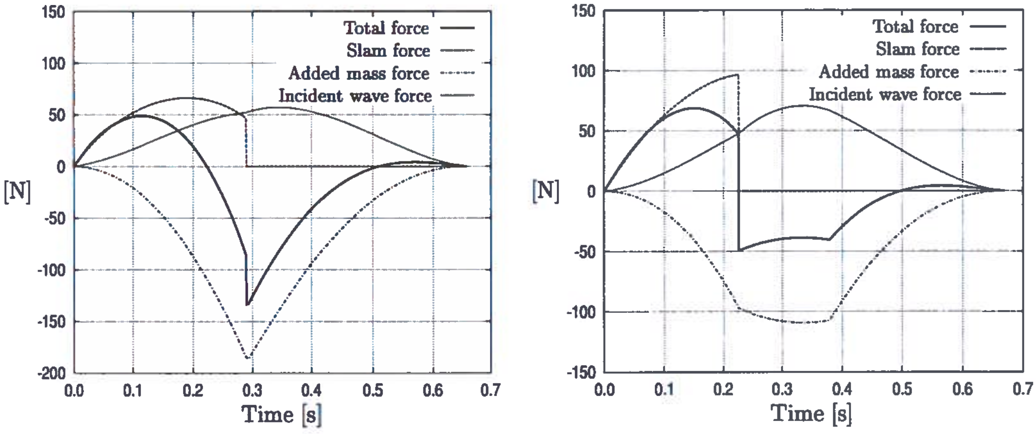

(a) $T = 1.11$s

(b) $T = 1.43$s

Figure 3.8: *The total impact force and its contributions from the slamming term, added mass term and incident wave term.* $\zeta_a = 0.06m$ *and* $\eta_{ag0} = 0.04m$.

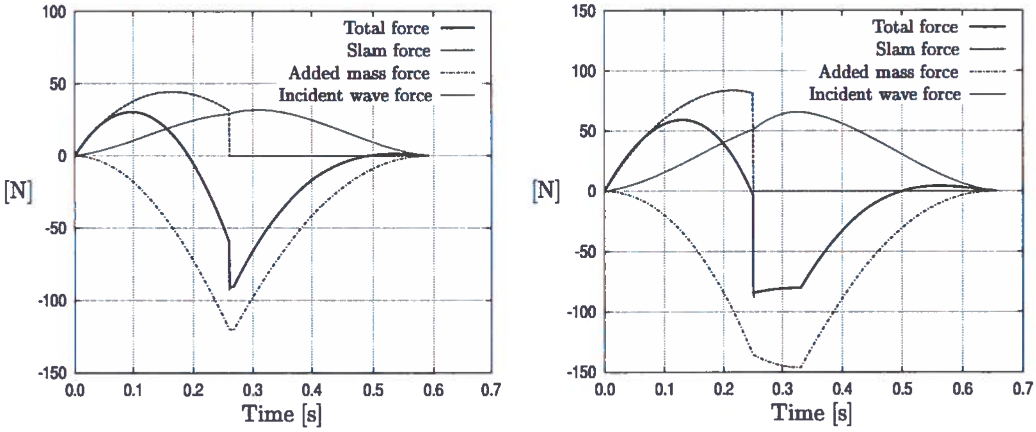

(a) $\zeta_{Ia} = 0.05$m

(b) $\zeta_{Ia} = 0.06$m

Figure 3.9: *The total impact force and its contributions from the slamming term, the added mass term and the incident wave term.* $T = 1.25s$ *and* $\eta_{ag0} = 0.04m$.

slamming force is always positive, but it is set equal to zero when the wetted area decreases. The added mass force is negative throughout the entire impact event since the fluid particle accelerations due to ϕ_I are negative in the wave crest. The magnitude of the added mass term has its maximum at the same time as the wetting of the deck does. The incident wave force is positive and yields a significant contribution to the total force.

Below, the influence of the primary parameters on the total impact force is discussed.

3.7.1 Wave period dependency on the impact force

The maximum vertical particle velocity in the wave crest of an undisturbed regular wave decreases with increasing wave period. From Equation (2.44) it is known that the vertical fluid particle velocity is crucial for the impact force. In spite of this, it can be noted from Figure 3.10(a) that for a given η_{ag0} and ζ_a, $F_{\max}$ increases as the wave period gets longer. This is mainly due to a more rapid wetting of the deck for increasing period. Longer waves allow the body to get wet faster because of lower wave steepness. Figure 3.10(b) shows how the wetted length evolves as function of time for the different wave periods, while Figures 3.11(a) and 3.11(b) show the corresponding wave period dependency of V_0 and $\dot{c}$, respectively. The time instants when $F_{\max}$ occurs are indicated with circles. Even if average impact velocity V_0 at the time instant where $F_{\max}$ occurs, is smallest for the longest wave period, this is compensated by an increased $\dot{c}$ and by a larger wetted area when $F_{\max}$ occurs. The latter is also a direct consequence of increased $\dot{c}$. A larger $\dot{c}$ implies that the slamming force dominates the total force to a greater extent. The wetted area is thus larger when the total force gets its largest value. Another consequence following from the more rapid wetting, is that the decay of V_0 with time is smaller for waves with smaller steepness than for steeper ones. If $\zeta_a \lesssim \eta_{ag0}$, however, the smallest of two wave periods may give the largest $F_{\max}$ because it yields the largest second order wave amplitude.

The maximum magnitude of the negative force peak, $|F_{\min}|$, occurs when the wetting of the deck is at its maximum. At this time instant only the incident wave force and the added mass force contributes. Given that the maximum wetted area is equal for two incident waves with different periods, $|F_{\min}|$ is smaller for the longer wave. This is mainly due to that the negative particle accelerations, and thus the negative added mass force, are proportional to T^{-2}. Figure 3.8 shows the contributions to the force relative to two different wave periods. The maximum magnitude of the negative added mass term is clearly larger for the shorter wave. Also the positive incident wave force is smaller at the point of maximum wetting for the shortest wave.

3.7.2 Wave amplitude dependency on the impact force

Figure 3.12 shows an example of the wave amplitude dependency on the total impact force and on the wetting of the deck. The wave period and the deck height are kept constant, while the wave impact is calculated for three different wave amplitudes. The wetted lengths during the initial water entry phase are relatively similar for the three different amplitudes, while the maximum force $F_{\max}$ is very dependent on the wave amplitude. Even if $\dot{c}(t)$ is not much affected by an increased amplitude, for constant T and η_{ag0}, $F_{\max}$ increases rapidly as the amplitude increases. Several reasons for this can be detected, *i.e.* by studying the contributions to the

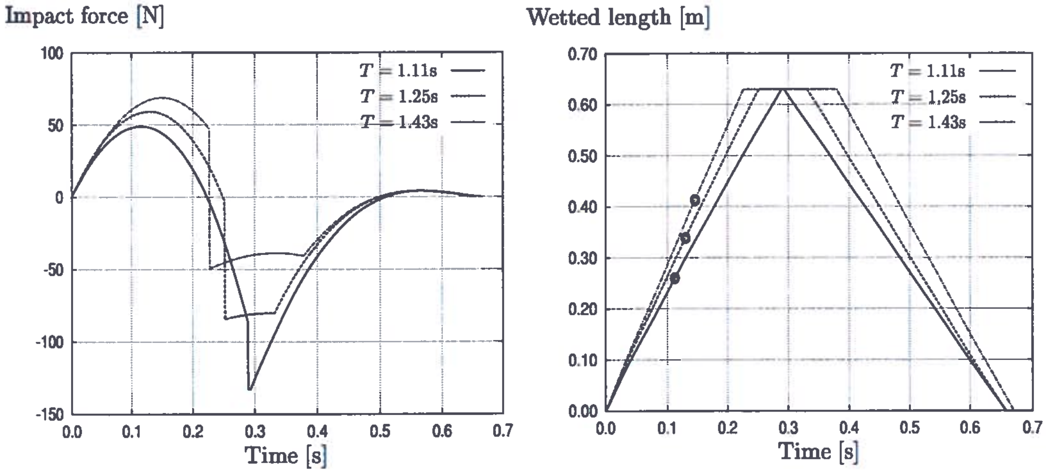

(a) Total impact force

(b) Wetted length

Figure 3.10: *The wave period dependency on the total impact force and the wetted area of the body.* $\zeta_a = 0.06m$ *and* $\eta_{ag0} = 0.04m$. *The circles indicate the wetting of the body at the time instant where* F_{max} *occurs.*

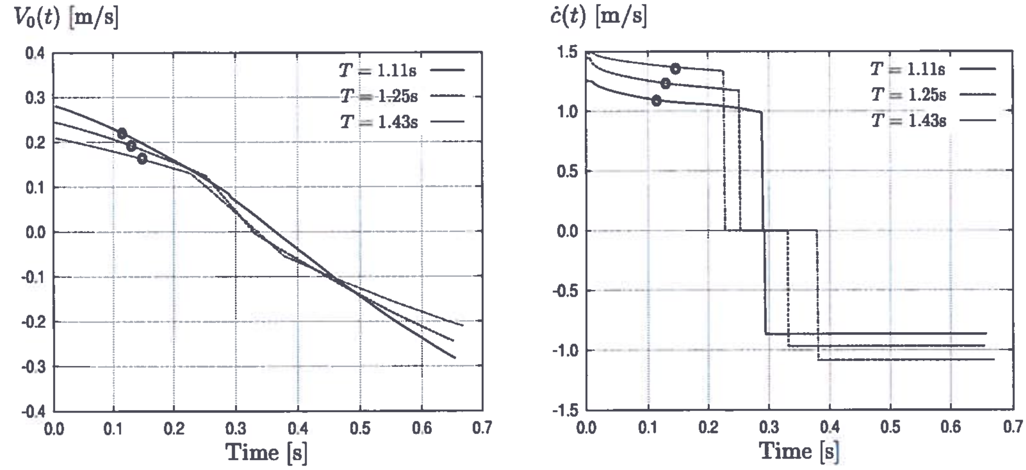

(a) Average impact velocity

(b) Velocity of wetting.

Figure 3.11: *The wave period dependency on the average impact velocity and the change of chord length with time.* $\zeta_a = 0.06m$ *and* $\eta_{ag0} = 0.04m$. *The circles indicate the velocities at the time instant where* F_{max} *occurs.*

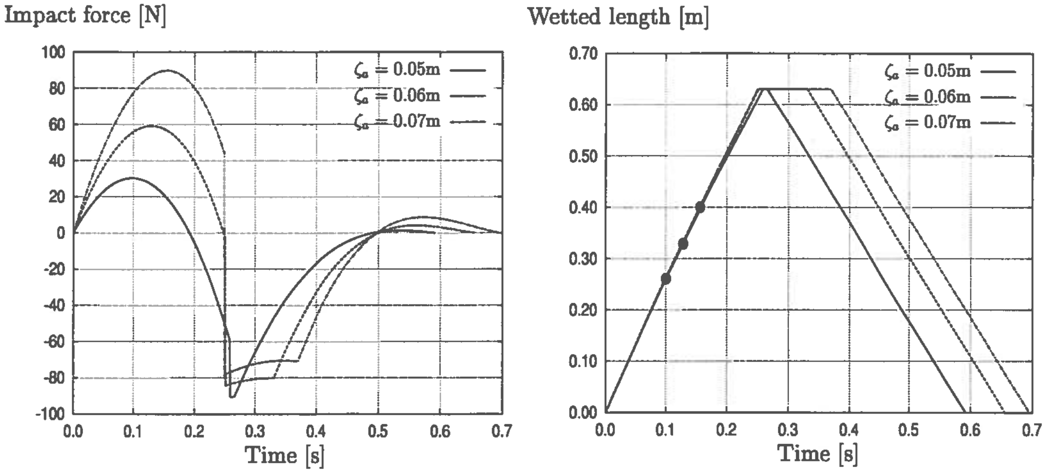

(a) Total impact force

(b) Wetted length

Figure 3.12: *The wave amplitude dependency on the total impact force and the wetted area of the body.* $T = 1.25s$ *and* $\eta_{ag0} = 0.04m$. *The circles indicate the wetting of the deck at the time instant where* F_{max} *occurs.*

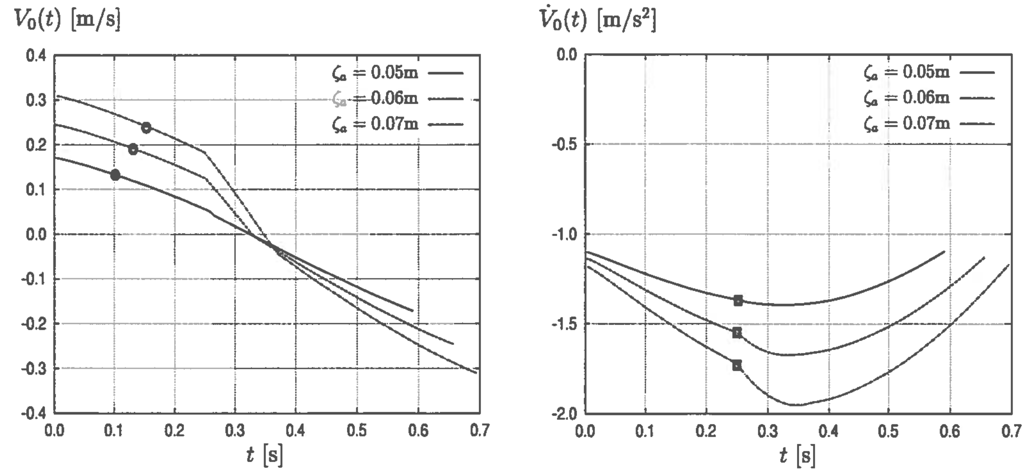

(a) Average impact velocity

(b) Average impact acceleration

Figure 3.13: *The wave amplitude dependency on the impact velocity and acceleration used in the force calculations.* $T = 1.25s$ *and* $\eta_{ag0} = 0.04m$. *The circles indicate the time instant where* F_{max} *occurs, while the squares indicate the occurrence of* F_{min}.

total force for the two wave amplitudes presented in Figure 3.9. Both the incident wave force and the added mass force are affected by the increase in wave amplitude, but the main contribution to the change in F_{max} comes from the change in the slamming force. $\dot{c}(t)$ remains quite unaffected by the increased wave amplitude in this case, but due to larger impact velocities the slamming term increases significantly. The amplitude dependence on V_0 is shown in Figure 3.13(a). The circles indicate the location where F_{max} occurs. The increase in V_0 is caused by two effects. When the wave amplitude increases the vertical fluid velocities in the undisturbed wave increase. The leading order term of the fluid velocity varies linearly with the wave amplitude. Also, as the wave amplitude increases, the first impact moves further downstream of the wave crest toward a location where the vertical fluid velocities are larger. Since the slam force increases more than the magnitude of the negative added mass force, the wetted area is larger for F_{max} for the higher wave. This is indicated by the circles in Figure 3.12(b).

In the present case, an increase in the wave amplitude does not significantly affect the magnitude of F_{min}. Here F_{min} occurs when the deck is fully wetted, but generally it occurs when the wetted area gets maximum value. The magnitude of the added mass force becomes larger due to an increase of averaged fluid accelerations across the wetted area. This is pointed out in Figure 3.13(b), where the squares indicate the time instant of maximum negative force. However, the increase in the incident wave force when increasing the wave amplitude, approximately compensates for the change in the added mass term.

Increased wave amplitude leads to a larger duration of the total impact event.

3.7.3 Deck height dependency on the impact force

The deck height for a fixed platform deck obviously affects the water impact greatly. In full scale the deck height is a parameter which can be controlled. Figure 3.14 shows time histories of the total impact force and the wetting of the deck for three different values of η_{ag0}. The wave conditions are the same for all three cases, $T = 1.11$s and $\zeta_a = 0.06$m. Though $\dot{c}(t)$ is not sensitive to η_{ag0} during the initial water entry phase, the loading is greatly affected by the change in deck height. This can easily be explained. Firstly, the reduction in the deck height gives a larger incident wave force. Secondly, $\dot{c}(t)$ is similar for the three cases initially, but a significant difference in V_0 can be noted from Figure 3.15(a) and thus a large difference in the slamming force. The latter gives the main explanation to the difference. The circles in the figure indicate the velocity at the location of maximum up-lift force. At first impact, V_0 is in this case almost two times as large for the smallest value of η_{ag0} than it is for the largest. The whole difference is due to the initial impact occurring at different positions on the wave crest. Also, since the slamming term dominates more for the smaller deck height, F_{max} will occur for a larger wetted area.

F_{min} is in this case also greatly affected by changes in η_{ag0}. This is mainly due to the difference in the maximum wetting, but the change in $\dot{V}_0$ plays also a certain role, see Figure 3.15(b). Because of a smaller positive incident wave force, the largest of two different deck heights may give the largest value for $|F_{\text{min}}|$ if the maximum wetted lengths are similar.

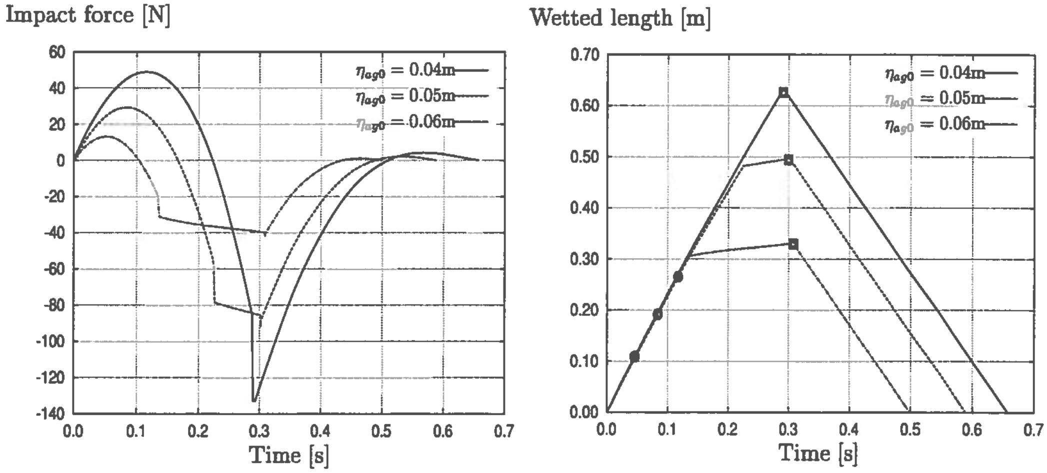

(a) Total impact force

(b) Wetted length

Figure 3.14: *The deck height dependency on the total impact force and the wetted area of the body.* $\zeta_a = 0.06m$ *and* $T = 1.11s$. *The circles indicate the wetting of the deck at the time instant where* F_{max} *occurs.*

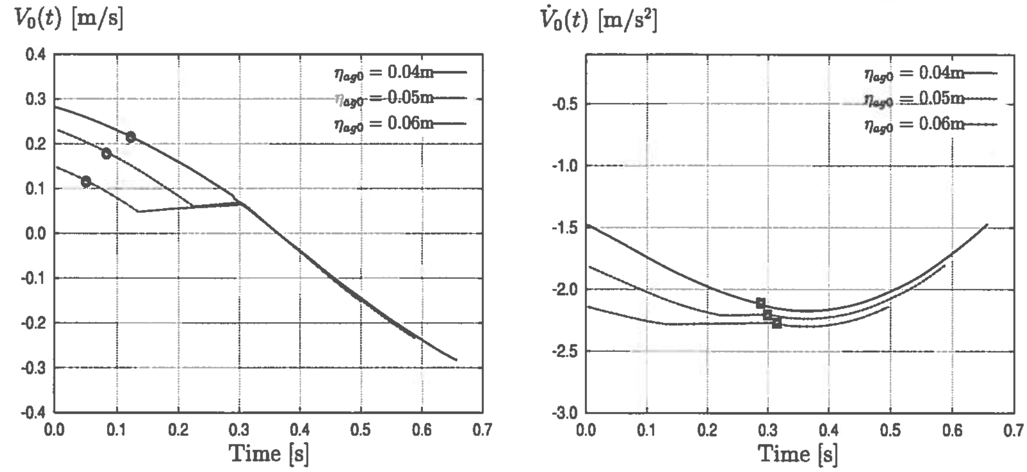

(a) Average impact velocity

(b) Average impact acceleration

Figure 3.15: *The deck height dependency on the impact velocity and acceleration used in the force calculations.* $\zeta_a = 0.06m$ *and* $T = 1.11s$. *The circles indicate the time instant where* F_{max} *occurs, while the squares indicate the occurrence of* F_{min}.

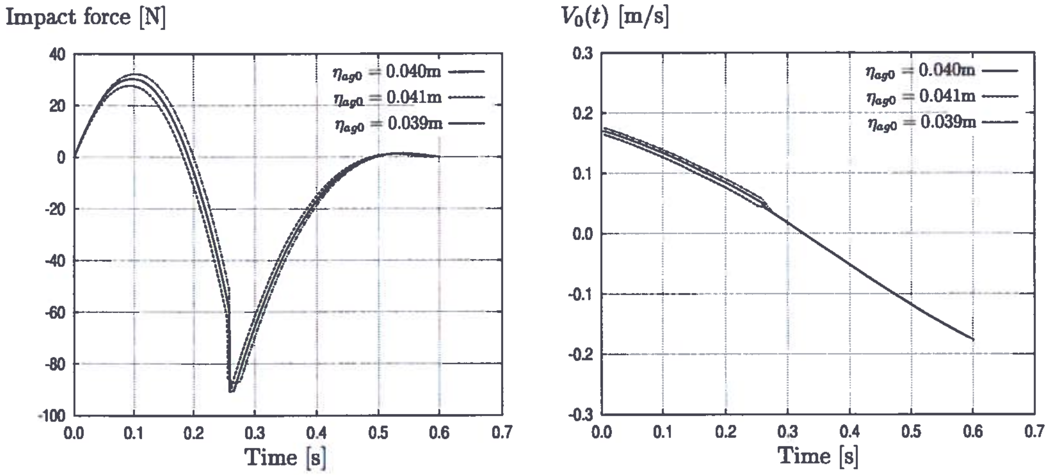

(a) Total impact force

(b) Average impact velocity

Figure 3.16: *The deck height dependency on the total impact force and the wetted area of the body.* $\zeta_a = 0.05m$ *and* $T = 1.11s$.

Since the total impact force is so strongly affected by η_{ag0}, the accuracy when determining the deck height in the experiments is crucial. Figure 3.16(a) shows how the results are affected by a small shift in the deck height. $\dot{c}(t)$ is almost unchanged for these three impact events, but V_0 is affected by the small change in the deck height, see Figure 3.16(b).

3.7.4 Two-dimensional *versus* three-dimensional flow condition

The results from the Wagner based method presented in the parametric study above, as well as the experimental results that will be presented in Sections 4.5, are all for two-dimensional flow conditions. However, when applying this theory on a real full scale platform, three-dimensional effects should be taken into account. Otherwise, the calculated results for the loading and the responses could be significantly overestimated. In Section 2.6.1 a method for correcting the two-dimensional calculations for three-dimensional flow is presented. The high frequency limit added mass coefficient is corrected using the simple empirical formula presented by Blagoveshchensky (1962). The formula for the correction factor $J(\kappa)$ is given in Equation (2.49), κ being the aspect ratio of the wetted area, $\kappa = \frac{2c}{B}$. In this section, results for two-dimensional flow will be compared with results corrected for three-dimensional effects.

The three-dimensional effects play an important role for the loading, both during the water entry and the water exit phase. Figure 3.17(a) presents results of force calculations with without accounting for three-dimensional effects. Only the slamming force and the added mass force are corrected. The wave condition is described by ζ_a = 0.05m and T = 1.25s, while the deck height is equal to 0.04m. In Figure 3.17(b), the corresponding time histories of the correction

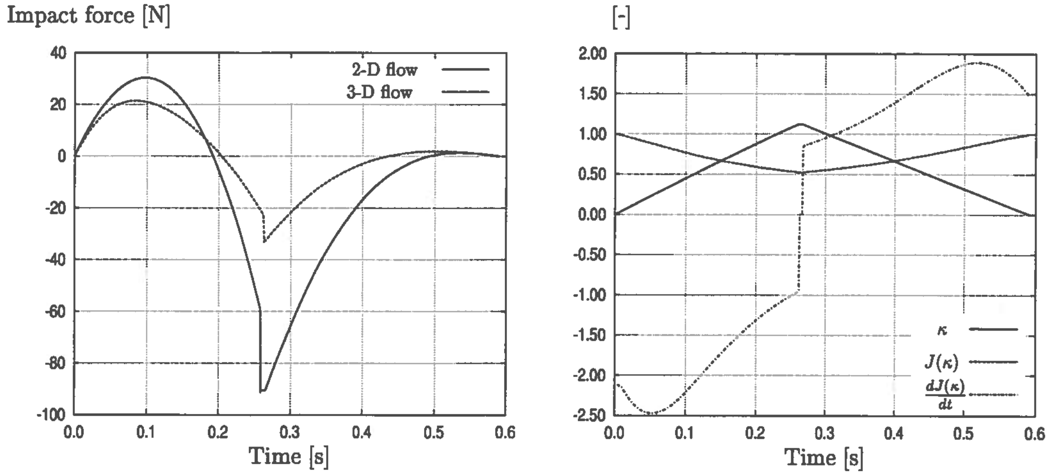

(a) Total impact force

(b) Correction factors

Figure 3.17: *The flow condition dependency of the total impact force. The deck has dimensions 0.63m by 0.56m, the deck height is 0.04m and the wave condition is given by* $T = 1.25s$ *and* $\zeta_a = 0.05m$. *On the right figure, the correction factors* $J(\kappa)$ *and* $\dot{J}(\kappa)$ *as well as the aspect ratio of the wetted area,* κ, *are shown for the same impact event.*

factors $J(\kappa)$ and $\dot{J}(\kappa)$ are presented together with the related value of κ. At the initial impact, κ is small and $J(\kappa)$ is close to unity, and the difference in the vertical impact force due to the two different flow conditions is small. But as the wetted ara increases, the three-dimensional effects tend to become significant. The term connected to $\dot{J}(\kappa)$ in Equation (2.50) gives an unimportant negative contribution for small wetted lengths, but at the location of the maximum positive impact force both the correction terms contribute. When F_{max} occurs for the three-dimensional flow, the added mass is only 81% of the two-dimensional one. The magnitude of the added mass force is reduced by 19%. Due to the term involving $\dot{J}(\kappa)$ the slamming term is reduced by an even larger factor. At the location of the maximum positive vertical force, the slamming force is only 71% of the corresponding two-dimensional slamming force at the same time instant. The maximum three-dimensional total force is in this case 70% of maximum two-dimensional total force.

Once κ reaches its maximum value only the added mass term is affected by three-dimensional effects. F_{min} occurs when the wetting is maximum. The value of κ is then 1.125 and the corresponding value of $J(\kappa)$ is 0.524, meaning that the added mass force for the three-dimensional flow condition is only 52.4 % of the corresponding value for the two-dimensional case. However, since the positive incident wave force is the same for both cases, the magnitude of the minimum force is now reduced by more than 60% due to three-dimensional effects.

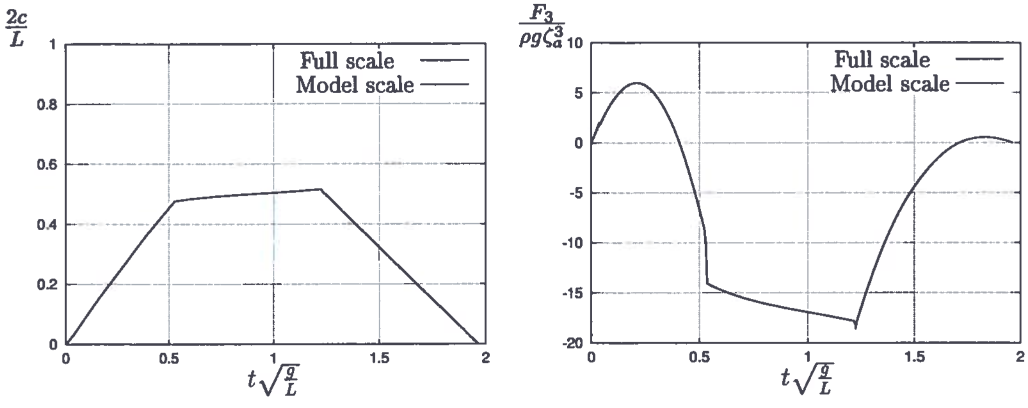

(a) Wetted length.

(b) Vertical force

Figure 3.18: *Dimensionless wetted length and vertical force as function of dimensionless time for full scale and model scale with scale 1:150.* $T = 1.11s$, $\zeta_a = 0.06m$ *and* $\eta_{ag0} = 0.06m$ *in model scale.* $T = 13.59s$, $\zeta_a = 9.0m$ *and* $\eta_{ag0} = 9.0m$ *in full scale.*

3.7.5 Full scale *versus* model scale

So far in the parametric studies, model scale has been used to describe the impact process, but for practical use full scale computations are important. From the force expressions in Section 3.4.1, one can show that if time is Froude scaled and length is linearly scaled, that the time series for the dimensionless vertical force acting on a fixed horizontal deck, $\bar{F}_3 = F_3/\rho g \zeta_a^3$ as function of the dimensionless time $t\sqrt{g/L}$ is constant for given η_{ag0}/λ and ζ_a/λ. This should also be the case for numerical solution results determined by the Wagner based method.

Figure 3.18 and Figure 3.19 show two specific examples on computations of the wetted length and the vertical force in model scale and in full scale. The model has the same dimensions as the model described in Chapter 4, $L = 0.63$m and $B = 0.56$m. A model scale of 1:150 is assumed, giving $L = 94.5$m and $B = 84.0$m in full scale. The same number of fluid particles, $N = 500$, is used for both model scale and full scale computations. On dimensionless form the vertical forces and the wetted lengths calculated in model scale and full scale, respectively, are close to identical.

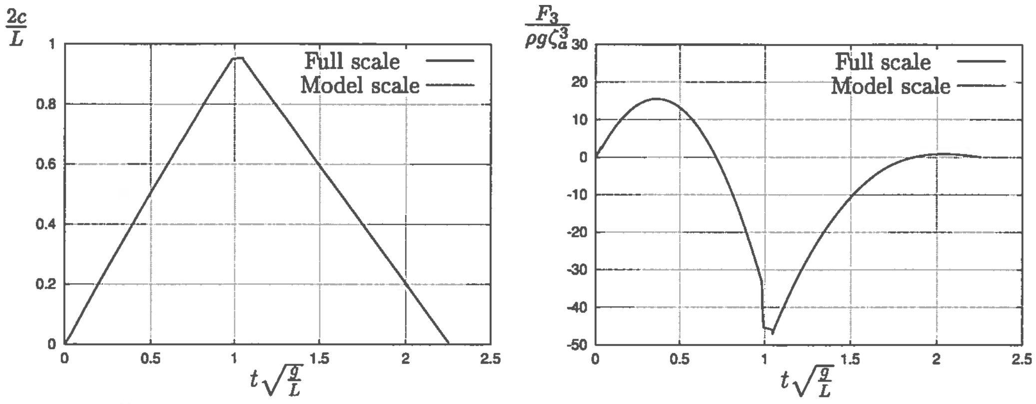

(a) Wetted length. (b) Vertical force

Figure 3.19: *Dimensionless wetted length and vertical force as function of dimensionless time for full scale and model scale with scale 1:150.* $T = 1.25s$, $\zeta_a = 0.06m$ *and* $\eta_{ag0} = 0.05m$ *in model scale.* $T = 15.31s$, $\zeta_a = 9.0m$ *and* $\eta_{ag0} = 7.5m$ *in full scale.*

CHAPTER 4

Experiments and results from the Wagner based method

4.1 Introduction

An important task when developing a numerical code is validation or verification. Verification means that the numerical solution is proved to be consistent with the theoretical basis of the method, *i.e.* the governing differential equation is correctly solved by the numerical method. The method can be verified by comparing to known analytical results or by performing convergence studies. Validation means that theory is compared to the physical reality, which means that experimental studies are needed. The most controlled way of doing this is by model tests. Of course one is then left with how to scale the results to full scale condition.

If analytical expressions are available for the given problem, this would be the best verification test case. For wave impact underneath a platform deck, no analytical solution is available. Experimental results for both impact in quay-aprons and on platform decks are published (see Section 1.2), but it is often difficult to extract the necessary information from these publications. By performing the experiments oneself, better control over the measurements and the design of the models and the equipment needed is obtained. Taylor made experiments for the given physical problem can then be performed. Also, model tests may provide important information about the physical approximation of the theory. This is a great advantage when analyzing the results. This was the main motivation for starting out with the experimental work.

The phenomenon of interest is the water impact process due to an incident wave reaching the deck and propagating through. To study the overall stability and global strength of a structure, it is necessary to consider the total force and moments acting on it. Therefore the main parameter to measure in the laboratory study, was chosen to be the total vertical wave induced force acting on the platform deck. The principle parameters governing the loading are assumed to be the wave

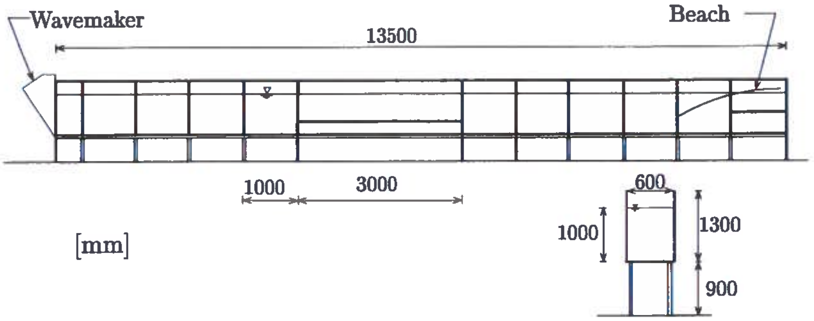

Figure 4.1: *The narrow wave flume at the Department of Marine Hydrodynamics, NTNU.*

amplitude, the wave period and the initial deck clearance. These parameters can readily be controlled in the laboratory. Additional effects on the load may be air cushioning due to entrapped air, compressibility of the fluid, three dimensional effects in the wave field and surface roughness.

In addition to the vertical impact force, the wetted area of the deck and the wave elevations at different position were measured.

This chapter describes the experimental work and findings as well as comparisons to theoretical results obtained by the Wagner based method.

4.2 Experimental set-up

4.2.1 The laboratory

The experiments were carried out in the wave flume at the Department of Marine Hydrodynamics, NTNU. This is a narrow wave flume, and the main dimensions are 13.5 m long, 1.3 m deep, and 0.6 m wide. It is designed for a water depth of 1.0 m. Figure 4.1 shows a sketch of the flume.

An important reason for choosing this tank was the possibility of getting visual observations, which may be helpful for the understanding of the physics involved. Other reasons were availability and costs of the experiments. By choosing this flume, two-dimensional experiments were possible to perform. This was considered to be an advantage, since the simple experiments made it easier to isolate the primary effects to be studied. In reality three-dimensional effects are important, but in the Wagner based method they are accounted for by the procedure described in Section 2.6.1.

The use of optical measurement techniques was a primary concern when the flume was designed. Both side walls and bottom of the flume are made of 19mm thick glass panes, which ensures good access for visual inspections and good conditions for optical measurements techniques. The glass is supported by a steel structure designed to withstand the static pressure present when the flume is filled, and to be stiff enough to avoid vibrations due to dynamic pressure. A wavemaker is installed in the flume. This is an electronically operated, computer controlled, single flap wavemaker. It is fitted with a control system that enables the flap to damp out reflected waves. The flap is hinged 0.10m above the bottom of the flume. The wavemaker is capable of generating regular, irregular and breaking waves. More information on the design and characteristics of the flume and the wavemaker can be found in Lader (2001).

To damp out the waves at the end of the flume, a beach was installed. This is a conventional type beach and it has a parabolic arc profile.

4.2.2 Specifications and design of the model

To isolate and study the important physical effects governing the impact process, a fixed horizontal platform deck in two-dimensional flow conditions was considered. Two-dimensional flow requires that the model has to cover the entire breadth of the flume. Further, no obstructions underneath the bottom plate of the model should be present.

A number of additional requirements for the model design and the experimental set-up, were specified. These specifications are listed below.

- Realistic relationships between the length of the model and the wavelengths should be used in the experiments.
- The deck clearance must be easy to change without changing the water level in the flume.
- The force transducers must be easy to remove for calibration or for replacement.
- The force transducers must absorb all the vertical forces acting on the bottom plate of the model.
- The model must be rigid enough to withstand the impact. Hydroelastic effects should be of no significance.
- The model must be water tight, and water must not be allowed to flow over the model.
- To reduce the hazard of damage to the side walls of the flume, the model must not be in contact with the glass panes, but to satisfy the two-dimensional flow conditions, water must not be allowed to escape up between the model and the flume side walls.
- The experimental set up must not be a hindrance for visual observation of the impact process.

In addition to these specifications, there was also a wish of being able to watch the impact from above. This requires a transparent model without any equipment inside.

The lowest eigenmode for transverse waves in the flume has a frequency equal to 1.14 Hz (7.16 rad/s). This is associated with a wavelength equal to two times the breadth of the flume. To avoid transverse waves from being excited, the highest wave frequency to be used was chosen to be 1.0Hz (6.283rad/s). On the other hand, the length of the flume sets restrictions on the maximum possible wavelength that can be used. If deep water waves are desired, the water depth limits the wavelength. Finite water depth was accepted, and wave periods equal to 1.0s, 1.11s, 1.25s and 1.43s were used in the experiments. The overall length of the model was 0.65m. Assuming a 1:150 scale, the full scale wave periods would be in the range of 12.24 to 17.5 seconds, while the full scale length of the platform would be 97.5m. These are realistic values. The width of the platform deck was limited by the width of the flume and was set to be 0.58m. This ensures a 10mm clearance on each side to protect the flume walls. In addition, the sides of the model parallel to side walls of the flume were covered with foam rubber. To keep the water from flowing into the model from above, it was built with 0.30m high sides walls.

From the specifications given above, two different models were made. One was made of aluminium, while the other was made of plexi-glass. The plexi-glass model was built purely for visual observations. Both the side walls and the bottom plate of the former model are made of 6mm thick aluminium plates. This was believed to ensure that structural response would be of little importance. To keep water from flowing up between the models and the side walls of the flume, rubber seals were glued along the flume/ model intersections. This ensured two-dimensional flow conditions. Since the total vertical force must be picked up by the force transducers, the bottom plate of the aluminium model had to be free from the side walls. The bottom plate was only connected to the force transducers. The plate was cut with a clearance to all the side walls of the box. The dimensions of the bottom plate was chosen to be 630mm by 560mm, this gave a 4mm clearance along all the sides. To keep water from penetrating through this clearance and into the model, a rubber membrane that covered the entire bottom plate, was glued onto the model. The rubber menbrane has very small bending stiffness, and thus the shear force transferred to the side walls is negligible. Also, since the bottom plate and the force transducers are stiff, the deformation of the rubber membrane is small, *i.e.* the vertical force transferred to the side wall through the membrane force may be disregarded compared to the total force acting on the bottom plate. This rubber membrane also served another purpose when measuring the wetted area. This will be described in Section 4.2.3.

In addition to the box itself, a rig to mount the model and the measuring equipment to the wave flume had to be made. To keep the bottom plate stable in the case of a skewed force distribution in the y-direction, three force transducers were distributed in a triangular configuration, as shown in Figure 4.2. The position of the force transducers are indicated by the shaded squares, and the wetted area measurement device is also shown. The instrumentation used is described below in Section 4.2.3. Figures 4.3(a) and 4.3(b) show sketches of the model seen from the side and the front, respectively. The lower ends of the force transducers were screwed onto the bottom plate and the upper ends were mounted on three beams parallel to the wave flume. These longitudinal beams were then mounted on two cross beams which were connected to the steel frame of the flume. The box itself was also connected to the cross beams. With the given configuration all the vertical forces acting on the bottom plate were transferred all the to the transducers. Clamps were used to fasten the model to the steel frame of the flume. The initial deck clearance could be easily changed by placing thin aluminium bricks with a given thickness under each of the four cross beam ends.

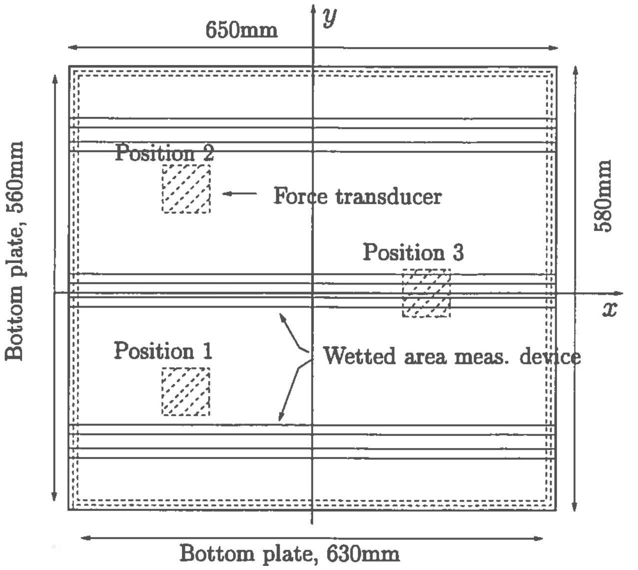

Figure 4.2: *Fish-eye view of the model. The position of the force transducers are shown. The total dimensions of the model are 580mm by 650mm, while the bottom plate on which the vertical force is measured, is 560mm by 630mm. The waves propagates in positive x-direction.*

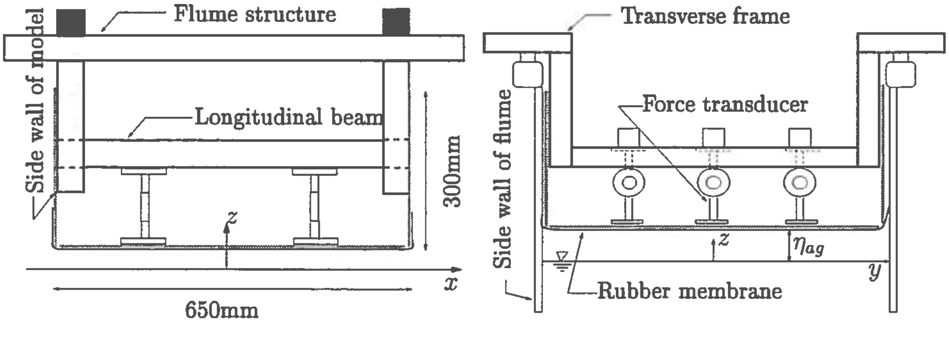

(a) x-z-view

(b) y-z-view

Figure 4.3: *Side view and front view of the model. The z-axis is positive upwards and positive x-axis is in the direction of the waves. The origin of the coordinate system is at the still water level.*

The model described above, satisfied all specifications, except for the wish of watching the impact process from above. This was satisfied by the plexi-glass model.

4.2.3 Instrumentation and calibration

Figure 4.2 shows the location of the most important measurement devices. The sampling frequency used in the experiments was 100 Hz, which was believed to be sufficient for force measurements.

The force transducers used in the experiments are in house made by Marintek (Norwegian Marine Technology Research Institute). They measure forces along three axes using strain gauges. In the present experiments, only the force along the z-axis was considered. The transducers are designed to measure force in the range ±1000N. To measure the wetted area of the bottom plate at any time instant, a wetted area measurement device was introduced. This device is based on the same principle as a capacitance type wave gauge. The idea is to use two parallel copper tapes along the bottom of the model. The distance between the two tapes was chosen to be approximately 20mm. The rubber membrane acted as an insulator. The output voltage from this device was directly proportional to the wetted tape length. Three pairs of copper tapes were used for the aluminium model, giving three independent measurements. Knowing the wetted length of the copper taper, good estimates for the wetted area can be obtained by simply multiplying by the width of the bottom plate. Surface piercing wave gauges, consisting of two vertical electrodes, 3mm in diameter and 12.5mm apart, were used to measure wave elevation. The instrumentation also included amplifiers, data logging and storage units for the data acquisition. In addition a camera and a digital video recorder were used to record the experiments.

The force transducers were carefully calibrated before they were mounted on the experimental set-up. They were also regularly calibrated during the experimental program. A detailed description of the initial calibrations are given in Appendix D. The wave gauges and wetted area measurement devices were cleaned and calibrated regularly. The latter were calibrated by fixing the model with an inclination and by stepwise increasing the water level in the flume. The wetting of the copper tapes could then be easily measured and calibration coefficients set.

4.3 Experimental work

4.3.1 Test conditions

Originally, the idea was to perform experiments for both regular and irregular waves. But the ambition of doing wave impact experiments with irregular waves was later dropped. There are several reasons for this decision. Most importantly, as the experiments for regular waves were ongoing, challenges that were not anticipated, arose. It was decided that it was important to address these new challenges properly for regular waves before extending the problem to irregular sea. Further, the suitability of the flume for irregular sea experiments that require long realization times, is questionable. Even though the beach functions well and that the flap of the wave generator is designed to damp out reflected waves, very long time series for free regular waves are difficult. After a time, cross waves may develop, and standing waves with wavelengths equal to twice the breadth of the flume occur. It has not been checked what will happen for free irregular waves, but since a irregular sea in principle contains all frequencies, it is likely that transverse standing waves will be excited and thus making valuable experimental data difficult to obtain.

By concentrating on the simple case with regular incident waves it is easier to study the impact process in details and to get a better understanding of the physics involved. It was believed that if the theory could be validated for regular waves, the theory also would be applicable for more general sea states. Thus, only regular incident waves were used in the experiments. For each wave period, several wave heights, H, were used, ranging from $H = 0.10$m to $H = 0.14$m. The steepest wave used in the experiments has wave period $T = 1.11$s and $H = 0.14$m, which corresponds to a wave steepness $H/\lambda = 0.073$ if deep water is assumed. The wave profile of this wave and the second order approximation are shown in Figure 3.1. Similarly, the least steep wave used has $T = 1.43$s and $H = 0.14$m, which corresponds to a wave steepness $H/\lambda = 0.031$. Also this wave is shown in Figure 3.1. When second order wave theory is applied, $\zeta_a = H/2$ is used in Equations (3.5) and (3.5) . The wave heights in the experiments are limited by a criterion of generating regular waves. If the wave steepness becomes to large, time series with regular waves are difficult to obtain since breaking may start to occur at the wave crest.

Three different deck clearances, η_{ag0}, were used. Those were $\eta_{ag0} = 0.04$m, $\eta_{ag0} = 0.06$m and $\eta_{ag0} = 0.08$m. The deck clearance is defined as the clearance between the model and the mean free surface. The deck clearances were changed by inserting thin aliminium bricks between the transverse beams and the flume frame, when fixing the model to the flume structure. The given values for η_{ag0} assume constant water level in the tank. Due to a small leak in the outlet valve in the flume, water had to added regularly, and the water level might differ slightly between test cases. For a given test case, however, the deck clearance can be considered constant. Since impact will not occur for many combinations, experiments for all combinations of the three parameters described above were not performed.

The model was fixed in the middle of the wave flume, equally far away from the wavemaker and the beach. The location was chosen so that it was sufficiently far away from the wavemaker to allow the waves to fully develop and also reasonable far away from the beach. This means that when steady state condition is obtained, there are negligible effects of the local flows at the wavemaker and at the beach. This location also provides good conditions for visual inspection of the water impact process.

4.3.2 Single impact event vs multiple impact events

As the experiments were ongoing, a significant difference in the impact process due to the first wave hitting the structure and the impact process due to the following waves was noted. The main reason for this deviation is that the preceding wave impact gives a significant disturbance to the free surface, which does not die out before the next wave reaches the deck structure. The second wave that hits the deck is therefore not equal to the regular incident wave. In addition to the slam that occurs when a wave hits the front end of the deck, the disturbance in the wave elevation causes a second slam when it hits the structure. This second slam was both clearly visible and audible, as well as clearly seen in the measurements. For the second slam, the water hits the deck in a manner which is analogous to a wedge of water impacting on a flat body. This leads to a rapid increase in the wetted area and a large impact force. Since this type of impact process occurs when more than one successive waves hit the deck structure, and because it leads to two slam events on the deck, this type of process is denoted as a *Multiple impact*

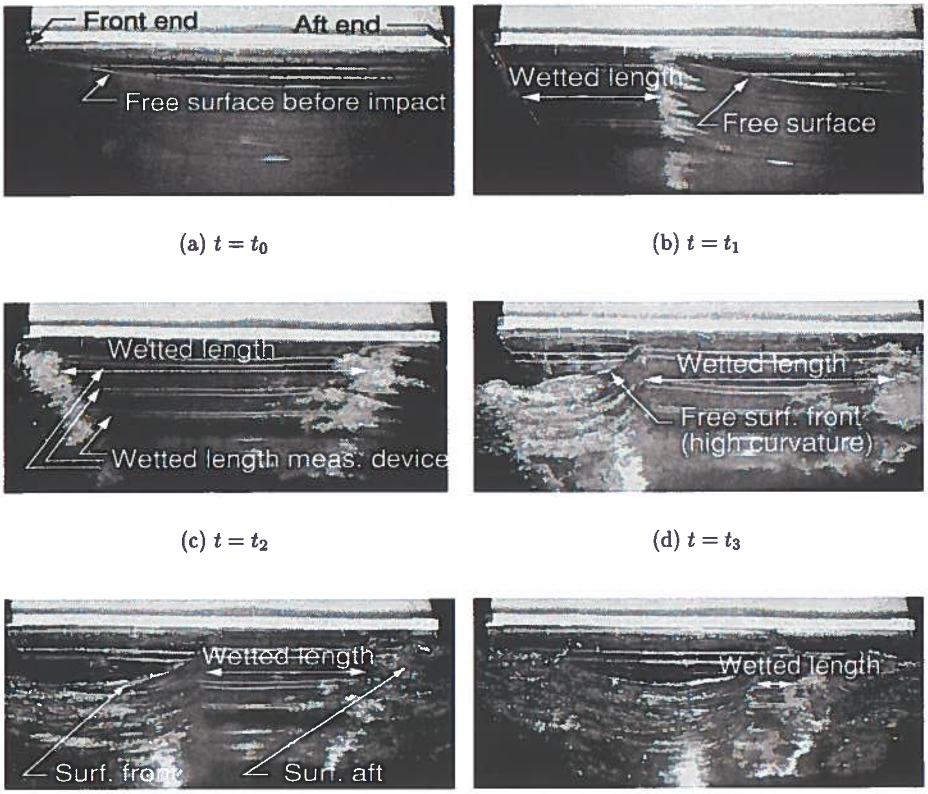

(a) $t = t_0$

(b) $t = t_1$

(c) $t = t_2$

(d) $t = t_3$

(e) $t = t_4$

(f) $t = t_5$

Figure 4.4: *Single impact event. Fish-eye view.* $T = 1.00s$, $H = 0.10m$ *and* $\eta_{ag0} = 0.04m$.

event. Similar, the impact due to the first wave reaching the deck or when only one wave hits the deck, is denoted as a *Single impact event.*

Figure 4.4 shows pictures at six time instants of the impact process associated with the first wave hitting the structure. The perspective in these pictures is approximately 45 degrees from the side and upwards, so that they show three dimensions. A part of the side plate of the model can be seen as light grey areas at the top of the pictures. The bottom plate is nearly black, but can be recognized by the three pairs of copper tape for the wetted area measurements. Also the wave profile can be observed. Since it might be difficult to see the physics of the impact process clearly when looking at it from this perspective, complementary sketches of the process seen from the side are shown in Figure 4.5. The sketches are purely two-dimensional and the indicated time instants correspond to the ones in Figure 4.4.

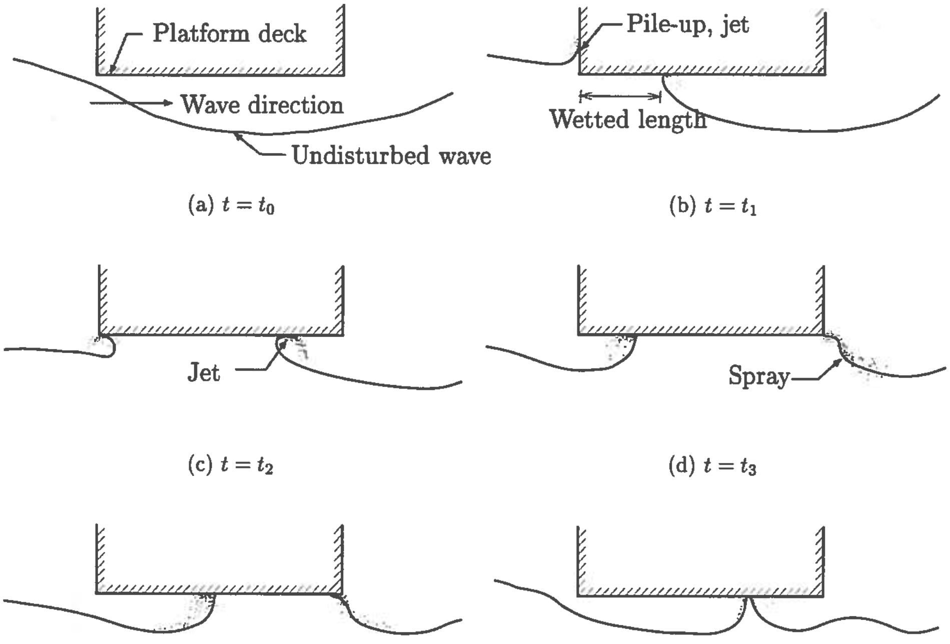

(a) $t = t_0$ (b) $t = t_1$

(c) $t = t_2$ (d) $t = t_3$

(e) $t = t_4$ (f) $t = t_5$

Figure 4.5: *Single impact event. The time instants t_j correspond to the time instants in Figure 4.4.*

The wave period is $T = 1.00$s, the wave height is $H = 0.10$m and $\eta_{ag0} = 0.04$m for this particular case. In the discussion below, it will mainly be referred to the sketches in Figure 4.5, but recall that these correspond to the corresponding pictures in Figure 4.4. The first sketch 4.5(a) shows the platform deck and the wave before impact occurs. The wave profile is smooth and undisturbed. The wave propagates from left to right. As the wave hits the deck at the front end, the wetted area increases smoothly and a pile-up of water and a jet is formed at the upstream end of the deck. Compared to the undisturbed wave, there will also be a significant pile-up of water downstream of the wetted body. The profile of free surface at a small distance downstream of the wetted part of the body is smooth with a relatively small curvature. But due to the impact it is given a perturbation compared to the undisturbed incident wave profile. At the body-free surface intersection a jet is formed, and foam on the free surface is observed close to the intersection.

In Figure 4.5(c) the upstream body/ free surface intersection has just moved around the corner at the front end of the deck to the bottom plate. The free surface near the intersection is characterized by high curvature. As the downstream intersection reaches the aft end of the deck, the fluid flow leaves the deck tangentially, which implies that fluid particles on the free surface at the immediate neighborhood of the body has no vertical velocity. This is showed in Figure 4.5(d). Spray is observed on the free surface behind the body. This originates mainly from spray caused by the jet at the downstream intersection before the fluid reach the aft end. Breaking is also observed behind the body. These effects will dissipate energy from the system, and the wave amplitude behind the body is reduced compared to the amplitude of the incident wave. The reduction is also caused by wave reflection from the front end and the bottom plate. The magnitude of this reduction will depend on both the wave condition and the deck clearance. If the difference between the maximum elevation of the incident wave and the initial deck clearance is small, the deck will experience a "gentle" impact. The reflected part of the wave will be small and also energy drain through the jet and wave breaking will be relatively small compared to more powerful impact events. The transmitted wave will therefore not be reduced much compared to the incident wave. On the other hand, if the maximum elevation of the incident wave is large relative to η_{ag0}, the reflected wave will be more significant. Also the more massive impact yields a greater energy dissipation through the jet and through wave breaking. The relative reduction in the transmitted compared to the incident amplitude will be greater in this case than for the more "gentle" impact. The dissipation of energy is not considered in this work.

After some time, depending on the wave condition and η_{ag0}, the downstream intersection starts to move forward again, and finally the water exits the deck in a manner as shown in Figure 4.5(f).

While the water entry phase behaves as expected according to the Wagner based method, the water exit phase, *i.e.* when the wetted surface decreases, behaves differently from what was anticipated. First, in the Wagner based method as it is described in Chapter 3, the upstream intersection point is found by the intersection between the body and the incident wave, which means that the upstream intersection propagates along the body with a velocity equal to the phase velocity of the incident wave. This is done in lack of a better way to determine this intersection point, and it is analogous to the approach by von Kármán (1929). Naturally, this is not the case since the front end gives a significant perturbation to the free surface. In reality, the water exit phase is complicated and its duration is greater than the duration obtained by considering the deck intersection with the incident waves. As the upstream intersection point has moved around the corner from the front end to the bottom plate, the water seem to "stick" to the bottom plate and the intersection propagates significantly slower than the undisturbed wave. This results in a free surface profile with high curvature close to the body. This can not be modeled with the present method. Especially, as the fluid flow goes around the front corner the free surface has high curvature locally. This will be discussed more in Section 6.2.2.

It was expected that the upstream free surface and intersection would behave differently from the von Karman approach, but the behavior of the downstream intersection was more surprising. In the Wagner based method, it is assumed that the aft end would be the last part of the bottom plate to become dry as the water exits the body, but this was in general not the case in the experiments. As the aft end gets wet, the water leaves the body tangentially, and the downstream body/ free surface intersection is located at the bottom/aft end corner of the body.

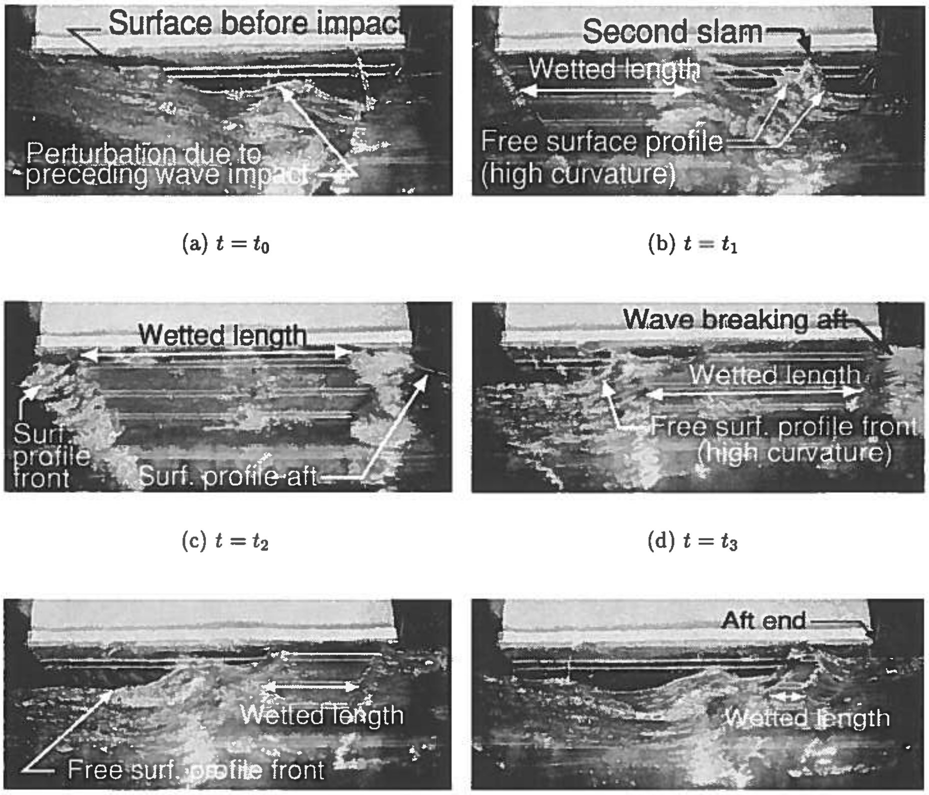

(a) $t = t_0$

(b) $t = t_1$

(c) $t = t_2$

(d) $t = t_3$

(e) $t = t_4$

(f) $t = t_5$

Figure 4.6: *Multiple impact event. Fish-eye view.* $T = 1.00s$, $H = 0.10m$ *and* $\eta_{ag0} = 0.04m$.

In the impact conditions tested, water did not wet the aft end plate of the model. After a while the downstream intersection starts to propagate upstream towards the fore body/ free surface intersection. The location of the final water exit is dependent on the impact condition, but in general it is located somewhere between the middle and the aft end of the deck.

The curvature of the free surface profile on both sides of the intersections are high as the water leaves the deck, and a significant perturbation of the free surface remains when the deck has become completely dry. This residual disturbance from the preceding impact event, greatly affects the water impact process due to the next wave. While Figure 4.4 shows pictures of the first wave hitting the structure, Figure 4.6 shows a series of pictures of the impact due to the next wave in the wave train . The pictures in Figure 4.6 are taken exactly one wave period later than the corresponding pictures in Figure 4.4, and the perspective is the same. Figure 4.7 shows corresponding sketches to illustrate the impact from a purely two-dimensional view.

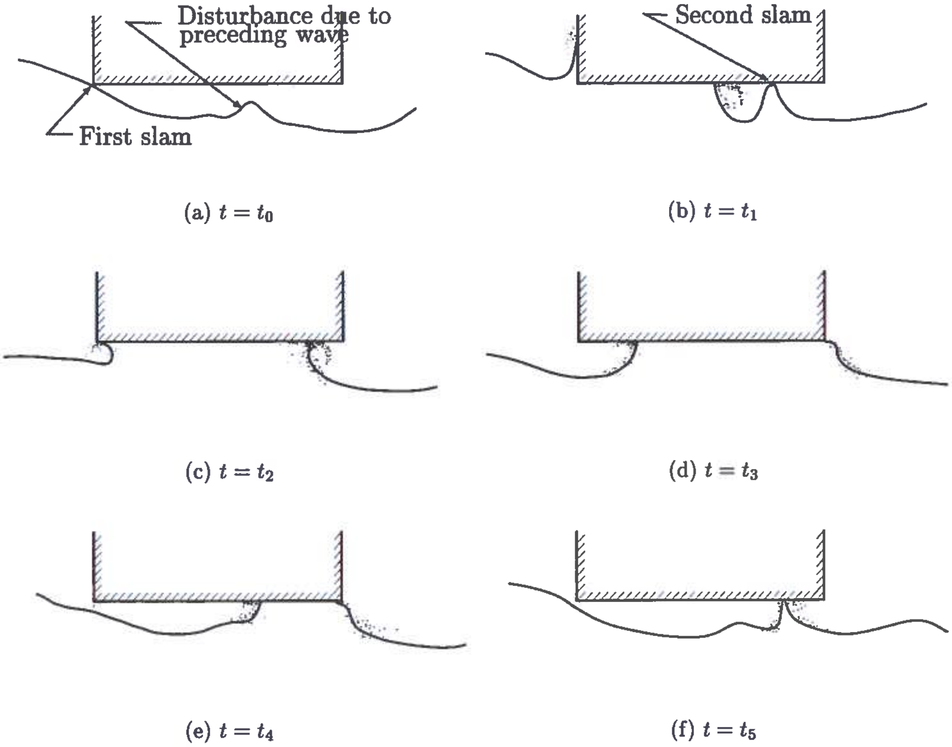

(a) $t = t_0$ (b) $t = t_1$

(c) $t = t_2$ (d) $t = t_3$

(e) $t = t_4$ (f) $t = t_5$

Figure 4.7: *Multiple impact event. The time instants t_j correspond to the time instants in Figure 4.6.*

Figure 4.7(a) is taken a small time instant before water impact occurs, and it can be noted that the wave profile is different from the undisturbed wave. The preceding wave impact has left a significant local maximum in the wave elevation beneath the location of final water exit of the preceding wave. The first phase of the impact for the second wave behaves similarly to the first impact event. The wetted length increases smoothly and a jet is formed at the front end. However, as seen in Figure 4.7(b), the local maximum steepens, and eventually it reaches the structure. This causes a severe second slam on the aft part of the deck, and a corresponding rapid increase in the wetted area.

Approximately from the time of maximum wetting and thereafter, the two different impact processes behave similarly. This means that the water exit phase is not much affected by the initial disturbance of the free surface. The impact events due to the following waves will behave as the one depicted in Figure 4.6.

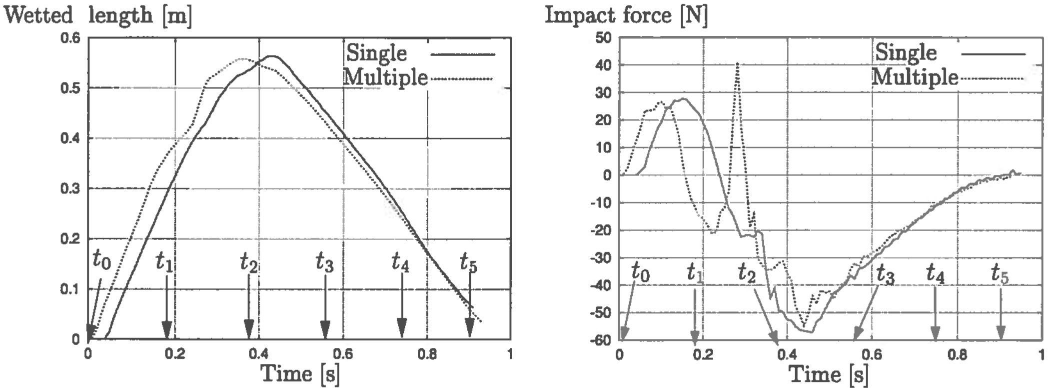

(a) Wetted length

(b) Vertical impact force

Figure 4.8: *Difference between single and multiple impact event. Experimental results.* $T = 1.00s$, $\zeta_{Ia} = 0.05m$, *and* $\eta_{ag} = 0.04m$. *The time instants indicated of the plots correspond to the time instants of the snapshots in Figures 4.4 and 4.6.*

Figure 4.8 presents the corresponding measurements made. The left figure shows the time histories for the wetted length for the two different impact events, while the right figure depicts the corresponding vertical force acting on the bottom plate. The time axes has been adjusted so that the two events can be directly compared. The wetted length measurements for the multiple impact event give the total wetted length from both impacts. The time instants marked with arrows in the plots, correspond to the time instants of the snapshots in Figures 4.4 and 4.6. Due to the uprise of the free surface elevation caused by the preceding impact, the first contact between water and body occurs a small time increment sooner for the second wave hitting the deck than it would given the incident wave. Still, during the first part of the water entry phase, the two events behave similarly. The curves for the wetting are nearly parallel and also the force histories are relative alike except for a small displacement in time. But from approximately $t = t_1$, the two events behave differently. For the first wave, the wetted length continues to increase at close to the same rate as before until water exit starts to occur at the front end of the deck. For the second wave, the local trough upstream of the local crest slows down the wetting process for a short time before the local maximum hits the structure. This leads to a rapid increase of the wetted length, and thereby a rapid increase in the added mass of the deck. The result is a positive peak in the impact force in Figure 4.8, which is larger than the maximum force for the first impact event. This force peak has a short duration and it acts locally in the region where the second slam occurs. High slamming pressures which are critical for local structural damages is the result. Hydroelasticity may be important for this type of impact. According to Haugen (1999) the local dead-rise angle between the deck and the free surface at impact will be crucial for the importance of hydroelasticity. The magnitude and the duration of the local slamming force are dependent on the test condition. For longer waves the second slam may dominate more than in the present example, and the global force peak due to water entry may be more or less

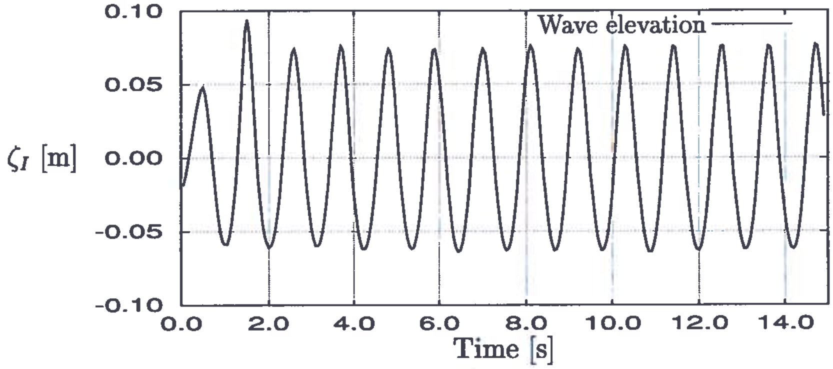

Figure 4.9: *Measurements of the wave elevation during the start up of the wavemaker.* $T = 1.11s$ *and* $H = 0.14m$*.*

absorbed by the second force peak.

Once maximum wetting has occurred, the water exit phase is similar for the two different impact events.

The significant difference in the wave impact process for the first wave hitting the deck and the for following waves yields a practical consequence for the performance of the experiments. The physical meaning of a single impact event is that a extreme wave reaches the deck, while the other waves pass under the deck. In the numerical program, it is assumed that this wave can be described by a regular wave. In the wave flume the wave field contains transient effects due to the start up of the wavemaker. These transient effects will die out after a few oscillation and steady state will be reached. Figure 4.9 shows a typical measured wave elevation in the middle of the tank with the model absent. The wave period is T = 1.11s and the wave height is H = 0.14m. The measurements are triggered 4 seconds after the wavemaker is started, and a transient phase can clearly be seen at the beginning of the time series. The wave amplitude is gradually increasing, and a large maximum occurs before steady state is reached at a lower amplitude level. Theory for flap wavemakers is given by *e.g.* Dean and Dalrymple (1994)

It is clear from Figure 4.9, that if the model had been present in this case, the first wave hitting the structure would not have been a regular wave, but a wave that contains transients. To avoid transient effects in the impact measurements, the structure must be kept out of reach of waves until steady state in the flume is reached. Since the strong influence on the impact process from the preceding wave impact was not anticipated beforehand, the original experimental rig was not designed with this in mind. Improvisations had to be made. The easiest and least expensive way to get around this problem, was to manually keep the model out of reach of the waves until steady state was reached, and then lower the model down in between two wave crests without allowing water to reach the box during this translation. Even if the model was not clamped to the flume structure, manual labor and large weight of the test rig itself relative to the impact force ensured that the deck could be considered fixed also in this case. A limiting parameter when using this procedure is the wavelength. The lowest period used where this scheme was successful was $T = 1.11$s. For shorter waves, it was very difficult to lower the model into position between two wave crests without disturbing the wave field. For testing in shorter waves, a shorter model would have been necessary.

4.4 Error sources in the experiments

Errors in the experiments may arise from a number of sources, and some are more severe than others. In this section some of the sources that may impose errors in the measurements will be discussed. First, the ability of the beach to damp out the waves may be questioned. In reality, a part of the amplitude of the incident wave will be reflected, and this will influence the wave elevation as well as the fluid particle kinematics. No comprehensive study has been conducted to determine the magnitude of the reflected wave from the beach, but since the model is situated in the middle of the flume, problems connected to reflection will not arise until the first wave in the wave train has traveled 1.5 times the length of the flume, namely 20.25m. The velocity of the wave train is characterized by the group velocity, c_g, which is the velocity in which the wave energy is transmitted by. The group velocity is expressed as

$$c_g = \frac{1}{2}\frac{\omega}{k}\left(1 + \frac{2kh}{\sinh kh}\right) \tag{4.1}$$

In deep water the group velocity simply becomes $c_g = \frac{1}{2}\frac{\omega}{k}$. Since the longest waves used in the experiments propagate fastest they are most critical. For waves with $T = 1.43$s the phase velocity is $c_g = 1.22$m/s. Thus, it takes 16.6s before the reflected amplitude reaches the position of the model. By doing the measurement of the single impact case within the first 15 seconds after the wavemaker is initiated, a reflected wave with a wavelength that corresponds to the fundamental frequency, should not affect the results. The measurements are conducted in the time window 10-15 seconds after the wavemaker is started. It is therefore believed that effects of reflection are precluded. Transient effects due to the start-up of the wavemaker may introduce waves of long wavelengths in the tank. A very long wave will propagate at a velocity equal to $\sqrt{gh} = 3.17$m/s and it will not be properly damped by the beach. However, based on the measurements of the wave elevation, the amplitudes of such long waves, if present, are small. When the fluid inside a tank is set in motion by some disturbance, such as by start-up of a wavemaker, it will oscillate at the natural periods of the fluid motion. This longitudinal sloshing in the tank is called seiching. To determine the seiching periods, T_n, the dispersion relation of finite water depth is used, *i.e.*

$$T_n = \frac{2l}{n\sqrt{\frac{g \tanh k_n h}{k_n}}} \tag{4.2}$$

where $k_n = \frac{n\pi}{l}$ and l is the length of the tank. In the middle of the tank the first sloshing mode will not influence the wave elevation, but the amplitude of the second mode has its maximum amplitude in the middle of the tank. The corresponding sloshing period is $T_2 = 4.28$s. From measurements of the free wave performed in the middle of the tank, it is difficult to detect a slowly varying wave elevation at this period. This indicates that the sloshing amplitude is small.

The control system of the wavemaker is designed to damp out such oscillations.

A second error source is transverse waves in tank. But as discussed in Section 4.2.2, the wave periods in the experiments were chosen so that transverse waves should not be excited. Also here, transient effects due to the start-up of the wavemaker may excite wavelengths that are critical for generation of transverse waves. However, from visual inspection of free waves, no cross waves were observed for the waves used in the experiments.

The wave gauges were carefully calibrated. But finite thickness of the wave gauge will influence the fluid flow locally, and thus give inaccurate measurements. The relative error will depend on the diameter of the probe wires and the wave amplitude. The surface tension causes the free surface to stick to any rigid surface that it intersects with. This effect causes, according to Lader (2001), an uncertainty in the measurements of approximately 1mm for the given wave gauge. Dirt on the electrodes may influence the surface tension effect, and the electrodes were therefore regularly cleaned. More important than the accuracy of the wave gauges measure is the wavemaker ability to give the correct wave according to the given input. The transfer function for generation of the waves is made by the producer of the wavemaker and especially fitted for the given flume and the water depth used in the experiments.

The wetted area measurements can be questioned. A possible error source is water sticking to the rubber between the copper tapes after the wave has detached. This would lead to measurements where dry areas are measured as wet. To prevent or minimize such errors, the rubber membrane was regularly treated with a chemical that destroys the surface tension of the water. Qualitative tests showed that water did not “stick” to the rubber membrane as the main bulk of water had left the membrane. Air cushion effects may also affect the measurements of the wetted length. From the visual observations no significant air cushions were observed for the single impact events. For the multiple impact events, however, air cushions were clearly observed. A quantitative test of the wetted length measurements was conducted during the experiments. Pictures such as those shown in Figure 4.4, were taken at given time instants during the water entry/ water exit process. The wetted lengths at these time instants were measured by studying the photographs and compared with the measured wetted length. Good agreement was found and this ensured confidence in the measurements.

The thickness of the bottom plate was chosen so that hydroelastic effects should be absent in the experimental results. The eigenperiod of the force transducers were checked and found to be much lower than the expected duration of the loading, but neither the wet or dry eigenperiods of the bottom plate mounted onto the force transducers were measured. It was believed that they were low. However, irregularities were noticed in the force histories that might originate from structural oscillations. These are especially noticeable for the most violent impact events. The magnitudes of these irregularities are much smaller than the dominating positive and negative force peaks. If these oscillations in the force histories are caused by hydroelasticity, a remedy would have been to weld longitudinal stiffeners on the upper side of the bottom plate. This was not recommended since welding could have caused buckling of the bottom plate, which is undesirable. Another un-attempted possibility could have been to glue the stiffeners onto the bottom plate. Due to negligible bending stiffness and small deformations, the rubber membrane will not introduces any significant error in the force measurements.

4.5 Results and comparisons to the Wagner based method

Only experimental results for single impact events can be directly compared to numerical results obtained by the Wagner based method. In this section, experimental results for single impact events will be presented and compared to the theory. By requiring that the model is to be placed into a fully developed wave field, a restriction for the wavelength arises. For each combination of wave condition and initial deck clearance, several experiments should be performed to ensure that reliable results are obtained. It was decided to study eleven different combinations of wave periods, wave amplitudes and deck clearances. These are listed in Table 4.1, which contains experimental results for the maximum vertical force, F_{max}, and the negative force peak, F_{min}, as well as the duration of the whole water entry/ water exit process, t_{imp}. The experimental results presented are average values for all the successful experiments for each case. An experiment is classified as successful based on two criteria. First, the model must be lowered into position without disturbing the wave field before impact occurs at the front end. This can be checked by studying at the recorded data for the wetted length. Second, no significant force peaks must be induced by the initial contact between the transverse beams of the model and the steel frame of the flume. Such peaks may easily be detected in the recorded force history. The model had to be set down carefully, and foam rubber on the top of the flume was used to damp the impact. This proved to work well, and the repeatability of the experiments was good.

Table 4.1 also gives corresponding numerical results for F_{max}, F_{min}, and t_{imp} computed by the Wagner based method. In Table 4.3 the wetted lengths at time instants corresponding to F_{max} and F_{min} are listed for both experiments and theory. These are denoted as $2c_{\text{max}}$ and $2c_{\text{min}}$, respectively. Also values for the maximum wetting, Max($2c$), are presented. The experimental wetted length histories used are mean values of the three individual recordings.

Table 4.3 presents values for standard deviations for some measured quantities. The standard deviations for F_{max} are relative small compared to the force itself, usually less than $0.05F_{\text{max}}$. Exceptions are for the most "gentle" impacts where F_{max} itself is small. For instance, for case no. 3, where $T = 1.11$s, $\zeta_a = 0.06$m and $\eta_{ag0} = 0.06$m, $\sigma_{F_{max}} = 0.158F_{\text{max}}$. Also for F_{min} and the wetted lengths, standard deviations are relatively small.

In the following, comparisons between experiments and theoretical results are discussed. Figures 4.10−4.13 show examples of comparisons for time histories for the wetted length and the total vertical force acting on the bottom plate. For each case, two experimental realizations are shown to illustrate the repeatability of the experiments. In the discussion it is convenient to separate the cases that leads to "gentle" impacts and those which lead to more powerful slamming forces. Figure 4.13 is an example of the first, while Figures 4.10- 4.12 are examples on the latter. The cases listed in Table 4.1 were $\zeta_a = \eta_{ag0}$ are here considered to be "gentle", *i.e.* case nos. 3, 7 and 11, while cases were $\zeta_a > \eta_{ag0}$ yields more powerful impacts.

Table 4.1: *Comparisons between the experimental results and numerical results from the Wagner based method for the maximum force, F_{max} and the minimum force F_{min} during the water entry/ water exit process. The total duration of the impact process t_{imp} is also compared. The experimental values are mean values for all experiments for each case.*

Case	Impact condition			Experimental results			Wagner based method		
no.	T [s]	ζ_a [m]	η_{ag0} [m]	$F_{\max}$ [N]	$F_{\min}$ [N]	t_{imp} [s]	$F_{\max}$ [N]	$F_{\min}$ [N]	t_{imp} [s]
1	1.11	0.05	0.04	29.3	-67.8	0.76	26.5	-82.0	0.60
2	1.11	0.06	0.04	49.1	-83.5	0.82	49.2	-133.0	0.66
3	1.11	0.06	0.06	7.1	-36.5	0.53	12.9	-41.1	0.49
4	1.11	0.07	0.06	31.7	-70.2	0.78	35.0	-100.3	0.58
5	1.25	0.05	0.04	37.0	-67.8	0.78	30.5	-90.7	0.61
6	1.25	0.06	0.04	65.2	-70.2	0.87	59.2	-84.5	0.66
7	1.25	0.06	0.06	11.2	-61.7	0.83	12.1	-36.6	0.47
8	1.25	0.07	0.06	41.0	-88.7	0.77	37.9	-110.9	0.56
9	1.43	0.05	0.038	53.0	-51.9	0.92	47.5	-52.7	0.64
10	1.43	0.06	0.038	97.5	-54.2	0.95	85.2	-45.2	0.69
11	1.43	0.06	0.06	14.5	-58.9	0.79	12.3	-45.0	0.45

Table 4.2: *Comparisons between the experimental results and numerical results from the Wagner based method for the wetted length. $2c_{max}$ is the wetted length when F_{max} occurs, and $2c_{min}$ is the wetted length when F_{min} occurs. Max(2c) is the largest wetting during the impact process. The experimental values are mean values for all experiments for each case.*

Case	Impact condition			Experimental results			Wagner based method		
no.	T [s]	ζ_a [m]	η_{ag0} [m]	$2c_{\max}$ [m]	$2c_{\min}$ [m]	Max($2c$) [m]	$2c_{\max}$ [m]	$2c_{\min}$ [m]	Max($2c$) [m]
1	1.11	0.05	0.04	0.244	0.549	0.564	0.214	0.525	0.525
2	1.11	0.06	0.04	0.275	0.585	0.619	0.271	0.630	0.630
3	1.11	0.06	0.06	0.106	0.342	0.350	0.125	0.331	0.331
4	1.11	0.07	0.06	0.156	0.546	0.558	0.189	0.487	0.487
5	1.25	0.05	0.04	0.338	0.597	0.619	0.254	0.630	0.630
6	1.25	0.06	0.04	0.390	0.630	0.630	0.338	0.630	0.630
7	1.25	0.06	0.06	0.164	0.560	0.574	0.135	0.370	0.370
8	1.25	0.07	0.06	0.302	0.625	0.630	0.229	0.582	0.582
9	1.43	0.05	0.038	0.423	0.630	0.630	0.378	0.630	0.630
10	1.43	0.06	0.038	0.492	0.630	0.630	0.482	0.630	0.630
11	1.43	0.06	0.06	0.272	0.571	0.561	0.170	0.447	0.447

For the water entry phase, *i.e.* when the wetted area increases, it can be noted that results by the Wagner based method correspond quite well with the measured results for the powerful impacts. Both magnitude and duration of the positive force peak, are described in a satisfac-

Table 4.3: *Standard deviations for quantities measured in experiments.*

	Impact condition			Standard deviations , σ				
Case no.	T [s]	ζ_a [m]	η_{ag0} [m]	$\sigma_{F_{\max}}$ [N]	$\sigma_{F_{\min}}$ [N]	$\sigma_{2c_{\max}}$ [m]	$\sigma_{2c_{\min}}$ [m]	$\sigma_{\mathrm{Max}(2c)}$ [m]
1	1.11	0.05	0.04	1.71	1.68	0.008	0.021	0.018
2	1.11	0.06	0.04	2.58	3.67	0.013	0.009	0.006
3	1.11	0.06	0.06	1.12	3.95	0.007	0.012	0.015
4	1.11	0.07	0.06	0.87	2.70	0.020	0.017	0.019
5	1.25	0.05	0.04	2.26	4.63	0.024	0.019	0.008
6	1.25	0.06	0.04	2.18	3.26	0.003	0.000	0.000
7	1.25	0.06	0.06	1.33	2.87	0.018	0.018	0.009
8	1.25	0.07	0.06	1.36	2.40	0.023	0.004	0.000
9	1.43	0.05	0.038	3.10	2.38	0.014	0.000	0.000
10	1.43	0.06	0.038	2.39	2.75	0.015	0.000	0.000
11	1.43	0.06	0.06	0.25	1.35	0.013	0.010	0.015

tory manner by the theory. Also for the wetted length, the Wagner based method corresponds well with experiments. For the water exit phase the results are less satisfactory. Particularly for short waves, results are poor. The maximum magnitude of the negative force, $|F_{\min}|$ is overestimated. For instance in case no. 2, which is shown in Figure 4.10, the calculated value of $|F_{\min}|$ is approximately 59% larger than the measured value. At the same time, the theory underestimates the duration of the water exit, and thus the duration of the entire water impact process. The intersection between the body and the incident wave is used to determine the wetted length during water exit, but the discussion in Section 4.3.2 showed that the free surface profile is very different from the incident wave. For all cases tested, water exit happens slower than exit of the undisturbed wave, and this affects the force histories.

Figure 4.13 shows a "gentle" impact event, where the magnitude of the positive force peak is relatively small. Nevertheless, $|F_{\min}|$ is in the same range of as for the impact conditions discussed above, and also the measured duration of the impact process is similar. In this case, the deck clearance is identical to half the wave height. This means that excess in the wave elevation over the deck level is only due to the nonlinearities in the wave elevation. The impact occurs close to the summit of the wave, where the vertical fluid velocities are small. Even if the wetting process in the present case does not differ significantly from the cases discussed above, the resulting maximum force is small. Since, the theoretical maximum wetting in Figure 4.13(a) is less than the measured, the theoretical value for $|F_{\min}|$ becomes smaller than the measured value.

For case no. 11, the theory underestimates the maximum force slightly, and the duration of the positive force peak is also underestimated. For the two other cases where $\zeta_a = \eta_{ag0}$, theoretical results for $F_{\max}$ are larger than measured. No clear trend can be noted, but a couple of important error sources for the water entry force can be outlined. First, when the initial deck clearance is approximately equal to the half the wave height, higher order contributions

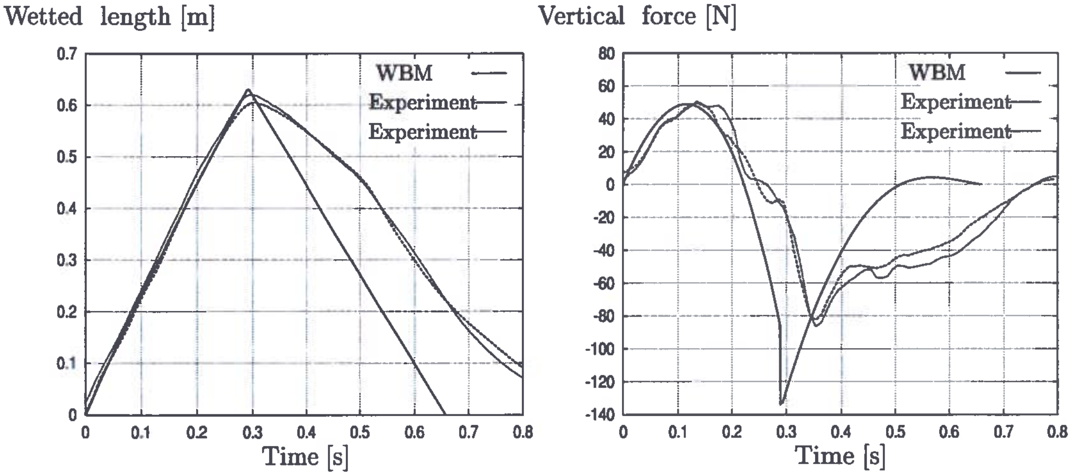

(a) Wetted length

(b) Vertical impact force

Figure 4.10: *Comparisons between experiments and the Wagner based method (WBM). Case no. 2:* $T = 1.11m$, $\zeta_a = 0.06m$ *and* $\eta_{ag0} = 0.04m$.

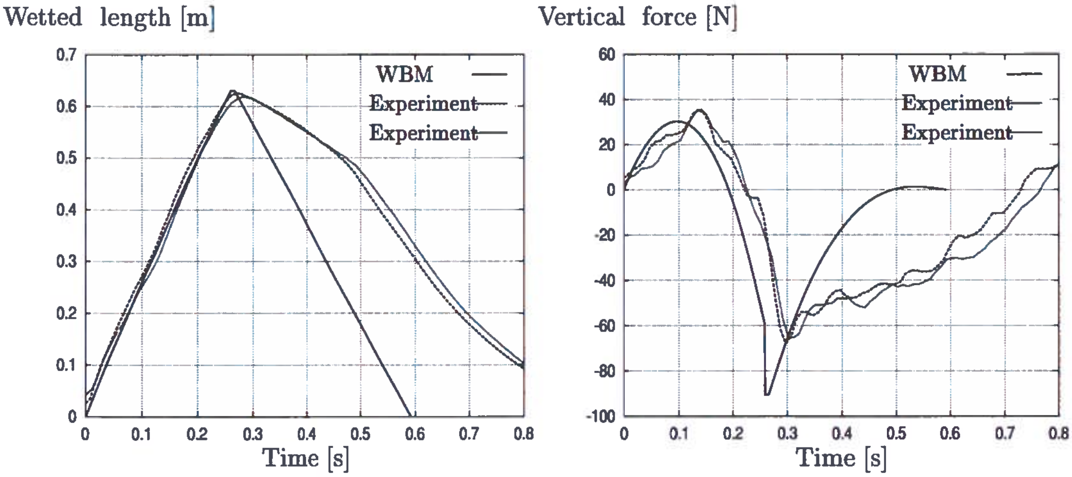

(a) Wetted length

(b) Vertical impact force

Figure 4.11: *Comparisons between experiments and the Wagner based method (WBM). Case no. 5:* $T = 1.25m$, $\zeta_a = 0.05m$ *and* $\eta_{ag0} = 0.04m$.

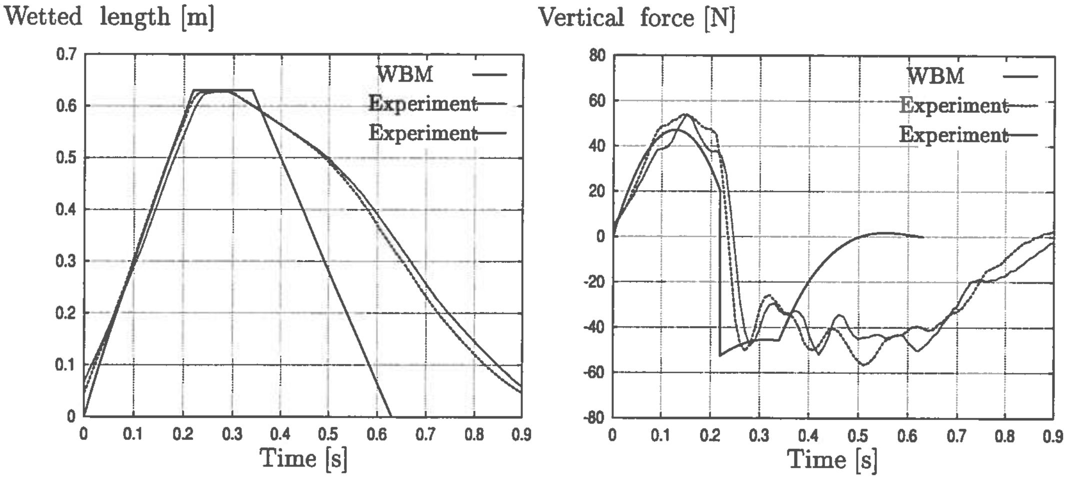

(a) Wetted length

(b) Vertical impact force

Figure 4.12: *Comparisons between experiments and the Wagner based method (WBM). Case no. 9:* $T = 1.43m$, $\zeta_a = 0.05m$ *and* $\eta_{ag0} = 0.038m$.

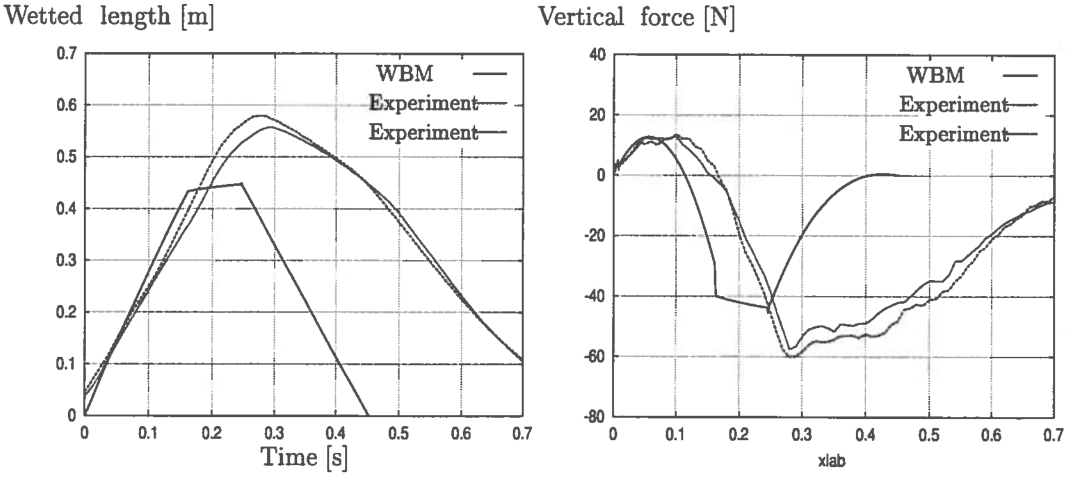

(a) Wetted length

(b) Vertical impact force

Figure 4.13: *Comparisons between experiments and the Wagner based method (WBM). Case no. 11:* $T = 1.43m$, $\zeta_a = 0.06m$ *and* $\eta_{ag0} = 0.06m$.

are crucial for the wave kinematics and thus for the wetted area. It can be questioned how well Stokes' second order theory describes the wave kinematics in the vicinity of the wave crest. Perhaps "infinite" order wave theory would improve the results. But probably more important is the accuracy of the deck clearance used in the experiments. In Section 3.7.3 is was shown that a relatively small change in η_{ag0} might lead to a relatively large shift in the resulting impact force. This is especially true when the deck clearance is close to the maximum wave elevation. If impact happens close to the wave summit, a small change in η_{ag0} and a corresponding shift in the position on the wave crest where impact occurs, will yield a significant change in the impact velocity and force. The accuracy of η_{ag0} in the experiments is also questionable. It is believed that inaccurate measurements for η_{ag0} partly can explain the relative large differences between theory and experiments. For more powerful impacts, inaccurate values for η_{ag0} may also partly explain discrepancies between theory and experiments for F_{max}. But for these cases the relative effect would be smaller. The reason why the theory underestimates $|F_{\text{min}}|$ for case 7 and case 11, is that the maximum wetted area is underestimated. This may also be related to the discussion above.

As a final remark, it can be said that the Wagner based method yields satisfactory results for both the magnitude and duration of the water entry force. But the theory describes water exit poorly. For two-dimensional flow, the largest absolute force may occur during water exit. Experiments show that the simplified free surface condition $\phi = 0$ and the von Karman type of approach can not be used if water exit is to be described properly. Deformation of the free surface upstream of the wetted body surface should then be taken into account.

4.6 Investigation of the importance of gravity

The comparisons between experiments and Wagner based method results, suggest that the role of gravity is probably not negligible in the later stage of impact process. If this is the case, the dynamic free surface condition, $\phi = 0$, is no longer valid. This could explain why, in particular during water exit, experimental and theoretical results deviate significantly. Definite conclusions about the detected differences between experiments and theory require further studies. The main objective of this section is to study the importance of gravity in the impact problem. Implicitly, also a quality check of the force measurements is provided by this study. This is done by studying a different problem. Experiments with the same equipment as described in Section 4.2 are performed to determine the damping coefficient in heave of rectangular cylinders oscillating in the free surface. The damping coefficient is not determined by performing forced oscillations, but by relating it to experimental results for the wave excitation force as described below. The experimental results are compared to experimental results found in the literature. The importance of gravity for the water exit force is qualitatively studied by using the steady state force on a thin plate located in the free surface to obtain an estimate for $|F_{\text{min}}|$. This estimate is compared to the experiments for water impact and to the results obtained by the WBM.

Haskind (1962) derived relationships between the exciting forces and the far field velocity potential in the case of forced oscillations in initially calm water. This means that the diffraction problem has not to be solved directly and the exciting forces are simply related to the hydrodynamic damping coefficients. Newman (1962) elaborated this further, and through Green's second identity he determined a simple formula for beam sea incident waves on an infinitely long horizontal cylinder which submerged part is symmetric about the vertical axis. The formula yields linear frequency domain results and it is valid for any frequency, but it assumes a body without forward speed and that no current is present. Newman (1962) writes the exciting force amplitude per unit length, $|F_i|$, as

$$|F_i| = \zeta_a \left(\frac{\rho g^2}{\omega} B_{ii}^{(2D)} \right)^{\frac{1}{2}} \quad , \quad i = 2, 3, 4 \tag{4.3}$$

where $B_{ii}^{(2D)}$ is the two-dimensional damping coefficient for the i-th DOF.

Later, when estimates for $|F_{\text{min}}|$ are found, the damping coefficients for thin plates are needed. These are difficult to determine both numerically and experimentally. MacCamy (1961) discussed the case of heaving motion of two-dimensional cylinders with negligible draft. MacCamy studied this problem by using an integral equation technique and obtained numerical results both for the added mass and for the damping coefficients as functions of the oscillation frequency. Vugts (1968) presented experimental and theoretical results for forced oscillations of cylinders. The theoretical results were based on linear theory. He reported good agreement between experiments and theory for heaving of box shaped sections. The comparisons were performed for 3 different B/D ratios (2, 4, and 8), where B is the breadth of the section and D its draft.

The theoretical results for the three B/D ratios presented by Vugts (1968) are used to estimate the damping coefficient for zero draft. This is done by extrapolation of Vugts' results to $D = 0$. In the experiments presented in Chapter 4, the dimensionless frequency, $\omega\sqrt{\frac{B}{2g}}$, is varied in the range $[0.66, 1.03]$. In this frequency range the damping coefficients computed by the two approaches differ significantly. This is shown in Figure 4.14. The results from MacCamy (1961), however, show reasonable agreement with the extrapolated curve. Though the results obtained by extrapolation and MacCamy's results overlap only in a relative narrow frequency band, they both give results in the frequency range of interest.

Experimental studies on the damping force acting on thin plates oscillating on the free surface are impossible to perform since finite amplitudes are required. Therefore experiments have been performed to study the damping coefficient of rectangular cylinders with shallow but finite draft. The same experimental set-up as described in Section 4.2 was used. The design of the set-up limits the minimum possible draft. As a quality check for the measurements, it would have been ideal to reproduce the Vugts' experiments, but the minimum B/D-ratio possible with the given set-up is 16. This corresponds to $D = 0.041$m. A wave amplitude of 0.005m and frequency values between $\omega = 2.51$ rad/s and $\omega = 6.28$rad/s were used in the tests. This corresponds to dimensionless frequencies in the range of $[0.457, 1.372]$. The exciting heave force was recorded and damping estimates were obtained from Newman's formula (4.3). The same experiments were repeated for a draft of 0.01m and of 0.03m, but for the latter case a wave amplitude of 0.015m was used. For these wave conditions the wave steepnesses are small and linear theory can be applied.

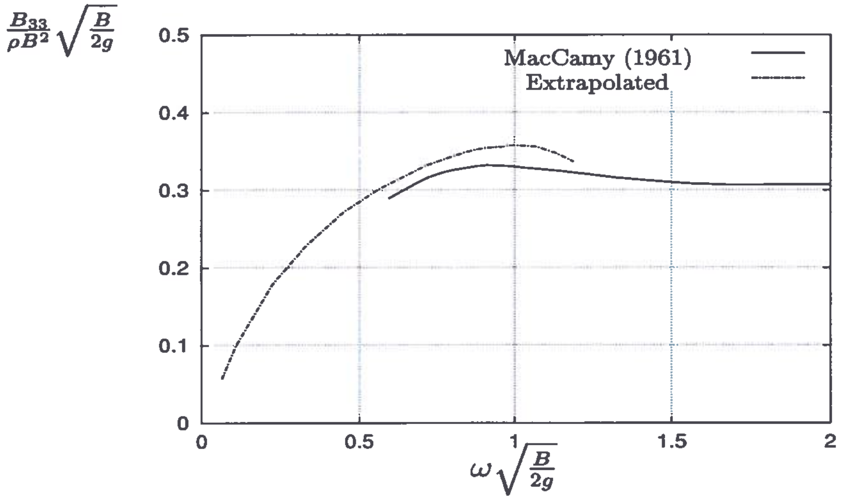

Figure 4.14: *The damping coefficient in heave for a plate with zero draft oscillating in the free surface.*

In Figure 4.15 the experimental values of the damping coefficient are presented together with the theoretical results by Vugts (1968) for finite drafts and by MacCamy (1961) for zero draft. The approximation based on on extrapolation of Vugts' results to $D = 0$ is included. Vugts' results show that the dimensionless damping coefficient is nearly independent of the B/D-ratio when $\omega\sqrt{\frac{B}{2g}} \lesssim 0.2$. For higher frequencies, the damping coefficient increases strongly with increasing B/D. Due to the physical limitations of the experimental set-up and of the wave flume, experiments were not performed for smaller dimensionless frequencies than 0.457. $B = 0.65$m was fixed, so the dimensionless frequency could only be varied by changing ω. The experimental results show that the damping coefficient increases with increasing B/D-ratio. This is consistent with the results by Vugts (1968). Also, the frequency dependency of the measurements is as anticipated. For the lowest frequencies, the experimental damping coefficients in the case of $B/D = 65$ are somewhat larger than the coefficients calculated by extrapolation. For the highest frequencies, the measurements agree well with MacCamy's computations.

A possible explanation for the deviation between the Wagner based method and the experimental results for the water exit phase, can be that the equipment did not record the forces correctly. While the deviations are relatively small for the positive force peak they are significant for the negative force peak. The magnitude of the negative force is largest for the numerical results. If incorrect force measurements are the reason for this then too small negative forces were measured, while the positive forces were approximately correctly measured. Now, by looking at the experimental results for steady state condition, it was noted that the measured force on the partly submerged rectangular cylinder was nearly sinusoidal without any noticeable difference between the magnitudes of the minima and maxima. The force transducers were calibrated so that the mean hydrostatic force was not accounted for in the measurements. This suggests that

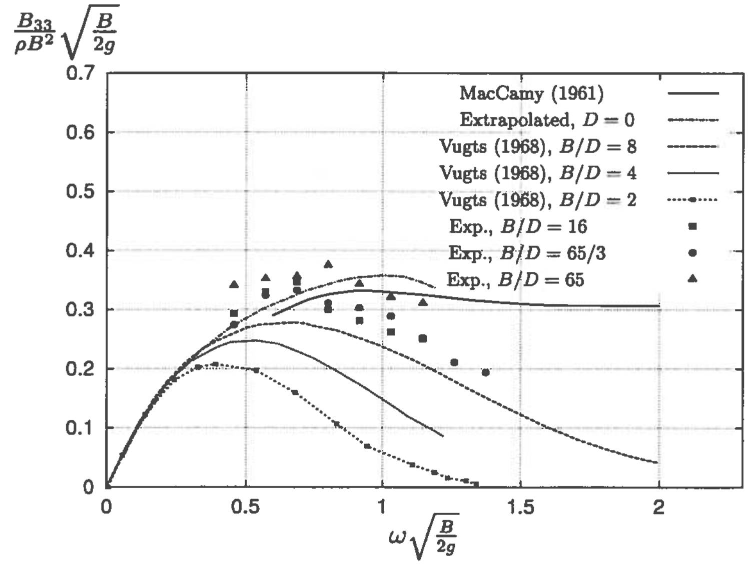

Figure 4.15: *The damping coefficient in heave for a rectangular cylinder oscillating in the free surface. Experimental values for small drafts. Results from MacCamy (1961) for a thin plate and two different schemes for extrapolating the results by Vugts (1968) to zero draft are shown.*

incorrect measurements can probably not explain the large difference between the experimental results and the results obtained from the Wagner based method.

Particularly for the smallest draft the measurements contain uncertainties. A small wave amplitude had to be applied. This implies a small resulting force on the model. The force transducers used were the same as those used for the water impact measurements, which gave much higher forces. The accuracy of the force transducers for such small forces thus is questionable. Calibrations with small weights indicated, however, that they are sensitive enough and give satisfactory measurements for small loads. Another error source equally important for all B/D-ratios is associated with the wavelengths used in the experiments. For the smallest frequencies the wavelengths were long compared to the dimensions of the flume. The beach at the end of the flume is not designed to damp out such long waves. Reflection from the tank ends became noticeable after a few oscillations, and this made it impossible to get long time series without reflected waves affecting the force on the model. Accurate steady state force amplitudes were therefore difficult to measure. In spite of this it may be concluded that the experiments gave fair results for the exciting force and thus for the damping coefficient. This suggests that the measurements of the water impact on the idealized platform deck are satisfactory.

Faltinsen (1983) studied the transient problem connected to the start-up of forced harmonic heave oscillations of a semi-submerged circular cylinder on the free surface. The total hydrodynamic force acting on the cylinder was found by both a linear transient theory derived by Faltinsen (1977) and a linear boundary element method. These two approaches gave almost

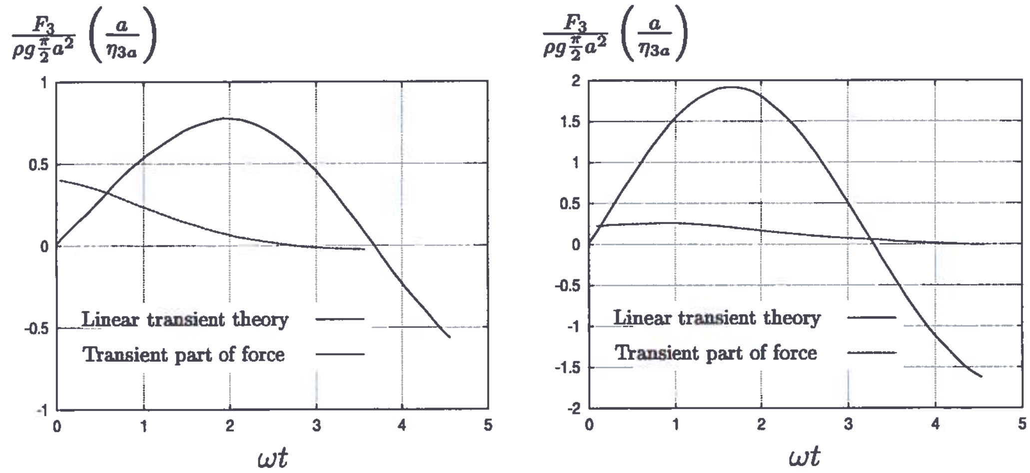

(a) $\omega\sqrt{\frac{a}{g}} = 1.0$

(b) $\omega\sqrt{\frac{a}{g}} = 1.5$

Figure 4.16: *Hydrodynamic force on circular cylinder (excluded linear restoring force) due to forced heave motion* $\eta_3 = \eta_{3a} \sin \omega t$. *Faltinsen (1983).*

identical force histories. The transient part of the force was derived from the linear transient theory. Figure 4.16 shows the hydrodynamic force acting on the cylinder at the start-up of the oscillations for two different oscillation frequencies, $\omega\sqrt{\frac{a}{g}} = 1.0$ and 1.5. a is the cylinder radius and ω is the circular oscillation frequency. The data are taken from Faltinsen (1983). The transient part of the force dies out rapidly and it becomes small compared to the amplitude of the hydrodynamic force after half of an oscillation period.

If a similar behavior can be assumed for a rectangular cylinder with small draft, the steady state force amplitude may be used as a first approximation for $|F_{\text{min}}|$. In Table 4.4 results for the steady state force amplitude, $|F_3^{(ss)}|$, for a number of different wave frequencies and amplitudes are presented. The same wave conditions as used in the experiments described in Section 4.3, are used here. The steady state hydrodynamic excitation force amplitude is found by applying Equation (4.3) and the damping coefficient is taken from MacCamy (1961). The breadth of the cylinder used in the computations is equal to the maximum wetted length obtained by using the Wagner based method. The hydrostatic and the Froude-Kriloff forces are added. The total force is denoted $|F^{ss}_{\text{min}}|$. These results are compared with the corresponding experimental results. By using $|F^{ss}_{\text{min}}|$ as an approximation for the magnitude of the negative force peak, values relatively close to the experimental results are obtained. In particular for small η_{ag0}, where the maximum wetted lengths are large, the steady state approach seems to yield better estimates than the Wagner based method. This suggests that the free surface condition $\phi = 0$ is not the proper one for water exit. It is believed that better estimates can be achieved if gravity is included in the boundary value problem. For the longest wave period the Wagner based method

Table 4.4: *Comparisons between finding the magnitude of the minimum force by using a steady state approach,* $|F^{ss}_{min}|$*, the Wagner based numerical method,* $|F^{WBM}_{min}|$*, and the results from the experiments,* $|F^{exp}_{min}|$*.* $|F_3|$ *is found from Equation (4.3), and* $|F^{ss}_{min}|$ *is* $|F_3^{ss}|$ *plus the hydrostatic force and the Froude-Kriloff force found from the Wagner based method.*

Case	Impact condition			Max. magnitude of negative force			
	T	ζ_a	η_{ag0}	$\lvert F_3^{ss}\rvert$	$\lvert F^{ss}_{\min}\rvert$	$\lvert F^{WBM}_{\min}\rvert$	$\lvert F^{exp}_{\min}\rvert$
no.	[s]	[m]	[m]	[N]	[N]	[N]	[N]
1	1.11	0.05	0.04	86.3	60.5	82.0	67.8
2	1.11	0.06	0.04	120.2	68.1	133.0	83.5
3	1.11	0.06	0.06	70.9	57.4	41.1	31.7
4	1.11	0.07	0.06	113.5	76.4	100.3	74.9
5	1.25	0.05	0.04	104.9	75.9	90.7	67.8
6	1.25	0.06	0.04	125.8	74.9	84.5	70.2
7	1.25	0.06	0.06	82.7	69.8	36.6	61.7
8	1.25	0.07	0.06	134.4	94.5	110.9	89.8
9	1.43	0.05	0.038	96.0	66.8	52.7	51.9
10	1.43	0.06	0.038	133.4	87.4	45.2	54.2
11	1.43	0.06	0.06	99.4	87.1	45.0	60.9

yields results closer to the experimental ones. However, also in this case the steady state results remain relative close to the experimental results. Note that the steady state approach is crude and it only meant to give an indication of the magnitude of $|F_{\min}|$. First, for the deck impact problem the breadth of the waterline of the body varies strongly with time. This may explain why the steady state results in Table 4.4 are better when η_{ag0} is small. For small η_{ag0} the wetted length is larger for a longer time than in the case of large values of η_{ag0}. A second error source is that Equation (4.3) is based on linear theory, while the incident waves in the experiments are nonlinear.

For steady state results gravity is important. It is therefore believed that better theoretical results for the force acting on the deck during water exit can be obtained by taking gravity into account. Further, one can expect that more correct boundary conditions would yield better predictions of the duration of the water exit phase, but they give a boundary value problem that is not analytically solvable. Motivated by this, it was decided to develop a boundary element method.

CHAPTER 5

A boundary element method

5.1 Formulation of the boundary value problem

Wave impact underneath a platform deck is a strongly nonlinear phenomenon. The experiments in Chapter 4 show large free surface deformations that cannot be described by linear theory. Particularly during water exit the free surface is very different from the undisturbed incident wave. By using a fully nonlinear boundary element method, Zhao and Faltinsen (1993) solved the problem where an arbitrarily shaped two-dimensional section enters an initially calm free surface. Zhao, Faltinsen, and Aarsnes (1996) showed that this methods provides estimates for the pressure distribution along the body and for the free surface deformation that are in good agreement with experiments performed. In the following a mathematical formulation of the two-dimensional nonlinear free surface problem and a solution procedure of it will be outlined.

5.1.1 The boundary value problem

Consider an infinitely long horizontal cylinder with arbitrary cross-sectional shape located on the free surface. The cylinder is assumed rigid and two-dimensional potential theory is assumed to be valid. Hence, a velocity potential Φ can be introduced. Φ has to satisfy the two-dimensional Laplace equation, $\nabla^2\Phi = 0$, in the fluid domain. Boundary conditions are required to solve the related problem. In particular by setting the pressure equal to the atmospheric pressure on the free surface, ζ, a dynamic free surface condition in the form

$$\frac{\partial \Phi}{\partial t} + \frac{1}{2}\left[\left(\frac{\partial \Phi}{\partial x}\right)^2 + \left(\frac{\partial \Phi}{\partial z}\right)^2\right] + g\zeta = 0 \qquad \text{on } z = \zeta(x,t) \tag{5.1}$$

follows from Bernoulli's equation. The (x, z)-coordinate system has its origin in the mean free surface with the z-axis pointing upwards. A kinematic free surface condition must also be imposed. This condition states that fluid particles on the free surface remain on the free surface and it can be written as

$$\frac{\partial\Phi}{\partial z} = \frac{\partial\zeta}{\partial t} + \frac{\partial\zeta}{\partial x}\frac{\partial\Phi}{\partial x} \qquad \text{on } z = \zeta(x,t) \tag{5.2}$$

Furthermore, the boundary condition

$$\frac{\partial\Phi}{\partial n} = U_{\mathrm{n}} \qquad \text{on } S_{\mathrm{B}} \tag{5.3}$$

requiring the body to be impermeable, must be satisfied on the instantaneous wetted body surface, S_B. In (5.3) U_{n} is the body's velocity normal to its own surface, thus for a fixed body $U_{\mathrm{n}} \equiv 0$. $\frac{\partial}{\partial n}$ denotes the derivative along the normal unit vector $\mathbf{n}$ of S_{B}. $\mathbf{n}$ is defined to be positive when pointing into the fluid domain. For finite water depths a similar condition must be imposed on the bottom, but in this work the water depth is assumed to be sufficiently large when compared to the wave length for the bottom condition to be omitted.

To solve this boundary value problem, initial conditions are also required.

5.1.2 Solution procedure

Inside fluid domain the velocity potential can be represented in terms of boundary integrals through Green's second identity,

$$-2\pi\Phi(x,z,t) = \int\limits_S \left(\Phi(\xi,\eta)\frac{\partial \log r}{\partial n(\xi,\eta)} - \frac{\partial\Phi(\xi,\eta)}{\partial n(\xi,\eta)}\log r\right) dS(\xi,\eta) \tag{5.4}$$

Here $r = \sqrt{(x-\xi)^2 + (z-\eta)^2}$, (x,z) is the field point where Φ has to be evaluated and (ξ,η) is a generic point along the boundary $S = S_B + S_F + S_\infty$. S_∞ is a control surface at $x = \pm\infty$. S_B and S_F are the instantaneous wetted body surface and the free surface, respectively.

If incident waves are present, the total velocity potential may be decomposed as $\Phi = \phi_I + \phi$, where ϕ_I represents the incident wave potential, and ϕ is the perturbation potential due to the presence of the body. Similar, the free surface elevation can be written as $\zeta = \zeta_I + \zeta_D$. Here ζ_D is the free surface elevation associated to the disturbance caused by the body, and ζ_I is the free surface elevation of the incident waves. In the following part of this section it is assumed that no incident waves are present, *i.e.* $\phi_I = 0$ and $\zeta_I = 0$, and that the boundary value problem can be solved as a transient problem. The BVP can then be solved as an initial value problem with initial condition

$$\phi = 0 \qquad \text{on } z = 0 \tag{5.5}$$

S_∞ is taken to be sufficiently far from the body so that its contribution the integral in Equation (5.4) is negligible. The equation then reduces to

$$-2\pi\phi(x,z,t) = \int\limits_{S_F+S_B} \left(\phi(\xi,\eta)\frac{\partial \log r}{\partial n(\xi,\eta)} - \frac{\partial\phi(\xi,\eta)}{\partial n(\xi,\eta)}\log r\right) dS(\xi,\eta) \tag{5.6}$$

Far away from the body, $|x| \geq x_b(t)$, the dynamic free surface can be approximated by $\phi = 0$ on $z = 0$, x_b being large compared to the cross-sectional dimensions of the body. Further, if infinite water depth is assumed, the perturbation velocity potential at $|x| \geq x_b(t)$ can be described by a sum of a vertical dipole and a multipole in the origin,

$$\phi = \frac{A_1 z}{x^2 + z^2} + \frac{A_2 x z}{(x^2 + z^2)^2} \tag{5.7}$$

where $A_1(t)$ is the dipole strength and $A_2(t)$ is the multipole strength. It is assumed that the z-axis goes through the center of the body. Expression (5.7) implies that the details of the body shape, crucial for ϕ in the vicinity of S_B, become unimportant for the fluid flow far from the body. The first and the second term in it, respectively account for dominating symmetric and anti-symmetric disturbances caused by the body.

By applying Equation (5.7) it is possible to integrate analytically the S_F contribution to the integral in Equation (5.6) for values of $|x| > x_b(t)$. In particular, by setting $\eta = 0$ in Equation (5.6), the integral from x_b to ∞ can be written as

$$\begin{aligned} I(x,z) &= I_1 + I_2 \\ &= A_1 \left\{ \frac{1}{x_b} \log \sqrt{(x_b - x)^2 + z^2} - \frac{x}{x^2 + z^2} \log \left[\frac{\sqrt{(x_b - x)^2 + z^2}}{x_b} \right] \right. \\ &\quad \left. + \frac{z}{x^2 + z^2} \left[\operatorname{sgn}(z) \frac{\pi}{2} - \tan^{-1} \left(\frac{x_b - x}{z} \right) \right] \right\} \\ &\quad + A_2 \left\{ \frac{1}{x_b^2} \log \sqrt{(x_b - x)^2 + z^2} - \frac{1}{x^2 + z^2} \left(\log(x_b) + \frac{x}{x_b} \right) \right. \\ &\quad + \frac{1}{(x^2 + z^2)^2} \left[2x^2 \log(x_b) - \frac{1}{2}(x^2 - z^2) \log\left((x_b - x)^2 + z^2\right) \right] \\ &\quad \left. + \frac{2xz}{(x^2 + z^2)^2} \left[\operatorname{sgn}(z) \frac{\pi}{2} - \tan^{-1} \left(\frac{x_b - x}{z} \right) \right] \right\} \end{aligned} \tag{5.8}$$

where I_1 and I_2 are the contributions associated with the dipole and the multipole, respectively. Similarly, the integral from $-\infty$ to $-x_b$ of Equation (5.6) can be expressed as

$$J(x,z) = I_1(-x,z) - I_2(-x,z) \tag{5.9}$$

Differently, the integral along the free surface inside $|x| \leq x_b(t)$ and the instantaneously wetted body surface, S_B, has to be evaluated numerically. In the numerical solution, an integral equation based on Equation (5.6) is set up for each time instant by letting (x, z) approach points on S. The free surface, S_F, inside $|x| \leq x_b$ and S_B are divided into N straight line segments. ϕ and $\frac{\partial \phi}{\partial n}$ are assumed to be constant on each segment. On the body $\frac{\partial \phi}{\partial n}$ is known from the body boundary condition given by Equation (5.3) while ϕ is unknown. At the free surface $\frac{\partial \phi}{\partial n}$ is unknown while ϕ is known from the free surface condition given by Equation (5.1). When the known quantities are inserted into the Fredholm integral equation, and the equation is imposed at the midpoint of each segment, a set of N linear equations is obtained. These are not sufficient to solve the problem. When the dipole and multipole strengths, $A_1(t)$ and $A_2(t)$, are included, the total number of unknowns is $N+2$. Two additional equations are necessary and can be obtained by requiring continuity of the velocity potential at $x = \pm x_b(t)$. A system of linear equations with number of equations equal to the number of unknowns is now obtained. This can be solved by a standard procedure.

By using the kinematic and dynamic free surface conditions, respectively, the position of S_F and the velocity potential on this surface can be integrated in time. The motion of the free surface is determined by integrating the fluid velocity on S_F. The dynamic free surface condition can be rewritten on Lagrangian form as

$$\frac{\mathrm{D}\phi}{\mathrm{D}t} = \frac{1}{2}\left[\left(\frac{\partial\phi}{\partial x}\right)^2 + \left(\frac{\partial\phi}{\partial z}\right)^2\right] - g\zeta \qquad \text{on } z = \zeta(x,t) \tag{5.10}$$

where $\frac{\mathrm{D}}{\mathrm{D}t}$ denotes the substantial derivative. The $\frac{\partial\phi}{\partial t}$ term in Equation (5.1) has been rewritten by applying $\frac{\mathrm{D}\phi}{\mathrm{D}t} = \frac{\partial\phi}{\partial t} + (\nabla\phi\cdot\nabla)\,\phi$. An algorithm for integrating ϕ and ζ will be discussed in more detail later.

5.1.3 The pressure distribution and the force action on the body

Once the velocity potential on the body is known, the pressure can be obtained from Bernoulli's equation

$$p - p_0 = -\rho\frac{\partial\phi}{\partial t} - \frac{1}{2}\rho\left[\left(\frac{\partial\phi}{\partial x}\right)^2 + \left(\frac{\partial\phi}{\partial z}\right)^2\right] - \rho g z \tag{5.11}$$

where z is the submergence. The first two terms on the right hand side may be denoted as hydrodynamic pressure, while the latter represents hydrostatic pressure. However, since all the terms have to be considered together, it is strictly speaking only when $\phi = 0$ that the last term is the hydrostatic pressure. In the numerical evaluation of the $\frac{\partial\phi}{\partial t}$ term, Zhao et al. (1996) introduce a generalization of the substantial derivative. They use

$$\frac{\mathrm{D}'\phi}{\mathrm{D}'t} = \frac{\partial\phi}{\partial t} + \mathbf{U}\cdot\nabla\phi \tag{5.12}$$

$\frac{\mathrm{D}'\phi}{\mathrm{D}'t}$ being the change of ϕ with time when the midpoint of an element of the discretization is followed, and U is the velocity of the midpoint. The total force on the body can be determined by integrating the pressure over the wetted body surface. Alternatively, the force may be calculated by imposing conservation of fluid momentum. In this case this can be expressed as

$$\mathbf{F} = \rho\frac{d}{dt}\int\limits_{S_B+S_F}\phi\mathbf{n}\,dS + \int\limits_{S_F}\rho g\zeta\mathbf{n}\,dS + \int\limits_{S_B}\rho g z\mathbf{n}\,dS \tag{5.13}$$

This equation was derived by Faltinsen (1977) and it represents a special case for transient problems. For a steady state problem, an integral along a far field control surface S_∞ must be included when the force on the body is evaluated.

The objective of the development of a boundary element method is to make available a nonlinear method for solving water impact on a platform deck in a consistent manner. Nonlinear free surface problems are difficult to solve. The mathematical difficulty arises essentially from the need to satisfy the dynamic free surface condition on the exact free surface. The free surface is a priori unknown and in this case highly time dependent. It was therefore decided to develop the numerical method in a stepwise manner, where each step can be validated by results available in literature. In the following sections a boundary element method for transient problems is described. Firstly, a linearized version is developed and validated. Then a fully nonlinear code for forced oscillations in initially calm fluid is developed. Comparisons to experiments performed by Tasai and Koterayama (1976) are used for validation. Finally, a nonlinear method for solving water impact underneath is presented in Chapter 6.

5.2 A linear boundary element method

As a first step a linear code has been built up. This is an important building brick in making the fully nonlinear code. Validation of the linearized version permits one to easily check for possible errors in the algorithm, before the nonlinearities complicates the solution procedure. When the problem is linearized, the free surface conditions in Equations (5.1) and (5.2) and the body boundary condition (5.3) are satisfied on the mean boundaries and simplified as

$$\frac{\partial \phi}{\partial t} = -g\zeta \qquad \text{on } z = 0 \tag{5.14}$$

$$\frac{\partial \phi}{\partial z} = \frac{\partial \zeta}{\partial t} \qquad \text{on } z = 0 \tag{5.15}$$

$$\frac{\partial \phi}{\partial n} = U_n \qquad \text{on } \bar{S}_B \tag{5.16}$$

where $\bar{S}_B$ is the mean wetted body surface. This implies that the boundary is known and fixed in time, thus the discretization of this surface can be made once for all. If long time series are required it may be efficient to increase the number of elements along the free surface and thereby increase the value of $x_b(t)$ with time. This allows for using few free surface elements at the beginning of the simulation when ϕ and ζ approaches zero quickly as the distance $|x|$ from the body increases. Later, when a larger part of the free surface needs to be discretized, new elements may be added. In this work, a constant number of segments and a constant x_b is used for each simulation. The free surface is discretized so that small segments are used close to the body, where the velocity potential and the free surface elevation vary strongly with the spatial coordinates, while larger elements are used far away from the body. On the body small elements are used near sharp corners and near the body/ free surface intersections. A second order Runge-Kutta scheme is used to integrate the solution in time. Below, some problems studied by the using linear boundary element method are discussed.

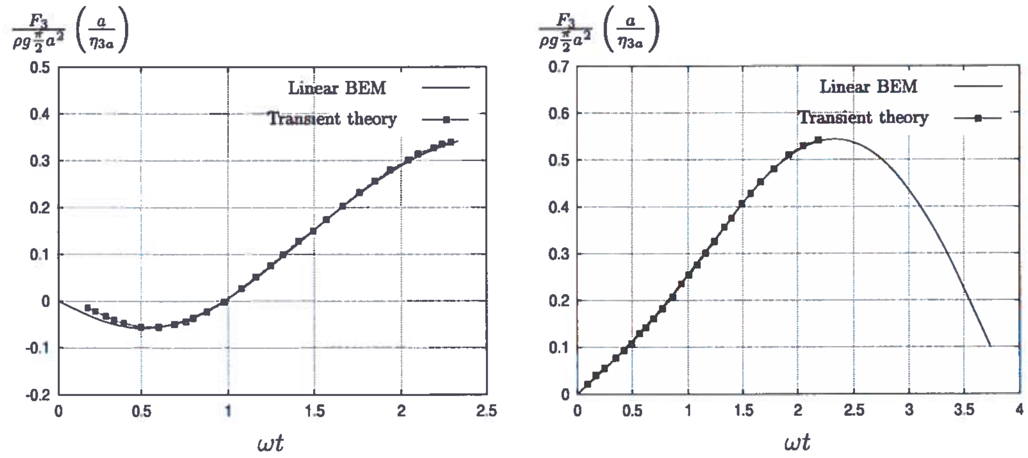

(a) $\omega\sqrt{\frac{a}{g}} = 0.5$ (b) $\omega\sqrt{\frac{a}{g}} = 0.8$

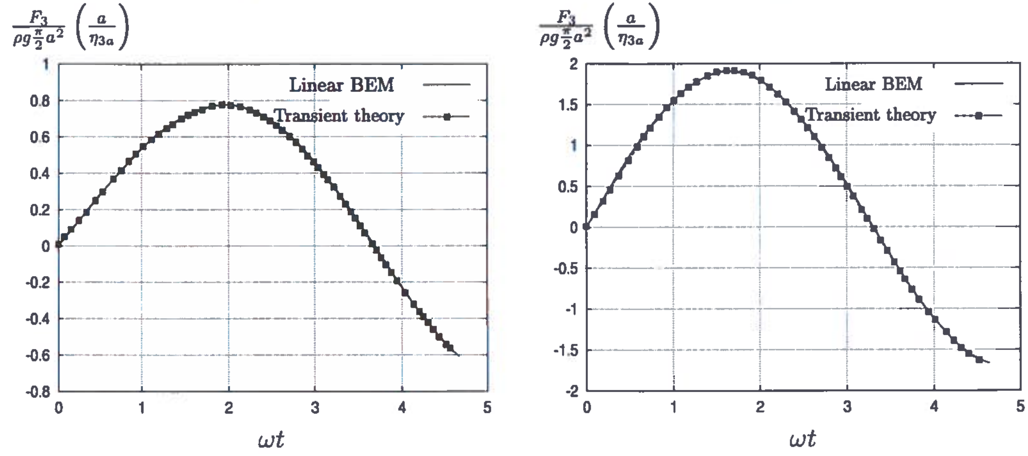

(c) $\omega\sqrt{\frac{a}{g}} = 1.0$ (d) $\omega\sqrt{\frac{a}{g}} = 1.5$

Figure 5.1: *Hydrodynamic force on circular cylinder (excluded linear restoring force) for forced heave motion, $\eta_3 = \eta_{3a}\sin(\omega t)$ during start-up of oscillations. Comparisons between the linear boundary element method and the linear transient theory by Faltinsen (1977).*

5.2.1 Start-up of forced heave oscillations

A semi-submerged circular cylinder undergoing forced heave oscillations is considered. Before the steady state condition is reached, the hydrodynamic force on the cylinder contains a transient part associated with the start-up of the oscillations. The transient problem is solved as an initial value problem with $\phi = 0$ and $\zeta = 0$ on $z = 0$ as initial conditions. Faltinsen (1977) derived a linear transient theory and Faltinsen (1983) documented excellent agreement for the force acting on the body computed by the transient theory and by a linear boundary element method applied to this problem. Similar comparisons are performed here. Figure 5.1 shows comparisons for four different dimensionless frequencies $\omega\sqrt{\frac{a}{g}}$, where ω is the oscillation frequency and a is the cylinder radius. The linear boundary element method agrees well with the linear transient theory by Faltinsen (1977). An exception is the beginning of the simulation for the lowest frequency (see Figure 5.1(a)). In this region the results from the present method deviate some from the linear transient theory.

5.2.2 Added mass and damping of cylinders oscillating on the free surface

If longer simulations are performed and the amplitude and the frequency of the oscillations are kept constant, the hydrodynamic force acting on the body will eventually reach steady state. The part of the force in phase with the acceleration of the body is defined as the added mass force, while the part in phase with the velocity can be identified as hydrodynamic damping force. If the body is given a forced harmonic oscillation in i-direction, η_i, a hydrodynamic steady state force in j-direction is originated. In the linear problem this force can be written as

$$F_j = -A_{ji}\ddot{\eta}_i - B_{ji}\dot{\eta}_i \tag{5.17}$$

where A_{ji} and B_{ji} are defined as the added mass and the hydrodynamic damping coefficient, respectively. Added mass and damping coefficients may easily be evaluated from the force history. Faltinsen (1990) presents results for the added mass and damping coefficients as functions of oscillation frequency for heave and sway motion for the case of a semi-submerged circular cylinder. Forced heave is a symmetric problem for a symmetric body. This means that the velocity potential and the free surface elevation are symmetric about the yz-plane. A_2 (see Eq. (5.7)) vanishes for symmetric problems. Similarly, forced sway is an anti-symmetric problem, *i.e.* the velocity potential and the free surface elevation are anti-symmetric about the yz-plane, thus $A_1 = 0$. For a symmetric body, symmetry and anti-symmetry conditions can be used, and the elements of the discretized boundaries with $x > 0$ can be reflected about the z-axis to represent the body and the free surface for $x < 0$. This reduces the number of unknowns in the numerical solution and consequently the computation time. Figure 5.2 presents comparisons between results obtained by the present method and results given by Faltinsen (1990) for the added mass and the damping coefficients in heave and sway for a circular cylinder. The results compare well for all the frequencies used in comparisons.

Vugts (1968) presents linear results for added mass and damping coefficients for rectangular cylinders oscillating on the free surface. Results are reported for different B/D-ratios, namely 2, 4 and 8. Here B is the breadth of the section and D is the mean draft. Figure (5.3) shows comparisons between the present method and the theoretical results by Vugts (1968). Vugts obtains his solution by following the method by Ursell (1949). Results for added mass and damping coefficients obtained by the present boundary element method compare well with linear results in Vugts (1968) for all three B/D-ratios. A wide range of frequencies is tested.

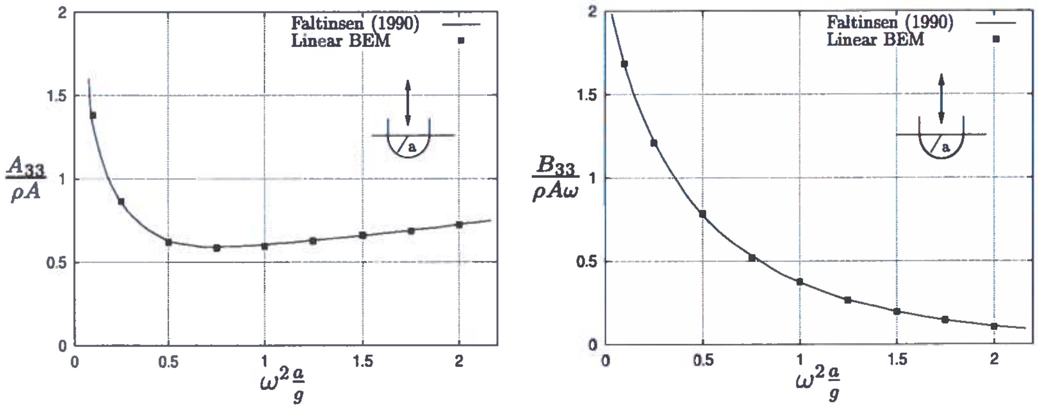

(a) Added mass in heave

(b) Hydrodynamic damping in heave

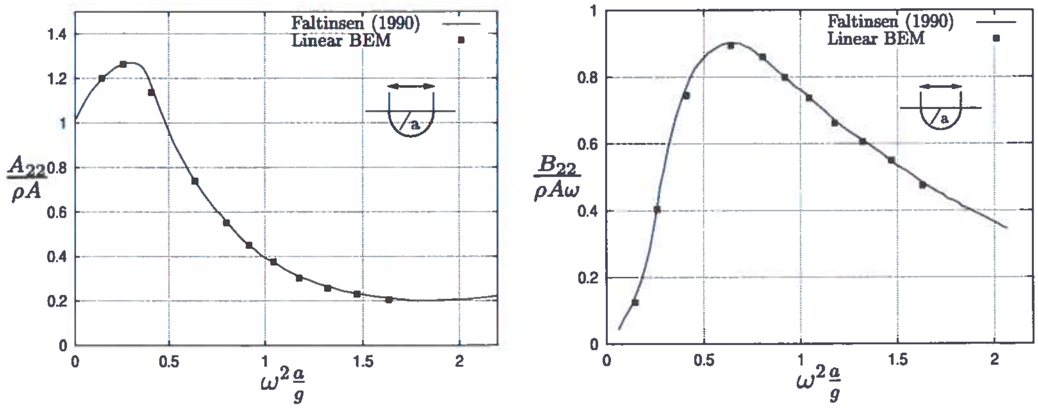

(c) Added mass in sway

(d) Hydrodynamic damping in sway

Figure 5.2: *Two-dimensional added mass and damping in heave and sway for a circular cylinder with axis in the mean free surface. Infinite water depth. Comparisons between the linear BEM and results given by Faltinsen (1990). (A_{33} =added mass in heave, B_{33} =damping in heave, A_{22} =added mass in sway, B_{22} =damping in sway, $A = 0.5\pi a^2$, ω =circular frequency of oscillation.)*

5.2.3 Excitation loads due to regular incident waves

Incident waves yields forces and moments acting on the body. Given linear waves and steady state conditions, the linear dynamic rigid body motions and the loads on the body oscillate

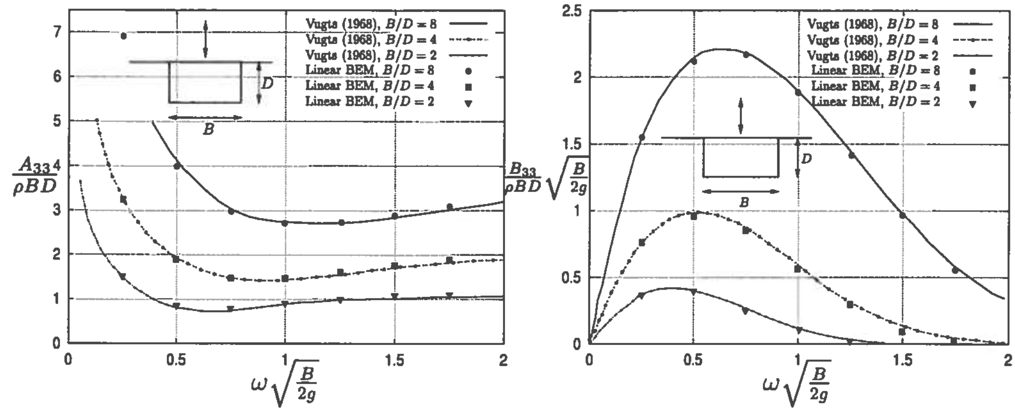

Figure 5.3: *Two-dimensional added mass and damping in heave for a rectangular cylinder oscillating on the free surface, for different B/D-ratios. Where B is the breadth of the cylinder and D is the draft. Infinite water depth. Comparisons between the linear BEM and results given by Vugts (1968). (A_{33} =added mass in heave, B_{33} =damping in heave, ω =circular frequency of oscillation.)*

harmonically with a frequency equal to the wave frequency. In this case it is convenient to split the total problem into two sub-problems (*e.g.* Faltinsen (1990)):

i) **The diffraction problem**: The body is fixed in its mean position, and the wave loads acting on the body are calculated. In this case the hydrodynamic loads are denoted wave excitation loads. They are composed of Froude-Kriloff and diffraction forces and moments.

ii) **The radiation problem**: The body is forced to oscillate with the wave frequency in any rigid body motion mode. There are no incident waves present. The hydrodynamic loads are in this case denoted as the added mass and damping forces and moments, as described by Equation (5.17), and the restoring forces and moments.

In linear theory the forces associated with each of these sub-problems may be superposed to give the total hydrodynamic forces. Similarly, for irregular waves, the results for each wave component can be linearly superposed.

The radiation problem has been solved for a considerable number of cases, while the wave excitation problem has not yet been considered. Vugts (1968) reports results for two-dimensional horizontal and vertical hydrodynamic excitation forces for a semi-submerged circular cylinder exposed to regular incident waves. If the body is kept fixed, the linear body boundary condition becomes

$$\frac{\partial \phi}{\partial n} = -\frac{\partial \phi_I}{\partial n} \qquad \text{on } \bar{S}_B \tag{5.18}$$

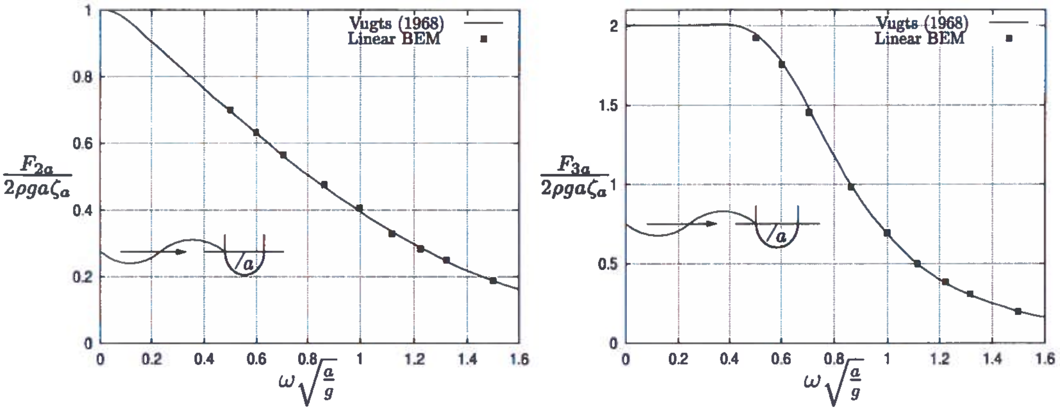

(a) Horizontal excitation force

(b) Vertical excitation force

Figure 5.4: *Two-dimensional horizontal and vertical excitation force on a semi-submerged circular cylinder due to linear incident waves with amplitude ζ_a and oscillation frequency ω. F_{2a} and F_{3a} are amplitudes of the sway and heave excitation forces, respectively. a is the cylinder radius. Comparisons between linear BEM results and results by Vugts (1968).*

The linear diffraction and Froude-Kriloff loads may be calculated by direct pressure integration as

$$\mathbf{F}_D = -\int_{\bar{S}_B} (p - p_0)_D \mathbf{n}\, dS = \rho \int_{\bar{S}_B} \frac{\partial \phi}{\partial t} \mathbf{n}\, dS \tag{5.19}$$

and

$$\mathbf{F}_I = \rho \int_{\bar{S}_B} \frac{\partial \phi_I}{\partial t} \mathbf{n}\, dS \ , \tag{5.20}$$

respectively. The total excitation load is $\mathbf{F}_{\text{exc}} = \mathbf{F}_D + \mathbf{F}_I$.

The incident velocity potential ϕ_I is given in Equation (3.5), and by inserting this one into Equation (5.18) the body boundary condition

$$\frac{\partial \phi}{\partial n} = -\zeta_a \omega e^{kz} \cos(kx - \omega t) n_1 - \zeta_a \omega e^{kz} \sin(kx - \omega t) n_3 \tag{5.21}$$

is obtained. n_1 and n_3 are respectively the horizontal and vertical component of the normal unit vector $\mathbf{n}$ of $\bar{S}_B$. If the body is symmetric about the yz-plane, the problem can be divided into a symmetric and an anti-symmetric problem which can be solved separately. The symmetric problem yields vertical excitation only and the anti-symmetric problem yields horizontal excitation only. Comparisons to results by Vugts (1968) have been performed. Vugts reports linear results for horizontal and vertical hydrodynamic excitation force on a fixed semi-submerged circular cylinder due to regular incident waves. The results are based on Equation (4.3), assuming the damping coefficient known. In the present boundary element method, the hydrodynamic excitation force is evaluated by using Equations (5.19) and (5.20). The results for horizontal and vertical excitation forces are presented in Figure 5.4.

As a concluding remark on the linear boundary element method one can say that it yields good results for several test cases. It predicts well the transient phase during the start-up of forced heave oscillation. Further, by simulating forced oscillations until steady state condition is reached, accurate estimates of the added mass and the hydrodynamic damping coefficients can be obtained. This is shown for both symmetric and anti-symmetric problems. Finally, the calculations show that the method gives good estimates for the excitation force on a fixed body subjected to linear incident waves.

5.3 Fully nonlinear boundary element method for forced oscillations

Once a reliable linear time-domain boundary element method has been established and validated, the next natural step is to solve the problem related to forced oscillations without incident waves by using a fully nonlinear method. This requires two important extensions to the linear method described above. Firstly, the nonlinear terms in the free surface conditions have to be included, and secondly, the boundary conditions have to be satisfied on the exact boundaries. The latter extension requires particular care to ensure stable solutions. Furthermore, an integration scheme able to give accurate estimates of the free surface elevation and of the velocity potential on S_F at the next time step must be applied.

5.3.1 Time integration scheme

In this work an integration algorithm similar to the one described by Zhao and Faltinsen (1993) is used. This algorithm ensures good mass conservation even when the free surface curvature becomes large. The time integration of the free surface is outlined in Figure 5.5.

Let $OP(i,j)$ be the coordinates of endpoints of segments at time instant j, and let $SP(i,j)$ be the coordinates of the free surface point midway between endpoints $OP(i,j)$ and $OP(i+1,j)$. The surface points are introduced to enable one to get better predictions of the free surface elevation and thus better mass conservation. The value of $SP(i,j)$ is a priori unknown while $OP(i,j)$ is known. A first estimate for $SP(i,j)$ is found by fitting a second order polynomial through $OP(i-1,j)$, $OP(i,j)$ and $OP(i+1,j)$ and letting $SP(i,j)$ be situated halfway between $OP(i,j)$ and $OP(i+1,j)$ along the second order curve. Similarly, a second estimate is found by constructing a second order polynomial based on the endpoints $OP(i,j)$, $OP(i+1,j)$ and $OP(i+2,j)$. The final estimate of $SP(i,j)$ is chosen to be the average of the two estimates.

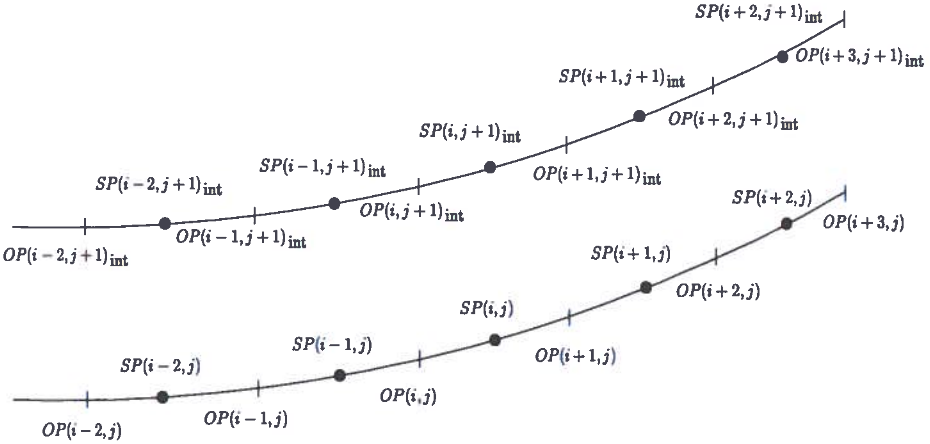

Figure 5.5: *Definitions of points used in the description and motion of the free surface in the nonlinear boundary element method.* $OP(i,j)$ *are the endpoint of the segments at time instant* j*, and* $SP(i,j)$ *are the free surface points.*

The fluid velocity at $SP(i,j)$ can be evaluated through its normal component to S_F, $\frac{\partial\phi}{\partial n}$, which is taken to be the solution of the boundary value problem at the midpoint of the straight line segment between $OP(i,j)$ and $OP(i+1,j)$, and its tangential component to S_F, $\frac{\partial\phi}{\partial s}$, which can be estimated by differentiating the velocity potential along the free surface. The fluid velocity vector is denoted as $\mathbf{V}$. Instead of tracking the midpoints of the straight line segments where the boundary value problem is solved, the evolution of the free surface points $SP(i,j)$ is followed. This is done to minimize the error in conservation of mass. The time stepping is performed in two steps. In the first step an intermediate new position $SP(i,j+1)_{\text{int}}$ at time instant $j+1$ is found based on the velocity $\mathbf{V}$ at $SP(i,j)$. The change in position then becomes $\mathbf{V}\Delta t_j$, where Δt_j is the time increment $t_{j+1}-t_j$. Similarly, an intermediate value of the velocity potential ϕ is found from the dynamic free surface condition when inserting the velocities and the free surface elevation found at $SP(i,j)$. Based on the free surface points $SP(i-2,j+1)_{\text{int}}$, $SP(i-1,j+1)_{\text{int}}$, $SP(i,j+1)_{\text{int}}$ and $SP(i+1,j+1)_{\text{int}}$, $OP(i,j+1)_{\text{int}}$ is found. This is done in the same manner as described above, by fitting two second order polynomials through the points. Two estimates for $OP(i,j+1)_{\text{int}}$ are then found by letting $OP(i,j+1)_{\text{int}}$ be situated half way between $SP(i-1,j+1)_{\text{int}}$ and $SP(i,j+1)_{\text{int}}$ along the second order curves. $OP(i,j+1)_{\text{int}}$ is chosen to be the average value of the two estimates. In the second step, straight line segments between $OP(i,j+1)_{\text{int}}$ and $OP(i+1,j+1)_{\text{int}}$ are constructed, and the boundary value problem at the intermediate position of the free surface is solved. The fluid velocities $\mathbf{V}_{\text{int}}$ on the intermediate free surface can then be evaluated at $SP(i,j+1)_{\text{int}}$.

The final position of the free surface points $SP(i,j+1)$ is calculated by using the average velocity at $SP(i,j)$ and $SP(i,j+1)_{\text{int}}$, $\mathbf{V}_{\text{avg}} = 0.5(\mathbf{V}+\mathbf{V}_{\text{int}})$. This implies that the displacement from $SP(i,j)$ to $SP(i,j+1)$ is $\mathbf{V}_{\text{avg}}\Delta t_j$. New free surface segments are found in the same way as for the intermediate position. The velocity potential on the final position is calculated

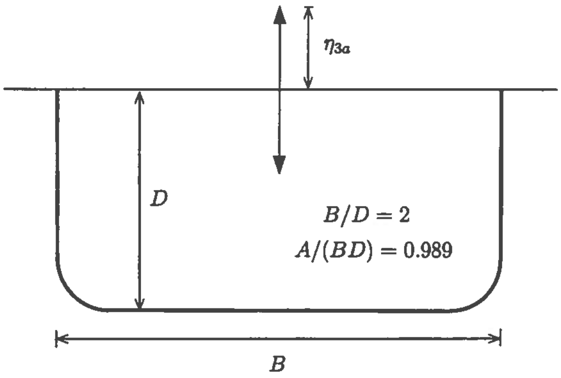

Figure 5.6: *The mean submerged cross-section of the Lewis formed cylinder used in the comparisons to the experiments by Tasai and Koterayama (1976).*

using $\mathbf{V}_{\text{avg}}$ and the mean surface elevation during the time increment Δt_j.

The body/ free surface intersection points are determined by extrapolating the free surface on to the body surface. On each side a linear function is constructed using the two surface points closest to the body, and the contact point is determined as this function's intersection with the body surface.

5.3.2 Validation of the nonlinear boundary element method

The fully nonlinear method has been validated by comparisons to experiments for forced heave motion of a Lewis form cylinder with $\frac{B}{D} = 2$ and $\sigma = \frac{A}{BD} = 0.989$, in initially calm water. The experiments were performed by Tasai and Koterayama (1976). Here B and D are the breadth at the waterline and the draft of the cylinder, respectively. A is the mean submerged cross-sectional area. The cross-section of the cylinder is illustrated in Figure 5.6. Steady state results from the nonlinear simulations are considered.

When a two-dimensional body performs heaving oscillations with a finite heave amplitude η_{3a} and circular frequency ω, the hydrodynamic force on the body contains higher order components. The first three harmonics of the hydrodynamic force have been considered in the comparisons. The different harmonics are extracted from the total force history. The first harmonic of the force oscillates with the oscillation frequency ω, and the oscillation frequencies of the second and third harmonics are 2ω and 3ω, respectively. Experiments were performed for three different heave amplitudes, $\epsilon = \eta_{3a}/(B/2)$, namely $\epsilon = 0.222$, 0.444 and 0.666, and for each amplitude 7 different oscillation frequencies were applied.

Figure (5.7) presents comparisons for the added mass force and damping force evaluated from the first harmonic of the total force. The whole lines are theoretical linear results given by Tasai and Koterayama (1976). These results are validated by the linear boundary element method

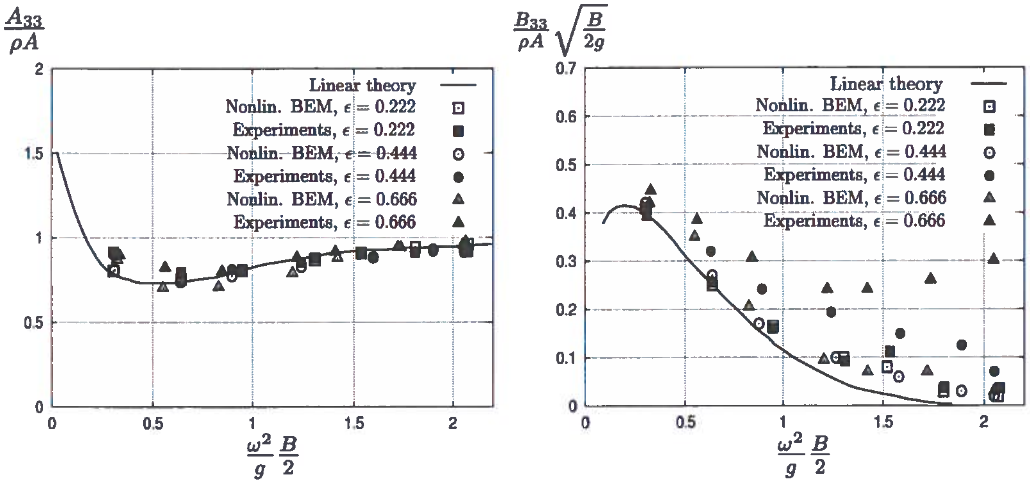

(a) Added mass

(b) Damping

Figure 5.7: *Added mass and damping coefficients in heave for Lewis form cylinder ($B/D = 2$ and $A/(BD) = 0.989$) for different heave amplitudes. Comparisons between numerical results using a fully nonlinear boundary element method and experimental results by Tasai and Koterayama (1976).*

given above. For the smallest amplitudes the experimental and the numerical results for the added mass coefficient compare well, while the deviations are larger for the largest amplitude. However, the added mass coefficients are relatively close to the linear results for all amplitudes and frequencies. The experimental values for the damping coefficient are larger than the numerical ones. For the smallest amplitude the deviations are small, while they increase with both amplitude and frequency. It is believed that the deviations are mainly related to viscous damping. While viscosity is not accounted for in the theory, vortex shedding at bilges in the experiments may give a significant contribution to the damping. Note that if a perturbation theory is applied, the first harmonic force also gets contribution from 3rd order, 5th order and so on.

Tasai and Koterayama (1976) define a first harmonic heave force that includes added mass, damping and restoring terms on the form

$$\begin{aligned} F_3^{(1)} &= \eta_{3a}\left[(A_{33}\omega^2 - \rho g A)\sin\omega t - B_{33}\omega\cos\omega t\right] \\ &= F_{3a}^{(1)}\sin(\omega t + \delta_1) \end{aligned} \tag{5.22}$$

where δ_1 is the phase difference between the heaving motion and the first harmonic of the force, and $F_{3a}^{(1)}$ is the amplitude of the force. Figure (5.8) shows comparisons between numerical and experimental results for the dimensionless first harmonic of the heave force $F^{(\omega)}$ and for δ_1. The dimensionless first harmonic force is defined as $F^{(\omega)} = \frac{F_{3a}^{(1)}}{\rho g B \eta_{3a}}$. The whole lines in the Figure (5.8) are linear results. The results for $F^{(\omega)}$ are actually added mass and damping forces presented

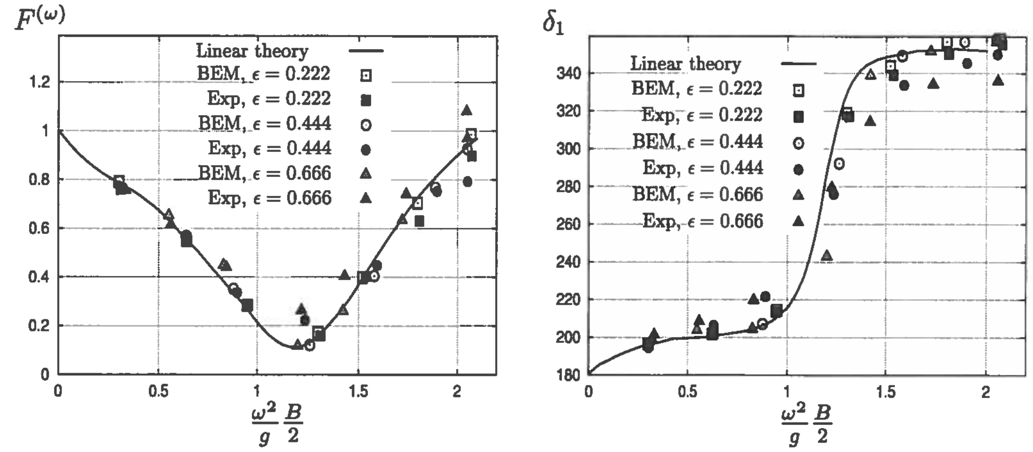

(a) First harmonic force.

(b) Phase angle of first harmonic force.

Figure 5.8: *Dimensionless first harmonic force amplitude and phase angle (in degrees). Comparisons between numerical results from the nonlinear boundary element method and experimental results by Tasai and Koterayama (1976).*

in a different manner. Since the added mass results are quite similar, the difference between numerical and experimental results is mainly due to the viscous damping. Thus, the nonlinear numerical results are closer to the linear results than the experiments. The minimum value for the linear force occurs when the added mass and restoring terms cancel each other out. In this region damping dominates $F_3^{(1)}$ and the relative difference between theory and experiments is therefore largest here. The same tendency can be observed for the phase angle, δ_1.

Figure 5.9 presents comparisons for the amplitude of the second harmonic of the force, $F_{3a}^{(2)}$, oscillating with frequency 2ω, and the amplitude of the third harmonic of the force, $F_{3a}^{(3)}$, oscillating with frequency 3ω. The dimensionless second harmonic force amplitude is defined as $F^{(2\omega)} = \frac{F_{3a}^{(2)}}{\rho g \eta_{3a}^2}$. $F_{3a}^{(3)}$ is normalized by the amplitude of the first harmonic, $F_{3a}^{(1)}$. The experimental values for the dimensionless second harmonic show a scatter, while the theoretical values follow the same trend for all three amplitudes. Particularly for high oscillation frequencies, the nonlinear boundary element method gives higher second harmonic force than the measured ones. Tasai and Koterayama (1976) also report that calculated values for the second order force on a semi-submerged circular cylinder, based on the second order perturbation method by Lee (1968), are larger than their experimental values. According to Ohkusu (1999), a possible explanation for this is that waves propagating along the model axis, *i.e.* in transverse tank direction, were observed during the experiments. These waves will reduce the energy of the outgoing waves. The transverse waves were most noticeable for high amplitudes and high frequencies. However, experiments and theory for $F_{3a}^{(2)}$ show best agreement for the highest amplitude. In general, it

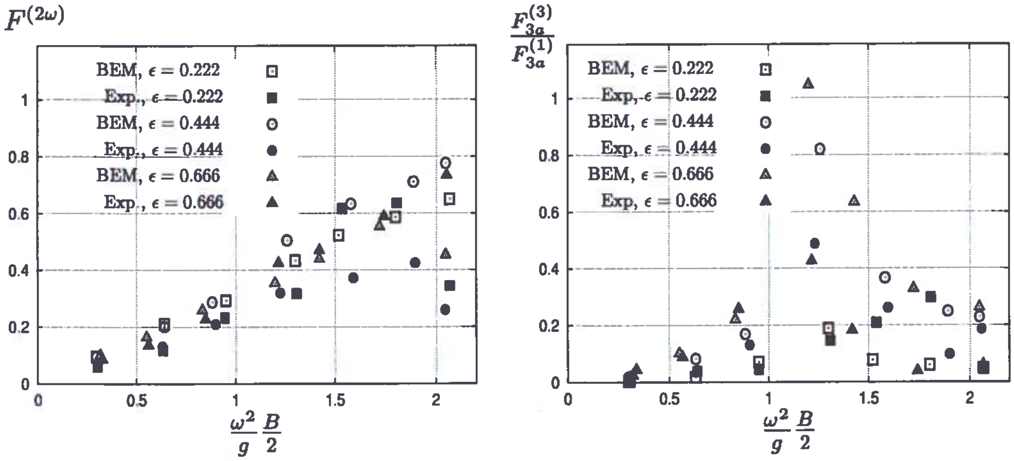

(a) Second harmonic part of the force

(b) Third harmonic part of the force

Figure 5.9: *Added mass and damping coefficients in heave for Lewis form cylinder ($B/D = 2$ and $A/(BD) = 0.989$) for different heave amplitudes. Comparisons between numerical results using a fully nonlinear boundary element method and experimental results by Tasai and Koterayama (1976).*

seems to be fair agreement between experiments and theory.

For the third harmonic part of the force, experimental and numerical results agree well for small oscillation frequencies. As the frequency increases, the results deviate, and the experimental results for the third harmonic are in some cases larger and in some cases smaller than the theoretical values. In the frequency range $\frac{\omega^2}{g}\frac{B}{2} = [1.0,\ 1.5]$ and for the largest amplitudes, Figure 5.9(b) shows much larger numerical values of $\frac{F_{3a}^{(3)}}{F_{3a}^{(1)}}$ than of the experimental ones. This is mainly caused by differences in $F_{3a}^{(1)}$ in the region where damping dominates the first harmonic (see Figure 5.8(a)), rather than small experimental values for the third harmonic. As for the damping coefficient, the experimental third harmonic part of the force gets contributions from viscous effects. Viscous effects may be discussed by using empirical drag formulae. The vertical viscous force per unit length can be written as

$$F_{3v} = \frac{1}{2}\rho C_D B|\dot{\eta}_3|\dot{\eta}_3 \tag{5.23}$$

where $\eta_3 = \eta_{3a}\sin\omega t$. Generally, the drag coefficient C_D is a function of η_{3a}, ω and t, but by assuming that C_D is time independent, expansion of F_{3v} into a Fourier series leads to a viscous force on the form

$$F_{3v} = \frac{1}{2}\rho C_D B\omega^2\eta_{3a}^2\left(\frac{8}{3\pi}\cos\omega t + \frac{8}{15\pi}\cos 3\omega t + \ldots\ldots\right) \tag{5.24}$$

Since the damping coefficient B_{33} is related to the part of the force oscillating with frequency ω, the first term in Equation (5.24) should be adopted when finding the viscous damping coefficient $B_{33}^{(v)}$. Hence, assuming that the empirical drag formula (5.23) to be valid, the viscous damping coefficient becomes

$$B_{33}^{(v)} = \frac{4}{3\pi}\rho B C_D \omega \eta_{3a} \tag{5.25}$$

and a dimensionless viscous damping coefficient can be written as

$$\overline{B_{33}^{(v)}} = \frac{B_{33}^{(v)}}{\rho A}\sqrt{\frac{B}{2g}} = \frac{2}{3\pi}\frac{C_D B \epsilon}{D\sigma}\omega\sqrt{\frac{B}{2g}} \tag{5.26}$$

Similarly, the viscous contribution to the third harmonic part of the force is given by the second term in Equation (5.24):

$$F_{3a}^{(v)} = \frac{4}{15\pi}\rho C_D B \omega^2 \eta_{3a}^2 \tag{5.27}$$

The empirical viscous force does not contribute to the force oscillating with frequency 2ω.

C_D in the previous expressions is an unknown. Keulegan and Carpenter (1958) investigated the drag force acting on bodies in unsteady flow. They obtained the drag coefficient C_D and the inertia coefficient C_M by measuring the hydrodynamic force on submerged cylinders and plates in standing waves. They concluded that the important parameter for determining C_D and C_M was the period parameter U_aT/D. Here U_a is the amplitude of the sinusoidal velocity, T is the oscillation period and D is the dimension of the cylinder or of the plate perpendicularly to the flow. This parameter is denoted as the Keulegan-Carpenter number, KC. In the present case, the Keulegan-Carpenter number becomes: $KC = \frac{\omega\eta_{3a}\frac{2\pi}{\omega}}{B} = \epsilon\pi$, which means that the KC number ranges from 0.7 to 2.1. C_D is strongly dependent on KC in this regime. Also, the Reynolds number, $Rn = \frac{\omega\eta_{3a}B}{\nu}$, can be very important for the drag coefficient. ν is the kinematic viscosity coefficient. Sarpkaya and Isaacson (1981) show how the drag coefficient varies with both KC and Rn for circular cylinders. The Reynolds number is not important if the separation points are well defined, such as at sharp corners, *i.e.* C_D is not sensitive to Rn for rectangular cylinders. The given Lewis form shaped cylinder is close to rectangular and separation will occur at the bilges. In this context it is therefore assumed that Rn is unimportant for C_D. There is a strong effect of the bilge radius, r, on the drag coefficients. Increasing the bilge radius means decreasing the drag coefficient. For the Lewis form shaped cylinder $\frac{2r}{B} = 0.22$. By using the results in Fig. 7.11 in Faltinsen (1990), one can argue that $C_D \approx 0.6$ for $KC = 10$ for this cylinder. No data is given for lower KC numbers. Faltinsen and Sortland (1987) present experimental results and theoretical results from a single vortex method for the drag coefficient of a cylinder when $KC \gtrsim 3$. The cylinder has $\frac{2r}{B} = 0.22$ and $\frac{B}{D} = 2.7$. Extrapolation of these results to lower KC numbers yields $C_D \approx 0.25$, $C_D \approx 0.4$ and $C_D \approx 0.55$ for KC numbers equal to 0.7, 1.4 and 2.1, respectively. Note that for $KC_{loc} = \frac{\pi\eta_{3a}}{r} \lesssim 2$ separation will not occur at the bilges. In the present case $KC_{loc} > 3$. Tasai and Koterayama (1976) have calculated the damping based on measurements of the amplitude of the outgoing waves. The measured damping was larger than the calculated ones. They postulated that the difference was caused by the viscous force.

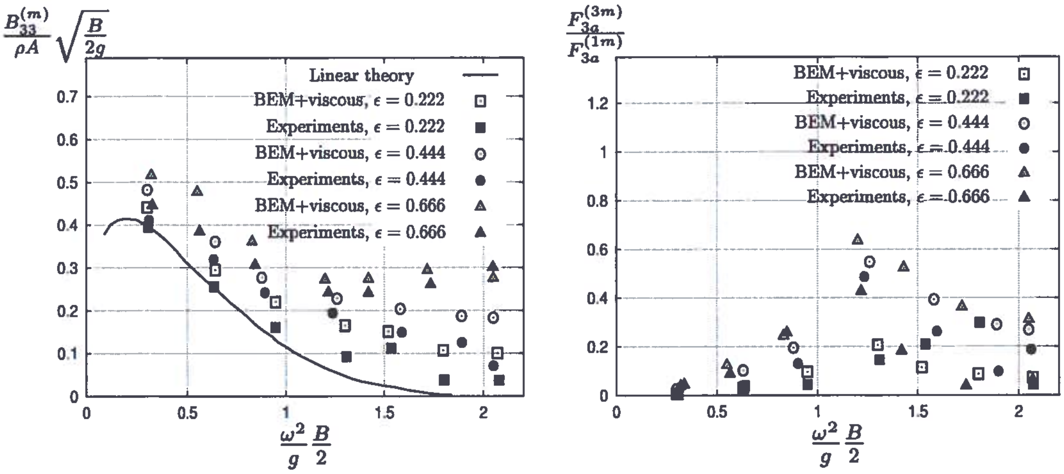

(a) Modified damping coefficient.

(b) Modified third harmonic part of the force.

Figure 5.10: *Dimensionless damping and third harmonic part of the force normalized by the first harmonic force. The damping coefficient and the first order force are modified by including viscous damping from Equation (5.25), while the third harmonic is modified by including viscous term where the amplitude is given in Equation (5.27).* $C_D = 0.6$. $F_{3a}^{(1m)}$ *and* $F_{3a}^{(3m)}$ *are modified amplitudes for the first and the third harmonic part of the force, respectively. Experiments from Tasai and Koterayama (1976).*

Based on this they determined the drag coefficient. They suggested to use $C_D = 0.6$ for all amplitudes and frequencies. The viscous damping coefficient given in Equation (5.26) may be added to the damping coefficient found by the nonlinear boundary element method. Similarly the third harmonic of the viscous force may be added to the third harmonic part of the force calculated by potential theory. Figure (5.10) shows comparison between the experiments by Tasai and Koterayama (1976) and the results found by using the nonlinear boundary element method and adding the viscous force, for the damping coefficient and the third harmonic part of the force. $C_D = 0.6$ is used.

The damping coefficient matches better with the experimental value when the viscous damping is added. The numerical values now are larger than the experimental values. This indicates that the viscous damping is overestimated. The use of a drag coefficient equal to 0.6 for all cases can be the reason. The results for $C_D = 0.6$ from Tasai and Koterayama (1976) show a scatter, but with a mean value close to 0.6. The suggested drag coefficients from extrapolation of the results by Faltinsen and Sortland (1987) would have given better agreement.

CHAPTER 6

A nonlinear boundary element method applied to deck impact

6.1 Introduction

In Section 5.3 a fully nonlinear boundary element method for solving forced oscillations was outlined. No incident waves were present, and the exact boundary conditions were satisfied on the exact boundaries. In this chapter this methodology will be extended to solve water impact underneath a platform deck due to regular incident waves.

A common method for solving nonlinear free surface problems when incident waves are present, is to use Green's second identity to establish an integral equation for the total velocity potential. In order to generate incident waves, a disturbance must be imposed on an upstream far field control surface. This can be handled by two different approaches: The upstream boundary itself can act like a physical wavemaker so that the motion of the impermeable upstream boundary generates the waves (see *e.g.* Buchner and Cozijn (1997)), or by specifying both Φ and $\frac{\partial \Phi}{\partial n}$ along the vertical upstream boundary (see *e.g.* Greco et al. (2000)). Finite water depth is required if the former approach is applied. The motion of the "wavemaker" and the specified quantities on the upstream control surface must be chosen so that the desired waves are generated. On the downstream far field boundary, a numerical beach is required to damp out the disturbances. Residuary effects may be removed by using a damping layer technique close to the downstream barrier (see *e.g.* Israeli and Orszag (1989)).

A different approach is chosen in this work. Analogously to the Wagner based method, the incident wave velocity potential and elevation are described a priori, and the perturbation velocity potential due to the presence of the body is solved. The latter approach is chosen for two reasons. First, the method described and validated in Section 5.3 may be extended to handle water impact due to specified incident waves without too many difficulties. Second and more important, if the incident waves are generated by the upstream boundary, the fluid flow contains transients similar to those generated by the start-up of a physical wavemaker. If impact due to regular incident waves is to be studied, long simulations without the body present may be necessary before steady state is reached. Differently, when the incident waves are specified beforehand, the simulation of the impact event can begin immediately.

6.2 Solution procedure

6.2.1 The boundary value problem and the solution technique

Two-dimensional potential theory is assumed. Hence, the two-dimensional Laplace equation becomes the governing equation in the fluid domain. The two-dimensional flow assumption was discussed in Section 3.2. The coordinate system used in the calculations has its origin in the mean free surface with the vertical axis pointing upwards through the center line of the body. The incident waves propagate in the direction of the positive x-axis, and their velocity potential ϕ_I is assumed known and in this work described by Stokes' second order theory. In principle, the incident waves can be expanded to any finite order, *e.g.* by the procedure presented by Bryant (1983). When using Stokes second order theory, simple formulae for ϕ_I and ζ_I are given a priori. The perturbation velocity potential due to wave impact, ϕ, is unknown and has to be determined. A dynamic free surface condition on the "exact" free surface ζ must be derived. The exact dynamic free surface condition can be written according to a Lagrangian description as

$$\frac{\mathrm{D}\Phi}{\mathrm{D}t} = \frac{1}{2}|\nabla\Phi|^2 - g\zeta \quad \text{on} \quad z = \zeta \tag{6.1}$$

where Φ is the total velocity potential and ζ is the exact free surface. Now, assuming that $\Phi = \phi + \phi_I$ and $\zeta = \zeta_D + \zeta_I$, where ϕ and ζ_D are the velocity potential and the surface elevation associated with the disturbance, respectively, Equation (6.1) can now be rewritten as

$$\frac{\mathrm{D}\phi}{\mathrm{D}t} + \frac{\mathrm{D}\phi_I}{\mathrm{D}t} = \frac{1}{2}|\nabla\phi|^2 + \frac{1}{2}|\nabla\phi_I|^2 + \nabla\phi\cdot\nabla\phi_I - g\zeta_D - g\zeta_I \quad \text{on} \quad z = \zeta \tag{6.2}$$

The incident waves satisfy Equation (6.1) with $\Phi = \phi$ on $z = \zeta_I$. By Taylor expansion of the free surface condition for ϕ_I from $z = \zeta_I$ to $z = \zeta_D + \zeta_I$, the condition can be written as

$$\frac{\mathrm{D}\phi_I}{\mathrm{D}t} = \frac{1}{2}|\nabla\phi_I|^2_{z=\zeta_I} - g\zeta_I + O(k\zeta_a)^3 \quad \text{on} \quad z = \zeta \tag{6.3}$$

Finally, the dynamic free surface condition for the perturbation potential ϕ is obtained by subtracting Equation (6.3) from Equation (6.2) and neglecting terms of $O(k\zeta_a)^3$, giving

$$\frac{\mathrm{D}\phi}{\mathrm{D}t} = \frac{1}{2}|\nabla\phi|^2 + \nabla\phi\cdot\nabla\phi_I - g\zeta_D \quad \text{on} \quad z = \zeta \tag{6.4}$$

Consistently with second order theory, terms involving ϕ_I are found by using Taylor expansion correct to the order $O(k\zeta_a)^2$.

In the Wagner based method, only the wetted part of the bottom plate was taken into account in the boundary value problem. Further, the spatial variation in the impact velocity was approximated by a linear function. Here, the exact body boundary condition according to Stokes' second order theory, is utilized, *i.e.*

$$\frac{\partial\phi}{\partial n} = -\frac{\partial\phi_I}{\partial n} = \frac{\partial\phi_I}{\partial x}n_1 + \frac{\partial\phi_I}{\partial z}n_3 \qquad \text{on } S_B \tag{6.5}$$

where S_B is the instantaneous wetted area. As for the free surface condition, Taylor expansion correctly to second order about $z = 0$ is used to find $\frac{\partial\phi_I}{\partial x}$ and $\frac{\partial\phi_I}{\partial z}$ on the body. Infinite water depth is assumed which implies that the bottom disturbance is negligible.

As usual in the mixed Eulerian-Lagrangian method for free surface flows, the problem is divided into two steps solved in sequence. These steps are described in Chapter 5 and in *e.g.* Faltinsen (1977). In the first step, the kinetic problem for the perturbation velocity potential is solved, with the specified mixed Dirichlet-Neumann boundary conditions. In the second step, the free surface conditions are integrated in time to update the geometry and the value of the perturbation velocity potential on the free surface.

The kinetic problem for ϕ is solved through Green's second identity. Equation (5.6) is satisfied on the midpoints of straight line elements. ϕ and $\frac{\partial\phi}{\partial n}$ are set to be constant over each segment. In Chapter 5, forced oscillations were solved using a fully nonlinear boundary element method. The problem was solved as a transient initial value problem. The velocity potential far away was represented by a dipole and a multipole in the origin. No incident waves were present, which means that the free surface elevation far away from the body was zero. Thus, the contribution due to Fredholm integral equation from the far field free surface could be evaluated analytically. The same procedure is used here, and it is assumed that a dipole and a multipole located in the origin represent the velocity potential on the form

$$\phi = \frac{A_1 z}{x^2 + z^2} + \frac{A_2 x z}{(x^2 + z^2)^2} \quad , \tag{6.6}$$

for $x < x_L$ and for $x > x_R$. $|x_L|$ and $|x_R|$ are large compared to the dimensions of the body. These regions are denoted as the far field. Different from before, approximations must now be performed. The analytical expressions require that $\zeta = 0$ in the far field, but in the present case $\zeta = \zeta_I$ far away from the body. No analytical solution when integrating along $\zeta = \zeta_I$ seems to be possible. Also, the far field solution should give $\phi = 0$ on the free surface, but Equation (6.6) yields $\phi = 0$ on $z = 0$. Despite these aspects, for simplicity, it is assumed that $\zeta = 0$ and Equation (6.6) are valid in the far field, and that the analytical expressions may be used. This does not matter since the relative difference in the distance from the body to $z = \zeta_I$ and $z = 0$ for a given value of x in the far field is negligible. This is analogous with moving the distribution of singularities on the exact body surface to a dipole and a multipole in the origin.

Figure 6.1 shows a sketch of the boundary value problem of interest.

The kinematic problem is solved by a time integration scheme similar to the one described in Section 5.3.1. This scheme is therefore not discussed further here, one must however note that in this case ϕ_I also contributes to the velocities on the free surface.

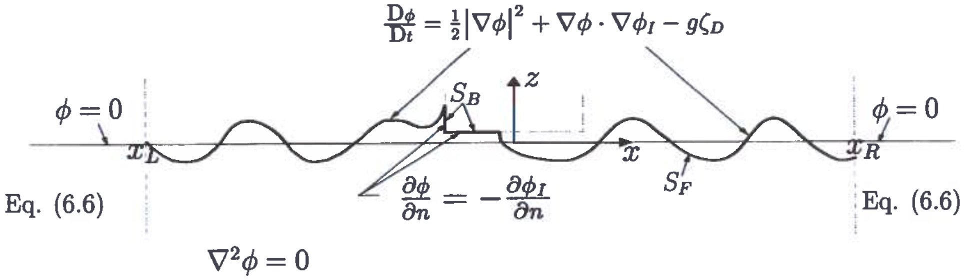

Figure 6.1: *The boundary value problem. S_B and S_F for $x_L \leq x \leq x_R$ are discretized by straight line segments. The problem is solved applying Greens' second identity. For $x \leq x_L$ and $x \geq x_R$, the perturbation velocity potential in the fluid is described by Equation (6.6). This yields $\phi = 0$ on $z = 0$.*

6.2.2 Upstream body/ free surface intersection

An important challenge is represented by the description of the flow around the front corner when the upstream body/ free surface intersection point moves from the front of the deck to the bottom plate. The upstream intersection point is denoted as I_{up}. Initially the impact causes a pile-up of water and a thin jet upstream of the body. I_{up} rises up along the front plate. After some time, gravity will pull it downwards again. Eventually I_{up} reaches the corner between the front and the bottom plate. Until this time instant, the intersection is found by extrapolation, as described in Section 5.3.1.

Figure 6.2 shows snapshots of the process when the flow turns the corner and I_{up} moves to the bottom plate. For clarity the free surface profile has been indicated by white lines. In the first picture I_{up} moves with a negative vertical velocity along the front plate. As it reaches the corner, it turns around to the bottom plate before it propagates downstream towards the aft end. In the third picture (bottom left picture) I_{up} has just turned the corner. Locally the free surface is characterized by overturning and high curvature. After a short period of time, the overturning breaks down into foam and spray and the curvature of the free surface decreases. This can also be noted from Figure 4.4. Since the phase when I_{up} turns the corner and overturning occurs has short duration, this can be handled in a simplified manner and this simplification is used in the numerical solution. When I_{up} reaches the corner, it is kept fixed at the corner until the angle between the bottom plate and the first free surface element α is greater than α_{free}. When $\alpha > \alpha_{\text{free}}$ the intersection point is once more free to move. This is indicated in the sketches in Figure 6.3. The value of α_{free} has to be properly chosen. If α_{free} is too small I_{up} tends to move too quickly when let free to move, and as a consequence the solution may break down. $\alpha_{\text{free}} = \frac{\pi}{10}$ seems to yield stable solutions. For the phase where I_{up} is kept fixed numerical instabilities/errors occur, but when it is set free to move stability is re-gained. If small free surface elements are used locally the transition phase has short duration in the numerical solution, and the solution is not sensitive to the choice of α_{free}. This will be discussed later. When I_{up} is set free the extrapolation scheme described in Section 5.3.1 is used to determine

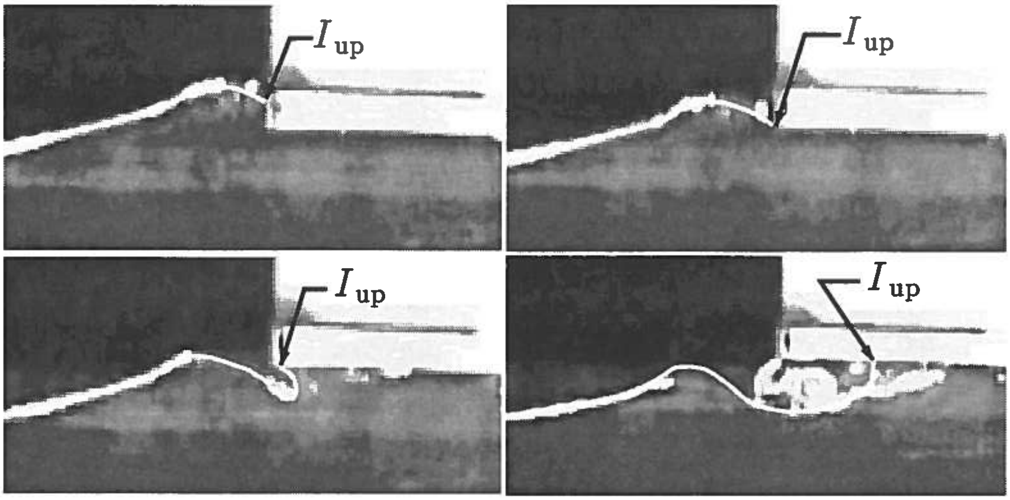

Figure 6.2: *Snapshots from the experiments of the flow around the front corner of the model.*

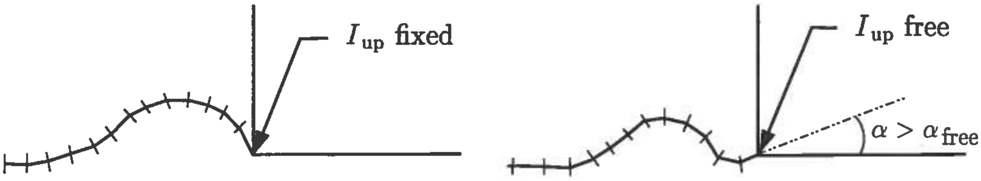

Figure 6.3: *The numerical procedure for moving the upstream body/ free surface intersection point around the front corner of the platform deck. In the left figure, the intersection point is kept fixed. In the right figure,* $\alpha > \alpha_{free}$ *and* I_{up} *can move freely.*

its position.

The way this phase is handled in the numerical solution is crude, and it was implemented as a first approximation for the flow around the front corner. It does not describe details in the flow such as the initial overturning of the free surface. But this does not seem to affect the rest of the water exit process significantly. Alternative approaches may be applied. For instance, a Kutta condition, stating that the flow leaves the front end tangentially can be imposed. In this case a new vertical free surface element at the intersection has be added. This is sketched in Figure 6.4(a). This procedure would probably ensure overturning of the free surface, but new problems may arise when tracking I_{up} when it moves downstream. It is believed that a vortex is

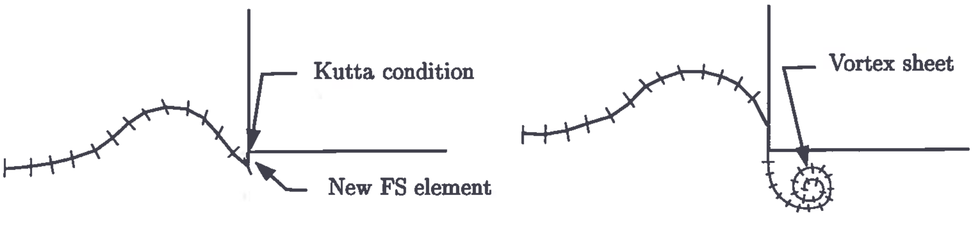

(a) Kutta condition at upstream corner (b) Include vortex sheet

Figure 6.4: *Alternative ways of handling the flow around the front corner of the deck.*

formed as the fluid flows around the corner, which locally influences the free surface profile. This is not taken into account in the present method. A possible way to handle this is to include a vortex sheet in the boundary element method, analogously to Faltinsen and Pettersen (1987). A vortex sheet is indicated in Figure 6.4(b). However, when including a vortex sheet the solution procedure becomes too complicated relative to the improvement it gives for the estimates of the variables of interest. Therefore, it was considered to be more important to describe the flow at the aft end corner properly than to include the vortex sheet in the solution.

6.2.3 Downstream body/ free surface intersection point

An accurate estimate of the downstream body/ free surface intersection point, here denoted as I_{down}, is crucial for obtaining reliable results for the impact load. During the water entry phase, *i.e.* when I_{down} propagates downstream along the bottom plate of the deck, I_{down} is found by extrapolation of the free surface onto the body. This yields a time history for the wetted area that compares well with both experiments and the Wagner based method. As mentioned previously, when I_{down} reaches the aft end corner of the deck the fluid flow leaves the deck tangentially. This can also be noted from snapshots in Figure 6.5. The pictures show a zoom up of the aft end of the body and of the local free surface. The free surface is indicated by white lines and its intersection with the body is located at the aft corner of the deck. As long as the aft end of the bottom plate is wetted, the free surface at I_{down} is horizontal for the horizontal deck. For a deck with an inclination, the free surface is also believed to leave the body tangentially. The boundary value problem that is depicted in Figure 6.1 can not describe this, and an additional physical condition must be imposed. In the case of steady lifting flow around an airfoil, the well-known Kutta condition is used to determine the circulation uniquely. The equivalent to a Kutta condition for the present problem is obtained by requiring ϕ to be continuous and the flow horizontal at I_{down}. This condition will hereafter be denoted as the Kutta condition.

The boundary value problem shown in Figure 6.1, yields a set of N+2 linear equations for

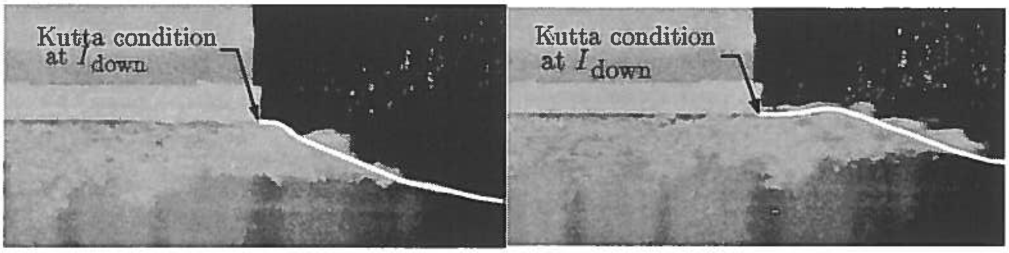

Figure 6.5: *The fluid flow at the aft end of the deck. The flow leaves the deck tangentially.*

N+2 unknowns, where the Fredholm integral equation (5.6) is satisfied on the midpoints of N body and free surface elements. However, since an additional condition stating continuous ϕ at I_{down} is formulated, Fredholm's integral equation cannot be satisfied at more than $N-1$ midpoints. It was decided to replace the body boundary condition at midpoint $N1+1$ (see Figure 6.6(a)) with the Kutta condition. The Kutta condition is written as

$$\begin{aligned} &\left(1-\frac{s_{N1+1}}{s_{N1+2}-s_{N1-1}}\right)\phi_{N1+1}+\frac{s_{N1+2}}{s_{N1+2}-s_{N1-1}}\phi_{N1+2} \\ &=\left(1-\frac{s_{N1}}{s_{N1}-s_{N1-1}}\right)\phi_{N1}+\frac{s_{N1-1}}{s_{N1}-s_{N1-1}}\phi_{N1-1} \end{aligned} \tag{6.7}$$

ϕ_i being the perturbation velocity potential at midpoint i and s_i is a curvilinear distance along the body and the free surface, so that s_i is the distance from I_{down} to midpoint i. Note that ϕ_{N1+1} and ϕ_{N1+2} are unknowns, while ϕ_{N1} and ϕ_{N1-1} are known quantities. This procedure is analogous to the one used by Faltinsen and Pettersen (1987) at the separation point for flow around blunt bodies.

When the numerical downstream body/ free surface intersection reaches the aft end of the deck, a new horizontal free surface element is introduced at I_{down}. The size of this element after one time step is determined by the total horizontal fluid velocity U_x at I_{down} so that the length equals $U_x\Delta t$. The element is allowed to grow until it has the same length as the neighboring free surface element. Thereafter the element size is kept fixed. The dynamic free surface condition is used to step the value of ϕ_{N1}. Since the midpoint gets zero vertical velocity, $\frac{\partial\phi}{\partial n}=-\frac{\partial\phi_I}{\partial n}$ is used on element number $N1$.

In the phase described above, I_{down} is kept fixed at the aft end corner of the deck. In the experiments it was noted that the downstream contact point started to propagate upstream during the final stage of the water exit phase. In the same manner as for I_{up}, a criterion must be formulated when I_{down} is to set to move freely again. In the present method this is done by monitoring the motion of element number $N1-1$. I_{down} is allowed to move freely when the slope of element number $N1-1$ and the total vertical velocity of the corresponding midpoint are both negative (see Figure 6.6(b)). In this context a challenge is represented by the evaluation of I_{down} when it propagates upstream. As a first approximation it was attempted to determine the contact point in the same manner as it was found during water entry, *i.e.* by extrapolation. This

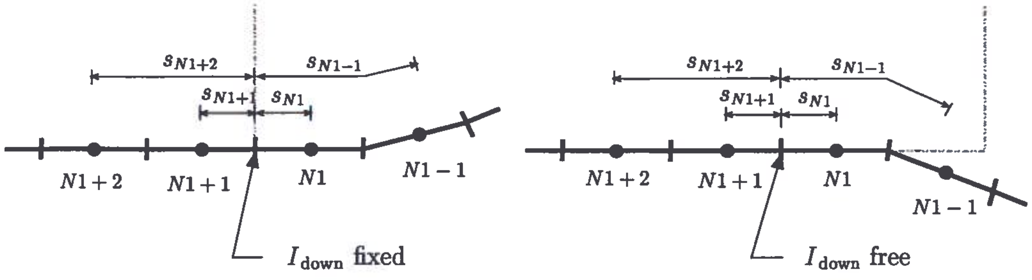

(a) Kutta condition at aft end corner.

(b) Kutta condition when I_{down} moves upstream.

Figure 6.6: *Zoom up of body surface and free surface near the downstream body/ free surface intersection point,* I_{down}. *The solid circles symbolize the midpoint of the elements where Fredholm integral equation is satisfied, and the vertical lines are element endpoints.* s_i *is the curvilinear distance from* I_{down} *to midpoint* i.

failed. When using this approach, the contact point propagates too quickly and consequently the numerical solution breaks down. A better approach must be developed.

Photos and video of the water exit phase were studied. Figure 6.7 shows four snapshots of the fluid at the aft end of the model during the final stage of the impact process. At this stage, the downstream intersection point propagates upstream. Due to the resolution of the pictures, for clarity the free surface is indicated by black lines. It can be noted that the free surface in the vicinity of I_{down} is nearly horizontal. Based on this observation, it was decided to prolong the use of the Kutta condition in Equation (6.7) with a horizontal free surface near the intersection also during this final stage, but with I_{down} free to move. The velocity of the intersection point is set to be

$$U_{I_{down}} = \frac{\partial \phi}{\partial x} + \frac{\partial \phi_I}{\partial x} \qquad \text{at } I_{\text{down}} \tag{6.8}$$

This provides a stable solution that makes it possible to simulate water exit almost until the deck becomes completely dry. Numerical instability may occur near the end of the water exit process. This may be caused by very small elements on the body compared to the near free surface elements. Therefore the simulations are stopped before the final exit. However, in this phase the force on the deck is small.

6.3 Pressure and force calculations

The main goal of these calculations is to determine the pressure and the resulting force acting on the platform deck. As mentioned in the sections concerning the Wagner based method, total force on the body may be computed by using two alternative approaches, direct pressure integration or conservation of fluid momentum. These approaches are discussed below.

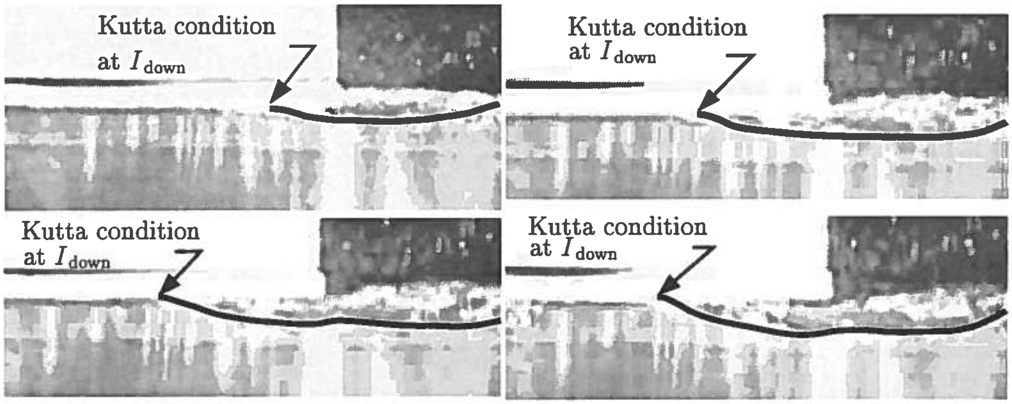

Figure 6.7: *Free surface profile near the aft body/ free surface intersection during as* I_{down} *propagates upstream during the water exit phase.*

6.3.1 Direct pressure integration

The total pressure on the body is found by letting the total velocity potential Φ satisfy Bernoulli's equation, *i.e.*

$$p - p_0 = -\rho\frac{\partial\Phi}{\partial t} - \frac{1}{2}\rho\left|\nabla\Phi\right|^2 - \rho g z \qquad \text{on } S_B \tag{6.9}$$

z being the vertical distance from the mean free surface. In Section 5.1.3 it was shown that the $\frac{\partial\Phi}{\partial t}$ term can be rewritten using a generalization of the substantial derivative. It is here assumed that the body is fixed. The pressure on an element midpoint can therefore be expressed as

$$p - p_0 = -\rho\frac{\mathrm{D}'\Phi}{\mathrm{D}'t} + \rho U_{sm}\frac{\partial\Phi}{\partial s} - \frac{1}{2}\rho\left(\frac{\partial\Phi}{\partial s}\right)^2 - \rho g z \qquad \text{on } S_B \tag{6.10}$$

where $\frac{\mathrm{D}'}{\mathrm{D}'t}$ yields the change with time when the midpoint of an element with velocity is followed, and $\frac{\partial}{\partial s}$ is the spatial derivative along the body surface. Since the body is fixed, the midpoint gets zero normal velocity. Note that $\frac{\partial\Phi}{\partial n} \equiv 0$ from the body boundary condition. To use Equation (6.10) the value of the total velocity potential at the midpoints of the body elements must be available. The perturbation velocity potential is known from the solution of the boundary value problem, while the known incident wave potential can be added to give Φ. The value of ϕ_I on the body is found by Taylor expansion about $z = 0$. Terms of $O(k\zeta_a)^3$ are neglected. It is assumed that the z-coordinates of the element midpoints are of $O(\zeta_a)$.

The procedure outlined above leads to an inconsistency. This arises when computing the velocity squared term in Equation (6.10). Due to the Taylor expansion $\frac{\partial\Phi}{\partial s}$ contains terms from ϕ_I that are of $O(k\zeta_a)^2$, thus $\left(\frac{\partial\Phi}{\partial s}\right)^2$ contains terms of higher order in $k\zeta_a$. This is not consistent with second order theory. To avoid this, one can rewrite Bernoulli's equation by applying $\Phi = \phi + \phi_I$.

The pressure can then be written on the form

$$\begin{aligned}
p - p_0 = & -\rho\frac{\mathrm{D}'\phi}{\mathrm{D}'t} - \rho\frac{\mathrm{D}'\phi_I}{\mathrm{D}'t} + \rho U_{sm}\frac{\partial\phi}{\partial s} + \rho U_{sm}\frac{\partial\phi_I}{\partial s} - \rho\frac{\partial\phi}{\partial s}\frac{\partial\phi_I}{\partial s} \\
& - \frac{1}{2}\rho\left[\left(\frac{\partial\phi}{\partial n}\right)^2 + \left(\frac{\partial\phi}{\partial s}\right)^2\right] - \frac{1}{2}\rho\left[\left(\frac{\partial\phi_I}{\partial n}\right)^2 + \left(\frac{\partial\phi_I}{\partial s}\right)^2\right] - \rho g z \\
= & -\rho\left(\frac{\mathrm{D}'\phi}{\mathrm{D}'t} + \frac{\mathrm{D}'\phi_I}{\mathrm{D}'t}\right) + \rho U_{sm}\left(\frac{\partial\phi}{\partial s} + \frac{\partial\phi_I}{\partial s}\right) - \rho\frac{\partial\phi}{\partial s}\frac{\partial\phi_I}{\partial s} \\
& - \frac{1}{2}\rho\left[\left(\frac{\partial\phi}{\partial s}\right)^2 + \left(\frac{\partial\phi_I}{\partial s}\right)^2\right] - \rho g z \qquad \text{on } S_B
\end{aligned} \tag{6.11}$$

where terms associated with ϕ_I are taken correctly to $O(k\zeta_a)^2$. The body boundary condition $\frac{\partial\phi}{\partial n} = -\frac{\partial\phi_I}{\partial n}$ is applied.

Once the pressure distribution on the body is determined, the resulting force on the platform deck can be evaluated. In the present case, only the vertical force component is considered. This can be written as

$$F_3 = -B\int\limits_{S_B}(p - p_0)n_3 dS \tag{6.12}$$

The vertical force has been computed both by using Equation (6.10) and by using (6.11) for the pressure. The alternative approaches do not give noticeable differences in the resulting force. This indicates that higher order pressure contribution from ϕ_I that arise from the velocity squared term in Bernoulli's equation, is significantly smaller than the leading order contribution.

6.3.2 Conservation of fluid momentum

Faltinsen (1977) derived a formula for the force on a body by imposing conservation of fluid momentum in a control fluid volume containing the body. For the present case the vertical force can be expressed as

$$\begin{aligned}
F_3 = & \rho\frac{\mathrm{d}}{\mathrm{d}t}\int\limits_{S_F+S_B}\phi_I n_3\,\mathrm{d}S + \rho\frac{\mathrm{d}}{\mathrm{d}t}\int\limits_{S_F+S_B}\phi n_3\,\mathrm{d}S \\
& + \rho\int\limits_{S_F} g\zeta_I n_3\,\mathrm{d}S + \rho\int\limits_{S_F} g\zeta_D n_3\,\mathrm{d}S + \rho\int\limits_{S_B} g z n_3\,\mathrm{d}S \\
& + \rho\int\limits_{S_\infty}\left[\frac{\partial\phi_I}{\partial z}\frac{\partial\phi_I}{\partial n} + \frac{\partial\phi_I}{\partial z}\frac{\partial\phi}{\partial n} + \frac{\partial\phi}{\partial z}\frac{\partial\phi_I}{\partial n} + \frac{\partial\phi}{\partial z}\frac{\partial\phi}{\partial n}\right]\mathrm{d}S
\end{aligned} \tag{6.13}$$

S_F being the instantaneous free surface inside $x_L \le x \le x_R$ and S_∞ being vertical control surfaces ranging from $z = -\infty$ to $z = 0$ at $x = x_L$ and at $x = x_R$. On S_∞, ϕ is given by Equation (6.6) and the contribution from S_∞ is evaluated analytically. Terms involving ϕ_I and ζ_I on

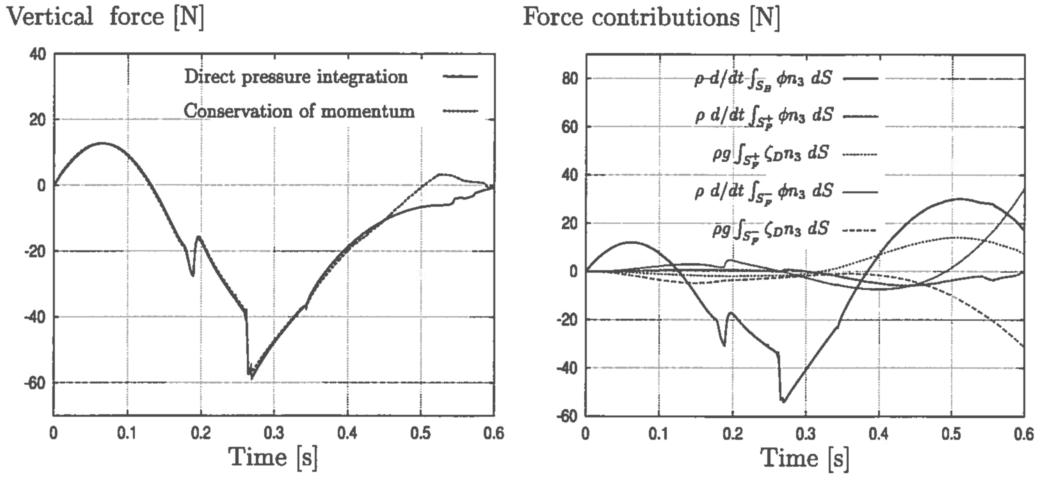

(a) Total vertical force

(b) Force contribution in cons. of mom.

Figure 6.8: *Direct pressure integration versus conservation of fluid momentum.*

S_F and S_B are also solved analytically, while the contributions from the other terms are found by numerical integration. The derivation and the full expression for F_3 are given in Appendix E.

A good check for the accuracy of the numerical code can be obtained by comparing force calculations based on direct pressure integration and by conservation of momentum. In principle, these two approaches yield the same force given that the numerical code solves the boundary value problem correctly. In Figure 6.8(a) a typical comparison is presented. The impact condition in this case is $T = 1.43$s, $\zeta_a = 0.06$m and $\eta_{ag0} = 0.06$m. The corresponding time history for the wetted length and comparisons with experiments are given below in Figure 6.24. Initially the alternative force calculations compare very well. This suggests that the integration of the surface elevation and of the velocity potential on the free surface are properly done. Furthermore, it suggests that the body/ free surface intersection points are well predicted. In addition, this indicates that the derivations for both the pressure distribution and the force expression based on conservation of momentum are correct and that the integration algorithms for the numerical evaluation of the force are satisfactory. During the final part of the water impact process, however, the two force estimates diverge. This implies that the solution of the boundary value problem at this stage has become inaccurate. In general, the force calculated by conservation of momentum is less negative than the integrated pressure and it also becomes positive during the final water exit stage. The force determined from direct pressure integration remains negative during the entire water exit process. This is similar to what is observed in the experiments. The vertical force approaches zero as the wetted area approaches zero for both methods.

In Figure 6.8(b) some of the contributions to the total force from conservation of momentum are given. Those are the contributions from ζ_D and from ϕ on the body and the free surface. S_F^- and

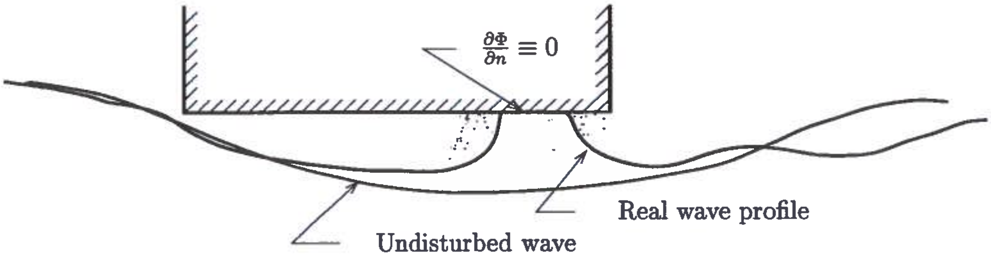

Figure 6.9: *A sketch of the exact and the undisturbed wave profile during the final stage of the water exit process.*

S_F^+ denote the upstream and the downstream free surface, respectively. By studying these force contributions it is difficult to determine the origin of the inaccuracies. From the experiments it is known that the free surface becomes highly deformed at the final part of the water exit phase, and the validity of the Kutta condition in this case becomes questionable. It is believed that the description of especially the downstream free surface is not good enough at this stage.

A different error source is associated with the theoretical modeling of the problem. The total velocity potential is divided into a perturbation velocity potential and the incident velocity potential. This leads to the body boundary condition given in Equation (6.5), where $\frac{\partial\phi_I}{\partial n}$ on S_B is found by Taylor expansion about the mean free surface. Strictly speaking, this condition is only valid on the part of the body surface that intersects with the incident wave. By imposing Equation (6.5) on the entire wetted body surface continuity of fluid mass is violated. This leads to unphysical flows which will affect the force calculations. In the case of a wedge of fluid impacting on a rigid impermeable wall, one can easily see that $\frac{\partial\phi}{\partial n} = 0$ outside the wedge's intersection with the wall is required for conservation of fluid mass. A similar argument can be used for the present case, but one can also argue that even though ϕ_I is not defined on the body outside its intersection with ζ_I, it will affect the fluid flow also in this region and $\frac{\partial\phi_I}{\partial n}$ has to taken into account in the boundary condition. Even though it is especially severe during the water exit phase for the present problem, this dilemma will also occur for other nonlinear problems when using the body boundary condition in Equation (6.5). In Figure 6.9 a sketch of the wave profile during the final part of the impact process and the undisturbed wave is presented. The exact free surface is very different from the incident wave described by ϕ_I. The body boundary condition used may not be accurate enough at this stage of the process. If the total velocity potential determined, the exact body boundary condition $\frac{\partial\Phi}{\partial n} \equiv 0$ is satisfied at each time step, and this specific problem does not occur.

These error sources need to be studied more carefully. Luckily the total force is small in the region where the inaccuracies occur. Since the resulting force obtained by direct pressure integration resembles the experiments more, this one is used in the following.

6.3.3 Three-dimensional effects

For the Wagner based method three-dimensional effects were accounted for by including a correction factor, $J(\kappa)$, for the added mass of the wetted deck area. The correction was taken from Blagovenshchensky (1962). This correction is strictly valid only when the high-frequency limit free surface condition $\phi = 0$ is applied. However, as a first approximation, a similar correction for the three-dimensional effects may be incorporated in the present case. In particular, a correction factor $J_2(\kappa)$ may be defined as

$$J_2(\kappa) = \frac{F^{(3D)}_{3,WBM}}{F^{(2D)}_{3,WBM}} \tag{6.14}$$

The subscript WBM in Equation (6.14) indicates that the impact force is calculated in the same manner as in the Wagner based method, where $\phi = 0$ on $z = 0$ is assumed valid. The wetted area used when evaluating Equation (6.14), however, is found from the boundary element method. $F^{(3D)}_{3,WBM}$ is the total vertical force from the simplified force calculations when three-dimensional effects are taken into account, while $F^{(2D)}_{3,WBM}$ is the total vertical force from the simplified force calculations without three-dimensional correction. Applying this the vertical force on the deck can be written as

$$F^{(3D)}_3 = J_2(\kappa) F_3 \tag{6.15}$$

where F_3 is taken from Equation (6.12) or from Equation (6.13).

6.4 Results and comparisons with experiments

6.4.1 Convergence tests

Convergence tests for the numerical program have been performed to examine the sensitivity of the computed results to different parameters. The latter parameters were varied one by one. First, convergence with respect to the time increment was investigated. The initial spatial grid was kept constant and the time increment Δt was varied. For each simulation Δt was kept constant during the entire simulation. The resulting force on the deck should converge as the time step is reduced. This is also the case. Figure 6.10 shows an example on a convergence test where the time increment is gradually decreased. $\overline{\Delta t}$ is the time increment normalized by the wave period. N_B is the number of body elements and N_F is the number free surface elements. An equal number of free surface elements are used upstream and downstream of the instantaneous wetted surface of the body. For a given discretization a limit exists for the maximum time increment that is applicable. If the time step is larger than this value the numerical solution will break down. In this case the surface points close to the body move too much within the time increment and thereby cause difficulties when finding the intersection points. When the time step is decreased this problem is avoided. Note that the results presented in Figure 6.10, are not necessarily optimized with respect to the other parameters.

The size of the elements on the free surface are limited by the time step. But given a small

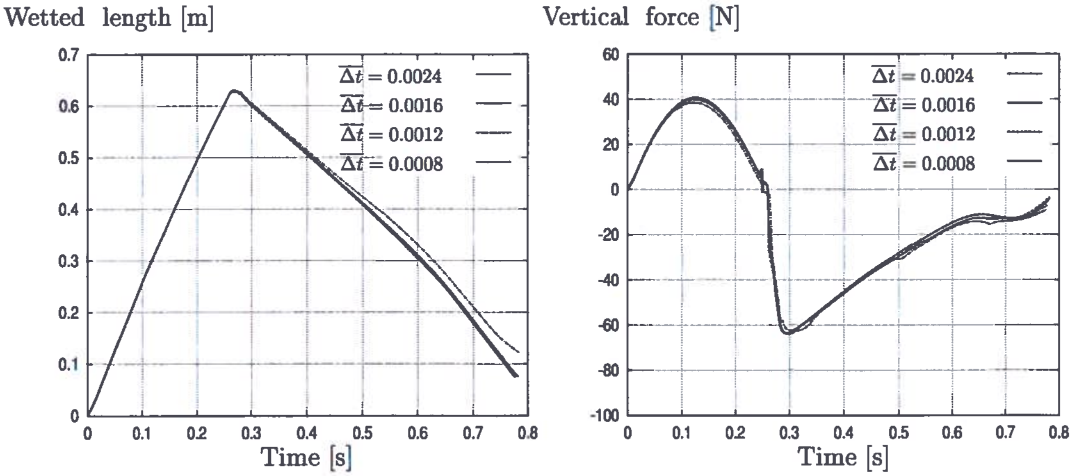

(a) Wetted length

(b) Vertical impact force

Figure 6.10: *Convergence with respect to time increment.* $T = 1.25s$, $\zeta_a = 0.05m$, $\eta_{ag0} = 0.04m$, N_B*=60 and* N_F*=200.* $\overline{\Delta t}$ *is the time increment normalized by the wave period.*

time step, the results should converge when the element size is reduced. Figure 6.11 shows an example of the sensitivity of the results when the size of the elements on free surface is varied. $\bar{l}_{min}$ is the length of the shortest free surface element normalized by the wavelength. Also in this case the results converge as the elements size is reduced. Initially the results are not very sensitive to the element length. The water entry phase is relative well predicted even when the largest free surface elements are applied. Differently, the water exit phase is sensitive to the element length. Several reasons may exists for this and a few is mentioned. Large elements in the upstream region of the body may lead to inaccuracies in the time instant when I_{up} reaches the front end corner of the deck and in the local description of the free surface profile. In addition, the flow around the front corner do not happen as smoothly as for shorter elements. Therefore, small elements should be used close to the body on the upstream side. At present a weakness exists in the computer program. If too small elements are used the solution breaks down even if the time increment is reduced. This occurs because the jet formed at the front plate becomes very thin and thus I_{up} goes towards infinity. A procedure similar to the one described by Zhao and Faltinsen (1993) for water entry of a wedge represents a possible remedy for this. Zhao and Faltinsen (1993) cut the jet when the angle between the body and the free surface at the contact point becomes small and satisfy the integral equation on the cut. This yields a stable solution. In this work case water exit is also considered, and cutting the jet may therefore not be preferable. In practice, this limitation does not seem to be a problem. The results converge with respect to element size before this becomes a problem.

It is also important that the free surface elements near I_{down} are small. Particularly for water exit. Large elements can not describe the details in the wave elevation and in the velocity po-

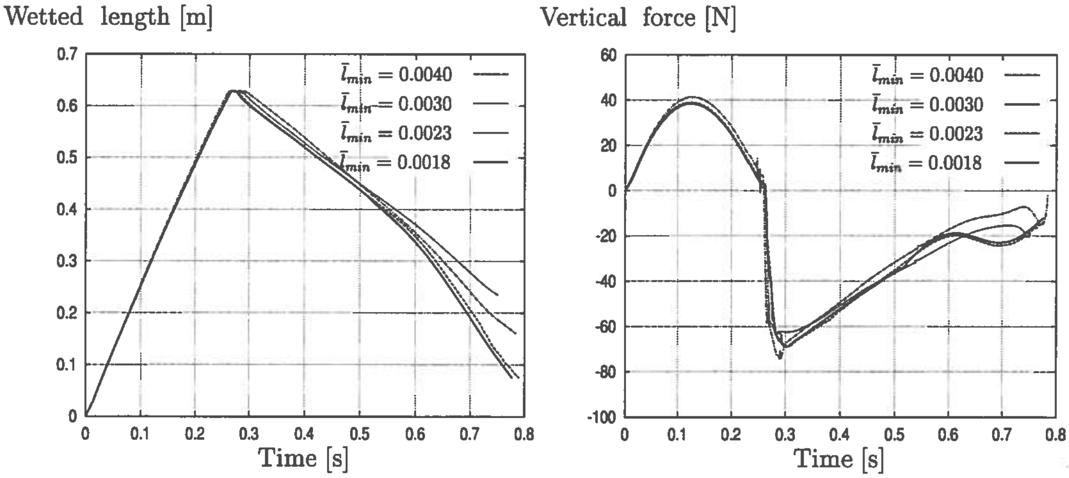

(a) Wetted length

(b) Vertical impact force

Figure 6.11: *Convergence with respect to element size on the free surface.* $T = 1.25s$, $\zeta_a = 0.05m$, $\eta_{ag0} = 0.04m$, N_B*=70 and* N_F*=180. Time increment* $\overline{\Delta t} = 0.0012$. $\bar{l}_{min}$ *is the length of the surface element next to the body on the upstream upstream side normalized by the wavelength. Here the size of the element next to the body on the downstream side is equal to* $1.33\bar{l}_{min}$.

tential on the free surface behind the body, which are important both for the time instant when I_{down} is set free and for its velocity when it propagates upstream. The most difficult part to simulate is the final stage of the water exit process. At this phase high accuracy is needed to get reliable results since the sensitivity to the element lengths on the free surface is large. However, as discussed in Section 6.3.2, the accuracy of the calculations is questionable at this stage in the simulation.

The free surface elements are increased by a constant factor away from the body. It is not shown here, but given that the free surface is long enough, the results are not very sensitive to this factor. For the calculations in this section, the element size is increased by 2.5% as their distance from the body increases, so that $l_{N_1-2} = 1.025 l_{N_1-1}$ *etc.* , where l_{N_1-2} is length of element number $N_1 - 2$ and so forth (see Figure 6.6).

In addition to the convergence in terms of the size of the free surface elements, also convergence with respect to N_F should be investigated. By doing this, the importance of the length of the discretized free surface is evaluated. Recall that the far field velocity potential is described by Equation (6.6) and that the free surface condition $\phi = 0$ on $z = 0$ is assumed. Figure 6.12(a) shows an example of a convergence test with respect to the length of S_F. N_F is gradually increased. Initially the length of the free surface is not particularly important, but during the final stage of the water exit process the results depends a little on the length of the free surface. The results converge as the length of free surface is increased.

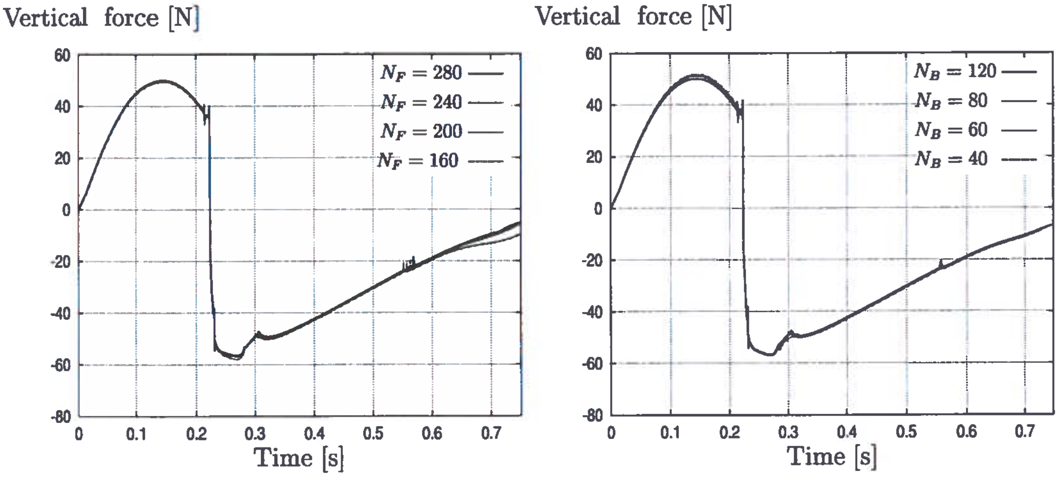

(a) Convergence with respect to N_F

(b) Convergence with respect to N_B

Figure 6.12: *Convergence with respect to number of elements.* $T = 1.43s$*,* $\zeta_a = 0.05m$*,* $\eta_{ag0} = 0.04m$*. Time increment* $\overline{\Delta t} = 0.001$*. In Figure 6.12(a)* $N_B = 80$ *and in Figure 6.12(b)* $N_F = 100$.

A convergence test with respect to the number of elements used on the body N_B is shown in Figure 6.12(b). The maximum force is weakly dependent on the element density on the body, but the results converge as N_B is increased. The ripples in the force in Figure 6.12 at $t \approx 0.22$s are caused by the introduction of the new horizontal free surface element at the aft end of the deck, while the ripples at $t \approx 0.56$s occur when I_{down} is set free to move upstream. These are numerical instabilities.

Finally, the sensitivity of the results with respect to α_{free} is checked. The results are shown in Figure 6.13. α_{free} is varied between $\frac{\pi}{30}$ and $\frac{\pi}{4}$. For $\alpha_{\text{free}} \geq \frac{\pi}{10}$, the resulting time series becomes almost independent from α_{free}. Some differences can be noted right after I_{up} is set free to move, otherwise the solution is relatively unaffected by the value of α_{free}. For the smallest value of α_{free} used in the simulation a big difference in the results compared with other values can be noted. A significant force peak can be observed in Figure 6.13(b) as the water leaves the upstream edge of deck. The reason for this force peak can be explained by studying the corresponding wetted length history shown in Figure 6.13(a). As the upstream intersection point is set to move freely for the smallest α_{free}, I_{up} propagates rapidly downstream before its velocity stabilizes. This rapid change in wetted area causes the large force peak. In general $\alpha_{\text{free}} = \frac{\pi}{10}$ seems to yield good results.

The numerical results converge well for the parameters tested. The results are most sensitive to the size of the free surface elements. However, the program can not handle the jet formed on the front side of the deck if the free surface elements become too small. As small as possible elements

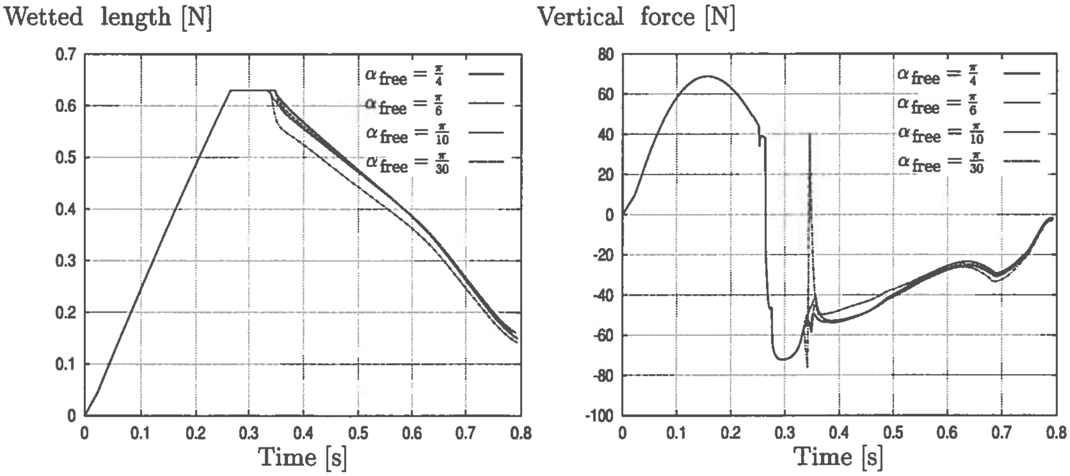

(a) Wetted length.

(b) Vertical impact force.

Figure 6.13: *Sensitivity with respect to at what angle* α_{free} *the upstream body/free surface intersection point is set free to move.* $T = 1.25s$, $\zeta_a = 0.06m$, $\eta_{ag0} = 0.04m$. *Time increment* $\Delta t = 0.0012$, $N_B = 70$ *and* $N_F = 180$.

should be applied on the free surface, and this implies a large number of free surface elements. The time step is linked to the size of the free surface elements, which yields a limitation on the maximum size of the time step applicable. The results converge when Δt is reduced. Small time steps should be used. Large N_F and small Δt results in time consuming calculations, and this must be taken into consideration when performing simulations. In general the final part of the water exit phase is the most difficult part to solve properly, but in this phase the resulting force is small.

6.4.2 Comparisons to experiments

Once the convergence of the nonlinear boundary element method is ensured, the corresponding results can be compared to the experiments described in Chapter 4. Results for the maximum vertical force on the deck F_{max} and for the largest vertical negative force F_{min} are given in Table 6.1. In Figures 6.14-6.24 comparisons for the wetted length and force histories are presented. In addition to the values obtained from the experiments and from the present method, the results obtained by the Wagner based method are included in the comparisons. To illustrate the repeatability of the experiments, two experimental realizations are included in the figures for each impact case.

The values both for F_{max} and F_{min} computed by the present method, compare in general well with the mean experimental results. In particular the estimates for F_{min} are significantly improved compared to the results obtained with the Wagner based method. Although the

Table 6.1: *Comparisons between the experimental results and numerical results from the Wagner based method and the nonlinear BEM for the maximum force, F_{max} and the minimum force F_{min} during the water entry/ water exit process.*

Case no.	Impact condition			Experiments		BEM		WBM	
	T [s]	ζ_a [m]	η_{ag0} [m]	$F_{\max}$ [N]	$F_{\min}$ [N]	$F_{\max}$ [s]	$F_{\min}$ [N]	$F_{\max}$ [N]	$F_{\min}$ [s]
1	1.11	0.05	0.04	29.3	-67.8	30.6	-76.1	26.5	-82.0
2	1.11	0.06	0.04	49.1	-83.5	55.1	-83.2	49.0	-133.0
3	1.11	0.06	0.06	7.1	-36.5	9.2	-45.9	12.9	-41.1
4	1.11	0.07	0.06	31.7	-70.2	35.1	-77.4	35.0	-100.3
5	1.25	0.05	0.04	37.0	-67.8	38.6	-68.9	30.5	-90.7
6	1.25	0.06	0.04	65.2	-70.2	68.8	-72.2	59.2	-84.5
7	1.25	0.06	0.06	11.2	-61.7	10.2	-60.8	12.1	-36.6
8	1.25	0.07	0.06	41.0	-88.7	41.3	-94.8	37.9	-110.9
9	1.43	0.05	0.038	53.0	-51.9	57.5	-55.7	47.5	-52.7
10	1.43	0.06	0.038	97.5	-54.2	99.6	-50.6	85.2	-45.2
11	1.43	0.06	0.06	14.5	-58.9	12.7	-58.7	12.3	-45.0

Wagner based method gives satisfactory results for both the magnitude and the duration of the positive water entry force peak, it yields poor estimates for the water exit phase. While the Wagner based method overestimates the magnitude of the negative force peak, the nonlinear boundary element method provides satisfactory results for $F_{\min}$. A major weakness of the WB-M is that water exit is solved by a von Karman type approach. This significantly underestimates the duration of the water exit phase, and the estimate of the total force impulse acting on the platform deck during the water impact event becomes unreliable. From Figures 6.14-6.24 it can be noted that especially for water exit the present method is superior to the Wagner based method. The duration of the water impact process is well predicted for most of the impact cases tested, and also the numerical and experimental force histories compare well for the entire water entry/ water exit process.

From the results presented it seems that the boundary element method describes powerful impacts better than gentle impacts, where η_{ag0} is close to the maximum wave elevation. Several reasons can cause this. The impact is highly dependent on the initial deck clearance and accurate measurements of η_{ag0} in the experiments are crucial for the resulting force on the deck. This is particularly important for gentle impacts. Futhermore, Stoke's second order theory may not provide good enough description of the kinematics in the vicinity of the wave crest. The steepest wave used in the experiments is characterized by $T = 1.11$s and $H = 0.14$m, which correponds to a steepness $H/\lambda = 0.073$. From Figure 3.1 one can see that the second order theory describes the free surface elevation satisfactorily for this wave. If the third order is included for $T = 1.11$s and $\zeta_a = 0.07$m, the amplitude of the second and of the third harmonics of the wave elevation for a deep water Stoke's wave, become 0.0080m and 0.0013m, respectively. Even for this wave that is relative steep, third order wave elevation is small.

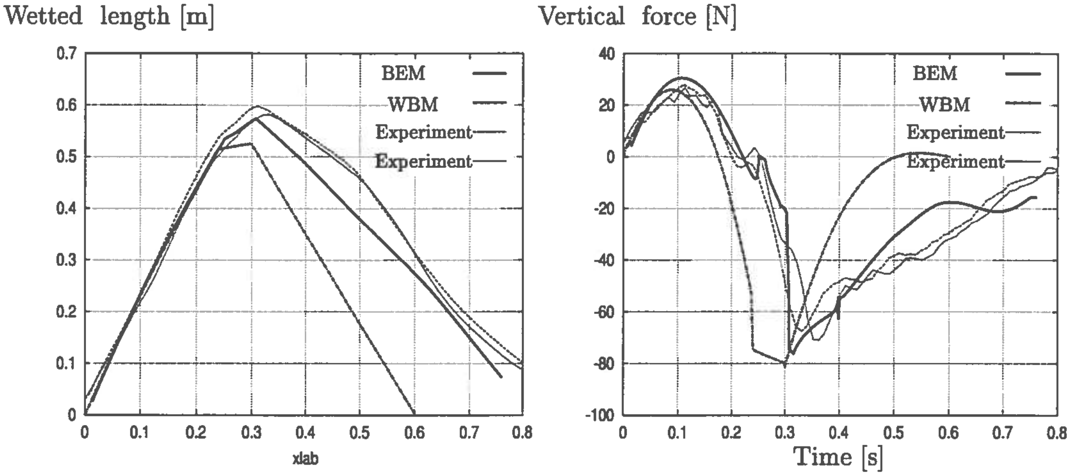

(a) Wetted length.

(b) Vertical impact force.

Figure 6.14: *Comparisons between experiments results and numerical results. Case no. 1:* $T = 1.11s$, $\zeta_a = 0.05m$ *and* $\eta_{ag0} = 0.04m$.

As a final remark, it can be said that the present method yields good results for water impact underneath a platform deck due to regular incident waves. Particularly for the water exit phase, major enhancements are made compared to the Wagner based method. This was the objective when starting out with the boundary element approach.

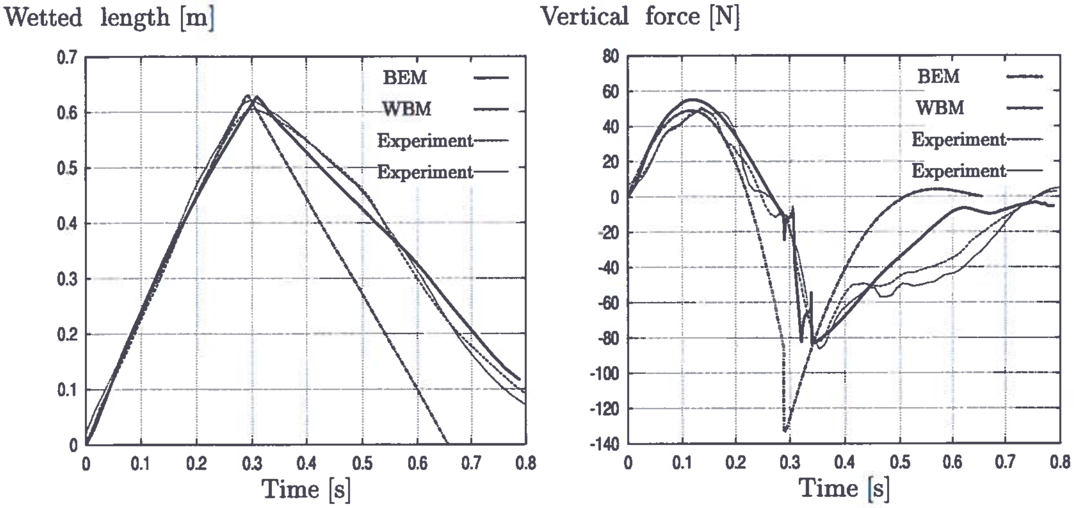

(a) Wetted length.

(b) Vertical impact force.

Figure 6.15: *Comparisons between experiments results and numerical results. Case no. 2:* $T = 1.11s$, $\zeta_a = 0.06m$ *and* $\eta_{ag0} = 0.04m$.

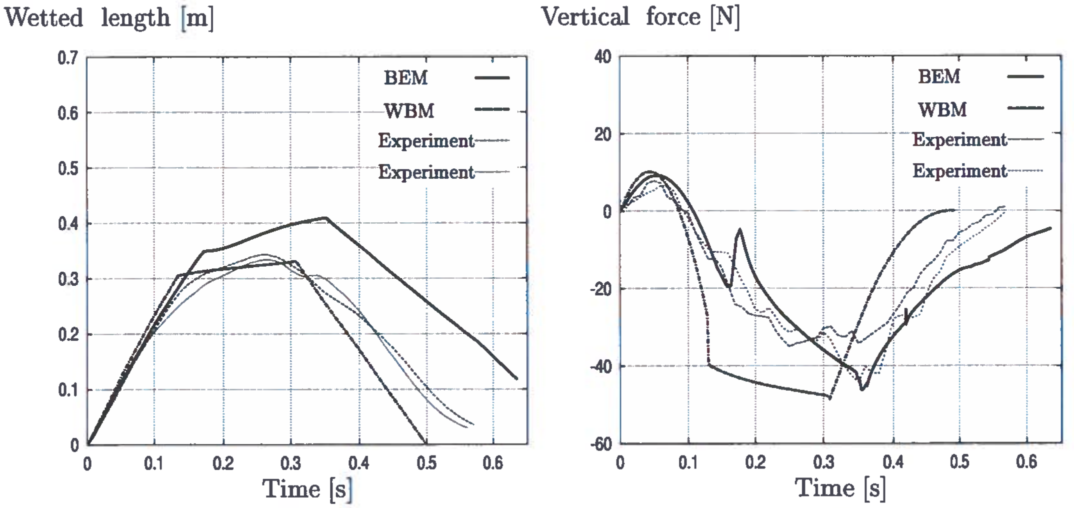

(a) Wetted length.

(b) Vertical impact force.

Figure 6.16: *Comparisons between experiments results and numerical results. Case no. 3:* $T = 1.11s$, $\zeta_a = 0.06m$ *and* $\eta_{ag0} = 0.06m$.

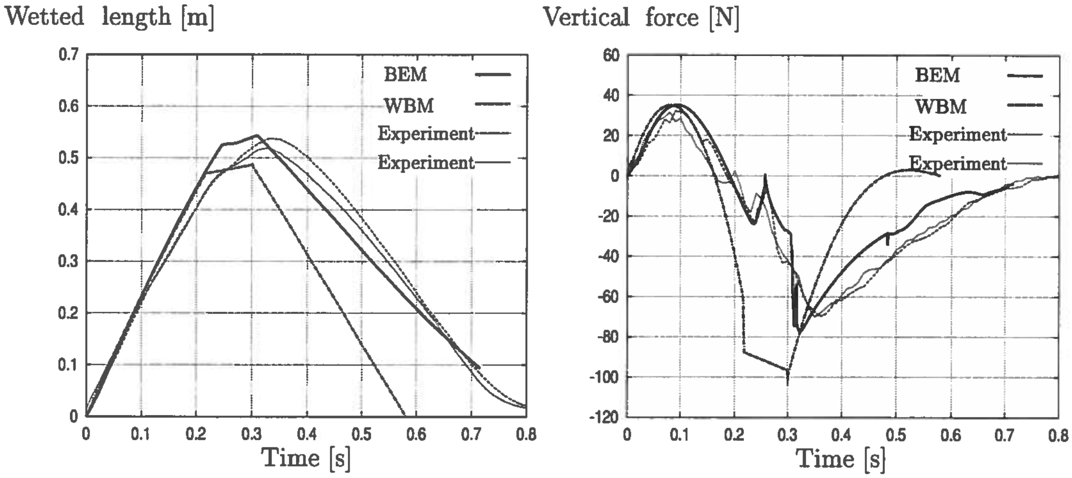

(a) Wetted length.

(b) Vertical impact force.

Figure 6.17: *Comparisons between experiments results and numerical results. Case no. 4:* $T = 1.11s$, $\zeta_a = 0.07m$ *and* $\eta_{ag0} = 0.06m$.

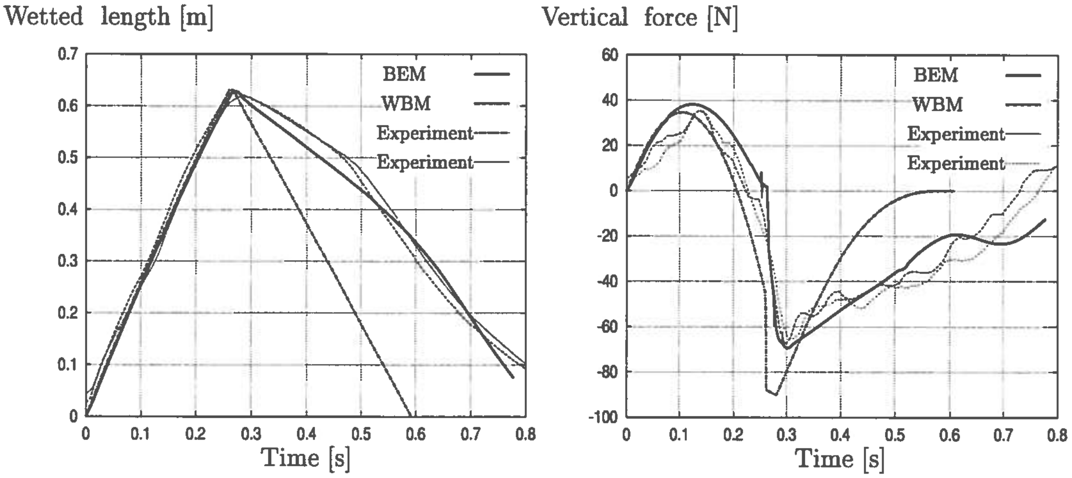

(a) Wetted length.

(b) Vertical impact force.

Figure 6.18: *Comparisons between experiments results and numerical results. Case no. 5:* $T = 1.25s$, $\zeta_a = 0.05m$ *and* $\eta_{ag0} = 0.04m$.

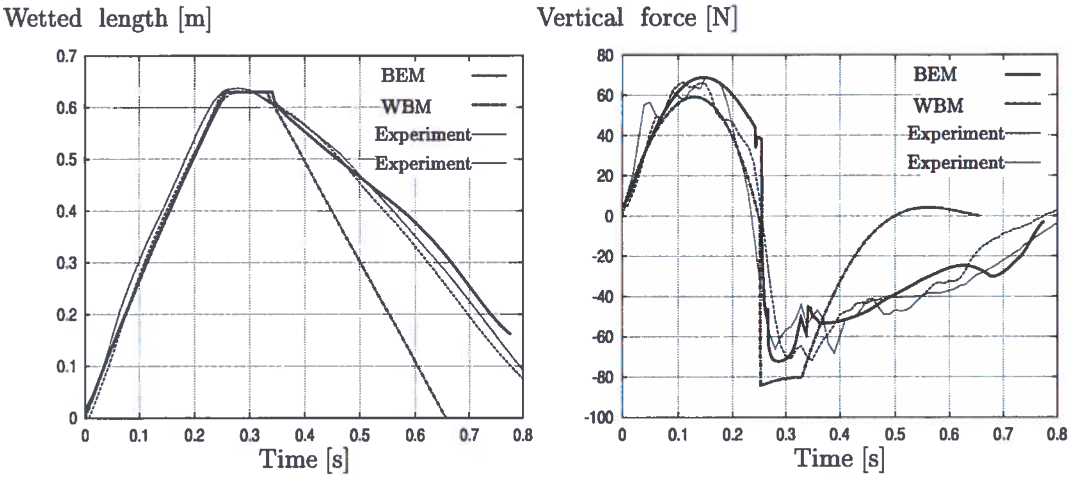

(a) Wetted length.

(b) Vertical impact force.

Figure 6.19: *Comparisons between experiments results and numerical results. Case no. 6:* $T = 1.25s$, $\zeta_a = 0.06m$ *and* $\eta_{ag0} = 0.04m$.

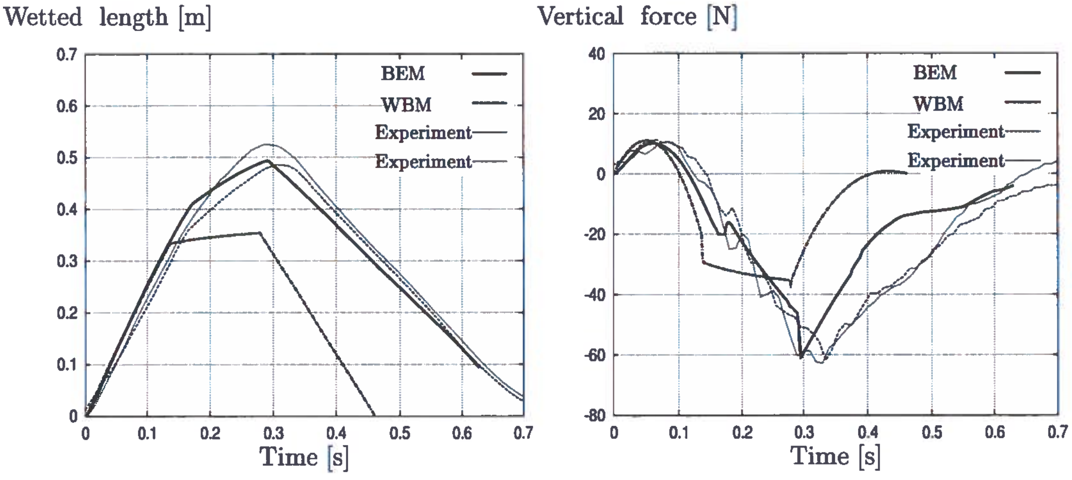

(a) Wetted length.

(b) Vertical impact force.

Figure 6.20: *Comparisons between experiments results and numerical results. Case no. 7:* $T = 1.25s$, $\zeta_a = 0.06m$ *and* $\eta_{ag0} = 0.06m$.

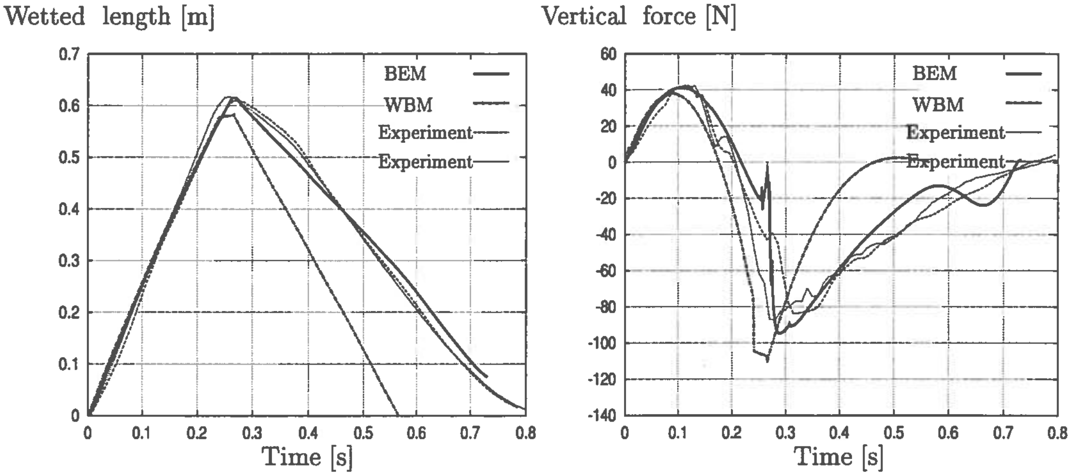

(a) Wetted length.

(b) Vertical impact force.

Figure 6.21: *Comparisons between experiments results and numerical results. Case no. 8:* $T = 1.25s$, $\zeta_a = 0.07m$ *and* $\eta_{ag0} = 0.06m$.

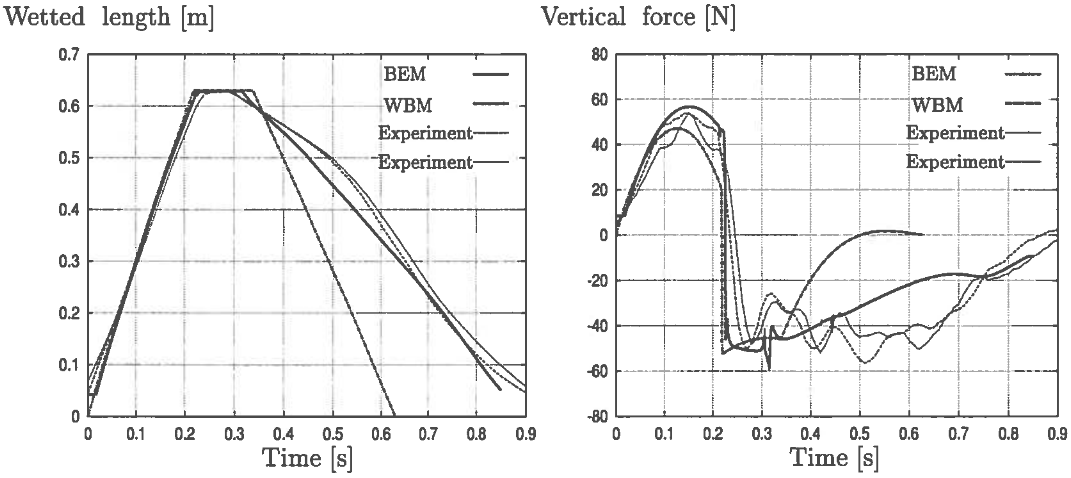

(a) Wetted length.

(b) Vertical impact force.

Figure 6.22: *Comparisons between experiments results and numerical results. Case no. 9:* $T = 1.43s$, $\zeta_a = 0.05m$ *and* $\eta_{ag0} = 0.038m$.

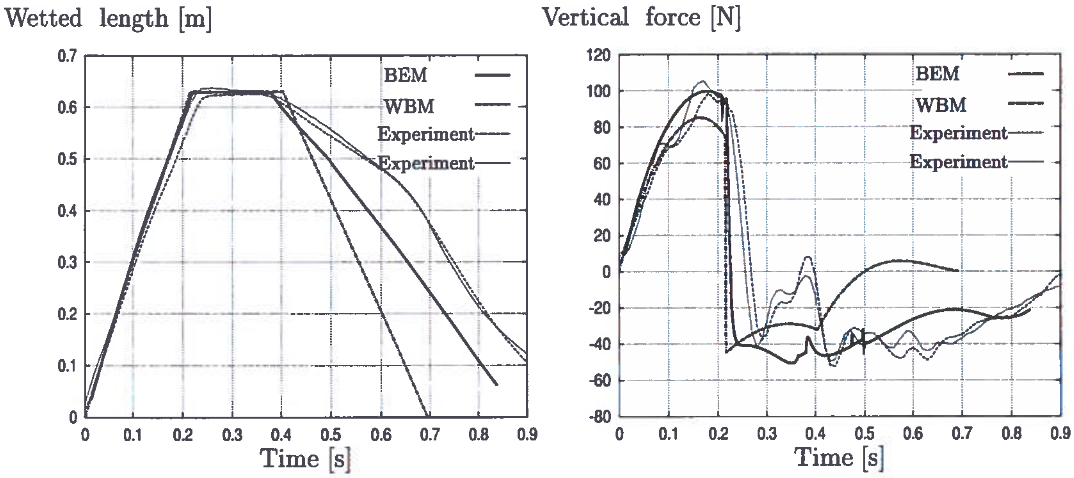

(a) Wetted length.

(b) Vertical impact force.

Figure 6.23: *Comparisons between experiments results and numerical results. Case no. 10:* $T = 1.43s$, $\zeta_a = 0.06m$ *and* $\eta_{ag0} = 0.038m$.

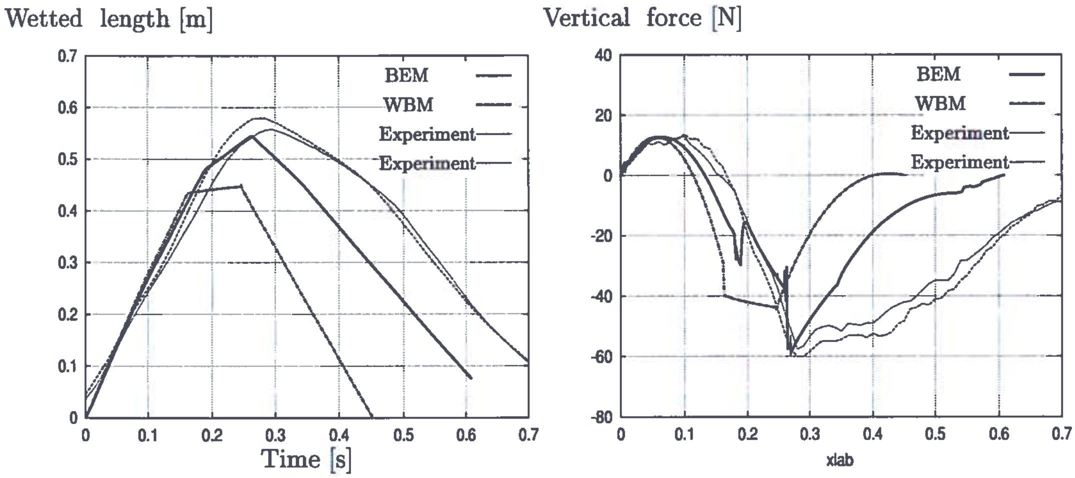

(a) Wetted length.

(b) Vertical impact force.

Figure 6.24: *Comparisons between experiments results and numerical results. Case no. 11:* $T = 1.43s$, $\zeta_a = 0.06m$ *and* $\eta_{ag0} = 0.06m$.

CHAPTER 7

Conclusions and recommendations for further research

7.1 Summary and conclusions

The main objective with this thesis has been to study the phenomenon of water impact underneath the deck of fixed or floating offshore platforms due to propagating waves. The emphasis has been on the impact loads. Two theoretical methods based on two-dimensional potential theory have been developed, namely a Wagner based method (WBM) and a nonlinear boundary element method (BEM). At present, the latter is only applicable for fixed platform decks. A rational procedure for accounting for three-dimensional effects is suggested. Second order Stokes' theory is applied to describe the incident waves, but other theories may be applied.

The Wagner based method is a generalization of the impact theory by Wagner (1932). By neglecting gravity and assuming a linear spatial distribution of the relative impact velocity, the resulting boundary value problem is solved analytically for each time step. A numerical scheme for stepping the wetted deck area in time is presented. During water exit a von Karman type approach is applied to determine the wetted area of the deck.

In the boundary element method gravity is included in the boundary value problem, and exact impact velocity is considered. The incident wave velocity potential is assumed known, and a boundary value problem for perturbation velocity potential caused by the impact, is defined. The boundary value problem is solved for each time step by applying Green's second identity. The exact boundary conditions are exerted on the exact boundaries. A Kutta condition is introduced as the fluid flow reaches the downstream end of the deck.

To validate the theories, experiments have been carried out in a wave flume. The experiments were performed in two-dimensional flow condition with a fixed horizontal deck at different vertical levels above the mean free surface. The vertical force on the deck and the wetting of the deck were the primary parameters measured. Only regular propagating waves were used in the experiments.

In general, the water entry/ water exit process due an incident wave yields a force history where the structure experience a positive slamming dominated force (upward directed) during the initial water entry phase, followed by a negative force as the wave becomes detached from the deck. The force in the latter phase is dominated by a negative added mass force due to negative vertical fluid particle accelerations in the wave crest. In addition, the Froude-Kriloff pressure and buoyancy contribute to the total force. The positive force peak, $F_{\max}$, is highly dependent on the impact condition. The force increases both with the wave amplitude and the wave period, but it is especially sensitive to the initial deck clearance. Both experiments and theory show that a small increase in the deck height may result in a considerable increase in $F_{\max}$. This is mainly due to that first impact will occur further downstream from the crest, and the impact velocity will thus be greater. Also the buoyant force will increase slightly. The magnitude of the negative force peak, $|F_{\min}|$, is less dependent on the impact condition. The peak occurs when the wetting of the deck is at its maximum. Given that the maximum wetting is the same, $|F_{\min}|$ is not much affected by a small change in the deck clearance. Except from the most violent impact events studied in the experiments, $|F_{\min}|$ is greater than $F_{\max}$ for two-dimensional flow condition. Thus, the water exit phase is important for global effects. The initial impact yields the highest average pressures, and is thus critical for local structural response in the deck. The relative reduction of the magnitude of the negative force due to three-dimensional effects is larger that the relative reduction of the positive force.

In both of the theoretical methods, the deck is assumed to be rigid. Initial studies of the importance of hydroelasticity were performed. The structural design of the lower deck of an existing floater was considered. A number of stiffened plated areas exposed to impact loads were studied by hydroelastic beam theory. For a given design wave, the local structural responses were found to behave quasi-static. Global structural response has not been studied.

Comparisons between experiments and theory have been performed for a number of impact conditions. The Wagner based method describes the water entry phase well. Both the magnitude and the duration of the positive force peak are well predicted. Also the wetted area calculated by the WBM, corresponds well with the experiments. However, the computations for the water exit phase are less satisfactory. Results for short waves are particularly poor. The WBM overestimates $|F_{\min}|$ and it underestimates the duration of the water exit, and thus the duration of the entire water impact process. This method uses a von Karman type of approach to describe water exit, but the experiments showed that the free surface becomes strongly deformed during this final stage.

In nonlinear boundary element method, the impact induced vertical force on the deck is calculated by imposing conservation of fluid momentum and by using direct pressure integration. These alternative force calculations yield similar force histories except during the final stage of water exit, where they diverge. This is caused by errors in the numerical solution and in the theoretical formulation of the boundary value problem. The force at this stage is small. The

BEM yields results that compare well with experiments for both the water entry and the water exit phase. Especially for the water exit phase the results are improved by the present method relative to the Wagner based method. More work is required in order to solve the final water exit consistently.

7.2 Suggestions for further work

At present time, the nonlinear boundary element method is only applicable for bottom-mounted platforms. However, water impact on deck is also important for floaters, and the BEM should therefore be generalized to include platform motions. This requires a procedure in which the impact induced rigid body responses are solved. Comparisons between direct pressure integration and force calculations using conservation of momentum, show that errors are introduced in the BEM towards the end of the water exit phase. The origin of these errors and possible methods to remove these errors need to be studied further.

The discussion in Section 3.2.3 showed that second order Stokes theory provides a good approximation for the exact waves for moderate wave steepnesses. For steep waves, however, a higher order theory for the incident waves is needed for accurate predictions of the wave elevation and the wave kinematics. These are crucial parameters for the impact loads. Therefore, "infinite" order waves based on *e.g.* Bryant (1983) should be implemented in the WBM and in the BEM. Further, the possibility of imposing irregular incident waves should be included. Also in this case a nonlinear theory is needed. For irregular waves impact does not necessarily occur at the front end of the deck.

It has been demonstrated in this thesis that problems arise when solving the impact problem for the perturbation velocity potential. In future development is should be considered to solve the boundary value problem for the total potential instead.

The loads computed should be used to assess the structural response caused by the impact. In co-operation with Norwegian Marine Technology Research Institute (MARINTEK), some efforts have been made to make these loads available to the nonlinear structural program USFOS (see USFOS (1999)). A model for calculation of structural response in platforms exposed to wave-in-deck loads has been implemented in the USFOS code. The pressure distribution history on the deck computed by the WBM or the BEM is used as input to USFOS. The interface file format used is the GLVIEW "vtf" format (see ViewTech (1999)). No comprehensive case studies of the structural response caused by water impact underneath platform deck have been performed. But this could give new insight of the importance of the impact induced loads. This could also become a useful tool when designing new platforms.

References

ABRAMOWITZ, M. AND I. A. STEGUN (1964). *Handbook of Mathematical Functions with Formulas, Graphs and Mathematical Tables.* New York: Dover Publications Inc.

ARMAND, J.-L. AND R. COINTE (1986). Hydrodynamic impact analysis of a cylinder. In *Proc. of 5th Offshore Mechanics and Arctic Engineering Conference*, Tokyo, Japan, pp. 250–256. ASME.

BAARHOLM, R. AND O. M. FALTINSEN (2000). Experimental and theoretical studies of wave impact on an idealized platform deck. In Y. GODA, M. IKEHATA, AND K. SUZUKI (Eds.), *Proc. Fourth Int. Conf. on Hydrodynamics*, Yokohama, Japan, pp. 181–186. ICHD2000 Local Organizing Committee.

BAARHOLM, R. AND O. M. FALTINSEN (2001). A boundary element method for solving water impact on a platform deck. In *Proc. of 20th Offshore Mechanics and Arctic Engineering Conference*, Rio de Janeiro, Brazil. ASME.

BAARHOLM, R., O. M. FALTINSEN, AND K. HERFJORD (2001). Water impact on decks of floating platforms. In *Proc. of 8th Int. Symp. on Practical Design of Ships and Other Floating Structures*, Shanghai, China. Elsevier Science Ltd.

BERGAN, P. G., P. K. LARSEN, AND E. MOLLESTAD (1986). *Svingning av konstruksjoner (in Norwegian).* Trondheim, Norway: Tapir forlag.

BLAGOVENSHCHENSKY, S. N. (1962). *Theory of Ship Motion.* New York, U.S.A: Dover.

BROUGHTON, P. AND E. HORN (1987). Ekofisk platform 2/4c: Re-analysis due to subsidence. In *Proc. Instn Civ. Engrs, Part 1*, pp. 949–979.

BRYANT, J. P. (1983). Waves and wave groups in deep water. In L. DEBNATH (Ed.), *Nonlinear Waves*, Chapter 6, pp. 100–115. Cambridge University Press.

BUCHNER, B. (1995). On the impact of green water loading of ship and offshore units design. In H. KIM AND J. W. LEE (Eds.), *Proc. 6th Int. Symp. Practical Design of Ships and Mobile Units , PRADS'95*, Seoul, South Korea, pp. 430–443. The Society of Naval Architects of Korea.

BUCHNER, B. AND J. L. COZIJN (1997). An investigation into the numerical simulation of green water. In *Proc. Int. Conference on the Behaviour of Offshore Structures, BOSS'97*, Delft, The Netherlands, pp. 949–979. Elsevier Science.

CHENEY, W. AND D. KINCAID (1985). *Numerical Mathematics and Computing.* Pacific Grove, California: Brooks / Cole Publishing Company.

COOKER, M. J. AND D. H. PEREGRINE (1995, August). Pressure-impulse theory for liquid impact problems. *J. of Fluid Mechanics 297*, 193–214.

DALTON, C. AND J. M. NASH (1976). Wave slam on horizontal members of an offshore platform. In *Proc. of 8th Offshore Technology Conference*, Dallas, Texas, pp. 769–780. Paper No. OTC 2500.

DEAN, R. G. AND R. A. DALRYMPLE (1994). *Water wave mechanics for engineers and scientists.* World Scientific: Advanced Series on Ocean Engineering - Volume 2.

DENSON, K. H. AND M. S. PRIEST (1971). Wave pressures on the underside of a horizontal platform. In *Proc. of 3rd Offshore Technology Conference*, Dallas, Texas, pp. 565–570. Paper No. OTC 1385.

DENSON, K. H. AND M. S. PRIEST (1972). Lift and drag forces due to wave action on elevated platforms. In *Proc. of 4th Offshore Technology Conference*, Dallas, Texas, pp. 495–500. Paper No. OTC 1559.

ELGHAMRY, O. (1963). Wave forces on a dock. Technical Report HEL-9-1, Hydraulic Engineering Laboratory, Institute of Engineering Research, University of California, Berkeley.

FALTINSEN, O. M. (1977). Numerical solutions of transient nonlinear free-surface motion outside or inside moving bodies. In *Proc. 2nd International Conference of Numerical Ship Hydrodynamics*, University of California, Berkeley, pp. 347–357. University Extension Publisher.

FALTINSEN, O. M. (1983, Sept.). Bow flow and added resistance of slender ships at high froude number and low wave lengths. *J. of Ship Research 27*(3), 160–171.

FALTINSEN, O. M. (1990). *Sea Loads on Ships and Offshore Structures.* Cambridge, England: Cambridge University Press.

FALTINSEN, O. M. (1997). The effect of hydroelasticity on ship slamming. *Phil. Trans. R. Soc. Lond. A. 355*, 575–591.

FALTINSEN, O. M. (1999, September). Water entry of a wedge by hydroelastic orthotropic plate theory. *J. of Ship Research 43*(3), 180–193.

FALTINSEN, O. M. (2000a). Hydroelasticity slamming. *J. of Marine Science and Technology 5*(2), 49–65. Review article.

FALTINSEN, O. M. (2000b). Water impact in ship and ocean engineering. In Y. GODA, M. IKEHATA, AND K. SUZUKI (Eds.), *Proc. Fourth Int. Conf. on Hydrodynamics*, Yokohama, Japan, pp. 17–36. ICHD2000 Local Organizing Committee. Keynote lecture.

FALTINSEN, O. M., O. KJÆRLAND, AND A. NØTTVEIT (1977). Wave impact loads and dynamic response of horizontal circular cylinders in offshore structures. In *Proc. of 9th Offshore Technology Conference*, Houston, Texas, pp. 119–126. Paper No. OTC 2741.

FALTINSEN, O. M., J. KVÅLVOLD, AND J. V. AARSNES (1997). Wave impact on a horizontal elastic plate. *J. of Marine Science and Technology* (2), 87–100.

FALTINSEN, O. M. AND B. PETTERSEN (1987). Application of a vortex tracking method to separate flow around marine structures. *J. of Fluid and Structures* (1), 217–237.

FALTINSEN, O. M. AND B. SORTLAND (1987). Slow drift eddymaking damping of a ship. *Applied Ocean Research 9*(1), 37–46.

FRENCH, J. A. (1969). Wave uplift pressures on horizontal platforms. Technical Report KH-R-19, W. M. Keck Laboratory of Hydraulics and Water Resources, California Institute of Technology.

FURUDOI, T. AND A. MUROTA (1966). Wave-induced up-lift forces acting on quay-aprons. *Technology Reports of the Osaka University 16*(734), 605–616.

GRADSHTEYN, I. S. AND I. M. RYZHIK (1994). *Table of Integrals, Series, and Products, 5th edition.* New York: Academic Press.

GRECO, M. (2001). Private communication.

GRECO, M., O. M. FALTINSEN, AND M. LANDRINI (2000, Sept.). Basic studies of water on deck. In *Proc. 23rd Symp. on Naval Hydrodynamics (ONR)*, Val de Reuil, France.

HASKIND, M. D. (1962, March). The exciting forces and wetting of ships in waves. *David Taylor Model Basin Translation* (307).

HASKIND, M. D. (1973). *Hydrodynamic Theory of Ship Motion (in Russian).* Moskow: Science.

HAUGEN, E. M. (1999). *Hydroelastic Analysis of slamming on stiffened plates with application to catamaran wetdecks.* Ph. D. thesis, Norwegian University of Science and Technology, NTNU, Trondheim, Norway.

HSE (1998). Review of wave in deck load assessment procedure. Health & Safety Executive, Offshore Technology Report - OTO 97 073.

ISRAELI, M. AND S. ORSZAG (1989). Approximation of radiation boundary conditions. *J. Computational Physics*, 115–135.

KAPLAN, P. (1987). Analysis of prediction of flat bottom slamming impact of advanced marine vehicles in waves. In *Int. Shipbuilding Progress*, pp. 44–53.

KAPLAN, P. (1992). Wave impact on offshore structures: Re-examination and new interpretations. In *Proc. of 24th Offshore Technology Conference*, Houston, Texas, pp. 79–86. Paper No. OTC 6814.

KAPLAN, P. AND A. MALAKHOFF (1978). Hard structure slamming of SES craft in waves. In *AIAA/SNAME Advanced Marine Vehicles Conference*, San Diego, California, pp. 1–10. Paper No. 78-746.

KAPLAN, P., J. J. MURRAY, AND W. C. YU (1995). Theoretical analysis of wave impact forces on platform structures. In *Proc. of 14th Offshore Mechanics and Arctic Engineering Conference*, Copenhagen, pp. 189–198. ASME.

KAPLAN, P. AND M. N. SILBERT (1976). Impact forces on platform horizontal members in the splash zone. In *Proc. of 8th Offshore Technology Conference*, Dallas, Texas, pp. 749–758. Paper No. OTC 2498.

KEULEGAN, G. H. AND L. H. CARPENTER (1958, May). Forces on cylinders and plates in an oscillating fluid. *J. of Research of the National Standards 60*(5), 423–440.

KOROBKIN, A. A. AND V. V. PUKHNACHOV (1988). Initial stage of water impact. *Ann. Rev. Fluid Mechanics 20*, 159–185.

KVÅLSVOLD, J. (1994). *Hydroelastic Modelling of Wetdeck Slamming on Multihull Vessels.* Ph. D. thesis, Norwegian Institute of Technology, NTH, Trondheim, Norway.

KVÅLVOLD, J., O. M. FALTINSEN, AND J. V. AARSNES (1995). Effects of structural elasticity on slamming against wetdecks of multihull vessels. In H. KIM AND J. W. LEE (Eds.), *Proc. 6th Int. Symp. Practical Design of Ships and Mobile Units , PRADS'95*, Seoul, South Korea, pp. 430–443. The Society of Naval Architects of Korea.

LADER, P. F. (2001). *Geometry and kinematics of breaking waves.* Ph. D. thesis, Norwegian University of Science and Technology, NTNU, Trondheim, Norway (To be published).

LAI, C. P. AND J.-J. LEE (1989, January). Interaction of finite amplitude waves with platform decks. *J. of Waterway, Port, Coastal and Ocean Engineering 115*(1), 19–39.

LAMB, H. (1932). *Hydrodynamics.* Cambridge, England: 6th ed. Cambridge University Press, Reprinted 1945 by Dover, New York.

LEE, C. M. (1968, December). The second-order theory of heaving cylinders in a free surface. *J. of Ship Research 12*(4).

LONGUET-HIGGINS, M. S. (1963). The effect of non-linearities on statistical distribution in the theory of sea waves. *J. of Fluid and Structures 17*(3), 459–480.

MACCAMY, R. C. (1961). On the heaving motion of cylinders of shallow draft. *J. of Ship Research*, 34–42.

MEI, C. C. (1989). *The Applied Dynamics of Ocean Surface Waves, Advanced Series on Ocean Engineering - Volume 1.* Singapore: World Scientific Publishing Co. Pte. Ltd.

MEYERHOFF, W. K. (1970, June). Added masses of thin rectangular plates calculated from potential theory. *J. of Ship Research*, 100–111.

MURRAY, J., P. KAPLAN, AND W. C. YU (1995). Experimental and analytical studies of wave impact forces on ekofisk platform structure. In *Proc. of 27th Offshore Technology Conference*, Houston, Texas, pp. 783–795. Paper No. OTC 7782.

NEWMAN, J. N. (1962). The exciting forces on fixed bodies in waves. *J. of Ship Research*, 10–17.

NEWMAN, J. N. (1977). *Marine Hydrodynamics.* Cambridge, USA: Massachusetts Institute of Technology, MIT.

NEWMAN, J. N., H. D. MANIAR, AND C.-H. LEE (1996). Analysis of wave effects for very large floating structures. In *Workshop on very large floating structures*, Hayama, Japan.

NEWMAN, J. N. AND P. D. SCLAVOUNOS (1988). The computation of wave loads on large offshore structures. In T. MOAN, N. JANBU, AND O. FALTINSEN (Eds.), *Proc. Int. Behaviour of Offshore Struct., (BOSS'88)*, Trondheim, Norway, pp. 605–622. Tapir Publishers.

NORSOK STANDARD (1999). Actions and action effects. Norwegian Technology Standards Institution, N-003, Rev. 1.

OHKUSU, M. (1999). Private communication.

PABST, W. (1930). Theorie des Landesstoßes von Seeflugzeugen. *Zeitschrift für Flugtechnik and Motorluftschiffahrt 21*(9), 217–228.

PRESS, W. H., B. P. FLANNERY, S. A. TEUKOLSKY, AND W. T. VETTERLING (1989). *Numerical Recipes in Fortran77.* Cambridge, England: Cambridge University Press.

RAMKEMA, C. (1978). A model law for wave impacts on coastal structures. In *Proc. of 16th Int. Conf. Coast. Engng.*, Volume 3, pp. 2308–2327. ASCE.

RIENECKER, M. M. AND J. D. FENTON (1981). A Fourier approximation method for steady water waves. *J. of Fluid Mechanics 104*, 119–137.

ROGNEBAKKE, O. F. AND O. F. FALTINSEN (2000). Damping of sloshing due to tank roof impact. In *Proc. of 15th Int. Workshop on Water Waves and Floating Bodies*, Caesarea, Israel.

SARPKAYA, T. (1978). Wave impact loads on cylinders. In *Proc. of 10th Offshore Technology Conference*, Houston, Texas, pp. 169–176. Paper No. OTC 3065.

SARPKAYA, T. AND M. ISAACSON (1981). *Mechanics of Wave Forces on Offshore Structures.* New York, U.S.A.: Van Nostrand Reinhold Company.

SCHWARTZ, L. W. (1974). Computer extension and analytic continuation of stokes' expansion for gravity waves. *J. of Fluid Mechanics 62*(3), 553–578.

SCHWARTZ, L. W. AND J. D. FENTON (1982). Strongly nonlinear waves. *Ann. Review Fluid Mechanics 14*, 39–60.

SHIH, R. W. AND K. ANASTASIOU (1989, March). Wave induced uplift pressures acting on a horizontal platform. In *Proc. of 8th Int. Conf. on Offshore Mechanics and Arctic Engineering (OMAE'89)*, The Hague, pp. 63–71.

SHIH, R. W. AND K. ANASTASIOU (1992). A laboratory study on the wave-induced vertical loading on platform decks. In *Proc. of Instn. Civ. Engrs. Wat., Marit. & Energy*, Number 96, pp. 19–33. Paper 9778.

SKJELBREIA, L. AND J. A. HENDERSON (1961). Fifth order gravity wave theory. In *Proc. 7th Conf. Coastal Eng., ACSE*, pp. 184–196.

STANSBERG, C. T. (1993). Second-order numerical reconstruction of laboratory generated random waves. In *Proc. of 12th Int. Conf. on Offshore Mechanics and Arctic Engineering (OMAE'93)*, Glasgow, U.K., pp. 143–151. ASME.

STANSBERG, C. T. (1994). Second-order effects in random wave modelling. In *Proc. of Int. Symp.: Waves- Physical and Numerical Modelling*, University of British Columbia, Vancouver, Canada, pp. 793–802.

STOKES, G. G. (1847). On the theory of oscillatory waves. *Trans. Camb. Philos. Soc. 8*, 441–455.

STOKKA, T. (1994). A third-order wave model. Cand. Scient. thesis DNV Research report no. 93-2071, University of Oslo, Det norske veritas.

TASAI, F. AND W. KOTERAYAMA (1976, November). Nonlinear hydrodynamic forces acting on cylinders heaving on the surface of a fluid. *Reports of Research Institute for Applied Mechanics XXIV*(77), 1–39.

URSELL, F. (1949). On the heaving motion of a circular cylinder on the free surface of a fluid. *Quarterly Journal of Mechanics and Applied Mathematics II*(2), 218–231.

USFOS (1999). A computer program for progressive collapse analysis of steel offshore platform structures. User's manual. Sintef.

VIEWTECH (1999). ViewTech file format. GLVIEW 6.0 reference guide. ViewTech ASA.

VON KÁRMÁN, T. (1929). The impact on seaplane floats during landing. In *National Advisory Committee for Aeronautics, NACA*, pp. 309–313. Technical Note.

VUGTS, J. H. (1968). The hydrodynamic coefficients for swaying, heaving and rolling cylinders in a free surface. Technical Report 112 S, Netherlands Ship Research Centre TNO, Technological University Delft.

WAGNER, H. (1932). Über Stoß- und Gleitvorgänge and der Oberfläche von Flüssigkeiten. *Zeitschr. für angewandte Mathematik und Mechanik 12*(4), 193–214.

WOOD, D. J. (1997). *Pressure-impulse Impact Problems and Plunging Wave Jet Impact.* Ph. D. thesis, School of Mathematics, University of Bristol, Bristol, U.K.

WOOD, D. J. AND D. H. PEREGRINE (1998). Pressure-impact theory for water wave impact on a structure with trapped air. In A. J. HERMANS (Ed.), *Proc. of 13th Int. Workshop on Water Waves and Floating Bodies*, Alphen aan den Rijn, The Netherlands, pp. 175–178.

WAMIT (2000). User's manual, versions 6.0, 6.0pc, 5.3s. Technical Report, Wamit Inc. and Department of Ocean Engineering, Massachusetts Institute of Technology.

YAMAMOTO, Y., M. MASATAKA, AND T. FUKASAWA (1980). Motion and longitudinal strength of a ship in head sea and the effects of non-linearities. *Naval Arch. and Ocean Eng., Soc. of Naval Arch. of Japan 18*, 91–100.

ZHAO, R. AND O. FALTINSEN (1992). Slamming loads on high-speed vessels. In W. D. C. NATIONAL ACADEMY PRESS (Ed.), *Proc. of the 19th ONR Conference*, Seoul, South Korea, pp. 131–147.

ZHAO, R., O. FALTINSEN, AND J. AARSNES (1996). Water entry of arbitrary two-dimensional sections with and without flow separation. In *Proc. of the 21st Symposium on Naval Hydrodynamics*, Trondheim, Norway, pp. 118–133.

ZHAO, R. AND O. M. FALTINSEN (1993). Water entry of two-dimensional bodies. *J. of Fluid Mechanics 246*, 593–612.

APPENDIX A

Importance of hydroelasticity

The structural design of the lower deck of a typical semi-submersible is studied. The characteristics of the stiffened plates between transverse and longitudinal bulkheads varies over the deck area. Six typical stiffened plate sections are chosen for this study. By using beam theory, it is checked whether the structural response due to wave impact is influenced by hydroelastic effects or if the response may be considered to be quasi-static. The bulkheads are considered infinitely stiff and the simple beams are used to analyze the stiffened plates between bulkheads. This is shown in Figure A.1 Some structural characteristics of the six different beams considered, are given in Table A.1. L is the longitudinal length of the beam and b is the breadth of the flange, and thus the spacing between the stiffeners . EI is the bending stiffness so that E is the Young's modulus and I is the area moment of inertia of the beam cross section divided by b. Seventy per cent of the flange breadth is used when calculating I. ρ is the fluid density and M_b is the structural mass per unit length of a longitudinal stiffener together with the flange divided by b.

The highest wet natural period T_{w1} is computed assuming that the beam is simply supported at both ends. This eigen period corresponds to the beam's first oscillation mode. These are found by interpolating the results given by Faltinsen et al. (1997). In reality, the beams will have a certain spring stiffness at their supports, and Faltinsen et al. (1997) show that T_{w1} decreases when this spring stiffness is increased.

Intuitively, for dynamic effects to be important, the loading of the plate and thus the wetting, should happen rapidly compared to the eigen period. Bergan et al. (1986) consider the dynamic effect from impulse loading of an one degree of freedom oscillator. Different load histories are considered. If the duration of the force impulse is longer then $0.5T_n$, where T_n is the natural period, they denote this as a long impulse. They claim that the maximum response is close to the quasi-static response for long impulses, if the load is slowly increasing. If the same conclusions are valid for the impact load on the beam, it can be said that, given that the eigen period is small compared to the duration of the loading, t_1, the structural response is close to the quasi-static one. The duration of the wetting can be associated with the duration of the loading.

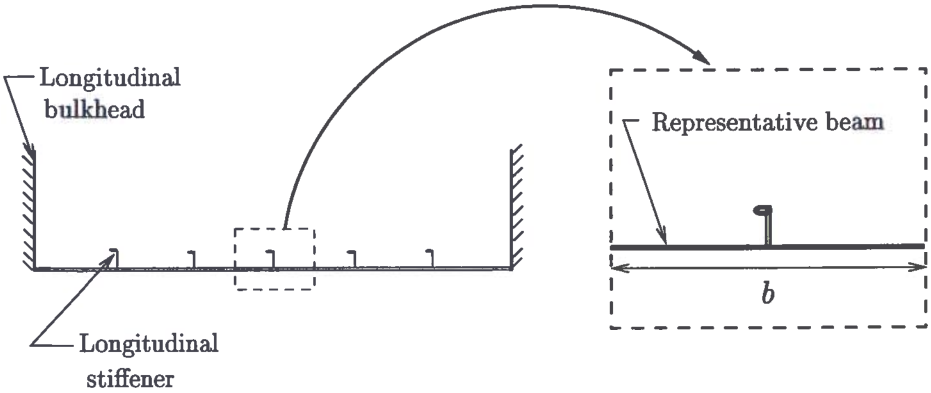

Figure A.1: *Stiffened plate between bulkheads, and the representative beam used in the beam theory.*

A realistic wave condition is chosen. Regular waves with wave height $H = 23.8$m and wave period $T = 15.0$s are assumed. This is the design wave at the Ekofisk field, Broughton and Horn (1987), and the initial deck clearance of the Ekofisk 4/2C platform $\eta_{ag0} = 13.49$m is assumed. The duration of the impulse is solved by the Wagner based method described in Chapter 3. Results for t_1/T_{w1} under these assumptions are presented in Table A.1. From these results it can be concluded that the wetting yields what Bergan et al. (1986) refer to as a long impulse on the stiffened plates. This should indicate that the structural response will be close to quasi-static.

Haugen (1999) studied the importance of hydroelasticity for stiffened plates impacting the fluid at different non-zero angles β and relative normal velocity V_R. She studied this both numerically by using beam theory and experimentally, and she presents results for a dimensionless stress amplitude at the middle of the beam are plotted as a function of a dimensionless time parameter $\sqrt{EI/\rho L^2}\tan\beta/|V_R|$. This showed that for a dimensionless spring stiffness $\frac{k_\theta L}{2EI} = 1.825$ at the beam's supports, hydroelasticity is important only for $\sqrt{EI/\rho L^2}\tan\beta/|V_R| < 0.3$. Otherwise the response behaves quasi-static. This can be given a physical interpretation. The highest wet natural period of the beam is according to the hydroelastic beam theory by Faltinsen (1997) approximately proportional to $(\rho L^5/EI)^{\frac{1}{2}}$. The wetting time of a rigid wedge is according to Wagner theory proportional to $L\tan\beta/V_R$. This means that the dimensionless time parameter is proportional to the ratio between the wetting time and the highest natural period of the beam. Here the value of this dimensionless time parameter is checked for the six beams at different impact conditions. The same incident wave as above is assumed, further the deck is assumed to be fixed. The impact velocity and the angle between the wave profile and the deck at impact β for 5 different initial air gaps are found using Stokes second order theory. From this $\sqrt{EI/\rho L^2}\tan\beta/|V_R|$ can be computed. The results are given in Table A.2.

If the conclusions given in Haugen (1999) also is valid here, it can be concluded that hydroelasicity is not important for the wave impact problem studied in this work. This is also supported

Table A.1: *Length of impulse t_1 due to impact relative to highest natural period T_{w1}. t_1 is found by using the Wagner based method. ω_{w1} is the lowest natural frequency of the beam when it is simply supported at its ends. The Young's modulus for steel is used, $E = 210 \cdot 10^9 N/m^2$.*

Beam no.	L [m]	b [m]	I [m^3]	$\frac{M_b}{\rho L}$ [−]	$\omega_{w1}\sqrt{\frac{\rho L^5}{EI}}$ [−]	T_{w1} [s]	$\frac{t_1}{T_{w1}}$ [−]
1	4.0	0.64	$4.77 \cdot 10^{-5}$	0.029	14.62	0.139	0.832
2	4.0	0.80	$4.67 \cdot 10^{-5}$	0.028	14.64	0.140	0.826
3	3.2	0.64	$4.77 \cdot 10^{-5}$	0.056	14.20	0.082	1.159
4	3.2	0.80	$5.61 \cdot 10^{-5}$	0.059	14.16	0.076	1.250
5	2.4	0.80	$9.64 \cdot 10^{-5}$	0.064	14.08	0.028	2.589
6	4.0	0.80	$6.88 \cdot 10^{-5}$	0.035	14.53	0.117	0.989

Table A.2: *Results for dimensionless time parameter for different impact conditions. $T = 15.0s$ and $H = 23.8m$ are assumed for the wave, and the water depth is set to $h = 70m$.*

Impact condition			$\sqrt{\frac{EI}{\rho L^2}}\frac{\tan\beta}{\lvert V_R\rvert}$					
η_{ag0} [m]	V_R [m/s]	$\tan\beta$	Beam 1	Beam 2	Beam 3	Beam 4	Beam 5	Beam 6
12.0	3.72	0.180	0.540	0.591	0.834	0.905	1.830	0.718
12.5	3.31	0.160	0.540	0.591	0.835	0.906	1.832	0.719
13.0	2.80	0.136	0.541	0.592	0.836	0.907	1.835	0.720
13.5	2.13	0.104	0.543	0.594	0.839	0.910	1.841	0.722
14.0	1.04	0.051	0.549	0.601	0.847	0.920	1.861	0.730

by Faltinsen (1999). He studied the importance of hydroelasticity based on orthotropic plate theory and concluded that hydroelasticity is important for $\sqrt{EI/\rho L^2}\tan\beta/|V_R| < 0.25$.

APPENDIX B

Exciting loads used in the Wagner based method

In this appendix, the full expressions for the exciting loads used in the Wagner based method are derived. These are exciting forces and moments in surge, heave and pitch due to both the impact pressure and the incident pressure. For the surge and heave the forces due to the impact pressure are given in Equations (3.35) and (3.36), while the Froude-Kriloff and hydrostatic forces are only given as an integral. In the local (x, z)-coordinate system, the incident pressure on the bottom plate can be written as

$$\begin{aligned}(p - p_0)_I(x_0, z_0 = \eta_z, t) =& \rho\zeta_a \left(g + (\eta_{ag0} + \eta_3 - (x + \tilde{x}_F - c)\eta_5)\omega^2\right) \\ & \times \cos\left(k(x + \tilde{x}_F + c - \eta_1) - \omega t\right) \\ & - \rho g(\eta_{ag0} + \eta_3 - (x + \tilde{x}_F - c)\eta_5)\end{aligned} \tag{B.1}$$

while the pressure on the front plate can be expressed as

$$\begin{aligned}(p - p_0)_I(x_0 = -\frac{L}{2} + \eta_1, z_0 = z + \eta_z, t) = & \rho\zeta_a \left(g + (z + (\eta_{ag0} + \eta_3 + \frac{L}{2}\eta_5))\omega^2\right) \\ & \times \cos\left(k(-\frac{L}{2} + \eta_1) - \omega t\right) \\ & - \rho g \left(z + \eta_{ag0} + \eta_3 + \frac{L}{2}\eta_5\right)\end{aligned} \tag{B.2}$$

By integrating the incident wave pressure over the wetted area and by applying that $dx_0 = -n_3 dx$, the incident wave forces in surge and heave are obtained as

$$\begin{aligned}
F_{1,FK} &= \frac{n_1}{n_3} B \int\limits_{\tilde{x}_F+\eta_1}^{\tilde{x}_F+2c+\eta_1} (p-p_0)_I(x_0,t)dx_0 - Gn_1 B \int\limits_{0}^{\zeta_I-\eta_z} (p-p_0)_I(\tilde{x} = -\frac{L}{2}, z, t)dz \\
&= \frac{n_1}{n_3} B \Bigg[\frac{\rho\zeta_a g}{k} \left\{ \sin\left(k(\tilde{x}_F + 2c + \eta_1) - \omega t\right) - \sin\left(k(\tilde{x}_F + \eta_1) - \omega t\right) \right\} \\
&+ \frac{\rho\zeta_a\omega^2}{k} (\eta_{ag0} + \eta_3 + \eta_1\eta_5) \left\{ \sin\left(k(\tilde{x}_F + 2c + \eta_1) - \omega t\right) - \sin\left(k(\tilde{x}_F + \eta_1) - \omega t\right) \right\} \\
&- \frac{\rho\zeta_a\omega^2\eta_5}{k^2} \left\{ \cos\left(k(\tilde{x}_F + 2c + \eta_1) - \omega t\right) - \cos\left(k(\tilde{x}_F + \eta_1) - \omega t\right) \right\} \\
&- \frac{\rho\zeta_a\omega^2\eta_5}{k^2} \left\{ k(\tilde{x}_F + 2c + \eta_1)\cos\left(k(\tilde{x}_F + 2c + \eta_1) - \omega t\right) - k(\tilde{x}_F + \eta_1)\cos\left(k(\tilde{x}_F + \eta_1) - \omega t\right) \right\} \\
&- \rho g(\eta_{ag0} + \eta_3)c + 2\rho g\eta_5(c^2 - c\tilde{x}_F) \Bigg] - n_1 BG \Bigg[\left(\rho\zeta_a \left(g + \eta_z\omega^2\right)\cos\Psi - \rho g\eta_z \right) \\
&\times \left(\zeta_a\cos\Psi + \frac{1}{2}\zeta_a^2 k\cos 2\Psi - \eta_z \right) + \frac{1}{2}\rho\left(\zeta_a\omega^2\cos\Psi - g\right)\left(\zeta_a\cos\Psi + \frac{1}{2}\zeta_a^2 k\cos 2\Psi - \eta_a \right)^2 \Bigg]
\end{aligned} \tag{B.3}$$

and

$$\begin{aligned}
F_{3,FK} &= B \int\limits_{\tilde{x}_F+\eta_1}^{\tilde{x}_F+2c+\eta_1} (p-p_0)_I(x_0,t)dx_0 \\
&= B \Bigg[\frac{\rho\zeta_a g}{k} \left\{ \sin\left(k(\tilde{x}_F + 2c + \eta_1) - \omega t\right) - \sin\left(k(\tilde{x}_F + \eta_1) - \omega t\right) \right\} \\
&+ \frac{\rho\zeta_a\omega^2}{k} (\eta_{ag0} + \eta_3 + \eta_1\eta_5) \left\{ \sin\left(k(\tilde{x}_F + 2c + \eta_1) - \omega t\right) - \sin\left(k(\tilde{x}_F + \eta_1) - \omega t\right) \right\} \\
&- \frac{\rho\zeta_a\omega^2\eta_5}{k^2} \left\{ \cos\left(k(\tilde{x}_F + 2c + \eta_1) - \omega t\right) - \cos\left(k(\tilde{x}_F + \eta_1) - \omega t\right) \right\} \\
&- \frac{\rho\zeta_a\omega^2\eta_5}{k^2} \left\{ k(\tilde{x}_F + 2c + \eta_1)\cos\left(k(\tilde{x}_F + 2c + \eta_1) - \omega t\right) - k(\tilde{x}_F + \eta_1)\cos\left(k(\tilde{x}_F + \eta_1) - \omega t\right) \right\} \\
&- \rho g(\eta_{ag0} + \eta_3)c + 2\rho g\eta_5(c^2 - c\tilde{x}_F) \Bigg]
\end{aligned} \tag{B.4}$$

respectively. Here $G = 1$ when $\zeta_I(-\frac{L}{2} + \eta_1, t) > \eta_{ag0} + \eta_3 + \frac{L}{2}\eta_5$ and zero otherwise, $\Psi = k(-\frac{L}{2} + \eta_1) - \omega t$, and $\eta_z = \eta_{ag0} + \eta_3 + \frac{L}{2}\eta_5$. The excitation forces in surge and heave then becomes:

$$F_1 = -\rho\pi c B n_1 \left(J(\kappa)\dot{c} + \frac{1}{2}\dot{J}(\kappa)c \right) V_0 - \frac{1}{2}\rho\pi c^2 B J(\kappa)\dot{V}_0 n_1 + F_{1,FK} \tag{B.5}$$

and

$$F_3 = -\rho\pi c B n_3 \left(J(\kappa)\dot{c} + \frac{1}{2}\dot{J}(\kappa)c \right) V_0 - \frac{1}{2}\rho\pi c^2 B J(\kappa)\dot{V}_0 n_3 + F_{3,FK} \tag{B.6}$$

Similar, the pitch moment can be found by integration of the pressure times the moment arm over the wetted area. The pitch moment due to the Froude-Kriloff pressure can be found as

$$\begin{aligned}
F_{5,FK} = & -B \int\limits_{\tilde{x}_F+\eta_1}^{\tilde{x}_F+2c+\eta_1} (x_0-\eta_1)(p-p_0)_I(x_0,t)dx_0 + GB \int\limits_{0}^{\zeta_I-\eta_z} (z-z_G)(p-p_I)(\tilde{x}=-\frac{L}{2},z,t)dz \\
= & \frac{\eta_1}{n_3}F_{3I} + \frac{B}{n_3}\Bigg[\frac{\rho\zeta_a g}{k^2}\big(\cos(k(\tilde{x}_F+2c+\eta_1)-\omega t) - \cos(k(\tilde{x}_F+\eta_1)-\omega t) \big) \\
& + \frac{\rho\zeta_a g}{k}\big((\tilde{x}_F+2c+\eta_1)\sin(k(\tilde{x}_F+2c+\eta_1)-\omega t) - (\tilde{x}_F+\eta_1)\sin(k(\tilde{x}_F+\eta_1)-\omega t) \big) \\
& + \frac{\rho\zeta_a\omega^2}{k^2}(\eta_{ag0}+\eta_3+\eta_1\eta_5)\big(\cos(k(\tilde{x}_F+2c+\eta_1)-\omega t) - \cos(k(\tilde{x}_F+\eta_1)-\omega t) \big) \\
& + \frac{\rho\zeta_a\omega^2}{k}(\eta_{ag0}+\eta_3+\eta_1\eta_5) \\
& \times \big((\tilde{x}_F+2c+\eta_1)\sin(k(\tilde{x}_F+2c+\eta_1)-\omega t) - (\tilde{x}_F+\eta_1)\sin(k(\tilde{x}_F+\eta_1)-\omega t) \big) \\
& - \frac{\rho\zeta_a\omega^2\eta_5}{k}\big((\tilde{x}_F+2c+\eta_1)^2\sin(k(\tilde{x}_F+2c+\eta_1)-\omega t) - (\tilde{x}_F+\eta_1)^2\sin(k(\tilde{x}_F+\eta_1)-\omega t) \big) \\
& + \frac{2\rho\zeta_a\omega^2\eta_5}{k^3}\big(\sin(k(\tilde{x}_F+2c+\eta_1)-\omega t) - \sin(k(\tilde{x}_F+\eta_1)-\omega t) \big) \\
& - \frac{2\rho\zeta_a\omega^2\eta_5}{k^2}\big((\tilde{x}_F+2c+\eta_1)\cos(k(\tilde{x}_F+2c+\eta_1)-\omega t) - (\tilde{x}_F+\eta_1)\cos(k(\tilde{x}_F+\eta_1)-\omega t) \big) \\
& - 2\rho g(\eta_{ag0}+\eta_3+\eta_1\eta_5)\left(c^2+c(\tilde{x}_F+\eta_1)\right) + \frac{1}{3}\rho g\eta_5\left((\tilde{x}_F+2c+\eta_1)^3-(\tilde{x}_F+\eta_1)^3\right) \Bigg] \\
& - GBz_G\Bigg[\left(\rho\zeta_a\left(g+\eta_z\omega^2\right)\cos\Psi - \rho g\eta_z\right)\left(\zeta_a\cos\Psi + \frac{1}{2}\zeta_a^2 k\cos 2\Psi - \eta_z\right) \\
& + \frac{1}{2}\rho\left(\zeta_a w^2\cos\Psi - g\right)\left(\zeta_a\cos\Psi + \frac{1}{2}\zeta_a^2 k\cos 2\Psi - \eta_z\right)^2 \Bigg] \\
& + GB\Bigg[\frac{1}{2}\left(\rho\zeta_a\left(g+\eta_z\omega^2\right)\cos\Psi - \rho g\eta_z\right)\left(\zeta_a\cos\Psi + \frac{1}{2}\zeta_a^2 k\cos 2\Psi - \eta_z\right)^2 \\
& + \frac{1}{3}\rho\left(\zeta_a w^2\cos\Psi - g\right)\left(\zeta_a\cos\Psi + \frac{1}{2}\zeta_a^2 k\cos 2\Psi - \eta_z\right)^3 \Bigg]
\end{aligned} \tag{B.7}$$

z_G is the z-coordinate of the center of gravity. In addition, the pitch moment will get a contribution from the water impact pressure. It was shown in Chapter 2, that even though the impact pressure from the outer solution is singular at $|x| = c$, the integrated force is finite. The same is the case for the pitch moment, and thus only the outer pressure is considered. The pitch moment due to the impact can be written as

$$\begin{aligned} F_{5,D} &= -B \int_{-c}^{c} (x + \tilde{x}_F + c)(p_{\text{outer}} - p_0)(x,t)dx \\ &= -\rho B \Big[\pi V_0 \dot{c} c (\tilde{x}_F + c) + \frac{\pi}{2} V_0 (-\dot{c} + \dot{a}) c^2 + \frac{\pi}{4} V_1 c^3 \dot{c} + \frac{\pi}{2} \frac{\partial V_0}{\partial t} (\tilde{x}_F + c) c^2 + \frac{\pi}{16} \frac{\partial V_1}{\partial t} c^4 \Big] \end{aligned} \tag{B.8}$$

where $(p_{\text{outer}} - p_0)$ is given in Equation (2.24). The total exciting pitch moment can be written as

$$F_5 = F_{5,FK} + F_{5,D} \tag{B.9}$$

Note that even if the $V_1 x$-term in the impact velocity, due to anti-symmetry, does not contribute to the force on the deck, it contributes to the pitch moment.

APPENDIX C

Water impact on a floating platform

In section 3.5 a procedure for solving water impact underneath a fixed horizontal deck using the Wagner based method was outlined. Here a solution procedure for the more general case of a impact underneath the deck of a floater is suggested. The problem can be split into sub-problems: estimation of the time instant of impact, evaluation of the relative impact velocity and prediction of the impact loads and of the resulting rigid body responses. Below, these sub-problems are discussed and a numerical scheme for the time integration of the problem is outlined. A case study using this procedure is presented in Baarholm et al. (2001).

C.1 Time instant for first impact

Before impact occurs, the platform only experiences wave induced motions. If linear theory is assumed for the wave induced rigid body motions, the platform oscillates in six degrees of freedom with frequency equal to the wave frequency ω, and the transfer functions for the motion can be used to simulate the total platform motion. The complex transfer function $H_{\eta_i\zeta}(\omega)$ contains information about both the motion amplitude and the phase difference between the motion and the incident wave. This can be expressed as

$$\eta_{ia} = \zeta_{Ia}\left|\sqrt{\{\Re(H_{\eta_i\zeta}(\omega))\}^2 + \{\Im(H_{\eta_i\zeta}(\omega))\}^2}\right| \quad \text{and} \quad \theta_i = \tan^{-1}\left(\frac{\Im(H_{\eta_i\zeta}(\omega))}{\Re(H_{\eta_i\zeta}(\omega))}\right) \tag{C.1}$$

where η_{ia} is the motion amplitude of the i-th degree of freedom and θ_i is the corresponding phase angle. $\Re(\cdot)$ and $\Im(\cdot)$ denote the real and the imaginary part, respectively. The motion is then defined as

$$\eta_{iw} = \eta_{ia}\cos(\omega t - \theta_i) \qquad i = 1, \ldots, 6 \tag{C.2}$$

The transfer functions for the platform motion must be solved a priori by a wave-body interaction computer program.

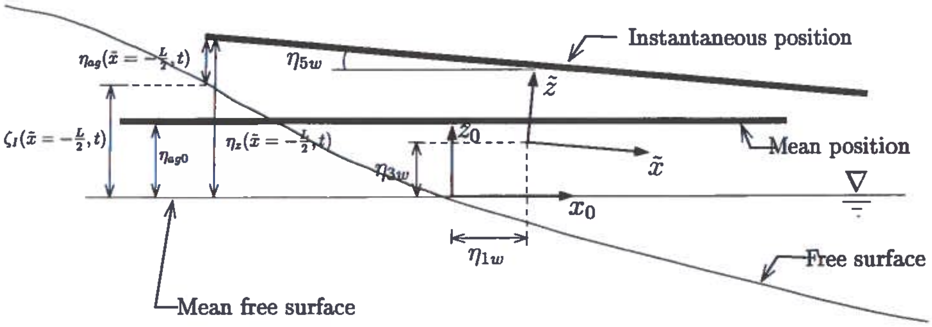

Figure C.1: *Air gap at upstream end of deck before impact occurs. The platform experience wave induced motions only.*

In the case of long-crested head sea and a submerged body volume with lateral symmetry only three modes are excited. These are surge, heave and pitch. This is assumed in the following discussion. To find the time instant when first impact occurs, the instantaneous air gap $\eta_{ag}(\tilde{x}, t)$ must be simulated. The fluid reaches first the deck level at the upstream end of the deck, *i.e.* at $\tilde{x} = -\frac{L}{2}$, where L is the length of the deck. The time instant of impact, t_0 can be found from

$$\begin{aligned} &\eta_{ag0} + \eta_{3a}\cos(\omega t_0 - \theta_3) + \frac{L}{2}\eta_{5a}\cos(\omega t_0 - \theta_5) \\ &- \zeta_a \cos\left(k\left[-\frac{L}{2} - \eta_{1a}\cos(\omega t_0 - \theta_1)\right] - \omega t_0\right) \\ &- \frac{1}{2}\zeta_a^2 k \cos\left(2\left(k\left[-\frac{L}{2} - \eta_{1a}\cos(\omega t_0 - \theta_1)\right] - \omega t_0\right)\right) = 0 \end{aligned} \tag{C.3}$$

by using *e.g.* a Newton-Raphson scheme.

C.2 Impact induced motion

Once the wave has reached the deck, the fluid impact will induce forces and moments on the deck. For head sea, the impact will induce surge, heave and pitch loads as shown in Equations (3.35), (3.36) and (3.38). These loads lead to additional rigid body responses for the platform which must be taken into account when solving the boundary value problem.

First, assume that the impact loads F_1, F_3 and F_5 are known. These loads are associated with the high frequency limit assumption. It is assumed that the total motion of the platform can be written as $\boldsymbol{\eta} = \boldsymbol{\eta}_w + \boldsymbol{\eta}_s$ where $\boldsymbol{\eta}_w$ is the wave induced motion and $\boldsymbol{\eta}_s$ is the impact, or slamming induced motion. Here regular waves and linear response are assumed, and $\boldsymbol{\eta}_w$ is given by (C.2). The impact induced motion can be written as

$$\boldsymbol{\eta}_s = \left[\eta_{1s}, \eta_{3s}, \eta_{5s}\right]^T \tag{C.4}$$

Similarly, the rigid body velocity and acceleration are divided into

$$\dot{\boldsymbol{\eta}} = \dot{\boldsymbol{\eta}}_w + \dot{\boldsymbol{\eta}}_s \quad \text{and} \quad \ddot{\boldsymbol{\eta}} = \ddot{\boldsymbol{\eta}}_w + \ddot{\boldsymbol{\eta}}_s \tag{C.5}$$

The wave induced rigid body responses are here calculated from the transfer functions, while the slamming induced rigid body responses are found by solving the equation of motion

$$(\mathbf{M} + \mathbf{A})\,\ddot{\boldsymbol{\eta}}_s + \mathbf{B}\dot{\boldsymbol{\eta}}_s + \mathbf{C}\boldsymbol{\eta}_s = \mathbf{F}_{\text{exc}} \tag{C.6}$$

where

$\mathbf{M}$	inertia matrix of the platform
$\mathbf{A}$	added mass matrix of the platform
$\mathbf{B}$	damping matrix of the platform
$\mathbf{C}$	restoring matrix of the platform
$\mathbf{F}_{\text{exc}}$	excitation force vector due to impact

Asumptotic values for the added mass and the damping coefficients for $\omega \to \infty$ for the submerged volume must be evaluated beforehand by using *e.g.* WAMIT (see *e.g.* Newman and Sclavounos (1988) and WAMIT (2000)). In addition the added masses due to wetted part of the deck have to be found. $A_{33}^{(\infty)}$ for the wetted deck is given by Equation (2.48), while the added mass in pitch may be approximated

$$A_{55}^{(\infty)} = (\tilde{x}_F + c)^2\, A_{33}^{(\infty)} \tag{C.7}$$

If the platform is freely floating the restoring forces follow from the hydrostatic equilibrium. For a moored platform additional restoring forces exist, but mooring lines have a small effect for wave induced motions, Faltinsen (1990). The excitation vector contains the impact induced loads acting on the deck,

$$\mathbf{F}_{\text{exc}} = \left[F_1, F_3, F_5\right]^T. \tag{C.8}$$

C.3 The relative impact velocity

To solve the equation of motion the excitation vector due to the impact must first be determined. The force expressions in Section 3.4 are based on the assumption that the relative impact velocity has a linear spatial distribution across the wetted length of the deck. While only the wave kinematics contributes in the fixed deck situation, for a floater also the rigid body responses contribute to the relative impact velocity. The assumption of linearly distributed impact velocity from the wave kinematics is a simplification, differently the contribution from rigid body responses can be exactly described by a linear function.

Assume that $\boldsymbol{\eta} = \boldsymbol{\eta}_w + \boldsymbol{\eta}_s$, $c(t)$ and $\tilde{x}_F$ are known. The "exact" relative velocity between the fluid and the deck can be written as

$$\begin{aligned} V_{R,exact}(x,t) = {} & \zeta_a \omega \left(1 + k(\eta_{ag0} + \eta_3 - (\tilde{x}_F + c + x)\eta_5)\right) \\ & \times \left[\sin\left(k\left(x + \tilde{x}_F + c + \eta_1\right) - \omega t\right) + \eta_5 \cos\left(k\left(x + \tilde{x}_F + c + \eta_1\right) - \omega t\right) \right] \\ & - \left[\left(\dot{\eta}_3 - (\dot{\tilde{x}}_F + \dot{c})\eta_5 - (\tilde{x}_F + c)\dot{\eta}_5\right) + \left(\dot{\eta}_1 + z_G \eta_5\right)\eta_5\right] + x\dot{\eta}_5 \end{aligned} \tag{C.9}$$

where z_G is the vertical distance from the deck to the center of gravity of the body. To obtain an impact velocity that has a linear variation along the wetted length, approximations must be performed. If the approximation denoted as alternative 2 in Section 3.2.4 is used, the relative impact velocity becomes $V_R(x,t) = V_0(t) + V_1(t)x$, where

$$\begin{aligned} V_0(t) = {} & \zeta_a \omega \left(1 + k(\eta_{ag0} + \eta_3 - (\tilde{x}_F + c)\eta_5)\right) \\ & \times \Big[\sin\left(k\left(\tilde{x}_F + c + \eta_1\right) - \omega t\right) + \eta_5 \cos\left(k\left(\tilde{x}_F + c + \eta_1\right) - \omega t\right) \Big] \\ & - \left[\left(\dot{\eta}_3 - (\dot{\tilde{x}}_F + \dot{c})\eta_5 - (\tilde{x}_F + c)\dot{\eta}_5 \right) + \left(\dot{\eta}_1 + z_G \eta_5 \right) \eta_5 \right] \end{aligned} \tag{C.10}$$

and

$$\begin{aligned} V_1(t) = {} & \frac{1}{c} \Big\{ \zeta_a \omega \left(1 + k(\eta_{ag0} + \eta_3 - (\tilde{x}_F + 2c)\eta_5)\right) \\ & \times \Big[\sin\left(k\left(\tilde{x}_F + 2c + \eta_1\right) - \omega t\right) + \eta_5 \cos\left(k\left(\tilde{x}_F + 2c + \eta_1\right) - \omega t\right) \Big] \\ & - \zeta_a \omega \left(1 + k(\eta_{ag0} + \eta_3 - (\tilde{x}_F + c)\eta_5)\right) \\ & \times \Big[\sin\left(k\left(\tilde{x}_F + c + \eta_1\right) - \omega t\right) + \eta_5 \cos\left(k\left(\tilde{x}_F + c + \eta_1\right) - \omega t\right) \Big] \Big\} + \dot{\eta}_5 \end{aligned} \tag{C.11}$$

Once $V_R(x,t)$ is established, the BVP can be solved and the excitation vector can be determined. $\dot{V}_0(t)$ is determined by numerical differentiation.

C.4 Time integration scheme for the platform motion

In this context the motion and the impact loads are jointly dependent, which means that the rigid body responses and the excitation must be solved simultaneously. The wave induced motions are known from the complex transfer functions, but the impact induced motion must be determined from the equation of motion. Equation (C.6) can be rewritten, giving an expression for the impact induced accelerations in the form

$$\ddot{\boldsymbol{\eta}}_s^j = \left(\mathbf{M} + \mathbf{A}^j\right)^{-1} \left(\mathbf{F}_{\text{exc}}^j - \mathbf{B}\dot{\boldsymbol{\eta}}_s^j - \mathbf{C}\boldsymbol{\eta}_s^j\right) \tag{C.12}$$

where the superscript j denote time step so that $t^{j+1} = t^j + \Delta t^j$. Note that $\mathbf{A}$ is time dependent since it contains the time dependent added mass of the wetted deck in addition to the added mass of the submerged volume.

The time integration of Equation (C.12) requires initial conditions. These are

$$\boldsymbol{\eta}_s(t_0) = \boldsymbol{\eta}_s^1 = \left[0,0,0\right]^T \quad \text{and} \quad \dot{\boldsymbol{\eta}}_s(t_0) = \dot{\boldsymbol{\eta}}_s^1 = \left[0,0,0\right]^T, \tag{C.13}$$

where t_0 is the time instant when impact first occur. t_0 is determined from Equation (C.3). The velocities and displacements in the coupled equation system in (C.12) with the given initial conditions may be integrated in time by the standard fourth order Runge-Kutta scheme as outlined in Bergan et al. (1986).

APPENDIX D

Calibrations

All the force transducers were carefully calibrated before they where mounted on to the experimental set up. Each individual force transducer was tested in a test rig, where they were loaded with accurately measure weights. The zero point was set and the output voltage was measured for different loading levels. The loading of the transducers ranged from approximately 98.1N to 490.5N. Each of the measurements was repeated three times and the average value was chosen, but the deviation between the individual recordings was negligible.

Figure D.1 shows calibration curves for the three force transducers used in the experiments. The hollow squares give the value at the measurement points, while the whole lines are linear regression curves fitted to the measurements. This indicates that the output voltage as function of the loading is nearly perfectly linear throughout the whole calibration range. Positive force in Figure D.1 is stretching of the transducer, while negative force represents compression. For compression the weights are simply put on top of the transducer, but for stretching a hook was mounted to the upper end of the the transducers and weights were placed on a tray which was hung over a pulley system and connected to the hook. In the latter case, the zero force point was set such as the weight of the tray and the wire did not contribute to the measured voltage.

The effect of skewed loading was also checked. 11kg was loaded onto the transducers in three different configurations, as depicted in Figure D.2, and the output voltage was recorded. The results are given in Table D.1. They show that for transducers nos. 5610 and 5820 the skewness of the load has no recorded effect on the measured vertical force. For transducer no. 5608, however, the skewness has effect on the output voltage. It is believed that the transducer in position 3 in Figure 4.2 will be in greatest danger of experiencing skewed loading. Based on this it was decided to use transducer no. 5608 in position 1 and transducers nos. 5610 and 5820 in position 2 and 3, respectively.

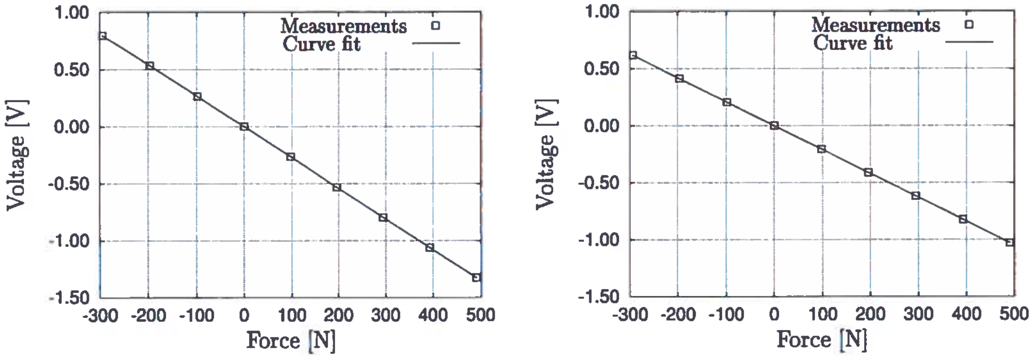

(a) Force transducer no. 5608.

(b) Force transducer no. 5610.

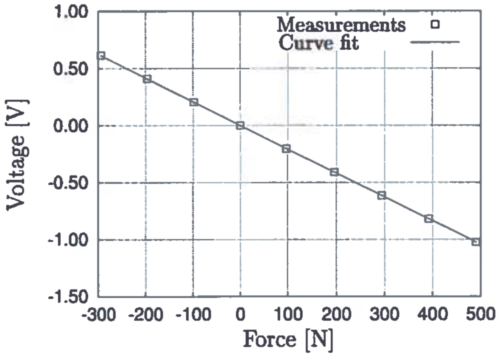

(c) Force transducer no. 5820.

Figure D.1: *Calibration curves for the three force transducers used in the experiments.*

Table D.1: *Output voltage [mV] for the load cases depicted in Figure D.2 for the three force transducers used in the water impact experiments.*

Load case	No. 5608	No. 5610	No. 5820
1	284	233	226
2	294	233	226
3	289	233	226

The force transducers were also calibrated regularly during the experimental program. This was done without removing the transducers from the model by placing a set of different weights

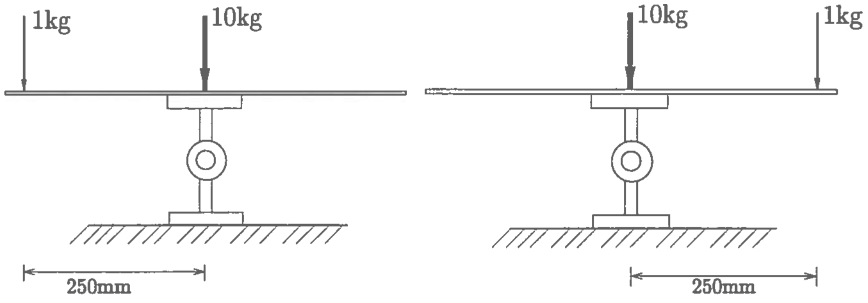

(a) Load case 1. (b) Load case 2.

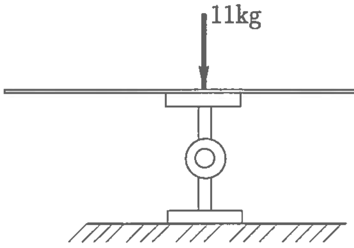

(c) Load case 3.

Figure D.2: *Calibration of force transducer with and without skewed loading.*

inside the model and measure the output voltage. Even though this is a less accurate procedure than the one described above, it seemed to be accurate enough to confirm that the transducer characteristics did not change during the experiments. However, the zero points were set before every run, since these might drift slightly. A second test that was applied regularly was to give the model a set of known submergences with no waves present, and check that the measured force equaled the analytical hydrostatic force. This procedure can of course not check the individual force transducers separately, but it can confirm whether the total vertical force measured is correct or not.

APPENDIX E

Exciting force by conservation of fluid momentum

Faltinsen (1977) derived a formula for the force on a body based on conservation of momentum in the fluid. This can be written as

$$\mathbf{F} = \rho\frac{\mathrm{d}}{\mathrm{d}t}\int\limits_{S_F+S_B} \Phi\mathbf{n}\,\mathrm{d}S + \rho\int\limits_{S_F+S_B} gz\mathbf{n}\,\mathrm{d}S + \rho\int\limits_{S_\infty}\left(\nabla\Phi\frac{\partial\Phi}{\partial n} - \frac{1}{2}|\nabla\Phi|^2\mathbf{n}\right)\mathrm{d}S \tag{E.1}$$

Here S_B and S_F are the body surface and the free surface, respectively, and S_∞ is a control surface in the far field so that S_B, S_F and S_∞ make a closed fluid domain. For a transient problem the contribution from S_∞ can be neglected. However, with incident waves present, contributions from the far field control surface must be taken into account. It is assumed that the total velocity potential can be split into a incident wave potential ϕ_I and a perturbation potential ϕ due to the presence of the body, so that $\Phi = \phi_I + \phi$. Similarly, the total wave elevation is written as $\zeta = \zeta_I + \zeta_D$. Infinite water depth is assumed, and the far field control surface is written as $S_\infty = S_\infty^- + S_\infty^+$ so that S_∞^+ and S_∞^- are vertical surfaces at x_R and x_L, respectively. The computational domain is shown in Figure E.1. x_R and x_L are here assumed to be constants. The vertical force on the body may then be written as

$$\begin{aligned} F_3 =&\rho\frac{\mathrm{d}}{\mathrm{d}t}\int\limits_{S_F+S_B}\phi_I n_3\,\mathrm{d}S + \rho\frac{\mathrm{d}}{\mathrm{d}t}\int\limits_{S_F+S_B}\phi n_3\,\mathrm{d}S \\ &+\rho\int\limits_{S_F} g\zeta_I n_3\,\mathrm{d}S + \rho\int\limits_{S_F} g\zeta_D n_3\,\mathrm{d}S + \rho\int\limits_{S_B} gzn_3\,\mathrm{d}S \\ &+\rho\int\limits_{S_\infty}\left[\frac{\partial\phi_I}{\partial z}\frac{\partial\phi_I}{\partial n} + \frac{\partial\phi_I}{\partial z}\frac{\partial\phi}{\partial n} + \frac{\partial\phi}{\partial z}\frac{\partial\phi_I}{\partial n} + \frac{\partial\phi}{\partial z}\frac{\partial\phi}{\partial n}\right]\mathrm{d}S \end{aligned} \tag{E.2}$$

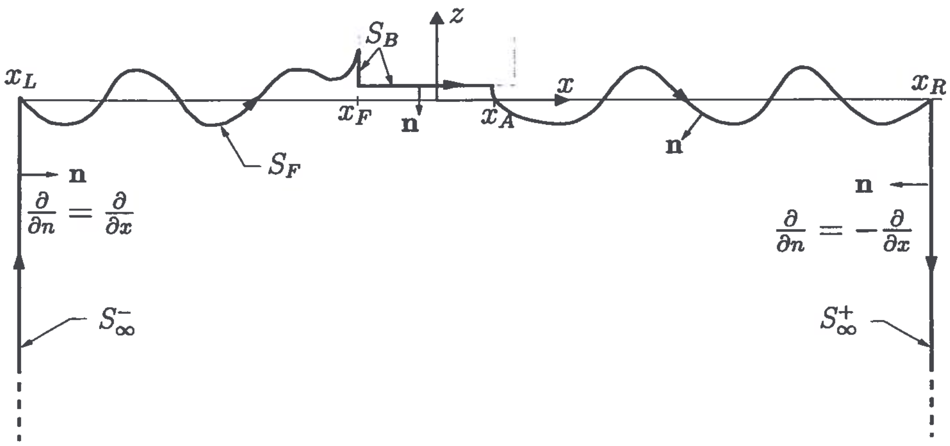

Figure E.1: *The computational domain used when calculating the force on the body by conservation of fluid momentum. Infinite water depth is assumed i.e.* S_∞^- *and* S_∞^+ *continue downward so that* $z \to -\infty$. *The normal vector points into the fluid domain that is enclosed by the surfaces. The integration direction is indicated by arrows along* S_∞, S_F *and* S_B.

In the following, the different terms in Equation (E.2) will be discussed separately. It is assumed that the incident waves are described by second order Stokes theory. Start out by considering the first integral in Equation (E.2). This can be split into a contribution from the free surface and a contribution from the body surface. By Taylor expansion about the mean free surface the incident velocity potential on the free surface can be written as

$$\begin{aligned}\phi_I(x, z = \zeta, t) &= \phi_I(x, 0, t) + \zeta \frac{\partial \phi_I(x, z = 0, t)}{\partial z} + O(k\zeta_a)^3 \\ &\approx \frac{\zeta_a g}{\omega} \sin(kx - \omega t) + \frac{1}{2}\zeta_a^2 \omega \sin(2(kx - \omega t)) \\ &+ \zeta_D \zeta_a \omega \sin(kx - \omega t)\end{aligned} \tag{E.3}$$

When integrating over the free surface the relation $n_3 \, \mathrm{d}S = -\,\mathrm{d}x$ is utilized:

$$
\begin{aligned}
I_1 &= \rho \frac{\mathrm{d}}{\mathrm{d}t} \int\limits_{S_F} \phi_I n_3 \,\mathrm{d}S = -\rho \frac{\mathrm{d}}{\mathrm{d}t} \int\limits_{x_L}^{x_F} \phi_I \,\mathrm{d}x - \rho \frac{\mathrm{d}}{\mathrm{d}t} \int\limits_{x_A}^{x_R} \phi_I \,\mathrm{d}x \\
&= \frac{\rho g \zeta_a}{k\omega} \frac{\mathrm{d}}{\mathrm{d}t} \left[\cos(kx_F - \omega t) - \cos(kx_L - \omega t) + \cos(kx_R - \omega t) - \cos(kx_A - \omega t)\right] \\
&+ \frac{\rho \zeta_a^2 \omega}{4k} \frac{\mathrm{d}}{\mathrm{d}t} \left[\cos(2(kx_F - \omega t)) - \cos(2(kx_L - \omega t)) + \cos(2(kx_R - \omega t)) - \cos(2(kx_A - \omega t))\right] \\
&+ \rho \zeta_a \omega \frac{\mathrm{d}}{\mathrm{d}t} \int\limits_{S_F} \zeta_D \sin(kx - \omega t) n_3 \,\mathrm{d}S \\
&= \frac{\rho g \zeta_a}{k} \left[\sin(kx_F - \omega t) - \sin(kx_L - \omega t) + \sin(kx_R - \omega t) - \sin(kx_A - \omega t)\right] \\
&+ \frac{1}{2} \rho \zeta_a^2 g \left[\sin(2(kx_R - \omega t)) - \sin(2(kx_A - \omega t))\right] \\
&+ \frac{\rho g \zeta_a}{\omega} \left[\frac{\mathrm{d}x_A}{\mathrm{d}t} \sin(kx_A - \omega t) - \frac{\mathrm{d}x_F}{\mathrm{d}t} \sin(kx_F - \omega t)\right] \\
&+ \frac{1}{2} \rho \zeta_a \omega \left[\frac{\mathrm{d}x_A}{\mathrm{d}t} \sin(2(kx_A - \omega t)) - \frac{\mathrm{d}x_F}{\mathrm{d}t} \sin(2(kx_F - \omega t))\right] \\
&+ \rho \zeta_a \omega \frac{\mathrm{d}}{\mathrm{d}t} \int\limits_{S_F} \zeta_D \sin(kx - \omega t) n_3 \,\mathrm{d}S
\end{aligned}
\tag{E.4}
$$

where x_L, x_F, x_A and x_R are defined in Figure E.3. The last term in Equation (E.4) must be solved numerically, and also $\frac{\mathrm{d}x_A}{\mathrm{d}t}$ and $\frac{\mathrm{d}x_F}{\mathrm{d}t}$ are found from the numerical solution. Similarly, the incident wave potential on the body can be found by Taylor expansion and the contribution from ϕ_I on S_B becomes

$$
\begin{aligned}
I_2 &= \rho \frac{\mathrm{d}}{\mathrm{d}t} \int\limits_{S_B} \phi_I n_3 \,\mathrm{d}S \\
&= -\rho \frac{\mathrm{d}}{\mathrm{d}t} \int\limits_{x_F}^{x_A} \left(\frac{\zeta_a g}{\omega} \sin(kx - \omega t) + \eta_{ag0} \zeta_a \omega \sin(kx - \omega t) \right) \,\mathrm{d}x \\
&= \left(\frac{\rho \zeta_a g}{k} + \rho \eta_{ag0} \zeta_a g \right) \left[\sin(kx_A - \omega t) - \sin(kx_F - \omega t)\right] \\
&- \left(\frac{\rho \zeta_a g}{\omega} + \rho \zeta_a \eta_{ag0} \omega \right) \left[\frac{\mathrm{d}x_A}{\mathrm{d}t} \sin(kx_A - \omega t) - \frac{\mathrm{d}x_F}{\mathrm{d}t} \sin(kx_F - \omega t)\right]
\end{aligned}
\tag{E.5}
$$

The contribution to force from the second integral in Equation (E.2) must be solved numerically.

$$
I_3 = \rho \frac{\mathrm{d}}{\mathrm{d}t} \int\limits_{S_F + S_B} \phi n_3 \,\mathrm{d}S \tag{E.6}
$$

Further, the force gets contributions from the wave elevation. The contribution from the incident wave can be determined analytically as

$$\begin{aligned} I_4 &= \rho \int\limits_{S_F} g\zeta_I n_3 \,\mathrm{d}S \\ &= -\rho \int\limits_{x_L}^{x_F} \left[g\zeta_a \cos(kx - \omega t) + \frac{1}{2} g\zeta_a^2 \cos(2(kx - \omega t)) \right] \mathrm{d}x \\ &\quad - \rho \int\limits_{x_A}^{x_R} \left[g\zeta_a \cos(kx - \omega t) + \frac{1}{2} g\zeta_a^2 \cos(2(kx - \omega t)) \right] \mathrm{d}x \\ &= -\frac{\rho g \zeta_a}{k} \left[\sin(kx_F - \omega t) - \sin(kx_L - \omega t) + \sin(kx_R - \omega t) - \sin(kx_A - \omega t) \right] \\ &\quad - \frac{1}{4} \rho g \zeta_a^2 \left[\sin(2(kx_F - \omega t)) - \sin(2(kx_L - \omega t)) + \sin(2(kx_R - \omega t)) - \sin(2(kx_A - \omega t)) \right] \end{aligned} \tag{E.7}$$

while the contribution from ζ_D must be solved numerically and can be written as

$$I_5 = \rho \int\limits_{S_F} g\zeta_D n_3 \,\mathrm{d}S \tag{E.8}$$

The contribution from the body, given that the deck height is fixed at $z = \eta_{ag0}$, simply becomes

$$I_6 = \rho \int\limits_{S_B} g z n_3 \,\mathrm{d}S = -\rho \int\limits_{x_F}^{x_A} g z \,\mathrm{d}x = -\rho g \eta_{ag0} (x_A - x_F) \tag{E.9}$$

Next, the contribution from the far field vertical control surfaces must be evaluated. Note that $\frac{\partial}{\partial n} = \frac{\partial}{\partial x}$ on S_∞^- and $\frac{\partial}{\partial n} = -\frac{\partial}{\partial x}$ on S_∞^+. Further, $\mathrm{d}S = \mathrm{d}z$ on S_∞^- and $\mathrm{d}S = -\mathrm{d}z$ on S_∞^+. This is also indicated in Figure E.1. The four different terms in the integral over S_∞ in Equation (E.2), will be treated separately. Start out with the integral containing ϕ_I only, and only terms to second order in ζ_a are kept. On S_∞^- this becomes

$$I_7 = \rho \int\limits_{S_\infty^-} \frac{\partial \phi_I}{\partial z} \frac{\partial \phi_I}{\partial x} \,\mathrm{d}S = \rho \int\limits_{-\infty}^{0} \frac{\partial \phi_I}{\partial z} \frac{\partial \phi_I}{\partial x} \bigg|_{x = x_L} \mathrm{d}z = \frac{1}{4} \rho \zeta_a^2 g \sin(2(kx_L - \omega t)) \tag{E.10}$$

while the contribution from S_∞^+ is

$$I_8 = \rho \int\limits_{S_\infty^+} \frac{\partial \phi_I}{\partial z} \frac{\partial \phi_I}{\partial x} \,\mathrm{d}S = -\rho \int\limits_{-\infty}^{0} \frac{\partial \phi_I}{\partial z} \frac{\partial \phi_I}{\partial x} \bigg|_{x = x_R} \mathrm{d}z = -\frac{1}{4} \rho \zeta_a^2 g \sin(2(kx_R - \omega t)) \tag{E.11}$$

Further, the contribution from S_∞ due to the term containing ϕ only, is evaluated. Recall that the perturbation velocity potential in the far field is described by a dipole and a multipole in the origin:

$$\phi = \frac{A_1 z}{x^2+z^2} + \frac{A_2 xz}{(x^2+z^2)^2} \tag{E.12}$$

where A_1 and A_2 are the dipole and multipole strengths, respectively. The contribution from S_∞^-, *i.e.* at $x = x_L$ can be written as

$$\begin{aligned} I_9 &= \rho \int\limits_{-\infty}^{0} \frac{\partial \phi}{\partial z}\frac{\partial \phi}{\partial x}\bigg|_{x=x_L} \mathrm{d}z = \rho A_1^2 \int\limits_{-\infty}^{0} \frac{2x_L z - 2x_L z^3}{(x_L^2+z^2)^4} dz \\ &\quad - \rho A_1 A_2 \int\limits_{-\infty}^{0} \frac{x_L^5 - 10x_L^3 z^2 + 5x_L z^4}{(x_L^2+z^2)^5} dz - \rho A_2^2 \int\limits_{-\infty}^{0} \frac{3x_L z - 10x_L^3 z^3 + 3x_L z^5}{(x_L^2+z^2)^6} dz \\ &= -\frac{1}{6}\rho A_1^2 x_L^{-3} + \frac{1}{10}\rho A_2^2 x_L^{-5} \end{aligned} \tag{E.13}$$

and similarly the contribution from S_∞^+, *i.e.* at $x = x_R$ becomes

$$I_{10} = -\rho \int\limits_{-\infty}^{0} \frac{\partial \phi}{\partial z}\frac{\partial \phi}{\partial x}\bigg|_{x=x_R} \mathrm{d}z = \frac{1}{6}\rho A_1^2 x_R^{-3} - \frac{1}{10}\rho A_2^2 x_R^{-5} \tag{E.14}$$

Finally, the contributions from the coupling terms between ϕ and ϕ_I on S_∞ must be evaluated. The first coupling term gives the following contribution:

$$\begin{aligned} \rho \int\limits_{S_\infty} \frac{\partial \phi_I}{\partial z}\frac{\partial \phi}{\partial n} n_3 \,\mathrm{d}S &= \rho \int\limits_{S_\infty^-} \frac{\partial \phi_I}{\partial z}\frac{\partial \phi}{\partial n} n_3 \,\mathrm{d}S + \rho \int\limits_{S_\infty^+} \frac{\partial \phi_I}{\partial z}\frac{\partial \phi}{\partial n} n_3 \,\mathrm{d}S \\ &= \rho \int\limits_{-\infty}^{0} \frac{\partial \phi_I}{\partial z}\frac{\partial \phi}{\partial x}\bigg|_{x=x_L} \mathrm{d}z - \rho \int\limits_{-\infty}^{0} \frac{\partial \phi_I}{\partial z}\frac{\partial \phi}{\partial x}\bigg|_{x=x_R} \mathrm{d}z = I_{11} + I_{12} \end{aligned} \tag{E.15}$$

where

$$
\begin{aligned}
I_{11} = \Bigg\{ & A_1 \int_{-\infty}^{0} \frac{e^{kz}}{x_L^2 + z^2} dz - 2A_1 x_L^2 \int_{-\infty}^{0} \frac{e^{kz}}{(x_L^2 + z^2)^2} dz \\
& - A_2 \int_{-\infty}^{0} \frac{z e^{kz}}{(x_L^2 + z^2)^2} dz - 4A_2 x_L^2 \int_{-\infty}^{0} \frac{z e^{kz}}{(x_L^2 + z^2)^3} dz \Bigg\} \rho\zeta_a\omega \sin(kx_L - \omega t) \\
= {} & \rho\zeta_a\omega \sin(kx_L - \omega t) \times \Bigg\{ A_1 \Bigg[\frac{1}{|x_L|} \big(\mathrm{ci}(k|x_L|) \sin(k|x_L|) - \mathrm{si}(k|x_L|) \cos(kx_L) \big) \Bigg] \\
& - 2A_1 x_L^2 \Big[\frac{1}{2|x_L|^3} \big\{ \mathrm{ci}(k|x_L|) - \mathrm{si}(k|x_L|) \cos(kx_L) - k|x_L| \big(\mathrm{ci}(k|x_L|) \cos(kx_L) \\
& + \mathrm{si}(k|x_L|) \sin(k|x_L|) \big) \big\} \Big] - A_2 \Big[- \frac{1}{2|x_L|^2} \Big(- k|x_L| \big(\mathrm{ci}(k|x_L|) \sin(k|x_L|) \\
& - \mathrm{si}(k|x_L|) \cos(kx_L) \big) \Big) \Big] - 4A_2 x_L^2 \Big[- \frac{k}{8|x_L|^3} \big(\sin(k|x_L|) - k|x_L| \cos(kx_L) \big) \mathrm{ci}(k|x_L|) \\
& - \big(\cos(kx_L) - k|x_L| \sin(k|x_L|) \big) \mathrm{si}(k|x_L|) - \frac{1}{4x_L^4} \Big] \Bigg\} \\
= \Bigg\{ & \left(\left(A_1 k - \frac{1}{2} A_2 k^2 \right) \cos(kx_L) + A_2 \frac{k}{x_L} \sin(kx_L) \right) \mathrm{ci}(k|x_L|) \\
& - \left(\left(A_1 k + \frac{1}{2} A_2 k^2 \right) \sin(kx_L) - A_2 \frac{k}{x_L} \cos(kx_L) \right) \mathrm{si}(k|x_L|) + \frac{A_2}{x_L^2} \Bigg\} \times \rho\zeta_a\omega \sin(kx_L - \omega t)
\end{aligned}
\tag{E.16}
$$

and

$$
\begin{aligned}
I_{12} = \Bigg\{ & - A_1 \int_{-\infty}^{0} \frac{e^{kz}}{x_R^2 + z^2} dz + 2A_1 x_R^2 \int_{-\infty}^{0} \frac{e^{kz}}{(x_L^2 + z^2)^2} dz \\
& + A_2 \int_{-\infty}^{0} \frac{z e^{kz}}{(x_R^2 + z^2)^2} dz + 4A_2 x_R^2 \int_{-\infty}^{0} \frac{z e^{kz}}{(x_R^2 + z^2)^3} dz \Bigg\} \rho\zeta_a\omega \sin(kx_R - \omega t) \\
= -\Bigg\{ & \left(\left(A_1 k - \frac{1}{2} A_2 k^2 \right) \cos(kx_R) + A_2 \frac{k}{x_R} \sin(kx_R) \right) \mathrm{ci}(kx_R) \\
& - \left(\left(A_1 k - \frac{1}{2} A_2 k^2 \right) \sin(kx_R) + A_2 \frac{k}{x_R} \cos(kx_R) \right) \mathrm{si}(kx_R) + \frac{A_2}{x_R^2} \Bigg\} \times \rho\zeta_a\omega \sin(kx_R - \omega t)
\end{aligned}
\tag{E.17}
$$

Here ci(·) and si(·) are the cosine integral function and sine integral function, respectively.

Similarly, the second coupling term's contribution to the vertical force on the body becomes

$$\begin{aligned}\rho \int\limits_{S_\infty} \frac{\partial \phi}{\partial z}\frac{\partial \phi_I}{\partial n} n_3 \,\mathrm{d}S &= \rho \int\limits_{S_\infty^-} \frac{\partial \phi}{\partial z}\frac{\partial \phi_I}{\partial n} n_3 \,\mathrm{d}S + \rho \int\limits_{S_\infty^+} \frac{\partial \phi}{\partial z}\frac{\partial \phi_I}{\partial n} n_3 \,\mathrm{d}S \\ &= \rho \int\limits_{-\infty}^{0} \frac{\partial \phi}{\partial z}\frac{\partial \phi_I}{\partial x}\bigg|_{x=x_L} \mathrm{d}z - \rho \int\limits_{-\infty}^{0} \frac{\partial \phi}{\partial z}\frac{\partial \phi_I}{\partial x}\bigg|_{x=x_R} \mathrm{d}z = I_{13} + I_{14}\end{aligned} \tag{E.18}$$

where

$$\begin{aligned}I_{13} = \Bigg\{ &- 2A_1 x_L \int\limits_{-\infty}^{0} \frac{z e^{kz}}{(x_L^2 + z^2)^2} dz + A_2 x_L \int\limits_{-\infty}^{0} \frac{e^{kz}}{(x_L^2 + z^2)^2} dz \\ &- 4A_2 x_L \int\limits_{-\infty}^{0} \frac{z^2 e^{kz}}{(x_L^2 + z^2)^3} dz \Bigg\} \rho \zeta_a \omega \cos(kx_L - \omega t) \\ = {}& \rho \zeta_a \omega \sin(kx_L - \omega t) \\ \times &\left\{ \left(A_1 k - \frac{1}{2} A_2 k^2\right) \sin(kx_L)\,\mathrm{ci}(|kx_L|) + \left(A_1 k - \frac{1}{2} A_2 k^2\right) \cos(kx_L)\,\mathrm{si}(|kx_L|) \right\}\end{aligned} \tag{E.19}$$

and

$$\begin{aligned}I_{14} = \Bigg\{ &2A_1 x_R \int\limits_{-\infty}^{0} \frac{z e^{kz}}{(x_R^2 + z^2)^2} dz - A_2 x_R \int\limits_{-\infty}^{0} \frac{e^{kz}}{(x_R^2 + z^2)^2} dz \\ &+ 4A_2 x_R \int\limits_{-\infty}^{0} \frac{z^2 e^{kz}}{(x_R^2 + z^2)^3} dz \Bigg\} \rho \zeta_a \omega \cos(kx_R - \omega t) \\ = {}& -\rho \zeta_a \omega \sin(kx_L - \omega t) \\ \times &\left\{ \left(A_1 k - \frac{1}{2} A_2 k^2\right) \sin(kx_R)\,\mathrm{ci}(kx_R) - \left(A_1 k - \frac{1}{2} A_2 k^2\right) \cos(kx_R)\,\mathrm{si}(kx_R) \right\}\end{aligned} \tag{E.20}$$

When calculating I_{11} and I_{13} one must keep in mind that $x_L < 0$, and caution must be used when evaluating the integrals. The absolute value $|x_L|$ must be used in ci and si. It is further used that $|x_L| = -x_L$ and that $\sin(k|x_L|) = -\sin(kx_L)$ and $\cos(k|x_L|) = \cos(kx_L)$.

All contributions to the vertical force given in Equation (E.2) are now evaluated and the vertical force per unit width can now be determined from

$$\begin{aligned}
F_3 &= \sum_{j=1}^{14} I_j \\
&= \rho g \zeta_a \left(\frac{1}{k} + \eta_{ag0}\right) \left[\sin(kx_A - \omega t) - \sin(kx_F - \omega t)\right] \\
&\quad - \frac{1}{4}\rho \zeta_a^2 g \left[\sin(2(kx_A - \omega t)) - \sin(2(kx_F - \omega t))\right] \\
&\quad + \frac{1}{2}\rho \zeta_a^2 \omega \left[\frac{\mathrm{d}x_A}{\mathrm{d}t} \sin(2(kx_A - \omega t)) - \frac{\mathrm{d}x_F}{\mathrm{d}t} \sin(2(kx_F - \omega t))\right] \\
&\quad - \rho \zeta_a \eta_{ag0} \omega \left[\frac{\mathrm{d}x_A}{\mathrm{d}t} \sin(kx_A - \omega t) - \frac{\mathrm{d}x_F}{\mathrm{d}t} \sin(kx_F - \omega t)\right] \\
&\quad + \rho \frac{\mathrm{d}}{\mathrm{d}t} \int\limits_{S_F} \zeta_D \zeta_a \sin(kx - \omega t) n_3 \,\mathrm{d}S + \rho \frac{\mathrm{d}}{\mathrm{d}t} \int\limits_{S_F + S_B} \phi n_3 \,\mathrm{d}S + \rho \int\limits_{S_F} g \zeta_D \,\mathrm{d}S \\
&\quad - \rho g \eta_{ag0}(x_A - x_F) + \frac{1}{6}\rho A_1^2 (x_R^{-3} - x_L^{-3}) - \frac{1}{10}\rho A_2^2 (x_R^{-5} - x_L^{-5}) \\
&\quad + \Bigg\{ \left[\left(A_1 - \frac{1}{2}A_2 k^2\right) (\cos(kx_L) + \sin(kx_L)) + A_2 \frac{k}{x_L} \sin(kx_L) \right] \mathrm{ci}(k|x_L|) \\
&\quad - \left[\left(A_1 + \frac{1}{2}A_2 k^2\right) \sin(kx_L) + \left(A_1 - \frac{1}{2}A_2 k^2\right) \cos(kx_L) + A_2 \frac{k}{x_L} \cos(kx_L) \right] \mathrm{si}(k|x_L|) + \frac{A_2}{x_L^2} \Bigg\} \\
&\quad \times \rho \zeta_a \omega \sin(kx_L - \omega t) \\
&\quad - \Bigg\{ \left[\left(A_1 - \frac{1}{2}A_2 k^2\right) (\cos(kx_R) + \sin(kx_R)) \right] (\mathrm{ci}(kx_R) + \mathrm{si}(kx_R)) + \frac{A_2}{x_R^2} \Bigg\} \\
&\quad \times \rho \zeta_a \omega \sin(kx_R - \omega t)
\end{aligned} \tag{E.21}$$

Gradshteyn and Ryzhik (1994) define ci(kx) and si(kx) as

$$\mathrm{ci}(kx) = \left[\gamma + \log(kx) + \sum_{j=1}^{\infty} (-1)^j \frac{(kx)^{2j}}{2j(2j)!}\right] \tag{E.22}$$

and

$$\mathrm{si}(kx) = \left[-\frac{\pi}{2} + \sum_{j=1}^{\infty} (-1)^{j+1} \frac{(kx)^{2j-1}}{(2j-1)(2j-1)!}\right] \tag{E.23}$$

where $\gamma = 0.57721\ 56649\ldots$ is Euler's constant. However, these alternating series expansions are difficult to make converge for large kx values. Abramowitz and Stegun (1964) give rational approximations for ci(kx) and si(kx) that are valid for $1 \leq kx \leq \infty$ as

$$\mathrm{ci}(kx) = f(kx)\sin(kx) - g(kx)\cos(kx) \tag{E.24}$$

and

$$\mathrm{si}(kx) = -f(kx)\cos(kx) - g(kx)\sin(kx) \tag{E.25}$$

where

$$f(kx) = \frac{1}{kx}\left(\frac{(kx)^8 + a_1(kx)^6 + a_2(kx)^4 + a_3(kx)^2 + a_4}{(kx)^8 + b_1(kx)^6 + b_2(kx)^4 + b_3(kx)^2 + b_4}\right) + \epsilon_1(kx) \tag{E.26}$$

and

$$g(kx) = \frac{1}{(kx)^2}\left(\frac{(kx)^8 + c_1(kx)^6 + c_2(kx)^4 + c_3(kx)^2 + c_4}{(kx)^8 + d_1(kx)^6 + d_2(kx)^4 + d_3(kx)^2 + d_4}\right) + \epsilon_2(kx) \tag{E.27}$$

These approximations are used in the numerical calculation of the cosine and sine integral functions, and the error is given as $|\epsilon_1(kx)| < 5 \cdot 10^{-7}$ and $|\epsilon_2(kx)| < 3 \cdot 10^{-7}$ according to Abramowitz and Stegun (1964). The coefficients are given as

$$\begin{array}{llll}
a_1 = 38.027264 & b_1 = 40.021433 & c_1 = 42.242855 & d_1 = 48.196927 \\
a_2 = 265.187033 & b_2 = 322.624911 & c_2 = 302.757865 & d_2 = 482.485984 \\
a_3 = 335.677320 & b_3 = 570.236280 & c_3 = 352.018498 & d_3 = 1114.978885 \\
a_4 = 38.102495 & b_4 = 157.105423 & c_4 = 21.821899 & d_4 = 449.690326
\end{array}$$

To find the total vertical force on a deck of with finite width, the force from Equation (E.21) must be multiplied by the deck width, B.

PREVIOUS DR.ING. THESES

Department of Marine Hydrodynamics

Løtveit, Magne : A Study of Pressure- and Velocity Relations in the Slip-Stream of Propellers of Single Screw Ships to clarify the Propeller Action behind the Hull. 1963. (in Norwegian)

Dahle, Emil Aall : A Study of the Coefficients in the Differential Equations for the Rolling Motion of a Vessel. 1971, (in Norwegian)

Langfeldt, Jan N. : A Theoretical and Experimental Study of the Feasibility of Two-Phase (Gas-Water) Jet Propulsion of Craft. 1972.

Berg, Tor Einar : Manoeuvring of Vessels. 1978. (in Norwegian)

Skjørdal, Svein O. : Wave Induced Oscillations of Ship Hulls. 1978.

Nielsen, Finn G. : Hydrodynamic Relations of Oil Booms. 1980.

Liapis, Nicolas : Hydrodynamic Analysis of the Ship-Buoy System. 1980.

Pettersen, Bjørnar : Calculation of Potential Flow about Ship Hulls in Shallow Water with Particular Application to Manoeuvring. 1980.

Rye, Henrik : Ocean Wave Groups. 1981.

Utnes, Torbjørn H. : Forward-Speed Effects on the Hydrodynamic Motion Coefficients of a Surface-Piercing Body. 1982

Børresen, Rolf : The unified theory of ship motions in water of finite depth. 1984.

Aarsnes, Jan Vidar : Current Forces on Ships. 1984.

Skomedal, Nere : Application of a Vortex Tracking Method to Three-Dimensional Flow Past Lifting Surfaces and Blunt Bodies. 1985.

Løken, Arne Edvin : Three-dimensional second order hydrodynamic effects on ocean structures in waves. 1986.

Aanesland, Vidar : A Theoretical and Numerical Study of Ship Wave Resistance. . 1986.

Sortland, Bjørn : Force Measurements in Oscillating Flow on Ship Sections and Circular Cylinders in a U-Tube Water Tank. 1986.

Falch, Sigurd : A numerical study of slamming of two-dimensional bodies. 1986.

Lian, Walter : A numerical study of two-dimensional separated flow past bluff bodies at moderate KC-numbers. 1986

Braathen, Arne : Application of a vortex tracking method to the prediction of roll damping of a two-dimensional floating body. 1987.

Gang Miao : Hydrodynamic Forces and Dynamic Responses of Circular Cylinders in Wave Zones. 1989.

Greenhow, Martin : Linear and Non-Linear Studies of Waves and Floating Bodies. Part I and Part II. 1989.

Chang Li : Force Coefficients of Spheres and Cubes in Oscillatory Flow with and without Current. 1989.

Jæger, Arild : Seakeeping, Dynamic Stability and Performance of a Wedge Shaped Planing Hull. 1989.

Hoff, Jan Roger : Three-dimensional Green function of a vessel with forward speed in waves. 1990.

Rong Zhao : Slow-Drift of a Moored Two-Dimensional Body in Irregular Waves. 1990.

Løland, Geir : Current Forces and Flow through Fish Farms. 1991.

Krogstad, Jørgen R. : Second-order Loads in Multidirectional Seas. 1991.

Mørch, Hans J. B. : Aspects of Hydrofoil Design; with Emphasis on Hydrofoil Interaction in Calm Water. 1992.

Steen, Sverre : Cobblestone Effect on SES. 1993.

Kvålsvold, Jan : Hydroelastic Modelling of Wetdeck Slamming on Multihull Vessels. 1994.

Ulstein, Tore : Nonlinear Effects of a Flexible Stern Seal Bag on Cobblestone Oscillations of an SES. 1995.

Solaas, Frøydis : Analytical and Numerical Studies of Sloshing in Tanks. 1995.

Bratland, Anne K. : Wave-Current Interaction Effects on Large-Volume Bodies in Water of Finite Depth. 1995.

Herfjord, Kjell : A Study of Two-dimensional Separated Flow by a Combination of the Finite Element Method and Navier-Stokes Equations. 1995.

Pedersen, Egil : A Nautical Study of Towed Marine Seismic Streamer Cable Configurations. 1996.

Hansen, Edmond H. : A Discrete Element Model to Study Marginal Ice Zone Dynamics and the Behaviour of Vessels Moored in Broken Ice. 1998.

Haugen, Elin Marita : Hydroelastic Analysis of Slamming on Stiffened Plates with Application to Catamaran Wetdecks. 1999.

Tønnesen, Rune : A Finite Element Method Applied to Unsteady Viscous Flow Around 2D Blunt Bodies with Sharp Corners. 1999

Haslum, Herbjørn Alf : Simplified Methods Applied to Nonlinear Motion of Spar Platforms. 2000.